Research Programme of the Research Fund for Coal and Steel

FIre and Seismic performances of Hybrid fire WALLs in case of single-storey industrial and commercial steel buildings (FISHWALL)

Fire parametric numerical studies

Christophe RENAUD – CTICM

WP3: Fire behaviour of a hybrid fire wall solution associated with unprotected steel structure

Deliverable: D3.5

Contributing partners		
	CVUT	Czech Republic

Grant agreement No: 101034083

Version	Issue	Purpose	Author	Reviewer	Approved
A	D3.5	25/06/2025	C. Renaud	All partners	
B	D3.5	30/06/2025 (Comments from partners considered)	C. Renaud	B. Zhao	C. Renaud

TABLE OF CONTENTS

ABSTRACT

It is well known that the intrinsic fire resistance of single-storey unprotected steel-framed buildings is largely sufficient to guarantee the evacuation of occupants in the event of fire. In consequence, for this type of building, the main concern of national fire regulations in Europe is how to prevent the spread of fire to the whole building. To achieve this objective, two performances shall be usually satisfied, namely, the appropriateness of constructive systems to ensure that there is no progressive collapse between fire compartments, and the efficiency of fire walls to stop the fire inside the initial compartment regardless of the state of structures exposed to fire. In practice, many constructional solutions can be implemented in order to preserve the integrity of the fire walls, while accepting that the fire exposed part of the structure may collapse. One of the most common solutions is to place a non-load bearing wall between two independent steel structures and to connect it to them by means of "fusible" links. In fire situation, these fusible links have to allow the wall to be disconnected from the structure affected by fire without endangering the separating function of the wall, which shall remain fixed to the steel structure on the other side of the wall and therefore not exposed to fire. However, due to the lack of corresponding scientific evidence, questions are being very often raised about the real efficiency of such systems in fire situation, which, in certain cases, have also to provide an adequate seismic resistance, if they are used in seismic areas.

Today, concrete or masonry wall solutions are frequently used for the compartmentation of buildings, predominately for low-rise commercial and industrial steel buildings. However, as an alternative, lightweight sandwich panels (comprising two thin flat metal faces and an insulated core) could become an appropriate steel fire wall solution, offering numerous benefits in comparison to other solutions, including fire resistance, durability, flexibility, easy dismounting and fast construction times. But, there is an evident lack of technical information about the adequate fire performance of such type of wall solutions when they are implemented in single-storey buildings with unprotected steel structure, which constitutes a major obstacle for their large use.

In this context, the overall goal of the FISHWALL project is to develop a design guidance and recommendations for an innovative hybrid fire wall solution based on lightweight steel-faced sandwich panels associated with unprotected steel structure under both fire and seismic actions, but considered individually. This will be achieved through the following specific tasks: i) Establishing of a full range of experimental evidence about the fire and seismic behaviour of the investigated hybrid fire wall solution by carrying out a number of tests; ii) Investigating intensively the fire and seismic performances of the above hybrid fire wall solution in combination with unprotected single-storey steel structures through a variety of parametric numerical studies by means of validated FE numerical models; iii) Developing both cost-effective and innovative "fusible" connection systems for fire walls to be used in combination with unprotected steel structures of single-storey buildings; and iv) Developing a design guidance and practical recommendations for the studied hybrid fire wall and fusible links solutions, on the basis of above studies, from which engineers can carry out very efficient design.

This report presents the results of various parametric numerical studies conducted as part of the project for the fire situation. These studies examined the fire resistance of the developed fusible link solutions, as well as the fire behaviour of single-storey, steel-framed buildings fitted with partition fire walls connected to these links. The studies also examined the behaviour of steel purlins passing through firewalls made of sandwich panels in the event of a fire.

1 INTRODUCTION

To develop simple analytical models for evaluating the ultimate bearing capacity of the developed fusible link solution under fire conditions, parametric studies were performed using the three-dimensional finite element model developed as part of the project and described in Deliverable D3.4 [12]. These studies involved varying the parameters affecting the fire resistance of the fusible links, considering fire exposure according to the standard fire curve. Three-dimensional global structural analyses were also performed to investigate the mechanical response of steel structures associated with firewalls when using the developed 'fusible' links under realistic fire conditions. This was done to ensure that the behaviour of the fusible links is appropriate when designed according to the design provisions defined in the project. A parametric study was then conducted on steel purlins passing through a fire wall made of sandwich panels, again using the FE models described in project deliverable D3.4. This study aimed to investigate purlin deformation close to the fire wall, as well as the effect of steel roof decking dimensions on purlin heating, particularly at the level of the purlin encasement. This provides additional data to complement the fire test results and could be useful for defining appropriate design provisions related to fire protection for steel purlins with the studied panel encasement system.

This deliverable presents the main results of these parametric studies and the case studies.

2 PARAMETRIC STUDY OF STEEL PURLINS CROSSING THROUGTH FIRE WALLS

A parametric numerical analysis of a steel purlin passing through a fire wall made of sandwich panels was carried out using the FE models described in project deliverable D3.4 [12]. The analysis considered steel sheets of different sizes and support conditions, as well as purlin spans. This parametric study aimed to investigate how the dimensions of the sheets affect the heating of the steel purlin, particularly at the level of the purlin encasement, as well as the deformations of the purlin close to the fire wall. The main results of the parametric study are summarised below.

2.1 Modelling assumptions and investigated parameters

The analyses were carried out using the same procedure and most of the modelling assumptions as those used in the numerical analysis of the fire test. However, the following changes should be highlighted:

- The models were updated according to the sizes of the considered steel sheet. The details of investigated steel sheets are reported in Figure 2.1. They have been chosen according to the wave widths, to cover a wide range of steel sheets with wave of varying widths. All sheets are 1 mm thick. They are assumed to be covered with 100 mm thick mineral wool insulation (125 kg/m³).
- The purlin and steel sheets are exposed to ISO standard fire.
- The purlin is made of S275 steel.
- The purlin is a double-span purlin across three supports, with one of the spans being exposed to fire. On the fire-exposed side, the purlin has 6m or 10m span.
- Different sets of boundary conditions are considered for the mechanical analyses (as illustrated in Figure 2.2 and Figure 2.3:
  - **"NFB Continuous" case**: The purlin is only laterally supported at the supports, allowing for free lateral-torsional buckling between the supports. Additionally, by considering a continuous member, the purlin end that is supported in the fire-exposed area is fixed throughout the cross-section (axially restrained), which prevent thermal expansion (see Figure 2.2).
  - **"FB Continuous" case:** The purlin at the connection to the trapezoidal steel sheeting is assumed to be laterally restrained by preventing lateral displacement at the connection points. This connection is also assumed to provide partial torsional restraint to the purlin. This partial torsional restraint given to the purlin by the sheet connected to its top flange is represented by rotational springs acting on the top flange of the purlin, with spring stiffness calculated according to EN 1993-1-3. Additionally, by considering a continuous member, the purlin end that is supported in the fire-exposed area is fixed throughout the cross-section (axially restrained), which prevent thermal expansion (see Figure 2.2).
  - **"NFB hinged" case:** The purlin is only laterally supported at the supports, allowing for free lateral-torsional buckling between the supports. Additionally, by considering a hinged member, the end purlin that is supported in the fire-exposed area is only fixed (axially restrained) at the level of the lower purlin flange (see Figure 2.3).
  - **"FB hinge" case:** The purlin at the connection to the trapezoidal steel sheeting is assumed to be laterally restrained by preventing lateral displacement at the connection points. This connection is also assumed to provide partial torsional restraint to the purlin. This partial torsional restraint given to the purlin by the sheet connected to its top flange is represented by rotational springs acting on the top flange of the purlin, with spring stiffness calculated according to EN 1993-1-3. Additionally, by considering a hinged member, the end purlin that is supported in the fire-exposed area is only fixed (axially restrained) at the level of the lower purlin flange (see Figure 2.2).

- In addition to its own weight, the purlin also carries a uniformly distributed load equal to the design distributed load that the purlin can support at normal temperatures, in accordance with the Eurocode guide published by CTICM. [16]. These loads are listed in Table 1. It is assumed that they will remain constant throughout the duration of the fire exposure.

a) ***JI-42-252-1010***

b) ***JID-137-310-930***

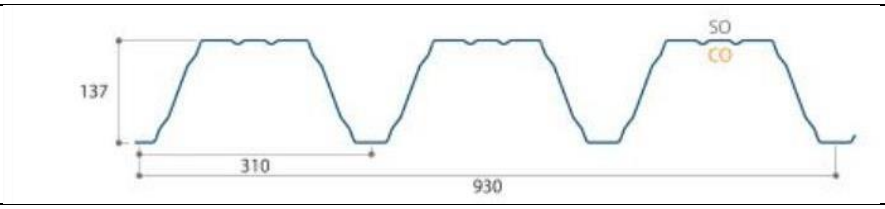

c) ***ALTEO 106.750***

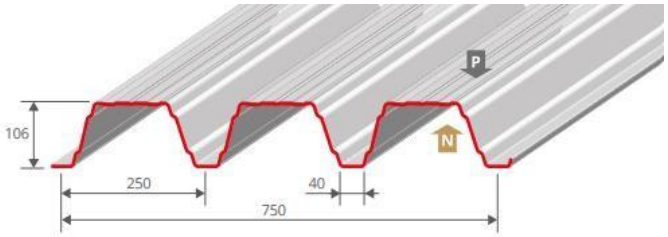

d) ***JI-73-195-780***

e) ***JI-113-320-960***

Figure 2.1: Geometrical details of steel sheets

Table 1: Uniform distributed load in KN/m applied on the purlin

Purlin span	Load (kN/m)
6m	11.31 x 1.13
6m	15.75 x 0.78
10m	3.86 x 1.13
10m	5.61 x 0.78

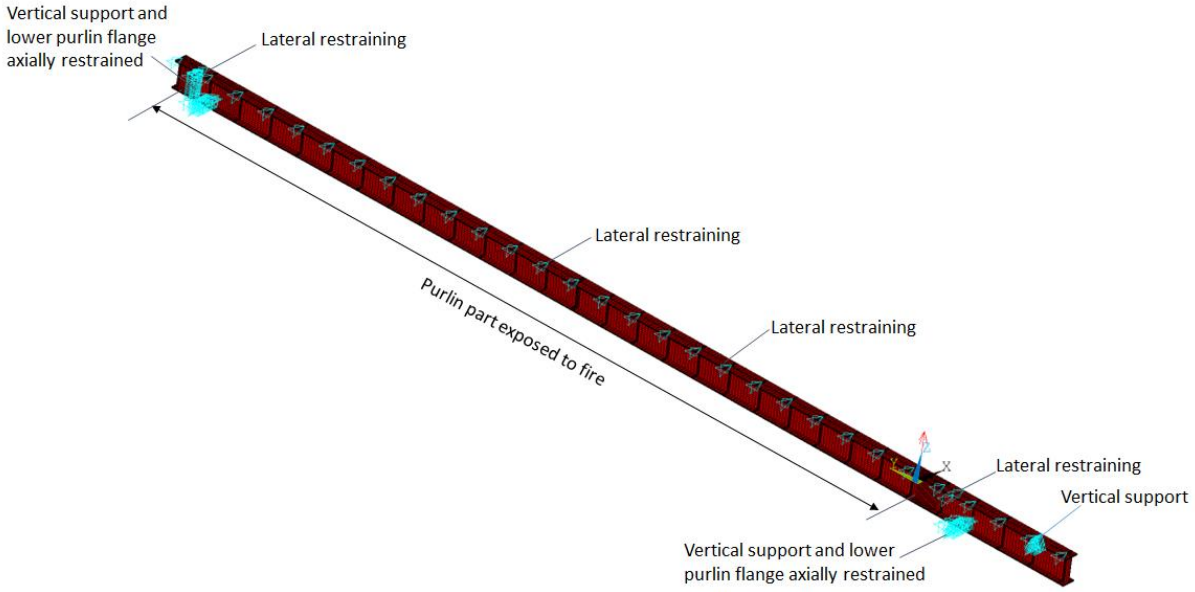

Figure 2.2: Mechanical model of the purlin with "FB hinged" boundary conditions

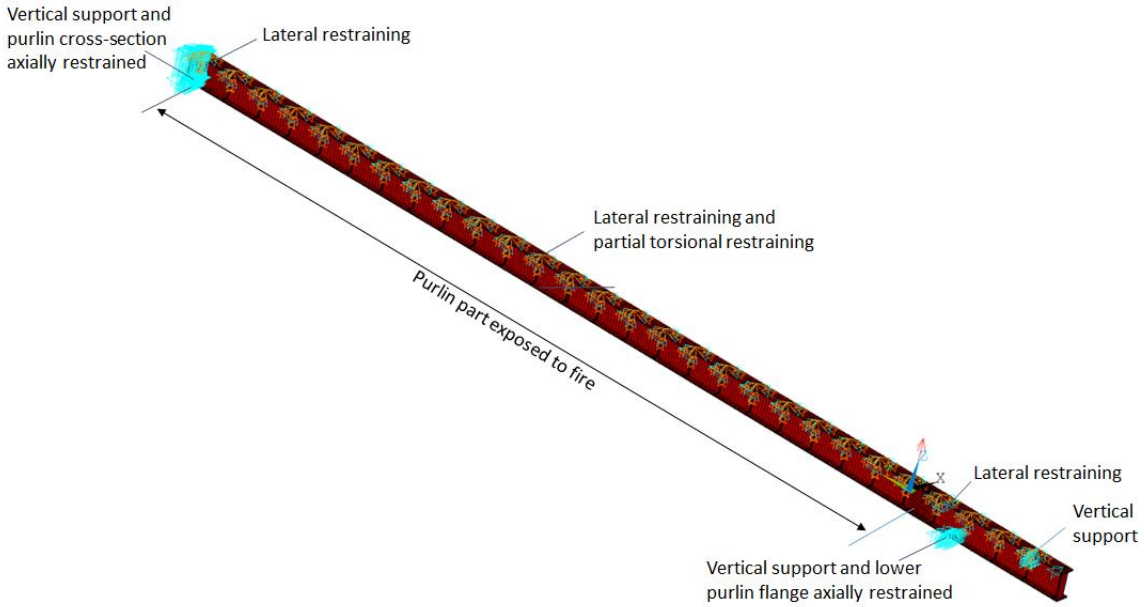

Figure 2.3: Mechanical model of the purlin with "NFB Continuous" boundary conditions

For information purposes, the following figures show the thermal models developed to determine the thermal behaviour of the parametric study cases. It should be noted that thermal analyses were conducted with the assumption that the wave cavities at the encasement level were either unfilled or filled with mineral wool, to evaluate the effect of filling the wave cavities on the purlin's thermal behaviour. Thermal analyses assuming filled wave cavities were performed on two types of profiled steel sheet only: the JI-42-252-1010 sheets, which have the smallest corrugations, and the JID-137-310-930 sheets, which have the largest.

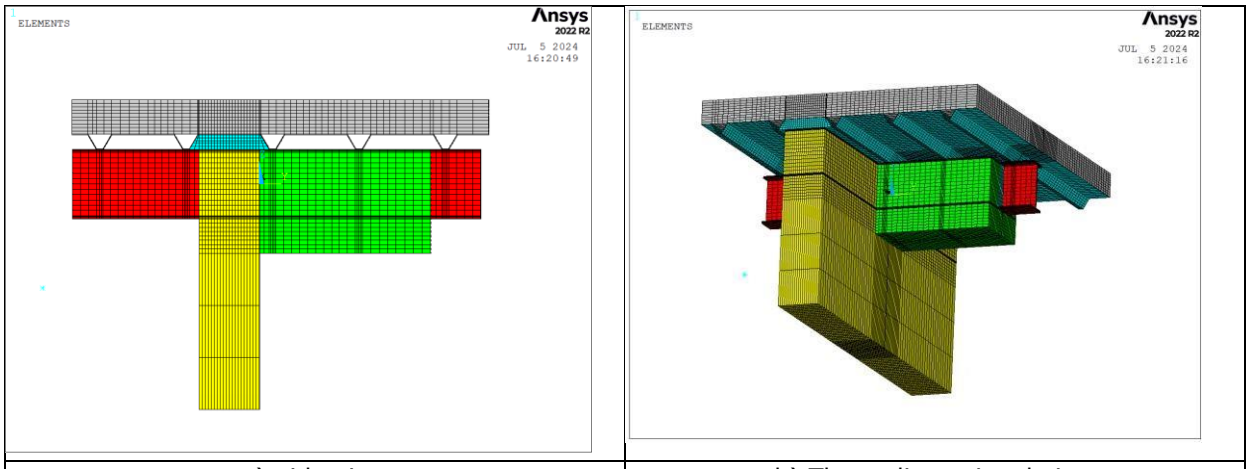

a) side view	b) Three-dimensional view

Figure 2.4: Thermal model developed for the steel sheet JI-42-252-1010

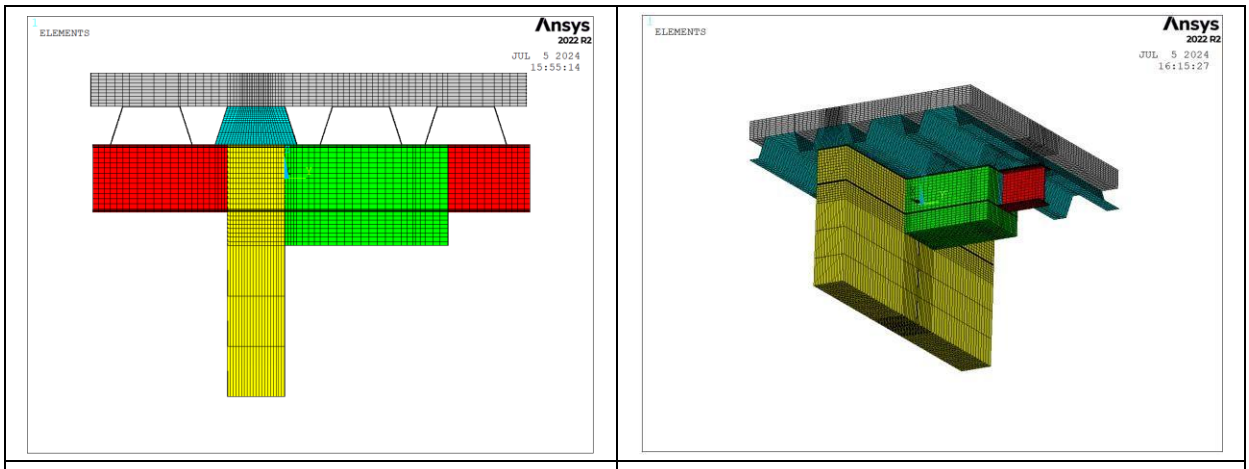

a) side view	b) Three-dimensional view

Figure 2.5: Thermal model developed the steel sheet JI-113-320-960

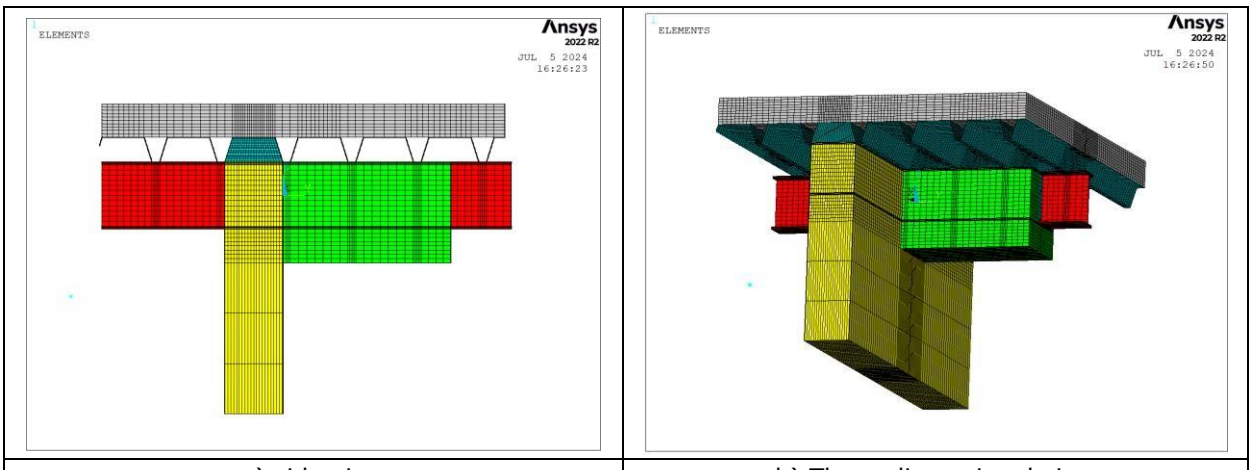

a) side view	b) Three-dimensional view

Figure 2.6: Thermal model developed for the steel sheet JI-73-195-780

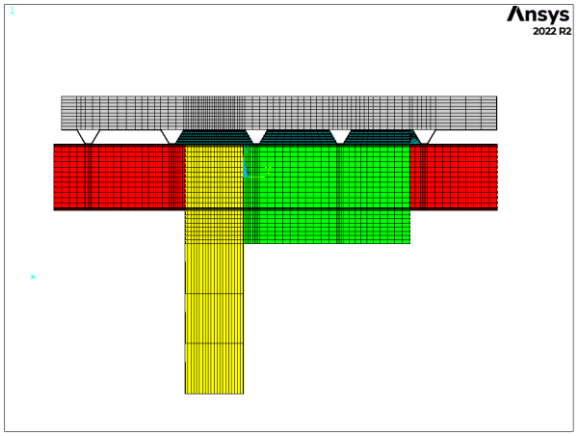

a) side view

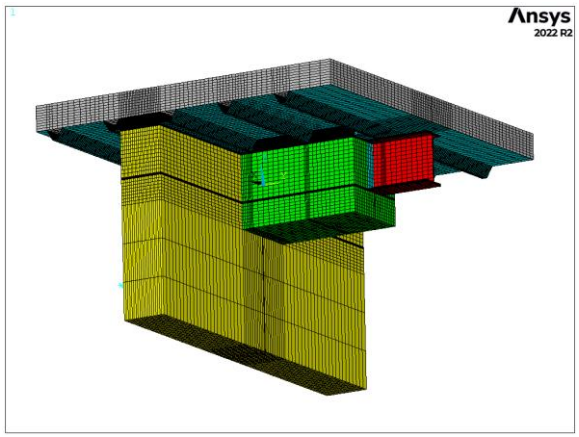

b) Three-dimensional view

Figure 2.7: Thermal model developed for the steel sheet JI-73-195-780 with cavities filled at the purlin encasement

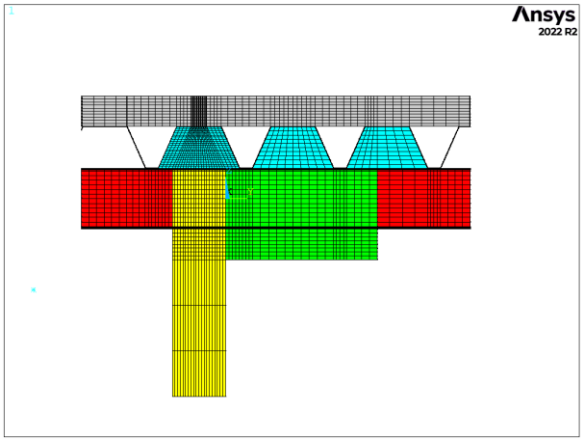

a) side view

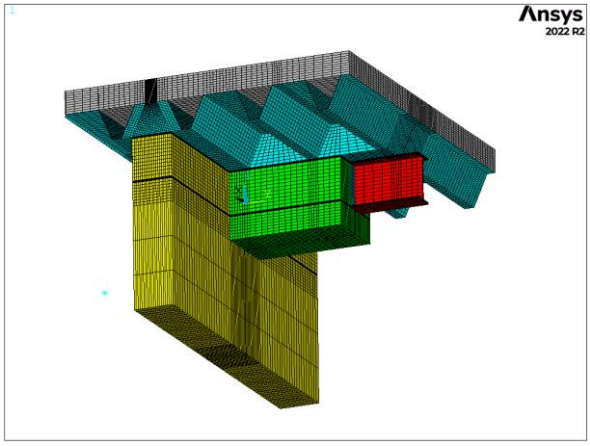

b) Three-dimensional view

Figure 2.8: Thermal model developed for the steel sheet JID-137-310-930 with cavities filled at the purlin encasement

2.2 Results of thermal analyses

2.2.1 Thermal response of studied steel sheet configurations without waves filling

In this section, the following figures show the predicted temperature fields in a steel purlin supporting the steel sheets "JI-73-195-780", "JI-42-252-1010" and "JID-137-320-960" without additional waves filling, at different fire exposure times. The other figures show a comparison of the temperature rise predicted for the same cases, across the purlin sections considered representative (see Figure 2.9. The sections considered are S1 (at the level where the trapezoidal sheet is in contact with the purlin) and S2 (at the level of a cavity formed between the top flange of the purlin and the trapezoidal sheet) immediately after the purlin encasement; S4 (at the level where the trapezoidal sheet is in contact with the purlin) and S5 (at the level of a cavity formed between the top flange of the purlin and the trapezoidal sheet) at the centre of the purlin encasement; and S7 (at the level where the trapezoidal steel sheet is in contact with the purlin) and S8 (at the level of a cavity formed between the purlin top flange and the trapezoidal steel sheet) located at the centre of the purlin span under consideration. . Detailed results for the other sections are given in the appendices.

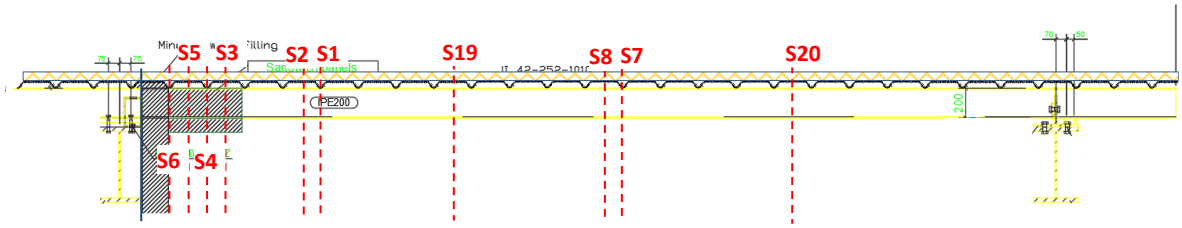

Figure 2.9: Location of temperature output sections along purlin

The analysis of the temperature rises calculated in the different purlin sections considered according to the three types of sheets: JI-42-252-1010, JI-73- 195-780 and JI-113-320-960 shows that:

- For section S1 (in contact with the steel sheet), in the part directly exposed to the fire, the temperature rise at purlin level for the three pans shows almost similar behavior over time, although purlin web (point P2) heats up more quickly and reaches the highest temperatures, particularly during the first phases of exposure to fire (up to 1750 seconds), while the upper flange (point P1) remains coolest and the lower flange (point P3) reaches intermediate temperatures (variation of around 10°C between the three parts). At the level of the purlin top flange (point P1) the heating of the three considered steel sheets shows a very small variation (around 5°C).

- For section S2, (located below the wave trough) in the area directly exposed to the fire, the heat-ups show that the three types of sheets exhibit a broadly comparable temperature evolution over time. However, the purlin web (points P3, P4, P5) shows a more rapid rise in temperature, reaching the highest values in the first 2,000 seconds, while the top flange (point P1) remains the coldest part, and the bottom flange (point P6) shows intermediate temperatures, with a difference of around 20°C between the three parts of the purlin. In the case of the top flange (point P1), as in the case of section (S1), the difference in temperature rise between the three steel sheets remains very small (around 5°C up to 2500 seconds), although the JI-73-195-780 sheet shows a slightly quickly temperature rise, followed by the JI-113-320-960 sheet, while the JI-42-252-1010 sheet has the lowest temperature rise. After 2500 seconds, temperatures gradually align to reach around 935°C at the end of the thermal analyses. On the other hand, for the purlin web (point sP3, P4, P5) and the bottom flange (P6), the temperature curves are virtually superimposed, indicating identical thermal behavior between the three steel sheets in these areas.

- For section S4 (in contact with the steel sheet), the differences in heating between the three parts of the purlin are more pronounced at the level of the encasement. At the level of the upper flange (point P1), a rapid rise in temperature is observed for all three types of steel sheet up to 1000 seconds. At this stage, the JI-73-195-780 sheet reaches a temperature of around 505 °C, the JI-113-320-960 sheet reaches 480 °C, and the JI-42-252-1010 sheet reaches 400 °C. This indicates a noticeable difference of 30–80 °C between the three types of steel sheet. This gap widens further between 1000 and 2000 seconds. After 2000 seconds, the temperature has risen to around 700 °C for the JI-73-195-780 sheet and 680 °C for the JI-113-320-960 sheet, compared to just 590 °C for the JI-42-252-1010 sheet — a differential of around 110 °C between the two extremes. This trend continues during the final fire exposure phase (from 2000 to 3600 seconds), during which time temperatures evolve more slowly but the gap remains constant. After 3600 seconds, the JI-73-195-780 sheet has reached approximately 830°C, the JI-113-320-960 sheet has approached 805°C and the JI-42-252-1010 sheet remains at around 720°C. The same behaviour as that observed at the upper flange (point P1) can be seen at the level of the purlin web (point P3). During the initial 1000 seconds of exposure to fire, the three sheets studied exhibited a rapid rise in temperature, reaching approximately 270°C for the JI-73-195-780 sheet, 260°C for the JI-113-320-960 sheet, and 160°C for the JI-42-252-1010 sheet. This indicates a significant temperature difference of 110°C between the extremes. Between 1000 and 2000 seconds, this difference increases: at 2000 seconds, temperatures reach around 490°C and 475°C for the JI-73-195-780 and JI-113-320-960 sheets respectively, compared with just 340°C for the JI-42-252-1010 sheet — a difference of around 150°C between the two extremes. In the

final phase (from 2000 to 3600 seconds), temperatures evolve more slowly, yet the gap remains constant. After 3600 seconds, the JI-73-195-780 sheet has reached around 670°C, the JI-113-320-960 sheet has approached 640°C and the JI-42-252-1010 sheet remains at around 540°C. The differential between the two extremes is around 130°C. The same behaviour can be observed at the lower flange (point P4) as at the purlin web (point P3). During the initial exposure to fire (up to 1000 seconds), the three sheets experience a rapid temperature increase, reaching approximately 200°C for the JI-73-195-780 sheet, 185°C for the JI-113-320-960 sheet, and 75°C for the JI-42-252-1010 sheet. This indicates an important temperature difference of 125°C between the extremes. Between 1000 and 2000 seconds, the temperature difference between the three steel sheets increases. At 2000 seconds, the temperature reaches around 420 °C for the JI-73-195-780 sheet and 400 °C for the JI-113-320-960 sheet, compared to 220 °C for the JI-42-252-1010 sheet. The difference between the two extremes is around 200 °C. In the final phase (from 2000 to 3600 seconds), temperatures evolve more slowly, but the gap remains constant. After 3,600 seconds, the JI-73-195-780 sheet reaches approximately 620 °C, the JI-113-320-960 sheet approaches 600 °C and the JI-42-252-1010 sheet remains at around 460 °C. The temperature difference between the extremes is approximately 160 °C. Throughout section S4, the JI-73-195-780 sheet heats up slightly faster than the JI-113-320-960 sheet, while the JI-42-252-1010 sheet experiences the least temperature increase.

- • For section S5, which is located in the enclosure below the wave trough, the heating trend shows more pronounced differences between the three types of steel sheet investigated. At the level of the upper flange (point P1), temperatures rise quickly during the first few seconds of exposure to the fire, reaching approximately 450°C for the JI-73-195-780 sheet, 420°C for the JI-113-320-960 sheet, and 350°C for the JI-42-252-1010 sheet after 1,000 seconds. This indicates significant heating differences of between 70 and 100°C. The difference increases further between 1000 and 2000 seconds when the temperatures peak at almost 650 °C, 610 °C and 535 °C for the JI-73-195-780, JI-113-320-960 and JI-42-252-1010 sheets respectively, representing a maximum difference of 120 °C. During the final fire exposure phase (2000 to 3600 seconds), although thermal progression slowed, these differences remained stable. The JI-73-195-780 sheet reached around 770°C, compared to 730°C for the JI-113-320-960 sheet and 680°C for the JI-42-252-1010 sheet. This represents a difference of around 90°C between the two extremes. A similar pattern was observed in the purlin web (points P3, P4 and P5), with an initial rapid rise in temperature in the upper part of the web (point P3). At 1000 seconds, temperatures reached around 295 °C, 245 °C and 200 °C for the JI-73-195-780, JI-113-320-960 and JI-42-252-1010 sheets, respectively, with a temperature difference of 95 °C. This difference increases to 150°C after 2,000 seconds and then remains relatively constant until 3,600 seconds, when the temperatures of the three sheets reach around 505°C, 450°C and 380°C respectively. In the central part of the web (point P4), the initial temperature rise is rapid. At 1000 seconds, the temperatures are around 200°C, 150°C and 130°C for the JI-73-195-780, JI-113-320-960 and JI-42-252-1010 sheets, respectively. The difference between the extremes is around 70°C. The difference increases to 140 °C after 2,000 seconds and then remains relatively constant until 3,600 seconds, when the temperatures of the three sheets reach around 440 °C, 370 °C and 300 °C respectively. Similarly, at point P5 in the lower part of the web, the temperature reaches approximately 145°C, 110°C and 85°C for the JI-73-195-780, JI-113-320-960 and JI-42-252-1010 sheets, respectively, at 1000 seconds. Even at this early stage, there is limited temperature difference between 30 and 60°C depending on the case. This difference increases further between 1000 and 2000 seconds, with temperatures peaking at almost 370°C, 310°C and 535°C for the JI-73-195-780, JI-113-320-960 and JI-42-252-1010 sheets respectively, representing a maximum difference of 215°C. During the final fire exposure phase (2000 to 3600 seconds), although thermal progression slowed, differences remained stable. The JI-73-195-780 sheet reached around 590°C, compared to 525°C for the JI-113-320-960 sheet and 437°C for the JI-42-252-1010 sheet. This represents a difference of around 150°C between the two extremes. The lower flange (point P6) followed a similar trend: at 1000 seconds, the temperatures were around 110 °C (JI-73-195-780 sheet), 70 °C (JI-113-320-960 sheet) and 50 °C (JI-42-252-1010 sheet), with a differential of 60 °C. By 2000 seconds, these values had risen to 315 °C, 245 °C and 160 °C respectively, with a difference of 150 °C between the two extremes. By the end of the thermal analysis,

the temperatures had stabilised to around 560 °C for sheet JI-73-195-780, 485 °C for sheet JI-113-320-960, and 390 °C for sheet JI-42-252-1010. This confirmed a consistent temperature difference of 170 °C. Throughout section S4, the temperature increase in sheet JI-73-195-780 was therefore greater than in sheet JI-113-320-960, while sheet JI-42-252-1010 remained the least affected thermally.

In summary, the thermal results reveal significant variations in temperature increase among the purlin sections, depending on their position and the steel sheets they support. For sections S1 and S2, which are directly exposed to the fire, the lower flange and web exhibit similar heating patterns and faster temperature increases. The upper flange, which is partially protected by the steel sheets, heats up more slowly. However, the differences in temperature rise between the purlin parts under the wave cavities and those in contact with the steel sheets are limited. Conversely, in sections S4 and S5, which are on the purlin encasement, the upper flange heats up more quickly. The web and lower flange, which are partially shielded by the encasement, experience delayed heating.

The geometry of the steel sheets also has a significant impact on purlin heating. For the same profile, the temperature increase in all sections depends on the sheet's dimensions. The wider the corrugations, the greater the temperature increase in all three parts of the purlin (top flange, web, and bottom flange). Sections with the JI-73-195-780 sheet consistently show the greatest temperature increase in all parts of the purlin, followed by those with the JI-113-320-960 sheet. Conversely, sections made from the JI-42-252-1010 sheet exhibit the lowest temperature increase.

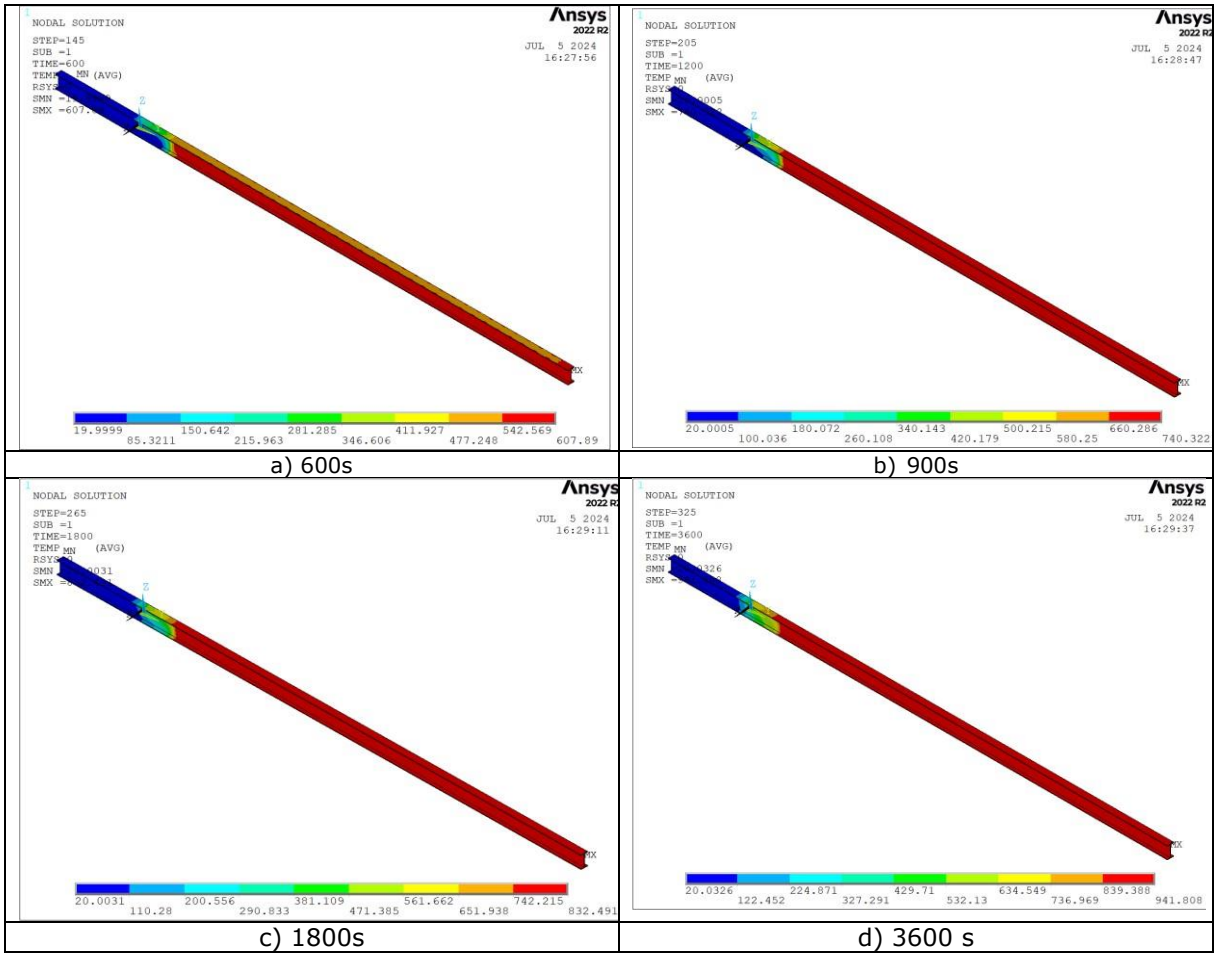

Figure 2.10: Temperature field in the purlin supporting steel sheets JI-73-195-780 after several fire exposure times

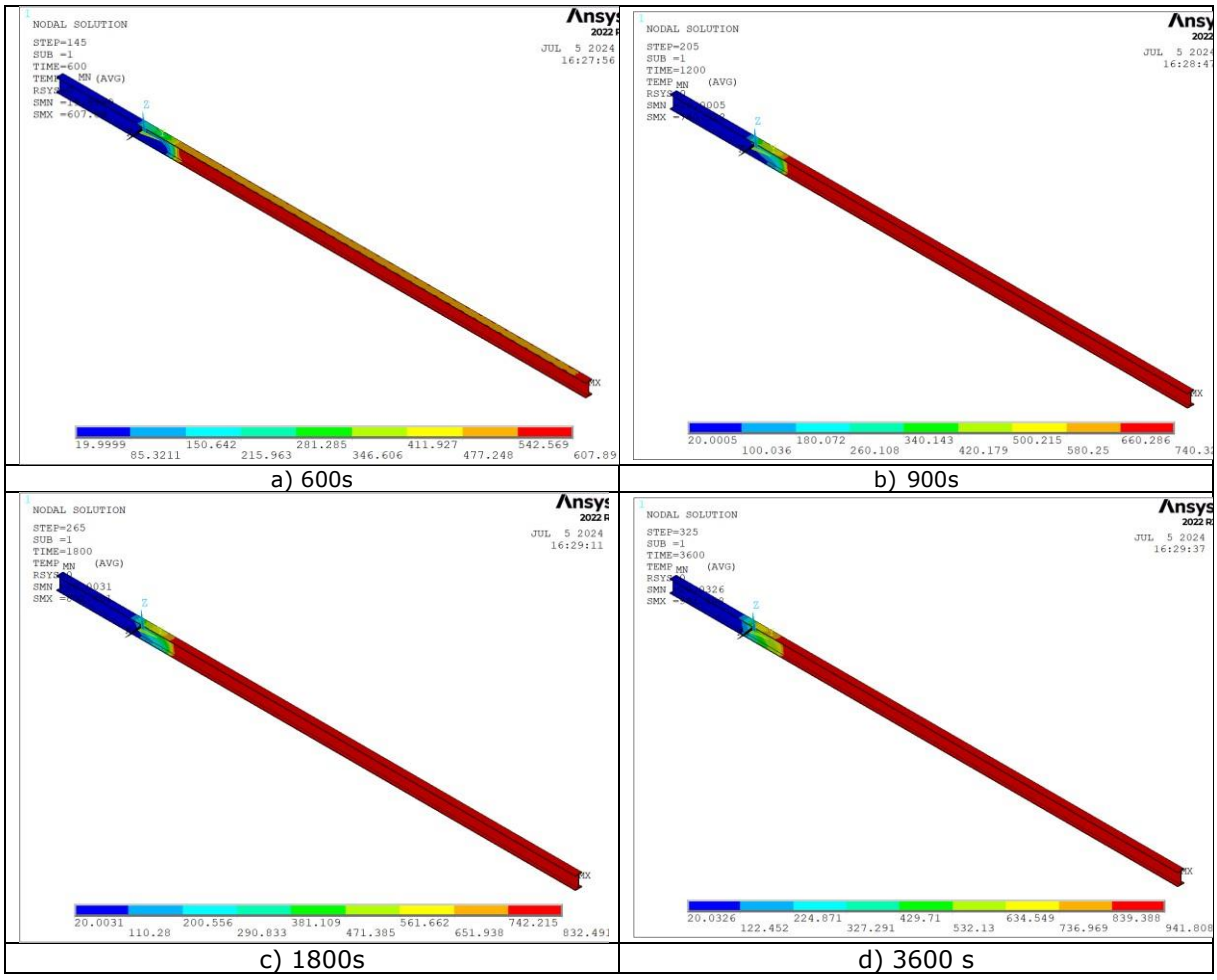

Figure 2.11: Temperature field in the purlin supporting steel sheets JID-137-320-960 after several fire exposure times

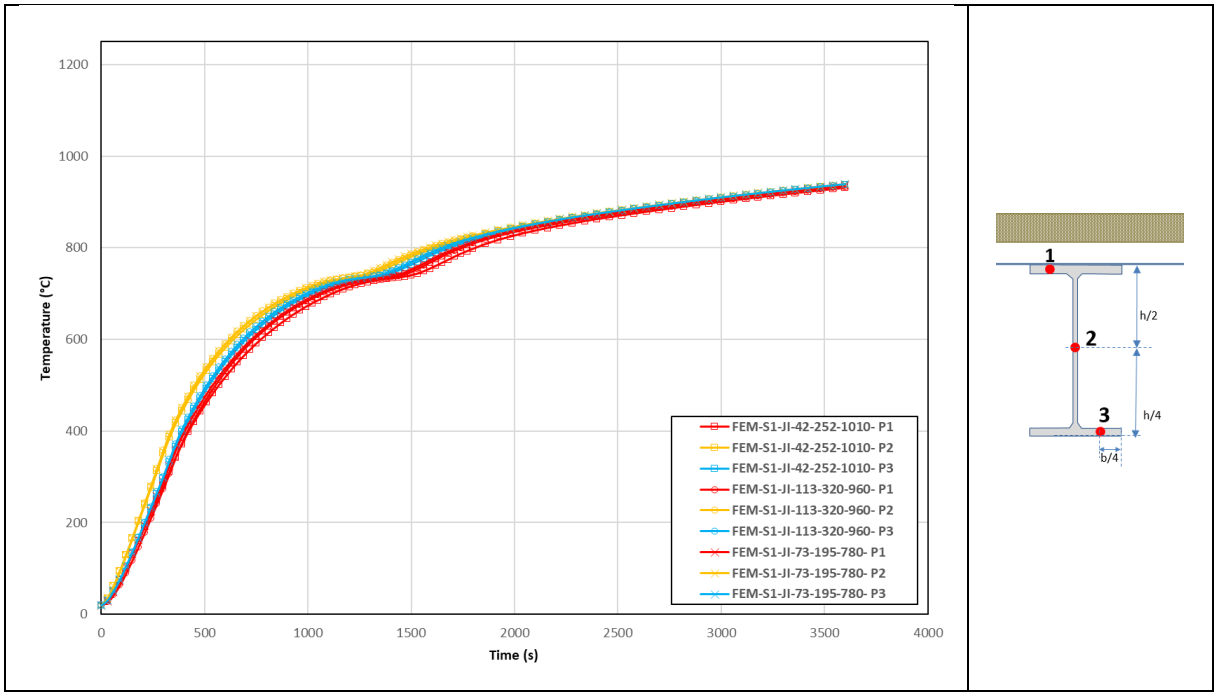

Figure 2.12: Comparison of the predicted temperatures of the purlin for the sheet steel cases JI-42-252-1010, JI-73-195-780 and JI-113-320-960, at the S1 section.

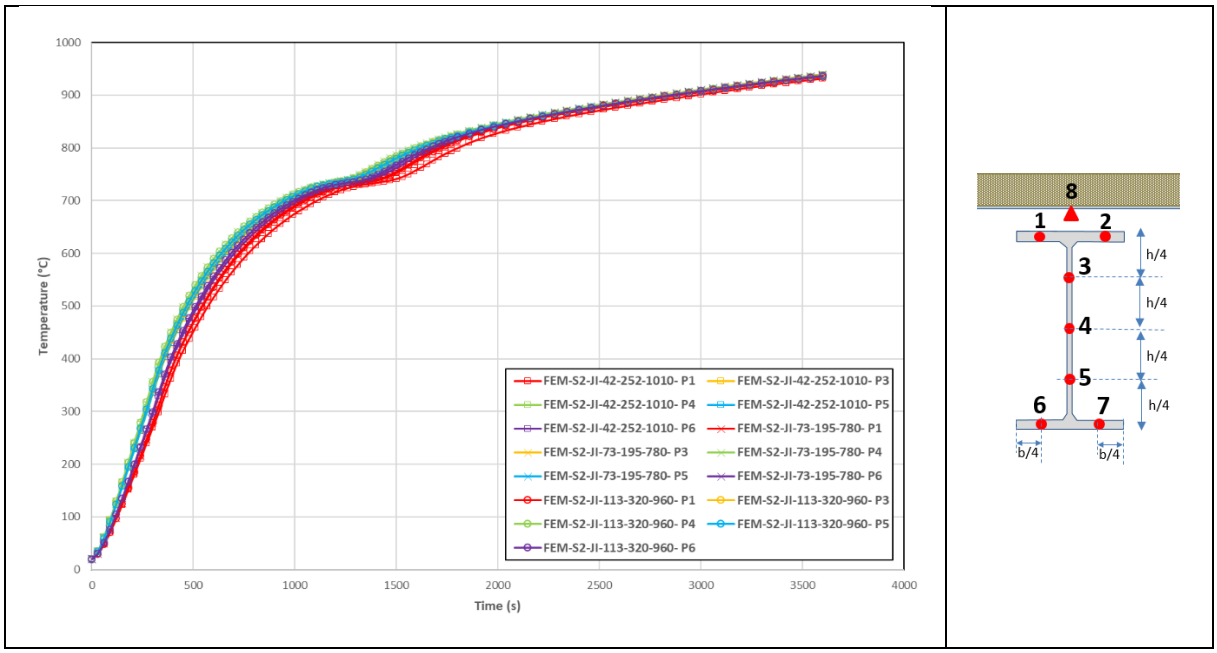

Figure 2.13: Comparison of the predicted temperatures of the purlin for the sheet steel cases JI-42-252-1010, JI-73-195-780 and JI-113-320-960, at the S2 section.

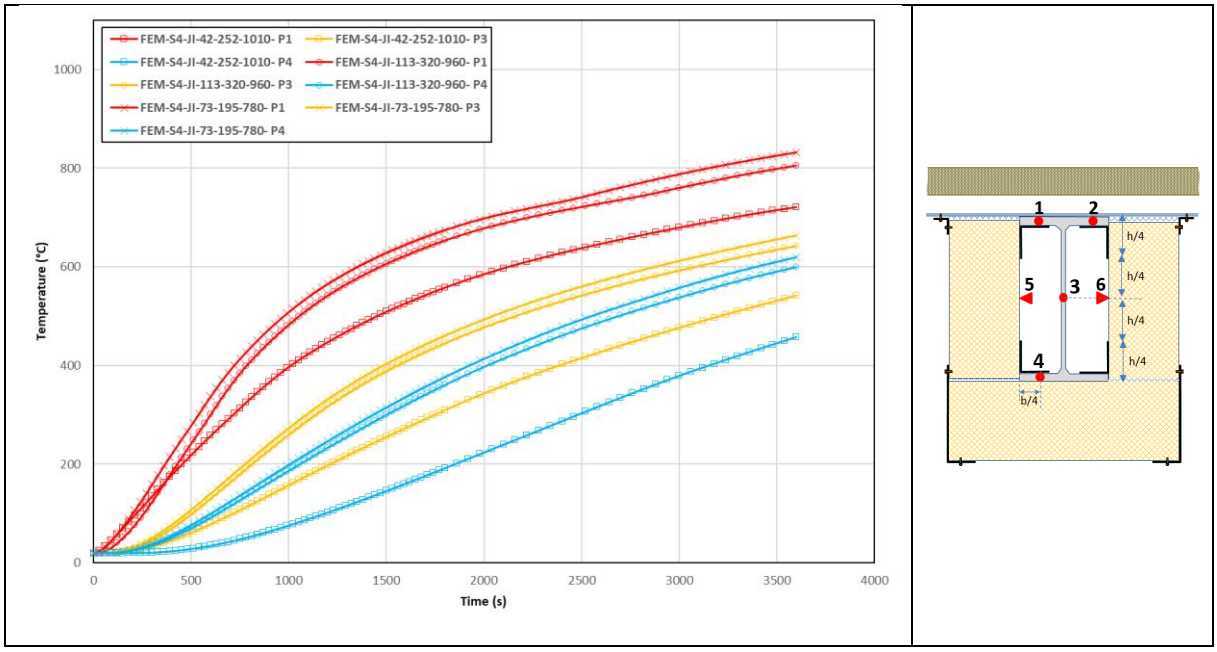

Figure 2.14: Comparison of the predicted temperatures of the purlin for the sheet steel cases JI-42-252-1010, JI-73-195-780 and JI-113-320-960, at the S4 section.

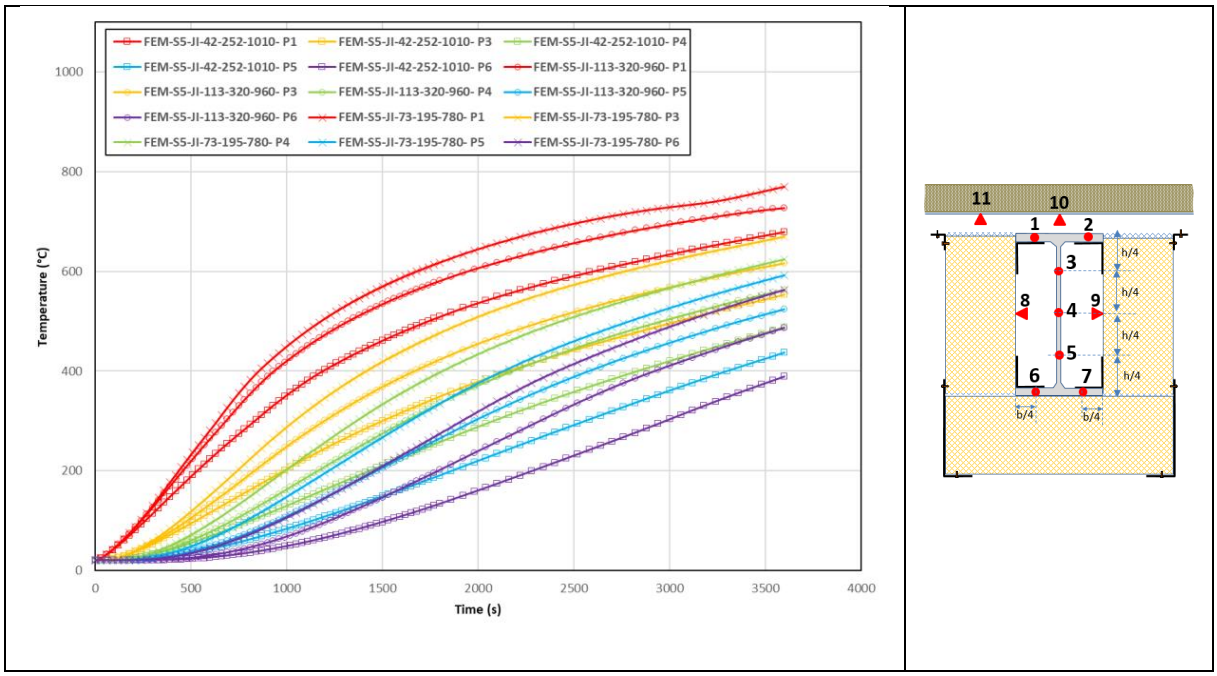

Figure 2.15: Comparison of the predicted temperatures of the purlin for the sheet steel cases JI-42-252-1010, JI-73-195-780 and JI-113-320-960, at the S5 section.

2.2.2 Thermal response of studied steel sheet configurations with additional waves filling

In this section, the following figures show the predicted temperature fields in a steel purlin supporting the steel sheets "JI-42-252-1010" and "JID-137-320-960" with additional waves filling at the level of the purlin encasement, at different fire exposure times. They are compared to the heating predicted for the same cases without additional waves filling.

The analysis of the temperature rises calculated in different purlin sections at level of the encasement shows that:

- For steel sheet JID-137-310-930, at section S4, which is located at the level of the encasement and is in direct contact with the steel purlin, notable thermal differences are observed between the purlin's different zones (points P1, P3 and P4), depending on whether the cavities are filled. For the upper flange (point P1), a rapid rise in temperature is predicted during the first few seconds of exposure to fire (up to 1000 seconds). At this stage, the temperature rise is around 235°C when the wave cavities are filled, whereas when they are not filled, the temperature rise is around 420°C, reflecting an initial thermal difference of around 185°C. Between 1000 and 2000 seconds, these differences narrow: temperatures rise to around 465°C and 575°C, respectively, giving a difference of 110°C between the two configurations. During the final fire exposure phase (2000–3600 seconds), although temperature increases more slowly, the gap narrows further. Temperatures then reach 642°C and 675°C, respectively, with a difference of around 30°C. A similar pattern emerges for the purlin web (point P3). Up to 1000 seconds, the temperature rise is relatively rapid but remains less significant than for the top flange (point P1). In the case where the cavities at the level of the encasement are filled, the temperature reaches 160°C, whereas in the unfilled case, it reaches 235°C — a difference of 75°C. By 2000 seconds, the temperatures had reached 315°C and 435°C, respectively, widening the gap to 120°C. By 3600 seconds, the trend has stabilised, but the difference remains at around 125°C. The bottom flange (P4) also follows this differentiated progression. Although a less rapid rise in temperature is predicted compared with the other parts of the purlins, it remains relatively superimposed in the initial stages for the two configurations studied, reaching 155°C and 160°C respectively, illustrating an initial difference of 5°C. At 2,000 seconds, the difference increases, with temperatures of 290°C and 360°C, i.e. a difference of 70°C. Finally, at 3600 seconds, the temperatures peak at 437°C for the filled cavities and 550°C for the unfilled cavities, with a final difference of 87°C between the two configurations. Overall, the thermal analysis of

section S4 reveals that the temperature rise of the purlin is higher in the case of unplugged cavities and lower in the opposite case.

- For section S5, which is located under the wave trough at the level of the encasement, the differences in heating become increasingly significant for the different purlin areas (P1, P3, P4, P5 and P6) depending on the configuration (whether the cavities are filled or not). A rapid rise in temperature is predicted for the upper flange (point P1) from the first few seconds of exposure to the fire (up to 1000 seconds). At this stage, the temperature rise is around 50°C when the wave cavities at the encasement level are filled. In the unfilled case, the temperature rise is 400°C, indicating an initial difference of around 500°C. Between 1000 and 2000 seconds, these differences narrow slightly: temperatures rise to an average of 150°C and 560°C, respectively, giving a difference of 410°C between the two configurations. During the final phase (2000–3600 s), although temperatures rise more slowly, the difference between the two configurations increases again. By the end of the simulation, the temperatures reached are 290°C and 675°C respectively, with a difference of around 385°C. For the purlin web (points P3, P4 and P5), temperature rises follow the same pattern as for the top flange. Up to 1000 seconds, the temperature rise is relatively rapid but still less significant than for the upper flange (P1). On average, the temperature rises by 40°C when the cavities are filled and by 160°C when they are not, i.e. a significant difference of 120°C. By 2000 seconds, the temperatures had reached 120°C and 340°C, respectively, increasing the difference to 220°C. By 3600 seconds, the trend has stabilised, but the difference remains, with an average temperature of 250°C and 520°C, respectively, giving a final differential of around 275°C. The bottom flange (P6) also exhibits this differentiated heating. Compared with the other purlin parts, a less rapid rise in temperature is observed, but the two configurations remain relatively superimposed in the first moments, with temperatures of 40°C and 70°C respectively, illustrating a difference of 30°C in this initial phase. At 2000 seconds, the difference increases, with predicted temperatures of 105 °C and 220 °C, creating a widened gap of 115 °C. Finally, at 3600 seconds, the temperature peaks at 235 °C for the filled cavities case and 445 °C for the unfilled case, resulting in a final difference of 210 °C between the two configurations. Overall, the thermal analysis of section S5 highlights a difference in purlin heating in the two configurations studied, with higher heating in the case of unfilled cavities and lower heating in the opposite case, as is the case for section S4.

- For the JI-42-252-1010 steel sheet, section S4, which is located at encasement level and is in direct contact with the steel pan, shows significant differences in heating between the purlin's different parts (P1, P3 and P4), depending on the cavities' configuration (whether they are filled or not). The upper flange (point P1) exhibits a swift temperature increase from the initial seconds of exposure to fire (up to 1000 seconds). When the cavities are filled, the temperature rises to around 100 °C compared to 400 °C in the unfilled case, representing a maximum difference of 300 °C. Between 1000 and 2000 seconds, the temperature continues to rise, but the difference becomes more significant, reaching 220°C and 585°C (i.e. a difference of 365°C). In the final fire exposure phase (2000–3600 s), heating slows, and differences narrow further: heat-up peaks at 386 °C (filled cavities) and 721 °C (unfilled cavities), a difference of around 335°C. Regarding the purlin web (point P3), a lower temperature rise was recorded. Up to 1000 s, temperature rise reached 75°C for filled cavities compared to 160 °C for unfilled cavities, a difference of 85 °C. At 2000 seconds, the gap widens further, with respective values of 175°C and 350°C, representing a difference of 175°C. Finally, at 3,600 seconds, temperatures reach 310°C (filled cavities) and 542°C (unfilled cavities) respectively, representing a final difference of around 230°C. For the bottom flange (point P4), a more moderate temperature increase is observed. At 1000 seconds, the two configurations show relatively similar values: 70°C (filled cavities) and 80°C (unfilled cavities), a difference of 10°C. At 2000 s, the difference increases: 160 °C versus 220 °C, a difference of 60 °C. By the end of the analysis at 3600 seconds, the temperature had reached 290 °C for the filled cavities and 460 °C for the unfilled cavities, corresponding to a difference of 170 °C. As with the other steel sheets studied, the thermal analysis of section S4 reveals a significant difference in purlin heating depending on the configuration: it is consistently higher when the cavities are unfilled, while it remains relatively low in the presence of filled cavities.

- In section S5, which is located at the level of the casing under the wave trough, there are significant differences in heating between the various parts of the purlins (P1, P3, P4, P5 and P6) depending on whether the cavities are filled. From the first seconds of exposure to fire (up to 1000 seconds), the upper flange (point P1) experiences a rapid rise in temperature. When the cavities are filled, the temperature reaches around 60 °C; when the cavities are left open, it reaches 350 °C, representing an initial difference of around 300 °C. Between 1000 and 2000 seconds, the temperature continues to rise in both cases, reaching 110°C and 540°C respectively, with the temperature difference increasing to 430°C. During the final fire exposure phase (2000–3600 s), the rate of change slows down, but the temperature difference remains high, peaking at 230 °C for filled cavities and 670 °C for unfilled cavities — a significant differential of 440 °C. The purlin web (points P3, P4 and P5) heats up more moderately. Up to 1000 seconds, the temperature reached an average of 30°C in the filled case and 130°C in the unfilled case, a difference of 100°C. By 2000 s, this difference had widened further, with average temperatures reaching 85 °C and 290 °C, respectively — a difference of around 205 °C. Finally, at 3600 seconds, the difference persists, with temperatures reaching 190 °C (filled cavities) and 490 °C (unfilled case), representing a final differential of 300 °C. The bottom flange (point P6) shows a more moderate increase in heating. At 1000 s, the two configurations show relatively similar values: 30 °C for the filled cavities and 50 °C for the unfilled cavities — a difference of only 20 °C. However, by 2000 seconds, the difference is more pronounced, with 80 °C and 160 °C respectively. By the end of the analysis (3600 seconds), the difference is more significant, with 180 °C in the filled case and 390 °C in the unfilled case.

In conclusion, as expected, filling all the wave cavities at the level of the purlin encasement significantly reduces the heating of the encased purlin parts. Undoubtedly, this measure will contribute to ensuring that fire-induced plastic hinges form sufficiently away from the walls, after the encasement ends, thus preventing damage to the walls due to the collapse of the purlins exposed to fire.

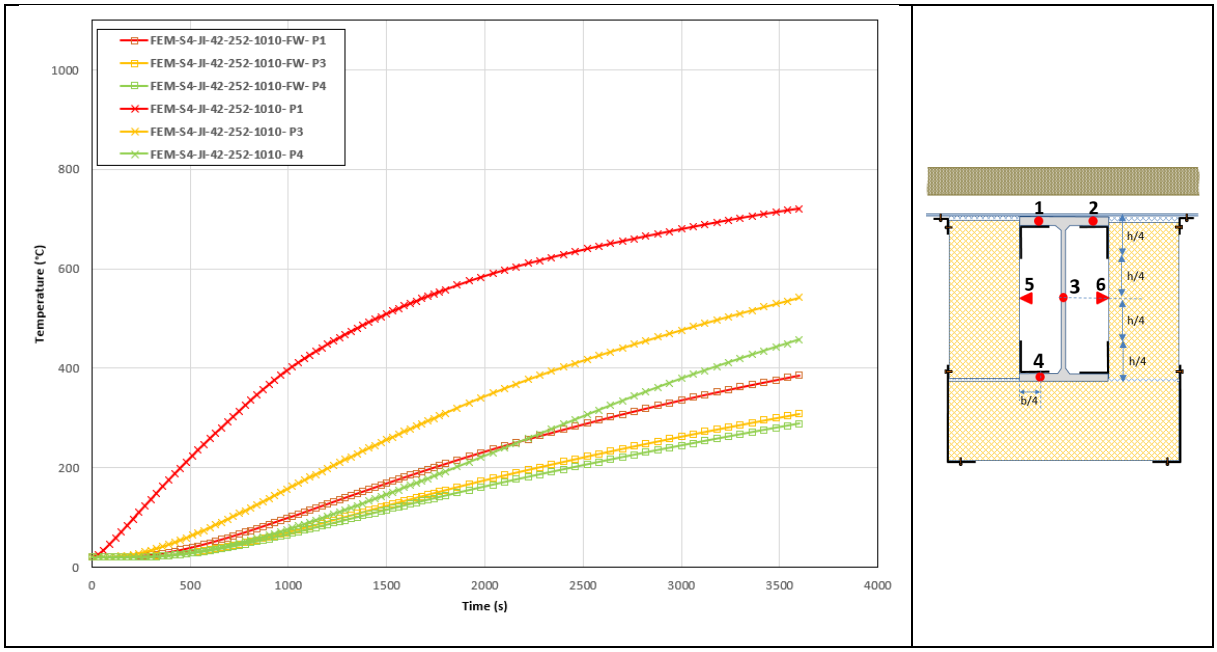

Figure 2.16: Comparison of the predicted temperatures of the purlin for the steel sheet case JI-42-252-1010, with filled or unfilled cavities at the purlin encasement, at the S4 section.

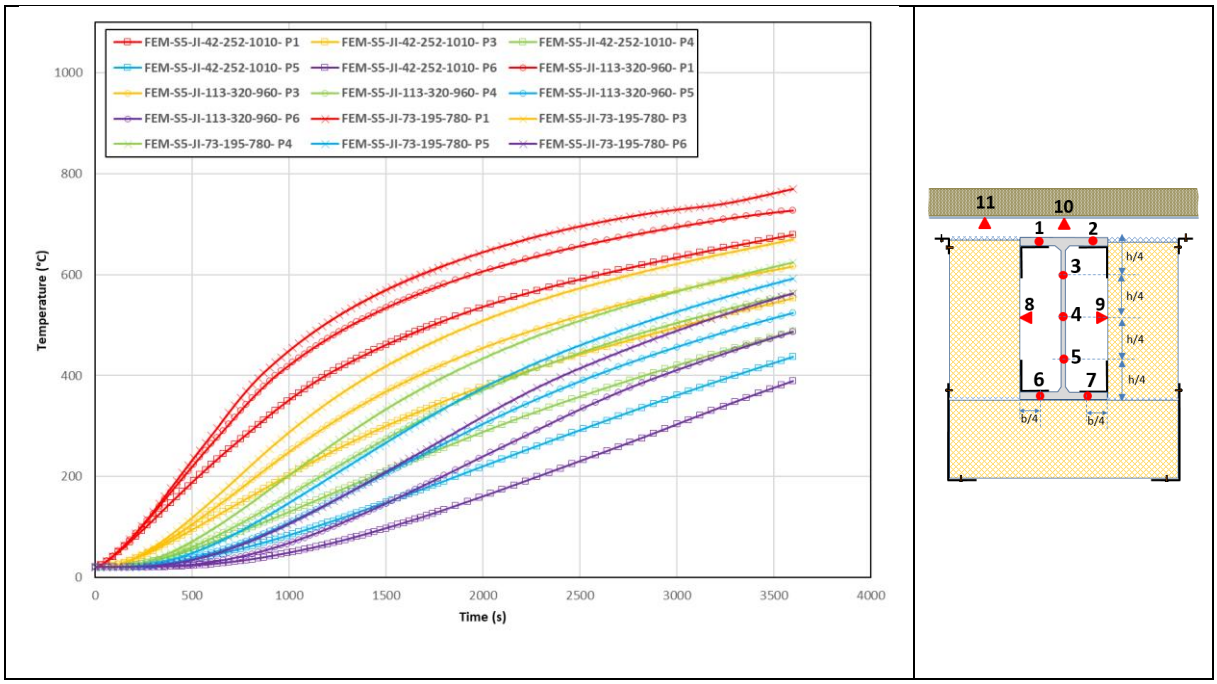

Figure 2.17: Comparison of the predicted temperatures of the purlin for the steel sheet case JI-42-252-1010, with filled or unfilled cavities at the purlin encasement, at the S5 section.

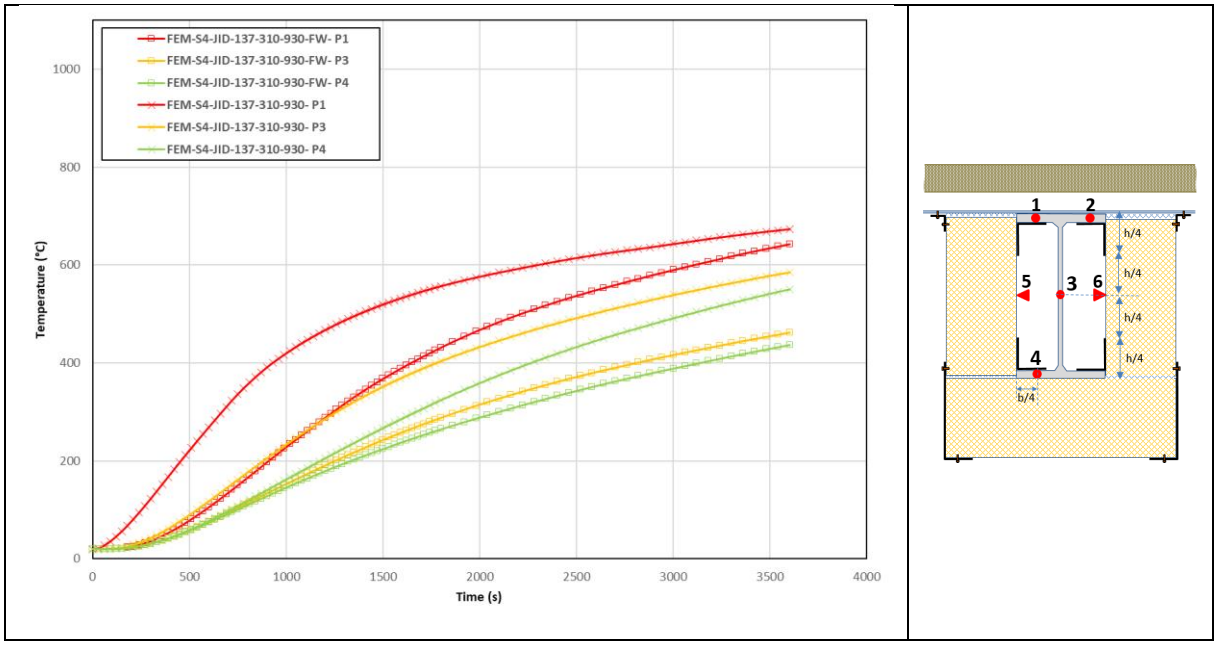

Figure 2.18: Comparison of the predicted temperatures of the purlin for the steel sheet case JID-137-195-930, with filled or unfilled cavities at the purlin encasement, at the S4 section.

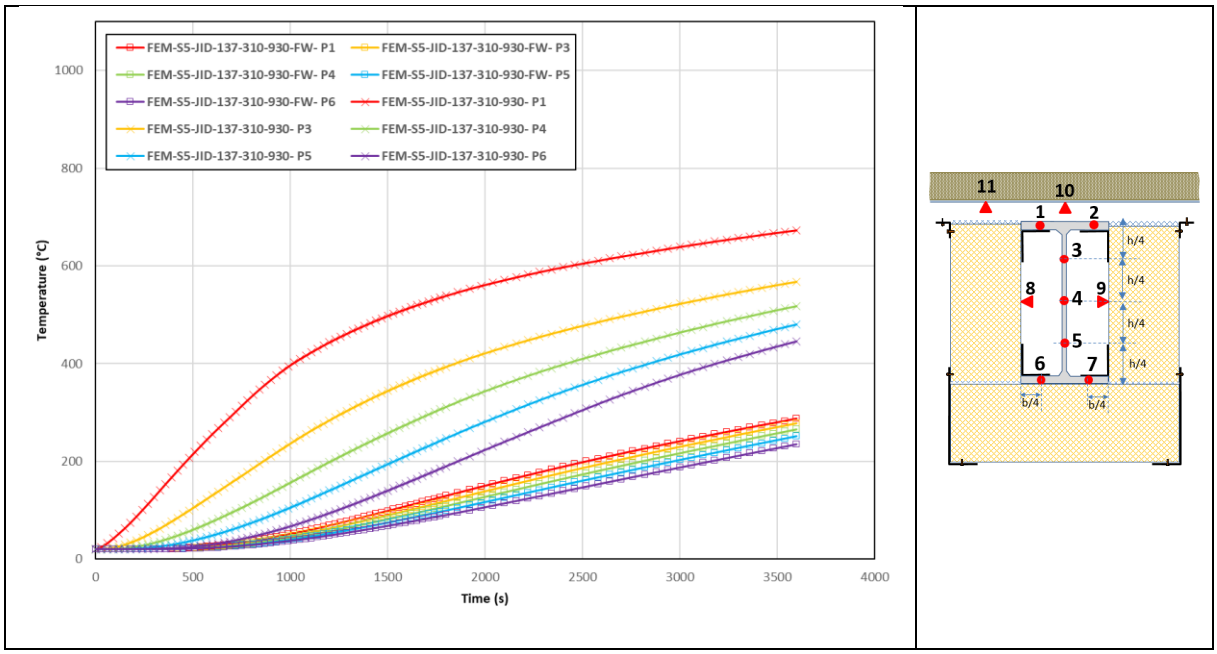

Figure 2.19: Comparison of the predicted temperatures of the purlin for the steel sheet case JID-137-195-930, with filled or unfilled cavities at the purlin encasement, at the S5 section.

2.3 Results of mechanical analyses

Due to the results obtained, it should be noted that the mechanical analyses were carried out on the selected steel sheets with the smallest and largest waves only (the JI-42-252-1010 and JID-137-310-930 sheets), with no additional wave cavity filling considered. Temperature rises and large temperature gradients have been observed in the purlin part encased with sandwich panels for these sheets.

2.3.1 Global structural behaviour

As analysing the overall fire behaviour of the purlins is not the main objective of the parametric analysis, the displacements calculated at the mid-length of the heated span of purlins, as well as the deformed shape obtained at failure time, are mainly provided for information purposes. Figure 2.20 shows the time-vertical displacements curves predicted at the mid-span of the purlin heated part for all the study cases while Figure 2.21 illustrates the predicted deformed shape at failure time of purlin cases with a 6 m span and a JI-42-252-1010 steel sheet only, as the failure modes are very similar for the different cases in the study.

Briefly, it can be noted that when no lateral or torsional restraint is provided to the purlins, they twist and deflect substantially under the combined effect of mechanical loading and temperature rise. The dominant failure mode is lateral-torsional buckling of the purlins. In contrast, laterally restrained purlins mainly bend, changing the failure mode from lateral-torsional buckling to flexural bending. This is associated with the local buckling of the purlin flanges in compression at the end of the encasement system placed around the purlin, as well as at the end of the purlin supported in the fire-exposed area. Moreover, the numerical models indicate that purlin failure tends to occur later in cases where the span between supports is 10 metres compared to 6 metres. Additionally, lateral torsional buckling seems to have a limited impact on the purlin failure times, since small differences in fire resistance times are observed between cases where lateral torsional buckling may or may not occur.

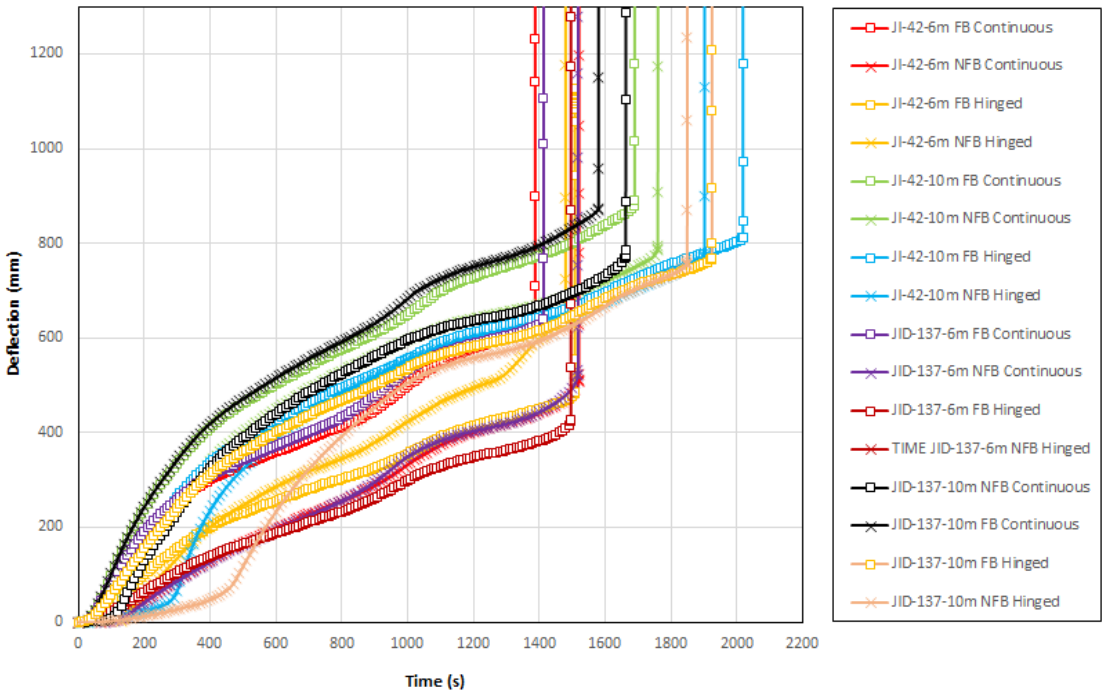

Figure 2.20: Time-displacement curves predicted at the mid-length of the heated span of purlins for all the cases analysed mechanically

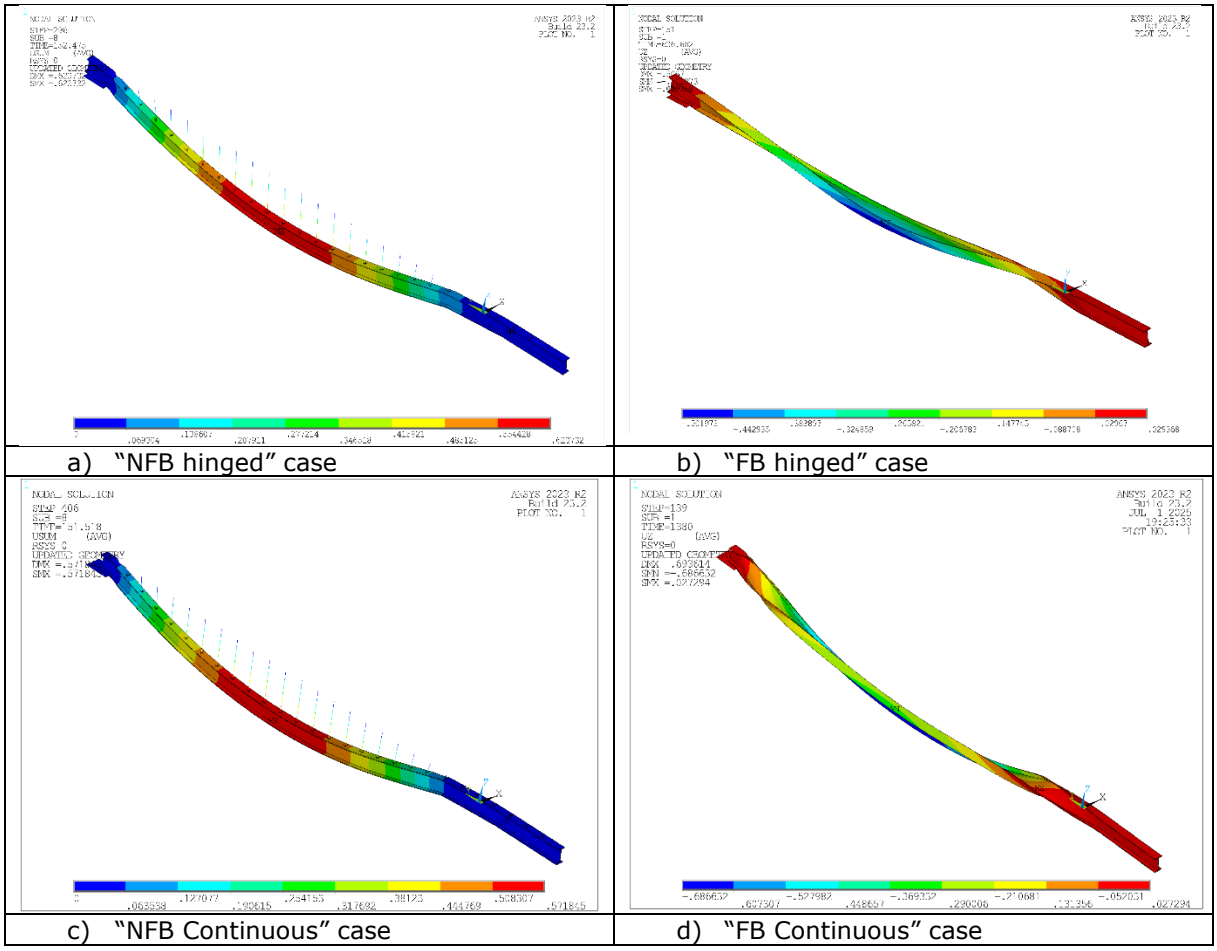

Figure 2.21: Deformed shape of purlins at failure time – purlin cases with a 6 m span and a JI-42-252-1010 steel sheet

2.3.2 local structural behaviour

The most interesting results from the numerical analyses are the local deformations of the purlins at part where they are encased with sandwich panels. Figure 2.22 and Figure 2.23 show the evolution of the torsional rotation that have been predicted for all the cases analysed mechanically, at the encasement end and at the wall level, respectively. The cases in which the top purlin flanges are laterally restrained by the roofing, allowing the purlin to undergo (FB) or not undergo (NFB) lateral torsional buckling, are distinguished. In addition, Figure 2.24 and Figure 2.25 shows the displacements predicted in the plane of the purlin cross-section in all cases where lateral restraint is applied, at the encasement end and at wall level.

From these figures, it can be noted that:

- During the initial phase of fire exposure, which lasts up to around 500 seconds, there is a rapid increase in rotations and displacements. Then, these values stabilise.
- As expected, the laterally unrestrained purlins exhibit the greatest rotation. Rotations range from 5° to 13° at wall level depending on the case (continuous or hinged purlin with a span of 6 or 10 metres), and from 15° to 40° at the encasement end. Where lateral restraint is applied, the purlins exhibit much lower rotations, with a maximum value of less than 2°.
- The displacements of the laterally restrained purlins are also limited. As the purlin's main deformation mode is bending around the strong axis, vertical displacement values are most important, with a maximum value lower than 100 mm at the encasement end. The maximum predicted vertical displacement at wall level is close to 35 mm. Out-of-plane displacements are much more limited, with a maximum value of less than 2 mm.

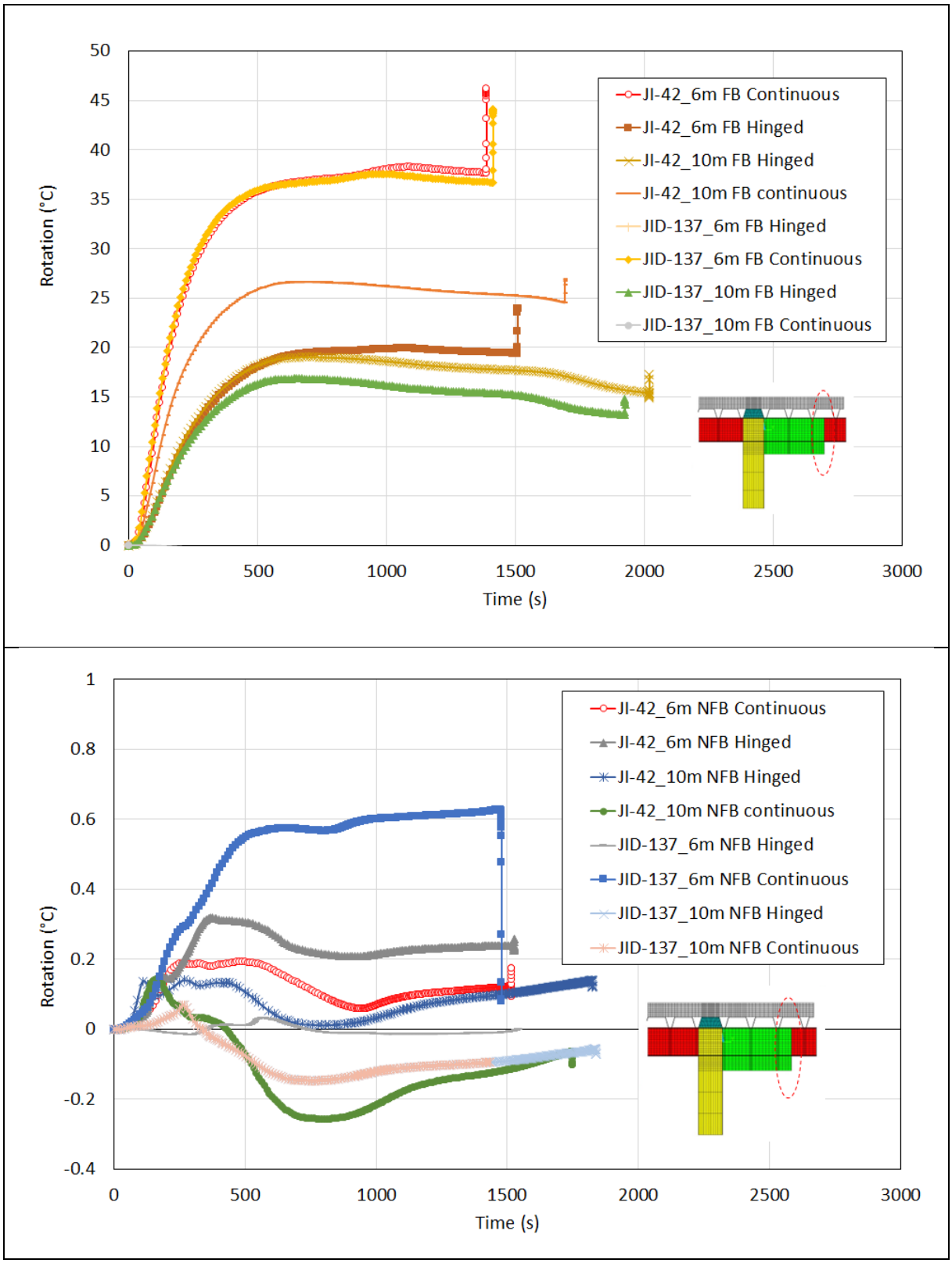

Figure 2.22: Time- torsional rotation predicted at the encasement end for all the cases analysed mechanically

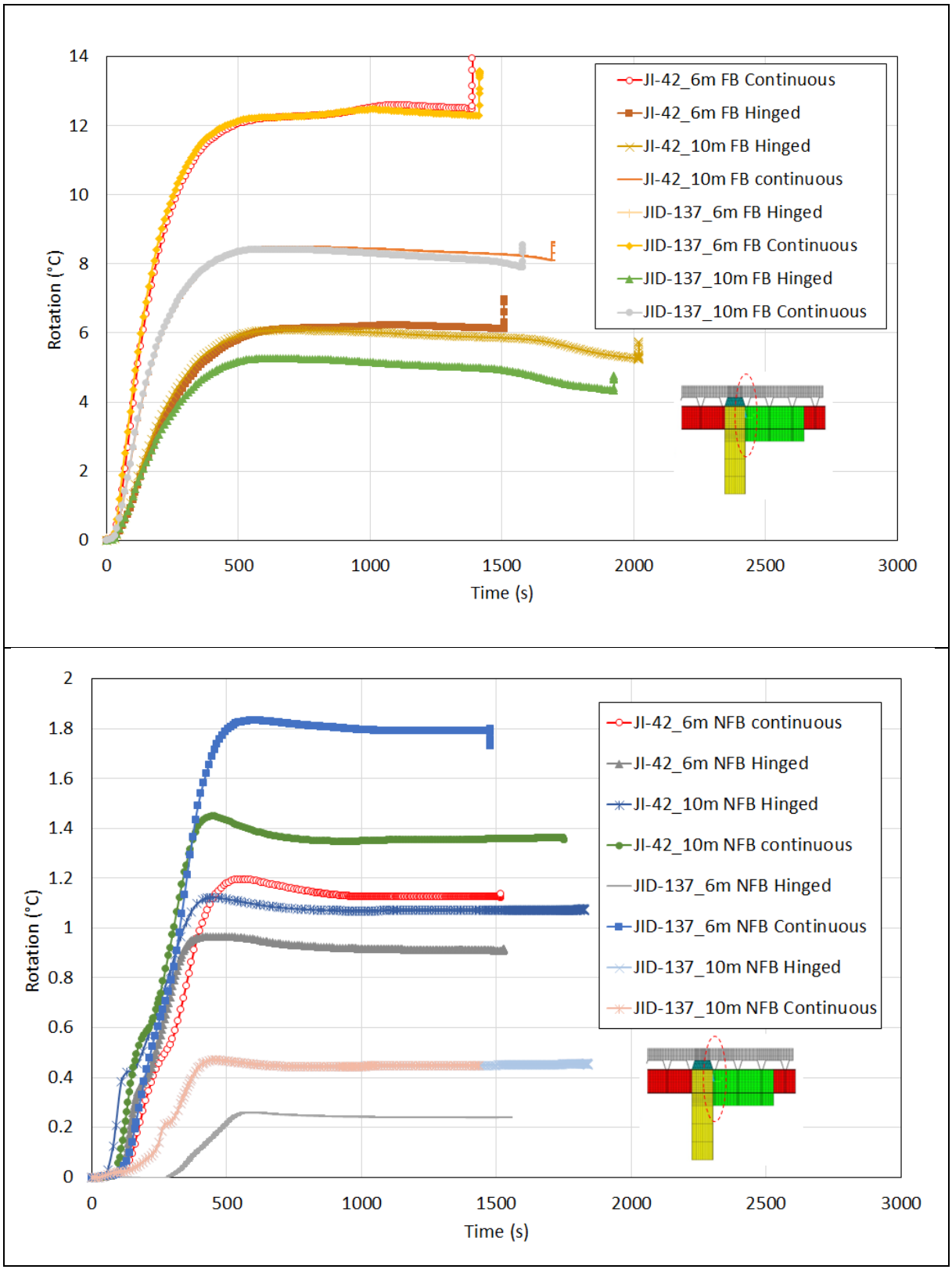

Figure 2.23: Time- torsional rotation predicted at the wall level for all the cases analysed mechanically

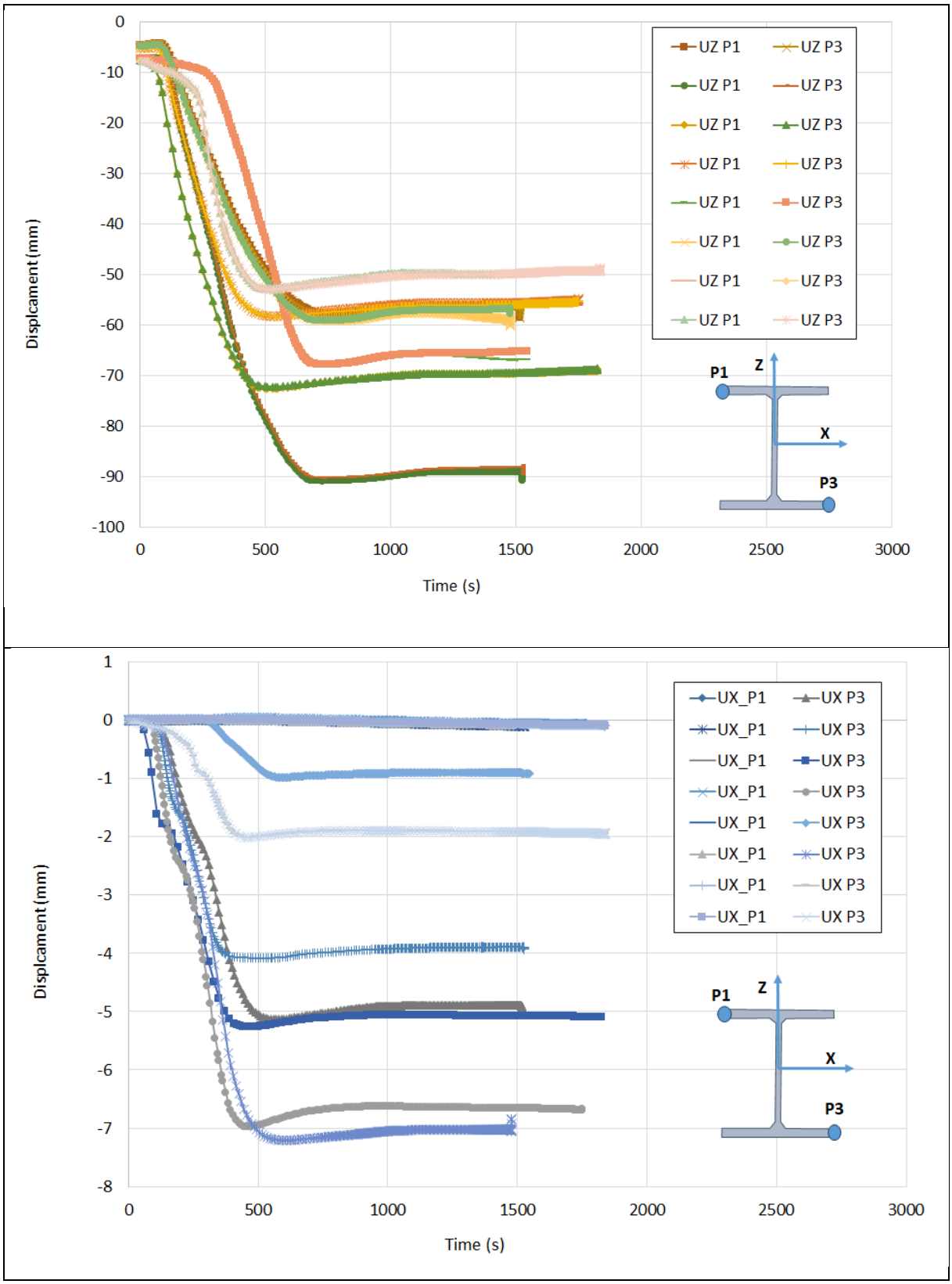

Figure 2.24: Displacements predicted in the plane of the purlin cross-section at the encasement end for all the purlin cases laterally restrained

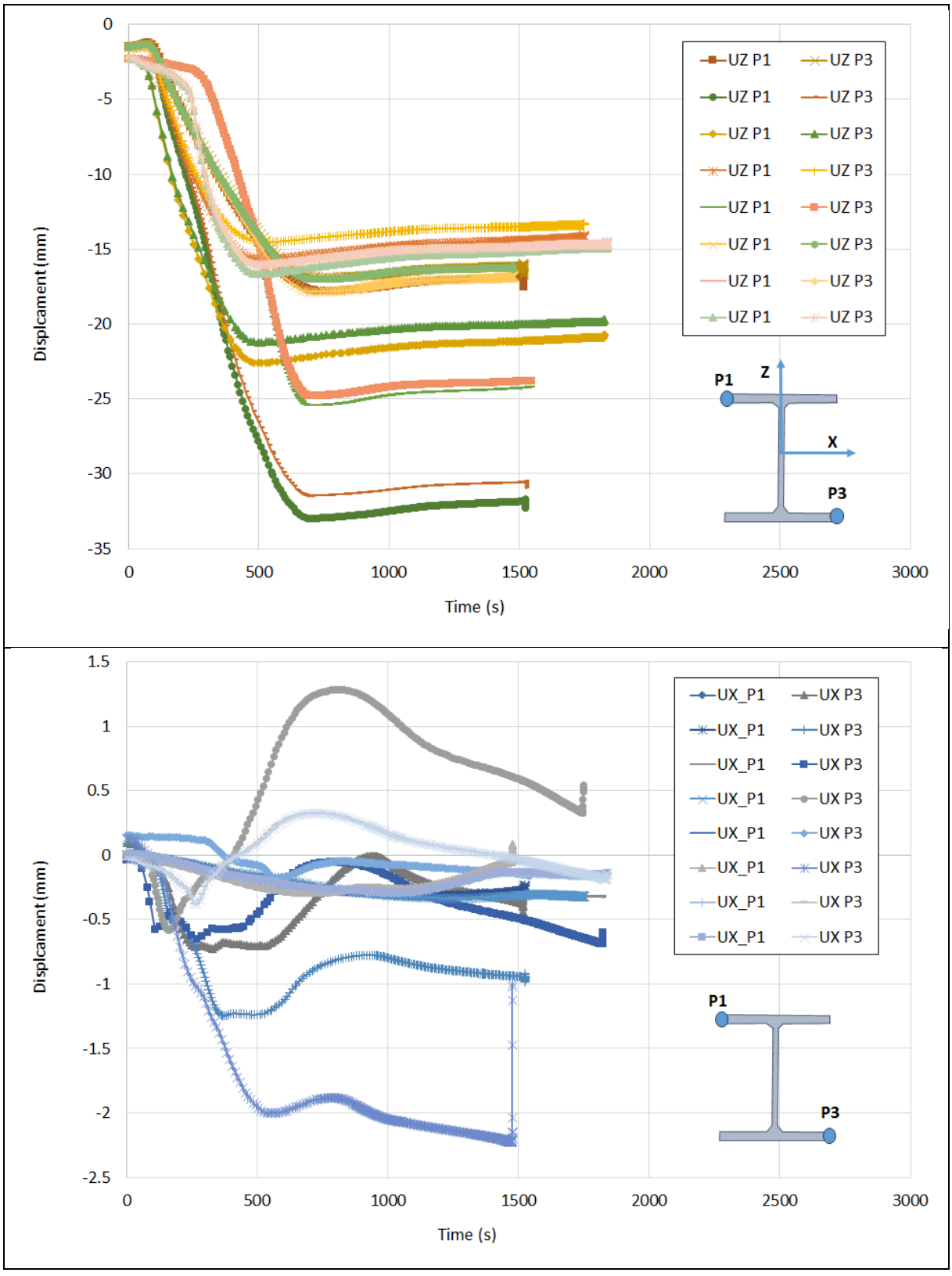

Figure 2.25: displacements predicted in the plane of the purlin cross-section at the wall level for all the purlin cases laterally restrained

2.4 Conclusion

As with the fire test, the thermal results of the parametric study showed significant temperature variations along the purlins, and that the encasement system studied leads to a drastic decrease in heating of the encased steel purlin parts regardless of the steel sheet dimensions. Overall, the greater the wave cavity (width x height), the greater the temperature increase in the upper purlin flange and the other purlin parts (web and bottom flange). However, the increase is less significant for the web and bottom flange as they are protected by the encasement.

The results of the mechanical analyses, based on calculated temperatures and considering that the trapezoidal steel sheeting provides lateral and rotational restraints to the purlin top flange, as was observed during the fire test, also confirmed that purlin deformations are limited to the level of the encasement when the purlins fail, with a plastic hinge forming at the end of the encasement.

Although the predicted and experimental displacements are more limited at wall level, it is recommended that the wall opening at purlin level is 100 mm larger than the purlin's cross-sectional dimensions. This should allow deformation of the purlins in and out of their plane to be absorbed without damaging the wall. It will also facilitate the purlin's passage through the wall and subsequent mineral wool filling of the hole. As with the fire test, a mineral wool strip should be placed between the wall and the encasement system. A strip at least 50 mm thick is recommended. Then, cover flashings enclosing the mineral wool strip should be fixed only to the wall panels.

3 PARAMETRIC STUDY OF FUSIBLE LINKS EXPOSED TO STANDARD FIRE

Parametric studies were performed using the three-dimensional finite element model developed for the project. These studies aimed to investigate the fire behaviour of the investigated fusible link solutions, identify all their potential failure modes, and obtain data to develop simple analytical models for evaluating the ultimate bearing capacity of the links when exposed to fire.

3.1 Investigated parameters

Parametric studies have been carried out on the fusible links schematised in Figure 3.1 by varying the parameters that affect their fire resistance and by considering a fire exposure to the standard fire curve. These parameters include the sizes of the steel profiles, the characteristics of the steel rods (length and diameter) and bolts (diameter) and the load level. A summary of the cases analysed in the parametric studies is provided in Table 2 to Table 4, according to the considered link solution. In addition to the parameters indicated in the previous tables, the position of the steel rods and steel bolts has also been modified depending on the case, including the distance between the rods or bolts and their distance from the profile's walls. The details of the studied cases are reported in Table 5 Table 4. The cases are distinguished by whether they were analysed at normal or elevated temperatures. Furthermore, in some cases, analysis has focused solely on the buckling resistance of steel rods and the bending resistance of the bottom flange of U- and Z-profiles. All the analyses in this parametric study considered a nominal yield strength of 275 MPa for the steel profiles, which is the most commonly used nowadays, and an 8.8 steel grade for both the steel rods and the bolts.

It should be noted that, as their fire resistance can easily be calculated, the characteristics of the steel bolts and stiffeners have been chosen to prevent them from failing in the conducted analyses.

The geometrical dimensions characterising the size of fusible link components are illustrated from Figure 3.2 to Figure 3.4.

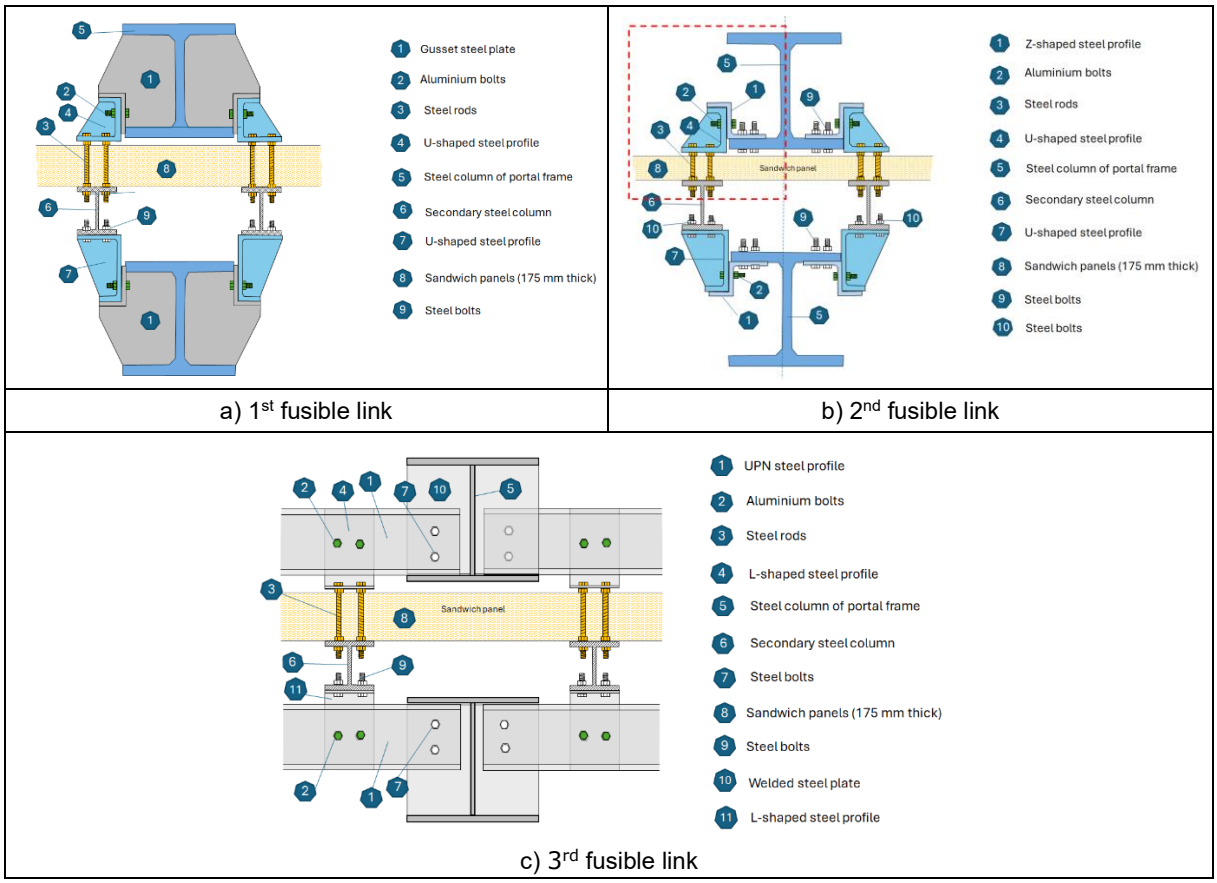

a) 1st fusible link

b) 2nd fusible link

c) 3rd fusible link

Figure 3.1: Schematic top view of three studied fusible links

Table 2 : Summary of the studied cases for the 1st fusible link solution

Parameters		Specified value
U-shaped steel profile	Thicknesses ($t_{bf,u}$, $t_{w,u}$)	6, 8, 9, 10, 12 and 14 mm
	Size ($b_{tf,u}$ × h_u × $b_{bf,u}$)	90×150×140, 90×240×140, 90×330×140 mm
	Stiffener ($t_{s,u}$)	10mm
Steel rods	Diameter	M12, M16, M18, M20 and M22
	length	100, 175 and 240mm
L-shaped steel plate	Size (h_L × b_L)	127 ×100 mm
	Thickness ($t_{b,L}$, $t_{w,L}$)	10mm
Gusset steel plate	thickness	10mm

Table 3 : Summary of the studied cases for the 2nd fusible link solution

Parameters		Specified value
U-shaped steel profile	Thicknesses ($t_{bf,u}$, $t_{w,u}$)	6, 8, and 12 mm
	Size ($b_{tf,u}$ × h_u × $b_{bf,u}$)	100×150×150 mm
Z-shaped steel profile	Thickness ($t_{bf,Z}$, $t_{w,Z}$)	6, 8, 10 and 12mm
	Size ($b_{bf,Z}$ × h_u × $b_{tf,Z}$)	142×128×100 mm
Steel rods	Diameter	M12, M16 and M20
	length	100, 175 and 240mm
Steel bolts	diameter	M20

Table 4 : Summary of the studied cases for the 3rd fusible link solution

Parameters		Specified value
UPN profile	Size	UPN 240 and UPN 300
	Length	6m
L shaped profile	Thickness (t_L)	8, 10 and 15 mm
	Size (b_L×h_L)	300×170 and 350×170
Steel rods	Diameter	M12, M16, M20 and M22
	length	100, 175 and 240mm
Steel bolts	Diameter	M22

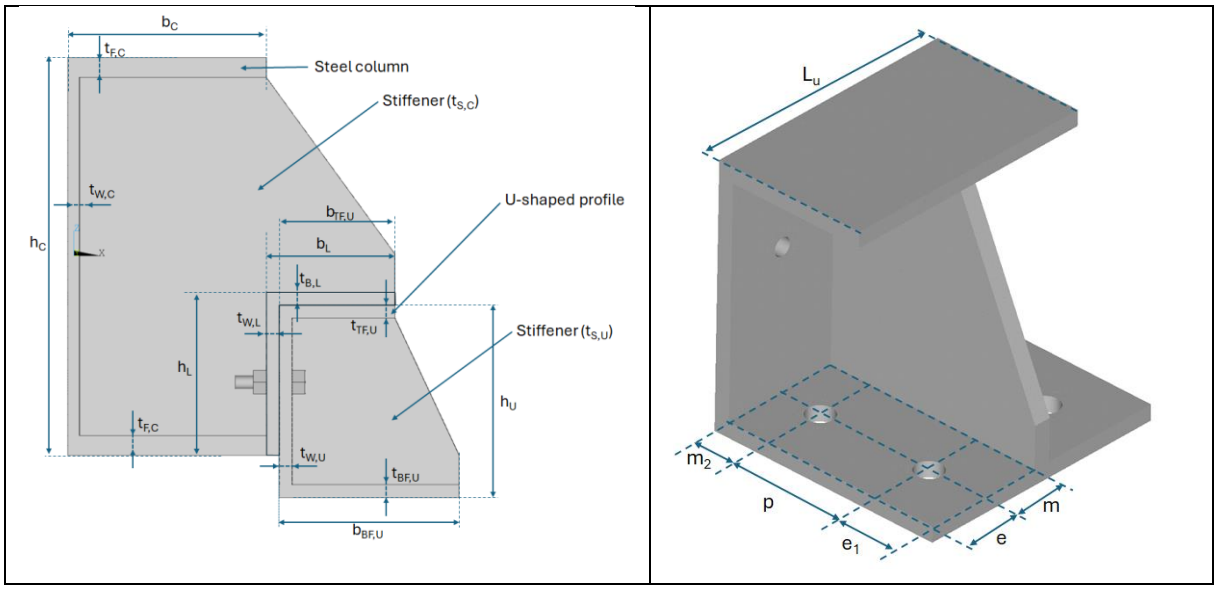

Figure 3.2: Definition of geometrical dimensions for the fusible link n°1

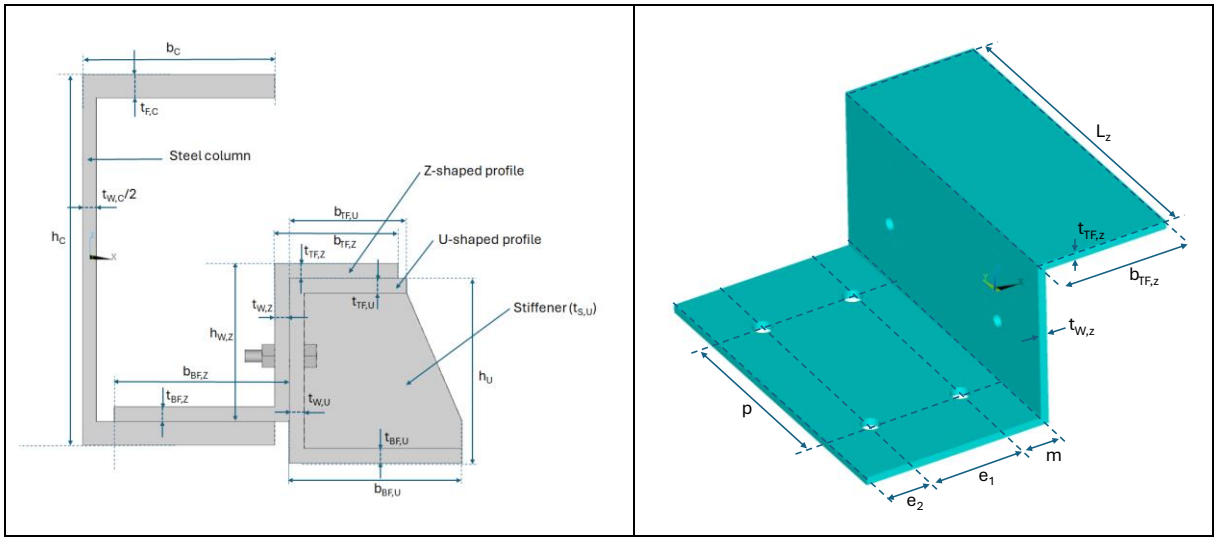

Figure 3.3: Definition of geometrical dimensions for the fusible link n°2

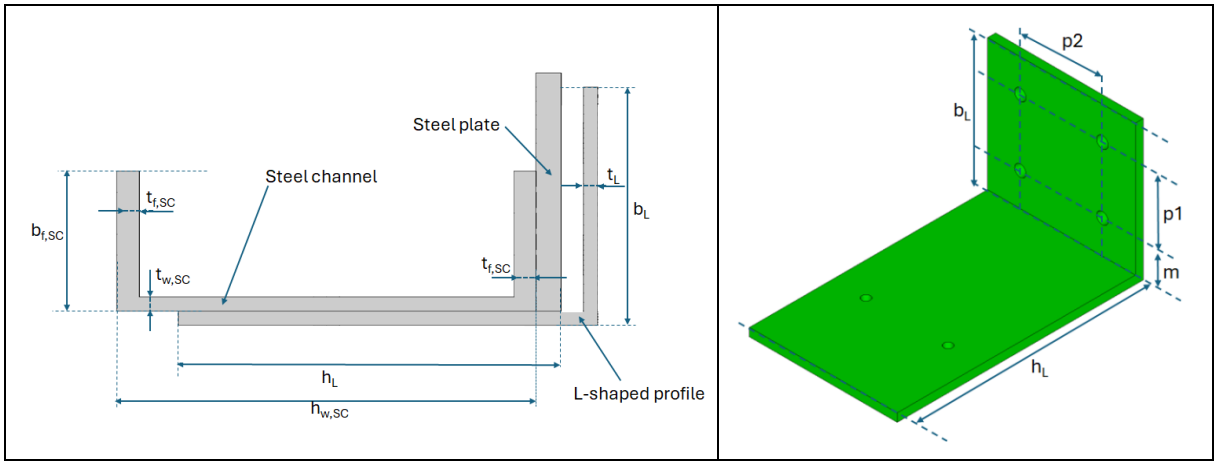

Figure 3.4: Definition of geometrical dimensions for the fusible link n°3

Table 5 : Details of studied cases for the 1st fusible link solution at normal temperature

Case	U-shaped steel profile				Steel rods position					L-shaped steel plate			Steel rods	
	$t_{bf,u}$	h_u	$b_{bf,u}$	$b_{tf,u}$	m	n	mx	p	ex	h_L	$t_{b,L}$, $t_{w,L}$	b_L	D	L
M12_L20_eU6_mx29_p70_m35	6	150	140	90	35	35	29	70	35	127	10	100	12	20
M12_L40_eU6_mx29_p70_m35	6	150	140	90	35	35	29	70	35	127	10	100	12	40
M12_L70_eU6_mx29_p70_m35	6	150	140	90	35	35	29	70	35	127	10	100	12	70
M12_L100_eU6_mx29_p55_m35	6	150	140	90	35	35	29	55	55	127	10	100	12	100
M12_L100_eU8_mx27_p70_m35	8	150	140	90	35	35	27	70	35	127	10	100	12	100
M12_L100_eU10_mx25_p70_m35	10	150	140	90	35	35	25	70	35	127	10	100	12	100
M12_L175_eU6_mx44_p70_m35	6	150	140	90	35	35	44	70	35	127	10	100	12	100
M12_L175_eU10_mx25_p70_m35	10	150	140	90	35	35	25	70	35	127	10	100	12	175
M12_L175_eU12_mx23_p70_m35	12	150	140	90	35	35	23	70	35	127	10	100	12	175
M12_L175_eU14_mx21_p70_m35	14	150	140	90	35	35	21	70	35	127	10	100	12	175
M12_L200_eU6_mx29_p70_m35	6	150	140	90	35	35	29	70	35	127	10	100	12	200
M12_L240_eU10_mx25_p70_m35	10	150	140	90	35	35	25	70	35	127	10	100	12	240
M16_L30_eU8_mx27_p70_m35	8	150	140	90	35	35	27	70	35	127	10	100	16	30
M16_L50_eU8_mx27_p70_m35	8	150	140	90	35	35	27	70	35	127	10	100	16	50
M16_L80_eU10_mx25_p55_m35	10	150	140	90	35	35	25	55	35	127	10	100	16	80
M16_L175_eU10_mx25_p70_m35	10	150	140	90	35	35	25	70	35	127	10	100	16	175
M16_L200_eU10_mx25_p70_m35	10	150	140	90	35	35	25	70	35	127	10	100	16	200
M16_L220_eU9_mx26_p70_m35	9	150	140	90	35	35	26	70	35	127	10	100	16	220
M16_L240_eU12_mx30_p50_m70	10	150	140	90	70	35	30	50	35	127	10	100	16	240
M16_L240_eU10_mx25_p70_m35	10	150	140	90	35	35	25	70	35	127	10	100	16	240
M12_L175_eU10_mx25_p50_m35	10	150	140	90	35	35	25	50	55	127	10	100	12	175
M12_L175_eU10_mx25_p70_m60	10	150	140	90	60	35	25	70	35	127	10	100	12	175
M12_L175_eU8_mx27_p70_m35	8	150	140	90	35	35	27	70	35	127	10	100	12	175
M12_L120_eU8_mx27_p70_m35	8	150	140	90	35	35	27	70	35	127	10	100	12	120
M12_L150_eU8_mx27_p70_m35	8	150	140	90	35	35	27	70	35	127	10	100	12	150
M12_L100_eU10_mx25_p70_m35	10	150	140	90	35	35	25	70	35	127	10	100	12	100
M12_L175_eU8_mx27_p70_m35	8	150	140	90	35	35	27	70	35	127	10	100	12	175
M12_L175_eU10_mx25_p70_m35	10	150	170	90	35	35	50	70	40	127	10	100	12	175
M16_L100_eU6_mx29_p70_m35	6	150	140	90	35	35	29	70	35	127	10	100	16	120
M16_L100_eU10_mx25_p70_m35	10	150	140	90	35	35	25	70	35	127	10	100	16	120
M16_L175_eU6_mx29_p70_m35	6	150	140	90	35	35	29	70	35	127	10	100	16	195
M16_L175_eU10_mx25_p70_m35	10	150	140	90	35	35	25	70	35	127	10	100	16	195
M20_L100_eU12_mx23_p70_m35	12	150	140	90	35	35	23	70	35	127	10	100	20	100
M20_L175_eU12_mx33_p70_m35	12	150	140	90	35	35	33	70	25	127	10	100	20	175
M20_L200_eU12_mx33_p70_m35	12	150	140	90	35	35	33	70	25	127	10	100	20	200
M20_L240_eU12_mx33_p70_m35	12	150	140	90	35	35	33	70	25	127	10	100	20	240
M12_L100_eU12_mx23_p70_m35	12	150	140	90	35	35	23	70	35	127	10	100	12	100
M12_L150_eU8_mx27_p70_m35	8	150	140	90	35	35	27	70	35	127	10	100	12	150
M16_L175_eU8_mx27_p70_m35	8	150	140	90	35	35	27	70	35	127	10	100	16	175
M16_L100_eU8_mx27_p70_m35	8	150	140	90	35	35	27	70	35	127	10	100	16	100
M16_L175_eU9_mx26_p70_m35	9	150	140	90	35	35	26	70	35	127	10	100	16	175
M18_L175_eU6_mx29_p70_m35	6	150	140	90	35	35	29	70	35	127	10	100	18	175
M18_L175_eU8_mx27_p70_m35	8	150	140	90	35	35	27	70	35	127	10	100	18	175
M18_L175_eU10_mx25_p70_m35	10	150	140	90	35	35	25	70	35	127	10	100	18	175
M16_L100_eU9_mx26_p70_m35	9	150	140	90	35	35	26	70	35	127	10	100	16	100
M14_L175_eU8_mx27_p70_m35	8	150	140	90	35	35	27	70	35	127	10	100	14	175
M14_L100_eU8_mx27_p70_m35	8	150	140	90	35	35	27	70	35	127	10	100	14	100
M20_L100_eU10_mx25_p70_m35	10	150	140	90	35	35	25	70	35	127	10	100	20	100
M20_L175_eU10_mx25_p70_m35	10	150	140	90	35	35	25	70	35	127	10	100	20	175
M20_L100_eU8_mx27_p70_m35	8	150	140	90	35	35	27	70	35	127	10	100	20	100
M20_L175_eU8_mx27_p70_m35	8	150	140	90	35	35	27	70	35	127	10	100	20	175
M22_L175_eU12_mx23_p70_m35	12	150	140	90	35	35	23	70	35	127	10	100	22	175
M22_L175_eU12_dx23_p60_m35	12	150	140	90	35	35	33	60	35	127	10	100	22	175
M20_L100_eU9_mx26_p70_m35	9	150	140	90	35	35	26	70	35	127	10	100	20	100
M20_L175_eU9_mx26_p70_m35	9	150	140	90	35	35	26	70	35	127	10	100	20	175
M18_L100_eU10_mx25_p70_m35	10	150	140	90	35	35	25	70	35	127	10	100	18	100
M18_L240_eU10_mx25_p70_m35	10	150	140	90	35	35	25	70	35	127	10	100	18	240
M18_L175_eU9_mx26_p70_m35	9	150	140	90	35	35	26	70	35	127	10	100	18	175
M18_L100_eU9_mx26_p70_m35	9	150	140	90	35	35	26	70	35	127	10	100	18	100
M22_L175_eU14_mx31_p60_m35	14	150	140	90	35	35	31	60	35	127	10	100	22	175

Table 6 : Details of the cases studied for the analysis of the bending resistance of the lower flange of the U-shaped steel profile at normal temperature

Case	U-shaped steel profile				Steel rods position					Steel rods	
	$t_{bf,u}$	h_u	$b_{bf,u}$	$b_{tf,u}$	m	n	mx	p	ex	D	L
M16_L100_eU12_mx23_p70_m35	12	150	140	90	35	35	23	70	35	16	100
M16_L175_eU12_mx23_p70_m35	12	150	140	90	35	35	23	70	35	16	175
M16_L240_eU12_mx23_p70_m35	12	150	140	90	35	35	23	70	35	16	240
M12_L175_eU12_mx23_p70_m35	12	150	140	90	35	35	23	70	35	12	175
M20_L175_eU12_mx23_p70_m35	12	150	140	90	35	35	23	70	35	20	175
M12_L240_eU12_mx23_p70_m35	12	150	140	90	35	35	23	70	35	12	240
M20_L240_eU12_mx23_p70_m35	12	150	140	90	35	35	23	70	35	20	240
M18_L175_eU12_mx23_p70_m35	12	150	140	90	35	35	23	70	35	18	175
M12_L175_eU14_mx23_p70_m35	12	150	140	90	35	35	23	70	35	12	175

Table 7 : Details of the cases studied for the analysis of the buckling resistance of the steel rods of the 1st fusible link solution at normal temperature

Case	U-shaped steel profile				Steel rods position					Steel rods	
	$t_{bf,u}$	h_u	$b_{bf,u}$	$b_{tf,u}$	m	n	mx	p	ex	D	L
M12_L20_eU8_mx27_p70_m35	8	150	140	90	55	35	27	70	35	12	20
M12_L20_eU6_mx29_p70_m35	6	150	140	90	35	35	29	70	35	12	20
M12_L20_eU6_mx29_p70_m55	6	150	140	90	55	40	29	70	35	12	20
M12_L20_eU6_mx39_p55_m35	6	150	140	90	35	35	39	55	40	12	20
M20_L20_eU8_mx27_p70_m35	8	150	140	90	35	35	27	70	35	20	20
M20_L20_eU10_mx25_p70_m35	10	150	140	90	35	35	25	70	35	20	20
M16_L20_eU10_mx25_p70_m35	10	150	140	90	35	35	25	70	35	16	20

Table 8 : Details of studied cases for the 3rd fusible link solution at normal temperature

Case	UPN	Steel bolts	L-steel profile					Steel rods	
		Diam	h_L	b_L	t_L	P2	P1	Diam	L(mm)
M16_L175_UPN240_eL10_p180_DX400	UPN240	22	300	170	10	100	80	16	175
M16_L175_UPN240_eL10_p180_DX200	UPN240	22	300	170	10	100	80	16	175
M20_L175_UPN240_eL10_p180_DX200	UPN240	22	300	170	10	100	80	20	175
M20_L175_UPN300_eL10_p180_DX200	UPN300	22	300	170	10	100	80	20	175
M16_L175_UPN300_eL10_p180_DX200	UPN300	22	300	170	10	100	80	16	175
M16_L100_UPN240_eL10_p180_DX200	UPN240	22	300	170	10	100	80	16	100
M16_L240_UPN240_eL10_p180_DX200	UPN240	22	300	170	10	100	80	16	240
M20_L240_UPN240_eL10_p180_DX200	UPN240	22	300	170	10	100	80	20	240
M16_L175_UPN240_eL8_p180_DX200	UPN240	22	300	170	8	100	80	16	175
M16_L175_UPN240_eL15_p180_DX200	UPN240	22	300	170	15	100	80	16	175
M16_L100_UPN240_eL10_p180_DX400	UPN240	22	300	170	10	100	80	16	100
M16_L175_UPN240_eL10_p1120_DX200	UPN240	22	300	250	10	100	150	16	175
M16_L175_UPN240_eL10_p1120_DX200	UPN240	22	300	170	10	100	50	16	175
M16_L175_UPN240_eL10_p150_DX200	UPN240	22	300	170	10	100	50	16	175
M16_L175_UPN240_eL10_p180_DX200	UPN240	22	300	170	10	100	80	16	175
M12_L175_UPN240_el10_p180_DX200	UPN240	22	300	170	10	100	80	12	175
M12_L175_UPN240_el10_p180_DX400	UPN240	22	300	170	10	100	80	12	175
M16_L175_UPN300_eL10_p180_DX400	UPN300	22	350	170	10	100	80	16	175
M20_L175_UPN300_eL10_p180_DX200	UPN300	22	350	170	10	100	80	20	175
M20_L175_UPN300_eL10_p180_DX400	UPN300	22	350	170	10	100	80	20	175
M20_L175_UPN300_eL12_p180_DX200	UPN300	22	350	170	12	100	80	20	175
M22_L175_UPN300_eL10_p180_DX200	UPN300	22	350	170	12	100	80	22	175
M20_L240_UPN300_eL12_p180_DX200	UPN300	22	350	170	12	100	80	20	240

Table 9 : Details of studied cases for the 2nd fusible link solution at normal temperature

Case	U-shaped steel profile				Steel rods position					L-shaped steel profile			Steel bolts position			Steel bolts		Steel rods	
	$t_{bf,u}$	h_u	$b_{bf,u}$	$b_{tf,u}$	m	e	mx	p	ex	$t_{bf,Z}$	$b_{tf,Z}$	$b_{bf,Z}$	m	e1	p	Number	Diam	Diam	L
M16_L175_eU12_hU150_eZ8_mx23_p80_m65	12	150	150	100	65	55	23	80	35	8	100	142	38	70	140	4	20	16	175
M12_L175_eU6_hU150_eZ12_mx29_p80_m65	6	150	150	100	65	55	29	80	35	12	100	142	42	70	140	4	20	12	175
M16_L175_eU12_hU300_eZ12_mx23_p80_m65	12	150	150	100	65	55	23	80	35	12	100	142	42	70	140	4	20	16	175
M16_L175_eU6_hU150_eZ12_mx29_p80_m65	6	150	150	100	65	55	29	80	35	12	100	142	42	70	140	4	20	16	175
M12_L150_eU12_hU150_eZ12_mx23_p80_m65	12	150	150	100	65	55	23	80	35	12	100	142	42	70	140	4	20	12	150
M12_L175_eU12_hU150_eZ12_mx23_60_m65	12	150	150	100	55	55	23	60	55	12	100	142	42	70	140	4	20	12	175
M16_L240_eU6_hU150_eZ12_mx29_p80_m65	6	150	150	100	65	55	29	80	35	12	100	142	42	70	140	4	20	16	240
M16_L175_eU6_hU150_eZ6_mx29_p80_m65	6	150	150	100	65	55	29	80	35	6	100	142	36	70	140	4	20	16	175
M12_L175_eU12_hU150_eZ6_mx23_p80_m65	12	150	150	100	65	55	23	80	35	6	100	142	36	70	140	4	20	12	175
M12_L240_eU12_hU150_eZ12_mx23_p80_m65	12	150	150	100	65	55	23	80	35	12	100	142	42	70	140	4	20	12	240
M16_L100_eU12_hU150_eZ8_mx23_p80_m65	12	150	150	100	65	55	23	80	35	8	100	142	38	70	140	4	20	16	100
M16_L175_eU8_hU150_eZ8_mx27_p80_m65	8	150	150	100	65	55	27	80	35	8	100	142	38	70	140	4	20	16	175
M16_L175_eU12_hU150_eZ6_mx23_p80_m65	12	150	150	100	65	55	23	80	35	6	100	142	36	70	140	4	20	16	175
M16_L240_eU12_hU150_eZ12_mx23_p80_m65	12	150	150	100	65	55	23	80	35	12	100	142	42	70	140	4	20	16	240

Table 10 : Details of the cases studied for the analysis of the bending resistance of the lower flange of the Z-shaped steel profile at normal temperature

Case	U-shaped steel profile				Steel rods position					L-shaped steel profile			Steel bolts position			Steel bolts		Steel rods	
	$t_{bf,u}$	h_u	$b_{bf,u}$	$b_{tf,u}$	m	e	mx	p	ex	$t_{bf,Z}$	$b_{tf,Z}$	$b_{bf,Z}$	m	e1	p	Numb	Diam	Diam	L
M16_L175_eU12_hU150_eZ6_m30_e170	12	140	140	100	65	55	23	80	25	6	100	142	36	70	140	4	20	16	20
M16_L175_eU12_hU150_eZ6_m40_e150	12	140	140	100	65	55	23	80	25	6	100	142	46	50	140	4	20	16	20
M16_L175_eU12_hU150_eZ6_m50_e150	12	140	140	100	65	55	23	80	25	6	100	142	56	50	140	4	20	16	20
M16_L175_eU12_hU150_eZ8_m30_e170	12	140	140	100	65	55	23	80	25	8	100	142	38	70	140	4	20	16	20
M16_L175_eU12_hU150_eZ8_m40_e150	12	140	140	100	65	55	23	80	25	8	100	142	48	50	140	4	20	16	20
M16_L175_eU12_hU150_eZ8_m50_e150	12	140	140	100	65	55	23	80	25	8	100	142	48	50	140	4	20	16	20
M16_L175_eU12_hU150_eZ12_m50_e150	12	140	140	100	65	55	23	80	25	12	100	142	62	50	140	4	20	16	20
M16_L175_eU12_hU150_eZ12_m30_e170	12	140	140	100	65	55	23	80	25	12	100	142	42	70	140	4	20	16	20

Table 11 : Details of studied cases for the 1st fusible link solution at elevated temperature

Case	U-shaped steel profile				Steel rods position					L-shaped steel plate			Steel rods	
	$t_{bf,u}$	h_u	$b_{bf,u}$	$b_{tf,u}$	m	n	mx	p	ex	h_L	$t_{b,L}$, $t_{w,L}$	b_L	D	L
30%_M12_L100_eU6_mx29_p70_m35	6	140	140	100	35	35	29	70	35	127	10	110	12	100
50%_M12_L100_eU6_mx29_p70_m35	6	140	140	100	35	35	29	70	35	127	10	110	12	100
70%_M12_L100_eU6_mx29_p70_m35	6	140	140	100	35	35	29	70	35	127	10	110	12	100
70%_M12_L100_eU10_mx25_p70_m35	10	140	140	100	35	35	25	70	35	127	10	110	12	100
50%_M12_L100_eU10_mx25_p70_m35	10	140	140	100	35	35	25	70	35	127	10	110	12	100
30%_M12_L175_eU10_mx25_p70_m35	10	140	140	100	35	35	25	70	35	127	10	110	12	175
50%_M12_L175_eU10_mx25_p70_m35	10	140	140	100	35	35	25	70	35	127	10	110	12	175
70%_M12_L175_eU10_mx25_p70_m35	10	140	140	100	35	35	25	70	35	127	10	110	12	175
30%_M12_L175_eU12_mx23_p70_m35	12	140	140	100	35	35	23	70	35	127	10	110	12	175
50%_M12_L175_eU12_mx23_p70_m35	12	140	140	100	35	35	23	70	35	127	10	110	12	175
70%_M12_L175_eU12_mx23_p70_m35	12	140	140	100	35	35	23	70	35	127	10	110	12	175
50%_M12_L175_eU14_mx21_p70_m35	14	140	140	100	35	35	21	70	35	127	10	110	12	175
30%_M12_L175_eU14_mx21_p70_m35	14	140	140	100	35	35	21	70	35	127	10	110	12	175
70%_M12_L175_eU14_mx21_p70_m35	14	140	140	100	35	35	21	70	35	127	10	110	12	175
70%_M12_L240_eU10_mx25_p70_m35	10	140	140	100	35	35	25	70	35	127	10	110	12	240
30%_M12_L240_eU10_mx25_p70_m35	10	140	140	100	35	35	25	70	35	127	10	110	12	240
50%_M16_L175_eU6_mx29_p70_m35	6	140	140	100	35	35	29	70	35	127	10	110	16	175
30%_M16_L175_eU6_mx29_p70_m35	6	140	140	100	35	35	29	70	35	127	10	110	16	175
70%_M16_L175_eU6_mx29_p70_m35	6	140	140	100	35	35	29	70	35	127	10	110	16	175
70%_M16_L240_eU12_mx23_p70_m35	12	140	140	100	35	35	23	70	35	127	10	110	16	240
30%_M16_L240_eU12_mx23_p70_m35	12	140	140	100	35	35	23	70	35	127	10	110	16	240
50%_M12_L175_eU6_mx29_p70_m35	6	140	140	100	35	35	29	70	35	127	10	110	12	175
70%_M12_L175_eU6_mx29_p70_m35	6	140	140	100	35	35	29	70	35	127	10	110	12	175
50%_M12_L175_eU8_mx27_p70_m35	8	140	140	100	35	35	27	70	35	127	10	110	12	175
70%_M12_L175_eU8_mx27_p70_m35	8	140	140	100	35	35	27	70	35	127	10	110	12	175
50%_M12_L175_eU10_mx25_p50_m35	10	140	140	100	35	35	25	50	35	127	10	110	12	175
70%_M12_L175_eU10_mx25_p50_m35	10	140	140	100	35	35	25	50	35	127	10	110	12	175
70%_M12_L175_eU10_mx25_p55_m35	10	140	140	100	45	35	25	55	35	127	10	110	12	175
50%_M12_L175_eU10_mx25_p55_m35	10	140	140	100	45	35	25	55	35	127	10	110	12	175
30%_M12_L175_eU10_mx25_p50_m35	10	140	140	100	35	35	25	50	35	127	10	110	12	175
50%_M16_L175_eU10_mx25_p70_m35	10	140	140	100	35	35	25	70	35	127	10	110	16	175
70%_M16_L175_eU10_mx25_p70_m35	10	140	140	100	35	35	25	70	35	127	10	110	16	175
30%_M16_L175_eU10_mx25_p70_m35	10	140	140	100	35	35	25	70	35	127	10	110	16	175
30%_M12_L175_eU8_mx27_p70_m35	8	140	140	100	35	35	27	70	35	127	10	110	12	175
50%_M12_L175_eU8_mx27_p70_m35	8	140	140	100	35	35	27	70	35	127	10	110	12	175
70%_M12_L175_eU8_mx27_p70_m35	8	140	140	100	35	35	27	70	35	127	10	110	12	175
R30_M12_L175_eU8_mx27_p70_m35	8	140	140	100	35	35	27	70	35	127	10	110	12	175
30%_M14_L100_eU8_mx27_p70_m35	8	140	140	100	35	35	27	70	35	127	10	110	14	100
50%_M14_L100_eU8_mx27_p70_m35	8	140	140	100	35	35	27	70	35	127	10	110	14	100
70%_M14_L100_eU8_mx27_p70_m35	8	140	140	100	35	35	27	70	35	127	10	110	14	100
30%_M14_L175_eU8_mx27_p70_m35	8	140	140	100	35	35	27	70	35	127	10	110	14	175
50%_M14_L175_eU8_mx27_p70_m35	8	140	140	100	35	35	27	70	35	127	10	110	14	175
70%_M14_L175_eU8_mx27_p70_m35	8	140	140	100	35	35	27	70	35	127	10	110	14	175
30%_M16_L100_eU10_mx25_p70_m35	10	140	140	100	35	35	25	70	35	127	10	110	16	100
50%_M16_L100_eU10_mx25_p70_m35	10	140	140	100	35	35	25	70	35	127	10	110	16	100
70%_M16_L100_eU10_mx25_p70_m35	10	140	140	100	35	35	25	70	35	127	10	110	16	100
30%_M16_L100_eU10_mx25_p70_m35_rig	10	140	140	100	35	35	25	70	35	127	10	110	16	99
50%_M16_L100_eU10_mx25_p70_m35_rig	10	140	140	100	35	35	25	70	35	127	10	110	16	100
70%_M16_L100_eU10_mx25_p70_m35_rig	10	140	140	100	35	35	25	70	35	127	10	110	16	100
50%_M16_L175_eU6_mx29_p70_m35	6	140	140	100	35	35	29	70	35	127	10	110	16	175
70%_M16_L175_eU6_mx29_p70_m35	6	140	140	100	35	35	29	70	35	127	10	110	16	175
50%_M16_L175_eU10_mx25_p70_m35	10	140	140	100	35	35	25	70	35	127	10	110	16	175
70%_M16_L175_eU10_mx25_p70_m35	10	140	140	100	35	35	25	70	35	127	10	110	16	175
R30_M16_L175_eU10_mx25_p70_m35	10	140	140	100	35	35	25	70	35	127	10	110	16	175
R30_M16_L175_eU10_mx25_p70_m35	10	140	140	100	35	35	25	70	35	127	10	110	16	175
30%_M18_L175_eU10_mx25_p70_m35	10	140	140	100	35	35	25	70	35	127	10	110	18	175
50%_M18_L175_eU10_mx25_p70_m35	10	140	140	100	35	35	25	70	35	127	10	110	18	175
70%_M18_L175_eU10_mx25_p70_m35	10	140	140	100	35	35	25	70	35	127	10	110	18	175
50%_M20_L100_eU12_mx23_p70_m35	12	140	140	100	35	35	23	70	35	127	10	110	20	175
70%_M20_L100_eU12_mx23_p70_m35	12	140	140	100	35	35	23	70	35	127	10	110	20	175
0.8_M20_L100_eU12_mx23_p70_m35	12	140	140	100	35	35	23	70	35	127	10	110	20	175
0.65_M20_L175_eU12_mx33_p70_m35	12	140	140	100	35	35	33	70	25	127	10	110	20	175
70%_M20_L175_eU12_mx33_p70_m35	12	140	140	100	35	35	33	70	25	127	10	110	20	175
R30_M20_L100_eU12_mx33_p70_m35	12	140	140	100	35	35	33	70	25	127	10	110	20	175
30%_M20_L175_eU12_mx23_p70_m35	12	140	140	100	35	35	23	70	35	127	10	110	20	175
50%_M20_L175_eU12_mx23_p70_m35	12	140	140	100	35	35	23	70	35	127	10	110	20	175
70%_M20_L175_eU12_mx23_p70_m35	12	140	140	100	35	35	23	70	35	127	10	110	20	175
30%_M22_L175_eU12_mx23_p70_m35	12	140	140	100	35	35	23	70	35	127	10	110	22	175
50%_M22_L175_eU12_mx23_p70_m35	12	140	140	100	35	35	23	70	35	127	10	110	22	175
70%_M22_L175_eU12_mx23_p70_m35	12	140	140	100	35	35	23	70	35	127	10	110	22	175
M12_L20_eU8_mx27_p70_m35	8	140	140	90	35	35	27	70	35	127	10	100	12	20
M12_L20_eU8_mx27_p70_m35	8	140	140	90	55	35	27	70	35	127	10	100	12	20
M12_L20_eU6_mx29_p70_m35	6	140	140	90	35	35	29	70	35	127	10	100	12	20
M12_L20_eU6_mx29_p70_m35	6	140	140	90	55	40	29	70	35	127	10	100	12	20
M12_L20_eU6_mx39_p55_m40	6	140	140	90	35	35	39	55	40	127	10	100	12	20
M16_L20_eU10_mx25_p70_m35	10	140	140	90	35	35	25	70	35	127	10	100	16	20
M12_L20_eU6_mx29_p70_m35	6	140	140	90	75	40	29	70	35	127	10	100	12	20

Table 12 : Details of studied cases for the 3rd fusible link solution at elevated temperature

Case	UPN	Steel bolts	L-steel profile					Steel rods	
		Diam	h_L	b_L	t_L	P2	P1	Diam	L(mm)
70%-M16_L175_UPN240_eL10_p180_DX400	UPN240	22	300	170	10	100	80	16	175
50%-M16_L175_UPN240_eL10_p180_DX400	UPN240	22	300	170	10	100	80	16	175
30%-M16_L175_UPN240_eL10_p180_DX400	UPN240	22	300	170	10	100	80	16	175
70%-M16_L175_UPN240_eL10_p180_DX200	UPN240	22	300	170	10	100	80	16	175
50%-M16_L175_UPN240_eL10_p180_DX200	UPN240	22	300	170	10	100	80	16	175
30%-M16_L175_UPN240_eL10_p180_DX200	UPN240	22	300	170	10	100	80	16	175
70%-M20_L175_UPN240_eL10_p180_DX200	UPN240	22	300	170	10	100	80	20	175
50%-M20_L175_UPN240_eL10_p180_DX200	UPN240	22	300	170	10	100	80	20	175
30%-M20_L175_UPN300_eL10_p180_DX200	UPN300	22	350	170	10	100	80	20	175
70%-M16_L175_UPN300_eL10_p180_DX200	UPN300	22	350	170	10	100	80	16	175
30%-M16_L175_UPN300_eL10_p180_DX200	UPN300	22	350	170	10	100	80	16	175
70%-M16_L100_UPN240_eL10_p180_DX200	UPN240	22	300	170	10	100	80	16	100
50%-M16_L100_UPN240_eL10_p180_DX200	UPN240	22	300	170	10	100	80	16	100
70%-M16_L240_UPN240_eL10_p180_DX200	UPN240	22	300	170	10	100	80	16	240
50%-M16_L240_UPN240_eL10_p180_DX200	UPN240	22	300	170	10	100	80	16	240
30%-M16_L240_UPN240_eL10_p180_DX200	UPN240	22	300	170	10	100	80	16	240
70%-M20_L240_UPN240_eL10_p180_DX200	UPN240	22	300	170	10	100	80	20	240
50%-M20_L240_UPN240_eL10_p180_DX200	UPN240	22	300	170	10	100	80	20	240
30%-M20_L240_UPN240_eL10_p180_DX200	UPN240	22	300	170	10	100	80	20	240
70%-M16_L175_UPN240_eL8_p180_DX200	UPN240	22	300	170	8	100	80	16	175
70%-M16_L175_UPN240_eL15_p180_DX200	UPN240	22	300	170	15	100	80	16	175
50%-M16_L175_UPN240_eL15_p180_DX200	UPN240	22	300	170	15	100	80	16	175
30%-M16_L175_UPN240_eL15_p180_DX200	UPN240	22	300	170	15	100	80	16	175
70%-M16_L100_UPN240_eL10_p180_DX400	UPN240	22	300	170	10	100	80	16	100
50%-M16_L100_UPN240_eL10_p180_DX400	UPN240	22	300	250	10	100	80	16	100
70%-M16_L175_UPN240_eL10_p1120_DX200	UPN240	22	300	250	10	100	150	16	175
50%-M16_L175_UPN240_eL10_p1120_DX200	UPN240	22	300	250	10	100	150	16	175
30%-M16_L175_UPN240_eL10_p1120_DX200	UPN240	22	300	170	10	100	150	16	175
70%-M16_L175_UPN240_eL10_p150_DX200	UPN240	22	300	170	10	100	50	16	175
50%-M16_L175_UPN240_eL10_p150_DX200	UPN240	22	300	170	10	100	50	16	175
50%-.M20_L175_UPN300_eL10_p180_DX200	UPN300	22	350	170	10	100	80	20	175
30%-M12_L175_UPN240_eL10_p180_DX200	UPN240	22	300	170	10	100	80	12	175
50%-M12_L175_UPN240_eL10_p180_DX200	UPN240	22	300	170	10	100	80	12	175
70%-M12_L175_UPN240_eL10_p180_DX200	UPN240	22	300	170	10	100	80	12	175
30%-M12_L175_UPN240_eL10_p180_DX400	UPN240	22	300	170	10	100	80	12	175
50%-M12_L175_UPN240_eL10_p180_DX400	UPN240	22	300	170	10	100	80	12	175
70%-M12_L175_UPN240_eL10_p180_DX400	UPN240	22	300	170	10	100	80	12	175
30%-M16_L175_UPN300_eL10_p180_DX400	UPN300	22	350	170	10	100	80	16	175
50%-M16_L175_UPN300_eL10_p180_DX400	UPN300	22	350	170	10	100	80	16	175
70%-M16_L175_UPN300_eL10_p180_DX400	UPN300	22	350	170	10	100	80	16	175
70%-M16_L175_UPN300_eL10_p180_DX200	UPN300	22	350	170	10	100	80	16	175
30%-M20_L175_UPN300_eL12_p180_DX200	UPN300	22	350	170	10	100	80	20	175
50%-M20_L175_UPN300_eL12_p180_DX200	UPN300	22	350	170	10	100	80	20	175
70%-M20_L175_UPN300_eL12_p180_DX200	UPN300	22	350	170	10	100	80	20	175

Table 13 : Details of the studied cases for the 2nd fusible link solution at elevated temperature

Case	U-shaped steel profile				Steel rods position					L-shaped steel profile			Steel bolts position			Steel bolts		Steel rods	
	$t_{bf,u}$	h_u	$b_{bf,u}$	$b_{tf,u}$	m	e	mx	p	ex	$t_{bf,Z}$	$b_{tf,Z}$	$b_{bf,Z}$	m	e1	p	Num.	Diam	Diam	L
70%-M16_L175_eU12_hU150_eZ8_mx23_p80_m65	12	150	150	100	65	55	23	80	35	8	100	142	38	70	140	4	16	16	175
50%-M16_L175_eU12_hU150_eZ8_mx23_p80_m65	12	150	150	100	65	55	23	80	35	8	100	142	38	70	140	4	16	16	175
30%-M16_L175_eU12_hU150_eZ8_mx23_p80_m65	12	150	150	100	65	55	23	80	35	8	100	142	38	70	140	4	16	16	175
70%-M16_L175_eU12_hU300_eZ12_mx23_p80_m65	12	150	150	100	65	55	23	80	35	12	100	142	42	70	140	4	16	16	175
50%-M16_L175_eU12_hU300_eZ12_mx23_p80_m65	12	150	150	100	65	55	23	80	35	12	100	142	42	70	140	4	16	16	175
70%-M16_L175_eU6_hU150_eZ12_mx29_p80_m65	6	150	150	100	65	55	29	80	35	12	100	142	42	70	140	4	16	16	175
50%-M16_L175_eU6_hU150_eZ12_mx29_p80_m65	6	150	150	100	65	55	29	80	35	12	100	142	42	70	140	4	16	16	175
70%-M12_L150_eU12_hU150_eZ12_mx29_p80_m65	12	150	150	100	65	55	23	80	35	12	100	142	42	70	140	4	16	12	150
50%-M12_L150_eU12_hU150_eZ12_mx23_p80_m65	12	150	150	100	65	55	23	80	35	12	100	142	42	70	140	4	16	12	150
30%-M12_L150_eU12_hU150_eZ12_mx23_p80_m65	12	150	150	100	65	55	23	80	35	12	100	142	42	70	140	4	16	12	150
70%-M16_L240_eU6_hU150_eZ12_mx29_p80_m65	6	150	150	100	65	55	29	80	35	12	100	142	42	70	140	4	16	16	240
50%-M16_L240_eU6_hU150_eZ12_mx29_p80_m65	6	150	150	100	65	55	29	80	35	12	100	142	42	70	140	4	16	16	240
30%-M16_L240_eU6_hU150_eZ12_mx29_p80_m65	6	150	150	100	65	55	29	80	35	12	100	142	42	70	140	4	16	16	240
70%-M16_L175_eU6_hU150_eZ6_mx29_p80_m65	6	150	150	100	65	55	29	80	35	6	100	142	36	70	140	4	16	16	175
50%-M16_L175_eU6_hU150_eZ6_mx29_p80_m65	6	150	150	100	65	55	29	80	35	6	100	142	36	70	140	4	16	16	175
30%-M16_L175_eU6_hU150_eZ6_mx29_p80_m65	6	150	150	100	65	55	29	80	35	6	100	142	36	70	140	4	16	16	175
30%-M16_L175_eU6_hU150_eZ12_mx29_p80_m65	6	150	150	100	65	55	29	80	35	12	100	142	42	70	140	4	16	16	175
70%-M12_L240_eU12_hU150_eZ12_mx23_p80_m65	12	150	150	100	65	55	23	80	35	12	100	142	42	70	140	4	12	12	240
50%-M12_L240_eU12_hU150_eZ12_mx23_p80_m65	12	150	150	100	65	55	23	80	35	12	100	142	42	70	140	4	12	12	240
30%-M12_L240_eU12_hU150_eZ12_mx23_p80_m65	12	150	150	100	65	55	23	80	35	12	100	142	42	70	140	4	12	12	240
30%-M16_L100_eU12_hU150_eZ8_mx23_p80_m65	12	150	150	100	65	55	23	80	35	8	100	142	38	70	140	4	16	16	100
70%-M16_L100_eU12_hU150_eZ8_mx23_p80_m65	12	150	150	100	65	55	23	80	35	8	100	142	38	70	140	4	16	16	100
70%-M16_L175_eU8_hU150_eZ8_mx27_p80_m65	8	150	150	100	65	55	27	80	35	8	100	142	38	70	140	4	16	16	175
50%-M16_L175_eU8_hU150_eZ8_mx27_p80_m65	8	150	150	100	65	55	27	80	35	8	100	142	38	70	140	4	16	16	175
30%-M16_L175_eU8_hU150_eZ8_mx27_p80_m65	8	150	150	100	65	55	27	80	35	8	100	142	38	70	140	4	16	16	175
R30-M16_L175_eU8_hU150_eZ8_mx27_p80_m65	8	150	150	100	65	55	27	80	35	8	100	142	38	70	140	4	16	16	175
70%-M16_L240_eU12_hU150_eZ12_mx23_p80_m65	12	150	150	100	65	55	23	80	35	12	100	142	42	70	140	4	12	16	240
50%-M16_L240_eU12_hU150_eZ12_mx23_p80_m65	12	150	150	100	65	55	23	80	35	12	100	142	42	70	140	4	12	16	240
30%-M16_L240_eU12_hU150_eZ12_mx23_p80_m65	12	150	150	100	65	55	23	80	35	12	100	142	42	70	140	4	12	16	240
50%-M16_L175_eU12_hU150_eZ6_mx23_p80_m65	12	150	150	100	65	55	23	80	35	6	100	142	36	70	140	4	16	16	175
30%-M16_L175_eU12_hU150_eZ6_mx23_p80_m65	12	150	150	100	65	55	23	80	35	6	100	142	36	70	140	4	16	16	175
R30-M16_L175_eU12_hU150_eZ6_mx23_p80_m65	12	150	150	100	65	55	23	80	35	6	100	142	36	70	140	4	16	16	175
70%-M12_L175_eU6_hU150_eZ12_mx29_p80_m65	6	150	150	100	65	55	29	80	35	12	100	142	30	70	140	4	16	12	175
50%-M12_L175_eU6_hU150_eZ12_mx29_p80_m65	6	150	150	100	65	55	29	80	35	12	100	142	30	70	140	4	16	12	175
30%-M12_L175_eU6_hU150_eZ12_mx29_p80_m65	6	150	150	100	65	55	29	80	35	12	100	142	30	70	140	4	16	12	175
70%-M20_L240_eU10_hU150_eZ10_mx25_p80_m65	10	150	150	100	65	55	25	80	35	10	100	142	30	70	140	4	16	20	240
50%-M20_L240_eU10_hU150_eZ10_mx25_p80_m65	10	150	150	100	65	55	25	80	35	10	100	142	30	70	140	4	16	20	240
30%-M20_L240_eU10_hU150_eZ10_mx25_p80_m65	10	150	150	100	65	55	25	80	35	10	100	142	30	70	140	4	16	20	240
30%-M16_L175_eU10_hU150_eZ10_mx25_p80_m65	10	150	150	100	65	55	25	80	35	10	100	142	30	70	140	4	16	16	175
50%-M16_L175_eU10_hU150_eZ10_mx25_p80_m65	10	150	150	100	65	55	25	80	35	10	100	142	30	70	140	4	16	16	175
70%-M16_L175_eU10_hU150_eZ10_mx25_p80_m65	10	150	150	100	65	55	25	80	35	10	100	142	30	70	140	4	16	16	175
30%-M16_L175_eU14_hU150_eZ14_mx21_p80_m65	14	150	150	100	65	55	21	80	35	14	100	142	30	70	140	4	16	16	175
30%-M16_L175_eU14_hU150_eZ14_mx21_p80_m65	14	150	150	100	65	55	21	80	35	14	100	142	30	70	140	4	16	16	175
30%-M16_L175_eU14_hU150_eZ14_mx21_p80_m65	14	150	150	100	65	55	21	80	35	14	100	142	30	70	140	4	16	16	175

3.2 Numerical modelling

3.2.1 Numerical approach

Numerical modelling of the fusible links was conducted using ANSYS [3]. To simulate the fire behaviour of the links, a sequentially coupled 3D thermal-mechanical analysis procedure was followed. First, a heat transfer analysis was conducted to determine the temperature field, followed by a mechanical analysis using the previously calculated temperature fields to calculate the structural response. Therefore, the same meshing is adopted for both the thermal and mechanical models, but the finite element formulations are switched to adapt to the type of analysis. The nodal temperatures computed from the thermal analysis are therefore stored as a function of time and used directly as thermal loads in the mechanical analyses. Furthermore, a static-dynamic procedure, which allows local instabilities to be passed through (which would cause singularities in a full static analysis) and enables the progressive failure of steel links under fire conditions to be simulated, was adopted to simulate the progressive failure mechanism of the investigated 'fusible' link solutions.

Moreover, the procedure employed to calculate the fire resistance of the investigated fusible link solutions is as follows:

- First, an FE calculation is performed at normal temperature to determine the load-bearing capacity of the fusible link when subjected to compressive loading. The compressive load is then gradually increased until the link fails.
- Next, calculations are carried out at elevated temperatures to determine the fire resistance of the links under consideration. The links are exposed to the standard fire curve and subjected to a compressive load equivalent to 30%, 50%, and 70% of their respective normal-temperature resistance. The temperature fields obtained from the thermal analysis are fed directly into the mechanical model and calculations are performed until the link fails.

3.2.2 Main assumptions

The 3D thermal-mechanical models developed for the three-link solutions are shown in Figure 3.5, Figure 3.6 and Figure 3.7, respectively. Several simplifications were considered in the modelling process to strike a balance between FE model accuracy and computational cost. All the modelled components were meshed using 20-node brick finite elements (FEs) to achieve suitable accuracy with a limited number of meshes (SOLID90 for the thermal models and SOLID186 for the mechanical models). The bolts and steel rods are modelled in as much detail as possible. However, some geometric features that are assumed to have an insignificant effect on the response of the fusible links were ignored. Firstly, the threaded parts of the bolts, rods and nuts are omitted, and the bolt–nut assembly is modelled as a single component. This assumes that relative motion between the bolts and nuts, or loosening, does not occur during loading. Secondly, no washers are modelled, and the bolt holes are slightly larger than the bolt diameter. No welds were modelled. Furthermore, thermal perfect contacts were assigned to all elements in the thermal models, while automatic surface-to-surface contact was used in the mechanical models, including frictional phenomena. This includes contact between the steel profiles and the bolts (heads and shanks), as well as contact between the steel profiles (upper surface and holes) and the threaded rods. The friction coefficient was fixed to 0.25. For both models, the y-axis relates to the height of the wall.

The fusible links are exposed to standard temperature–time curve (ISO 834 standard fire curve). According to EN 1991-1-2 [5], the heat transfer modes of conduction, convection and radiation were considered in the form of appropriate boundary conditions and material property values. Thus, convective heat transfer coefficients of 25 and 4 W/m²/K were assigned to the fire-exposed and unexposed surfaces of the studied fusible link respectively. The fire emissivity was fixed to 1.0 and the surface emissivity of materials was taken equal to 0.7 for the studied materials. To define the surface radiation, the physical properties, such as the Stefan-Boltzmann constant and the absolute zero temperature of the system, had to be specified as well. Moreover, thermal material properties of carbon steel and aluminium bolts such as specific heat, thermal conductivity and density are those given in EN 1993-1-2 [7] and EN 1999-1-2 [8] respectively, while the thermal properties of the mineral wool of sandwich panels (considered as independent of the temperature) were obtained from another analysis carried out in the scope of the FISHWALL project (density of 120 kg/m3, specific heat of 1000 J/kg.K and thermal conductivity of 0.045 W/m.K). The temperatures of modelled members at the beginning of the heating/analysis were predefined as 20 °C.

Only the fusible link, half of the portal frame column near the fusible link, and the steel threaded rods were modelled and meshed in the mechanical models. The non-modelled parts were accounted for using appropriate boundary conditions. Thus, the four threaded rods were assumed to be fully restrained at the level of the steel column supporting the sandwich panels, and any lateral restraint by the non-bearing wall was ignored. Additionally, lateral displacement Ux along the symmetrical plane of the profile web, as well as displacement Uy at one end of the portal frame column, are restrained. Furthermore, since only part of the UPN 240 length was meshed for the third fusible link, its end was restrained against longitudinal (X) displacement to account for the unmodelled part. All of these boundary conditions are shown in Figure 3.5 to Figure 3.7. The mechanical properties of the steel profiles at elevated temperatures are taken from EN 1993-1-2, considering the yielding plateau and strain hardening. The elevated temperature stress-strain curves of the studied materials are shown in Figure 3.9. It should also be noted that the melting temperature of aluminium is currently around 500°C. During the pushing phase, the aluminium bolts break before the system fails, either due to failure caused by the thermal expansion of the connected components or due to loss of resistance at the melting temperature. Consequently, the aluminium bolts are deactivated at the failure times determined during mechanical analysis.

In addition, it should be noted that reduced models based on the full-scale models were used to investigate the resistance of individual link components, such as the bending resistance of the lower flange of U-shaped and Z-shaped steel profiles, or the buckling resistance of rods. This was achieved by deleting or rigidifying some link parts where relevant, as illustrated in Figure 3.7.

More detailed information concerning the numerical model can be found in the project deliverable D3.3 [12].

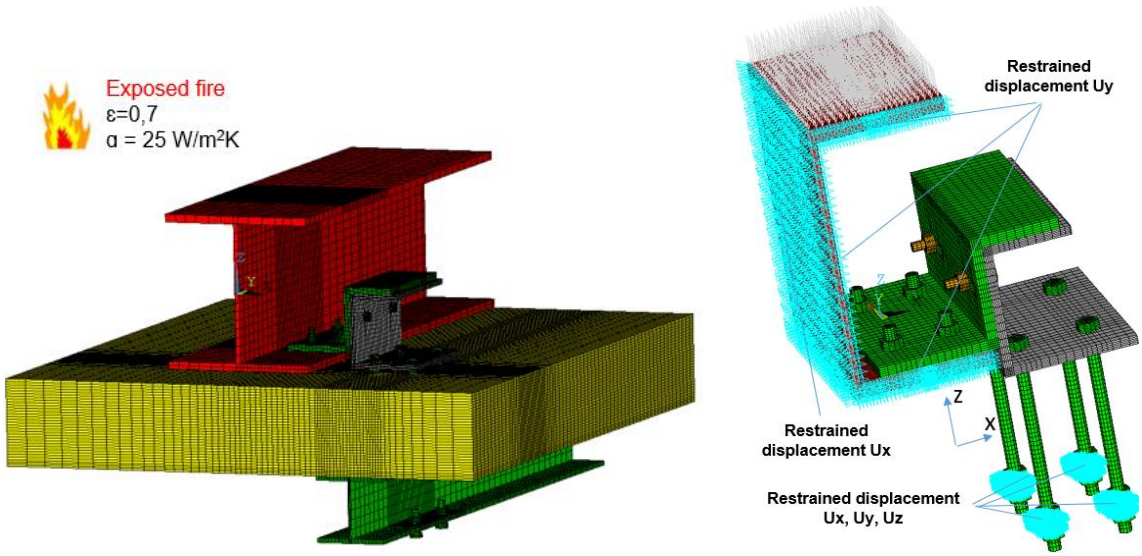

a) 3D FE thermal model b) 3D FE mechanical model

Figure 3.5: 3D FE models for the thermal and mechanical analysis of the first fusible link

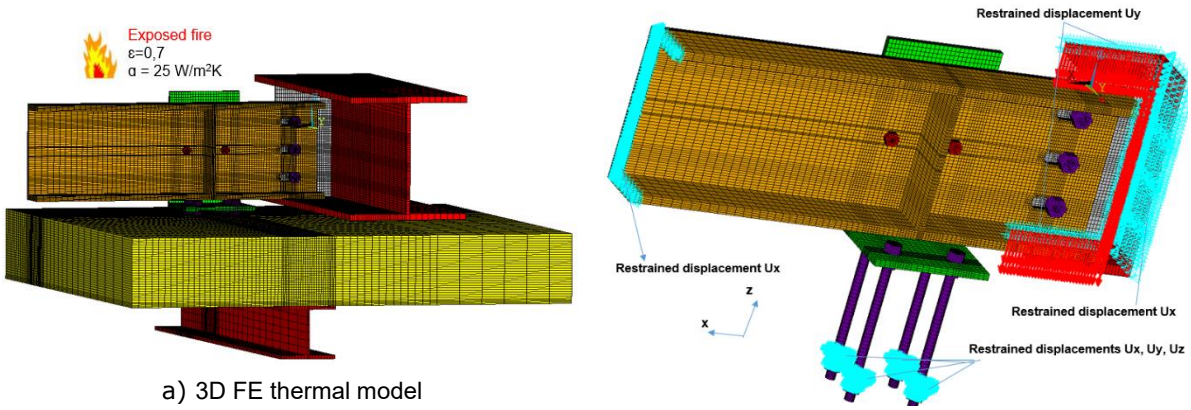

a) 3D FE thermal model

3D FE mechanical model

Figure 3.6: 3D FE models for the thermal and mechanical analysis of the 2nd fusible link

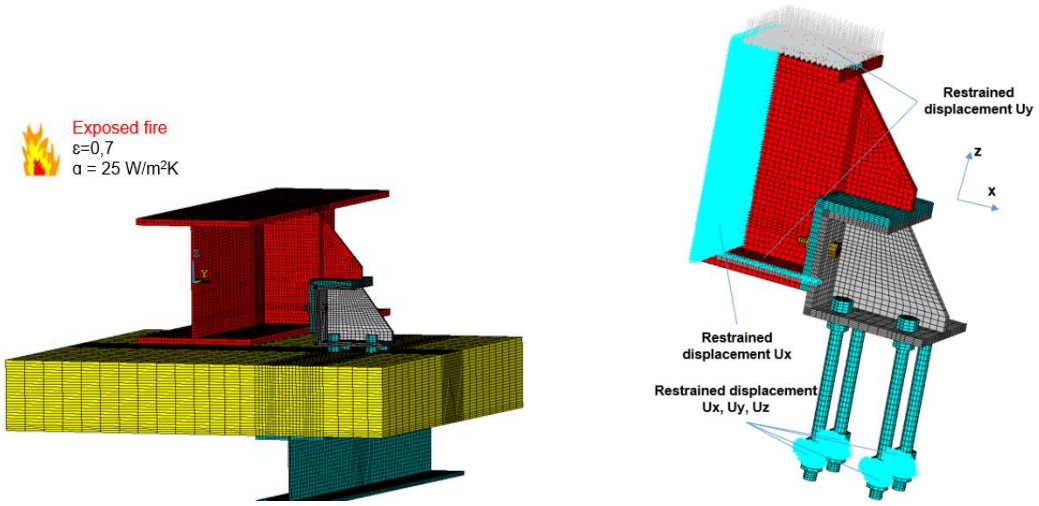

a) 3D FE thermal model b) 3D FE mechanical model

Figure 3.7: 3D FE models for the thermal and mechanical analysis of the 3rd fusible link

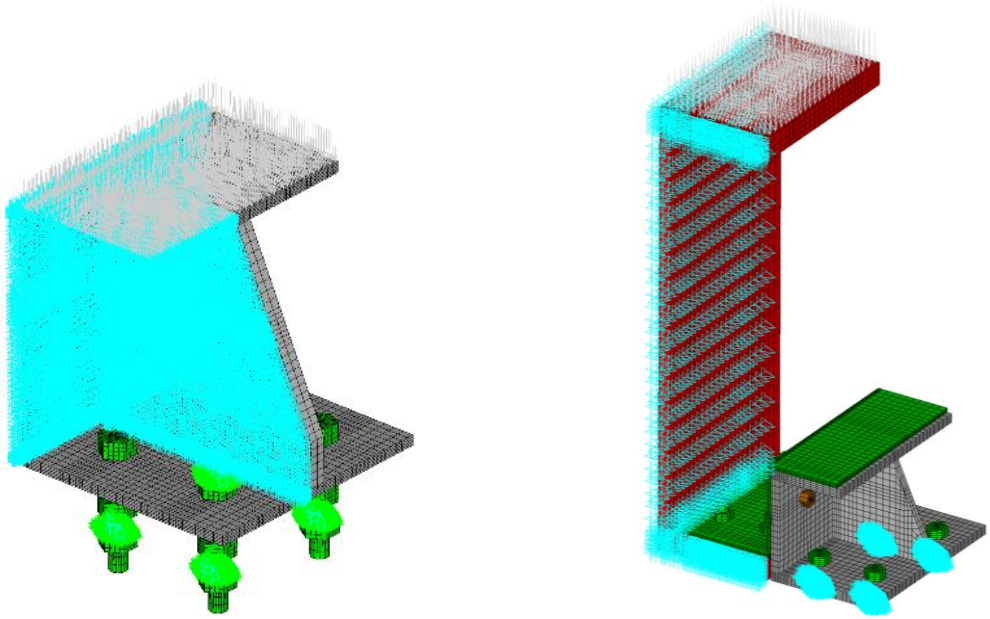

Figure 3.8: Reduced 3D FE models used to investigate the resistance of individual link components

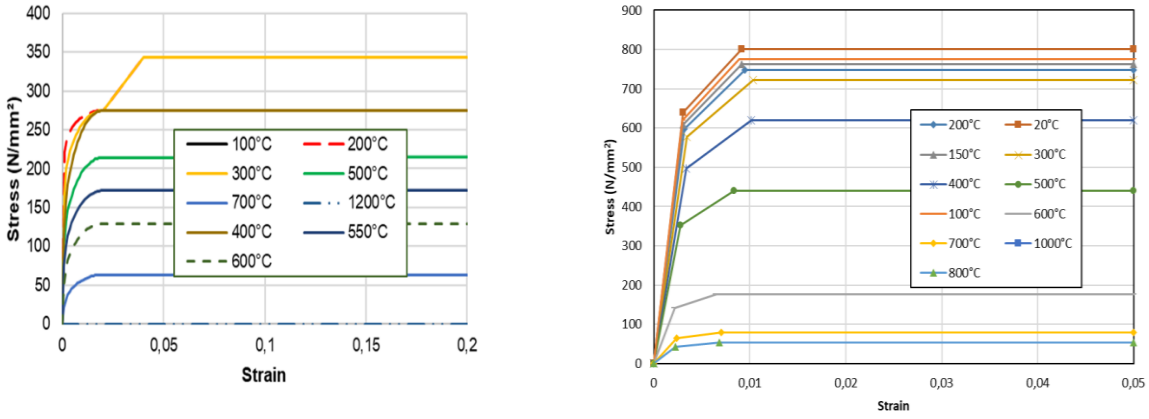

a) steel profiles b) Steel rods

Figure 3.9: Stress-strain curves of studied materials at elevated temperatures

3.3 Results and discussions

3.3.1 Heat transfer analyses

To avoid overloading the report, only the main results of the thermal analyses of the studied fusible links that were considered representative are presented in this section. Consequently, detailed results (temperature field and temperature rise curves) are provided for just three cases: one case for each of the three fusible link configurations studied. The temperature rises calculated in the components of studied fusible links, according to the considered link solution, the profile thicknesses and the rod sizes (diameter and length) are also provided. The thermal results have be used to develop simple rules for calculating the heating of the different components of the fusible links, which are required to determine their fire resistance.

For information purpose, Figure 3.10 to Figure 3.12 give some thermal results for the first fusible link solution. From these figures, the temperatures of the bolts are found to be very similar to those of the connected steel profiles. Due to the different thicknesses of profiles and the shadow effect, there are temperature gradients between all components of the link that are directly exposed to fire, which diminish with increasing fire exposure time. On the over hand, temperature gradients are more pronounced along the threaded rods, with steeper gradients occurring at higher temperatures. Figure 3.12 shows the temperature gradient in the steel rods. The upper part of the steel rods is significantly hotter than the side not exposed to the fire. For the presented case, after half an hour of exposure to the fire, the temperature of the upper part of the rods is around 900°C. Meanwhile, the sections located one quarter and halfway along the rods from the side exposed to the fire are at temperatures of around 520°C and 360°C, respectively. This temperature gradient is explained by the protection provided by the sandwich panels.

The same observations can be made for the other two link configurations (see Figure 3.13 to Figure 3.18).

Figure 3.18 to Figure 3.25 show and compare the temperature rises calculated for the components of the studied fusible links, considering many of the cases analysed in the parametric studies. The acronyms LF, W, UF, eU, eL and eZ stand for 'lower flange', 'web', 'upper flange', 'U thickness', 'L thickness' and 'Z thickness', respectively.

From these figures, it can be noted that:

- The heating predicted in steel profiles depends mainly on their thickness. The greater the thickness — whether of a single profile or the combined thickness of the profiles walls in contact — the smaller the temperature increase (see Figure 3.19, Figure 3.20, Figure 3.22or Figure 3.23).
- There are some differences in temperature rise between the various walls of the same profile (U-shaped profile, Z-shaped profile). These differences can be attributed to the presence of another profile in contact with it, as well as the shadow effect. In addition, Furthermore, the greater the height of the U-profile, the larger the temperature gradient along its web, between the part in contact with another profile and the part exposed to fire on both sides (see Figure 3.26).
- The temperature rise of the rods depends not only on their length (i.e. the thickness of the wall), but also on the thickness of the profile to which they are attached and their diameter. Overall, the thinner the profile, the greater the temperature increase of the part of the rod located on the wall side exposed to the fire (see Figure 3.24). The same phenomenon can be observed regarding the rod's diameter. However, the further away from the side exposed to the fire, the lower the temperature with the diminution of the rod's diameter (see Figure 3.21). This is because the temperature rise of the rods is mainly due to heat conduction along the threaded rod from the hottest part of the rod.

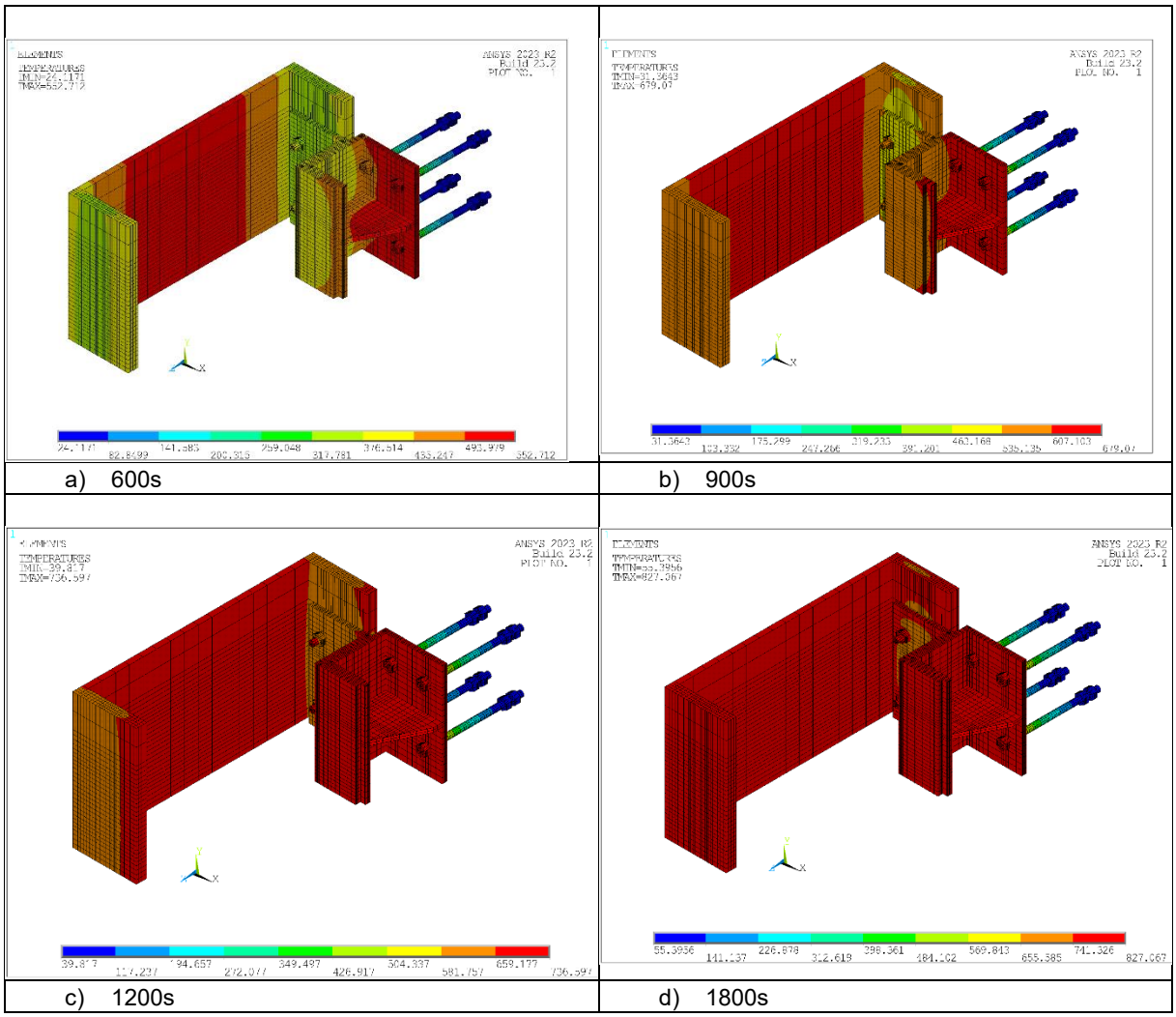

a) 600s b) 900s

c) 1200s d) 1800s

Figure 3.10: temperature field predicted in the link corresponding to the first fusible link solution at different fire exposure time

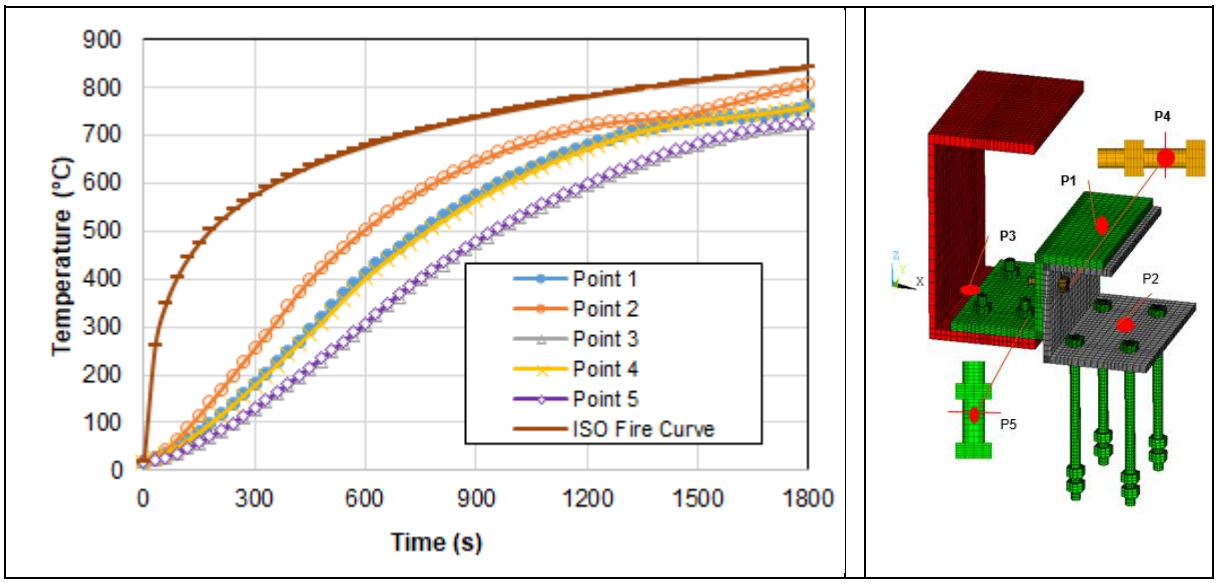

Figure 3.11: Time-temperature curves calculated at several points along the link, corresponding to the first fusible link solution

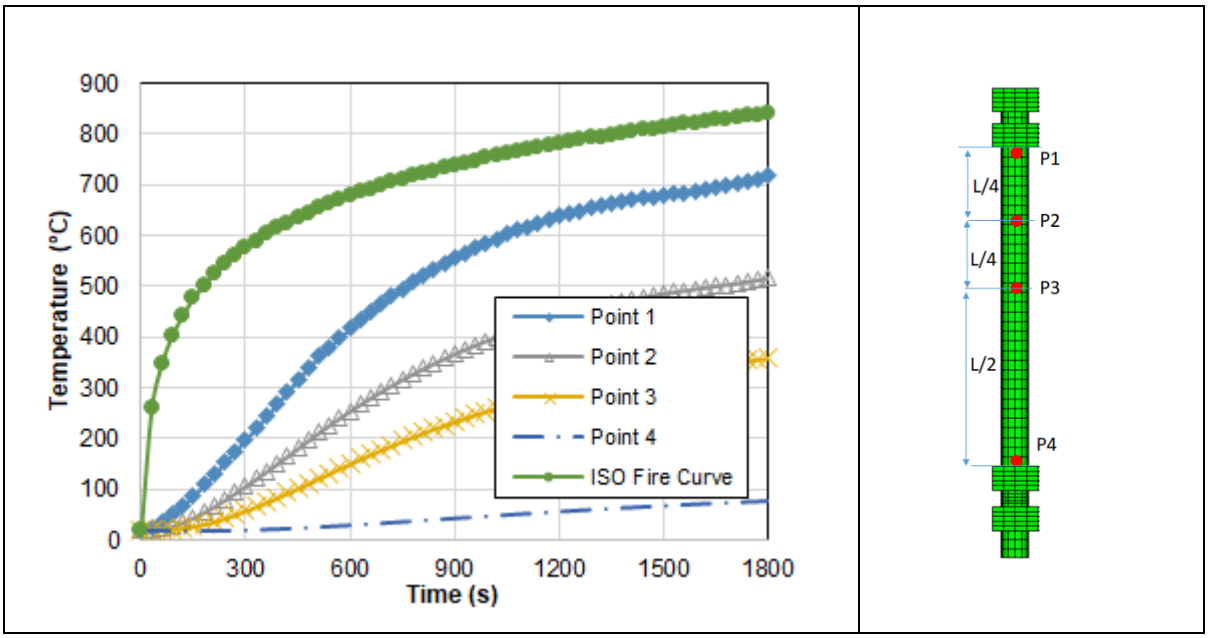

Figure 3.12: Time-temperature curves calculated at several points along the threaded rods, corresponding to the first fusible link solution

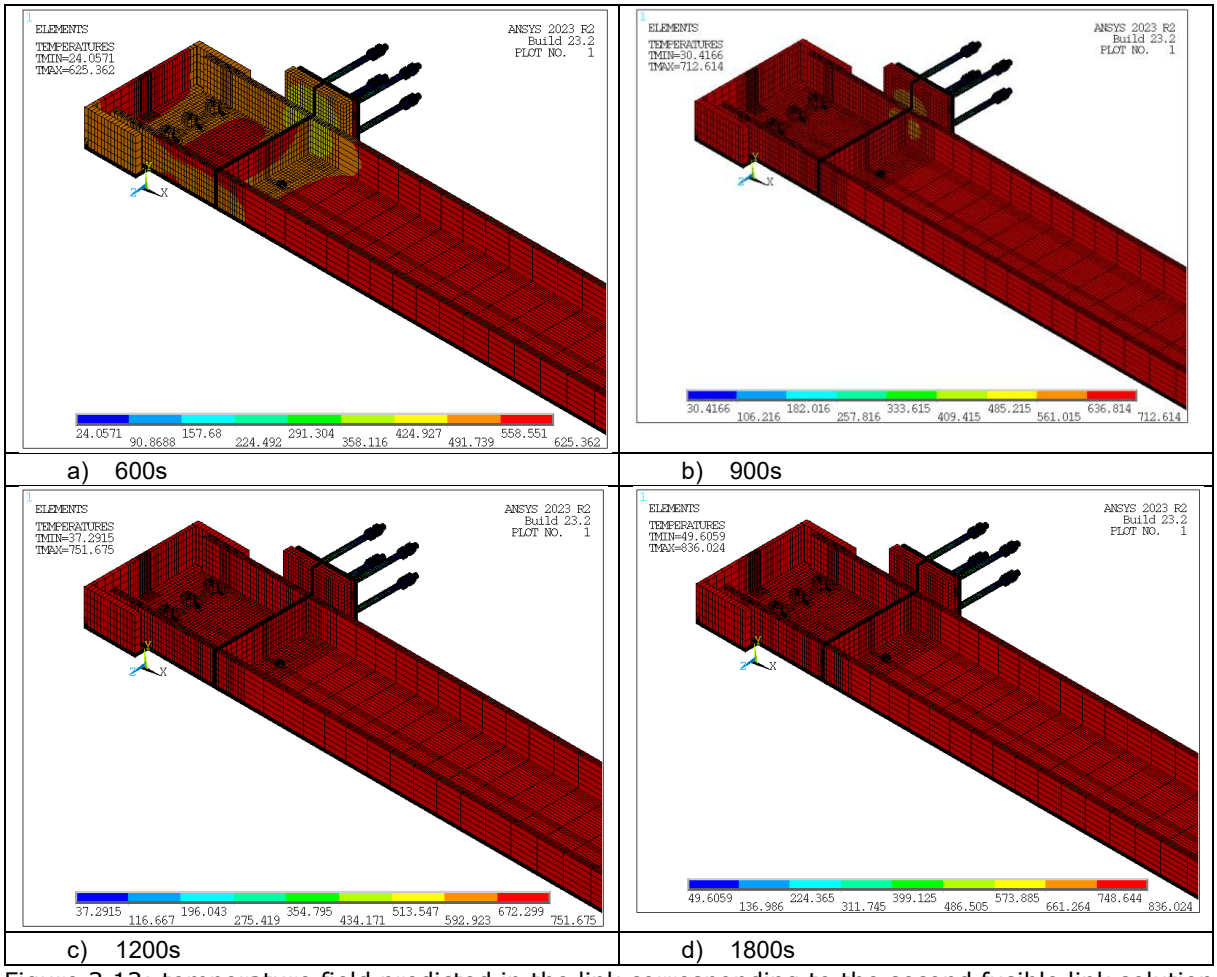

Figure 3.13: temperature field predicted in the link corresponding to the second fusible link solution at different fire exposure time

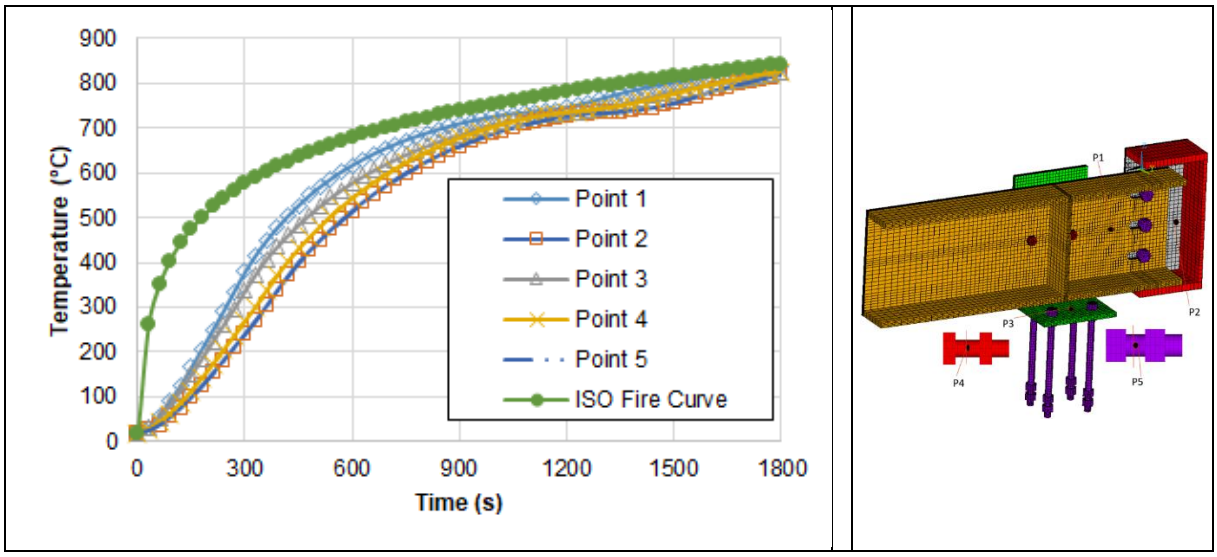

Figure 3.14: Time-temperature curves calculated at several points along the link, corresponding to the second fusible link solution

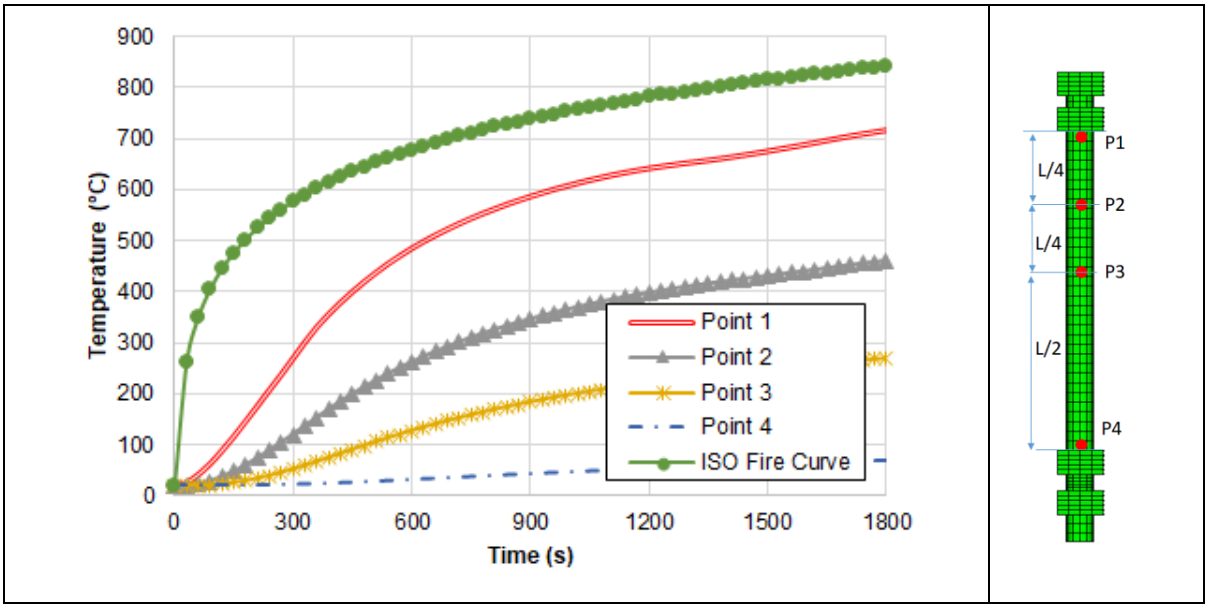

Figure 3.15: Time-temperature curves calculated at several points along the threaded rods, corresponding to the second fusible link solution

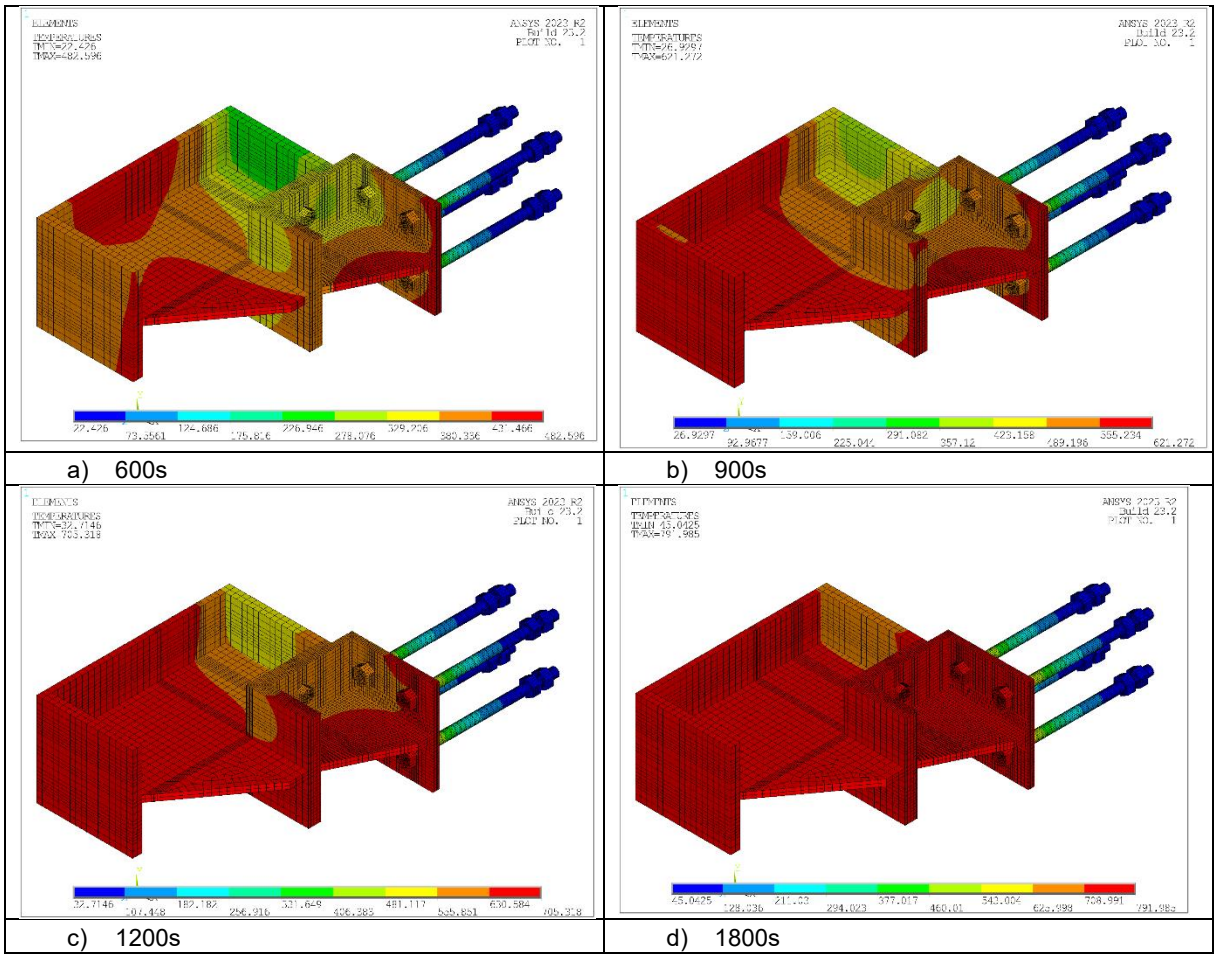

Figure 3.16: temperature field predicted in the link corresponding to the third fusible link solution at different fire exposure time

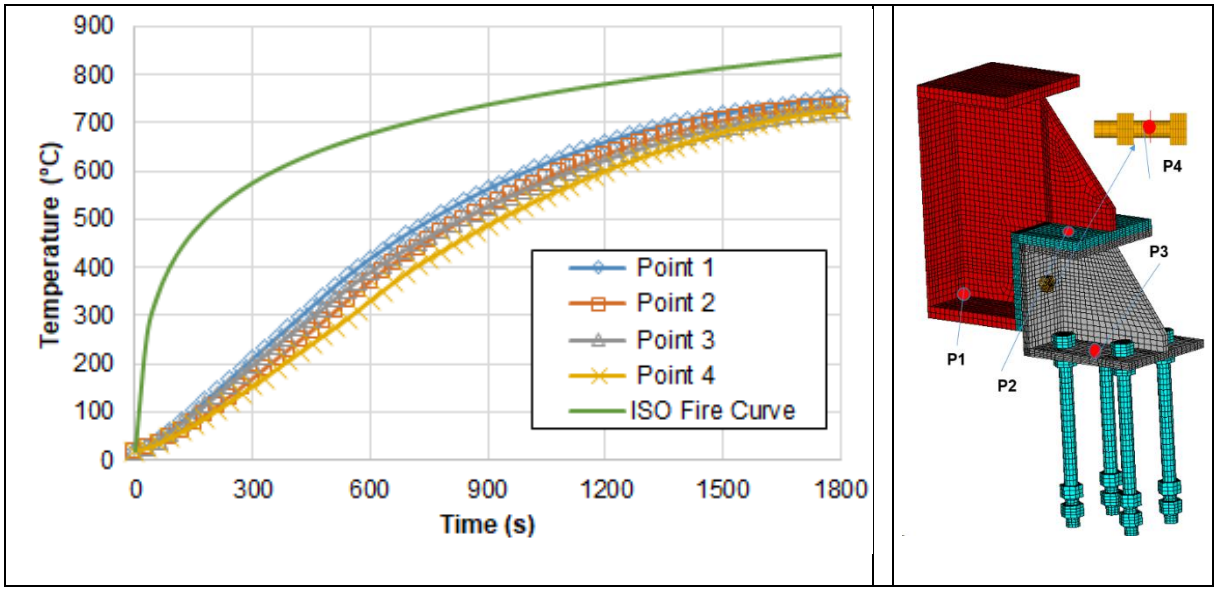

Figure 3.17: Time-temperature curves calculated at several points along the link, corresponding to the third fusible link solution

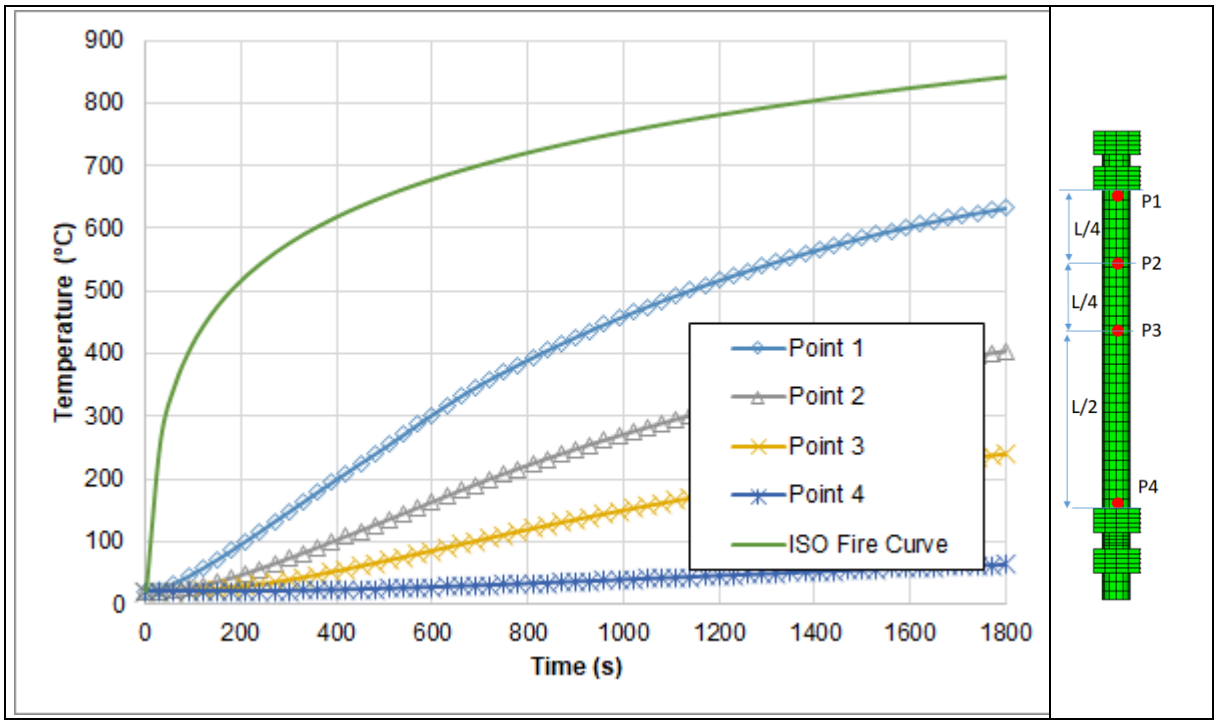

Figure 3.18: Time-temperature curves calculated at several points along the threaded rods, corresponding to the third fusible link solution

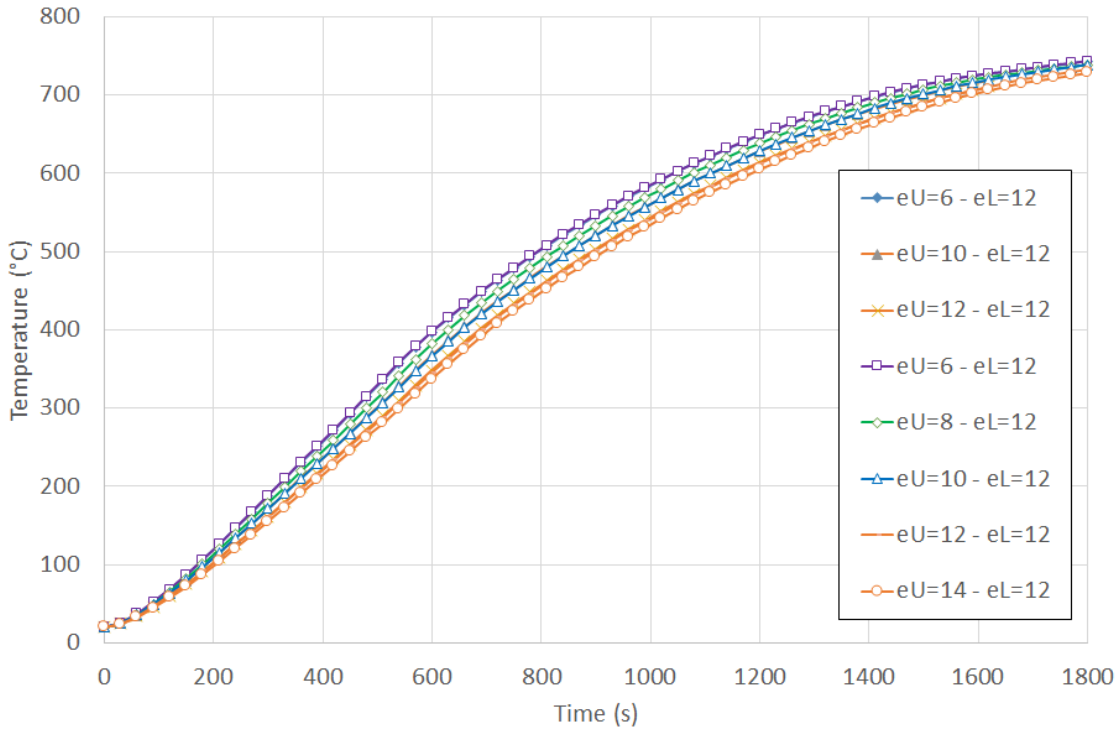

Figure 3.19: Time-temperature curves calculated in the L shaped steel profile for the third fusible link solution, according to the profile thicknesses

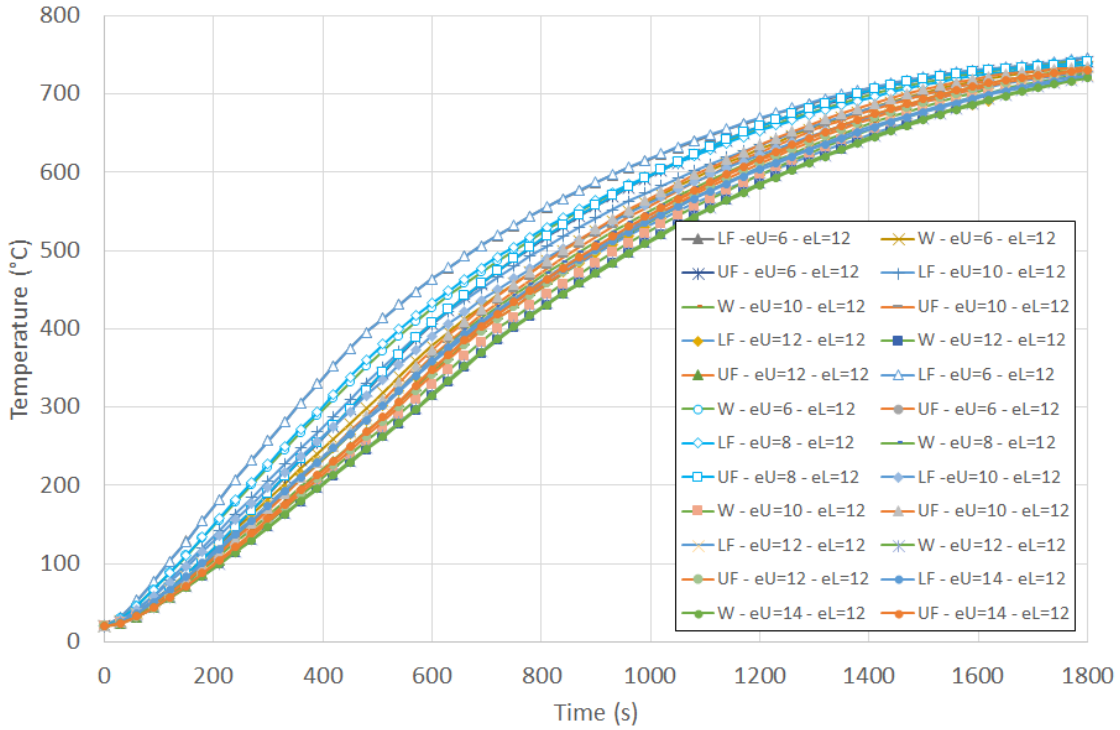

Figure 3.20: Time-temperature curves calculated in the U-shaped steel profile for the third fusible link solution, according to the profile thicknesses

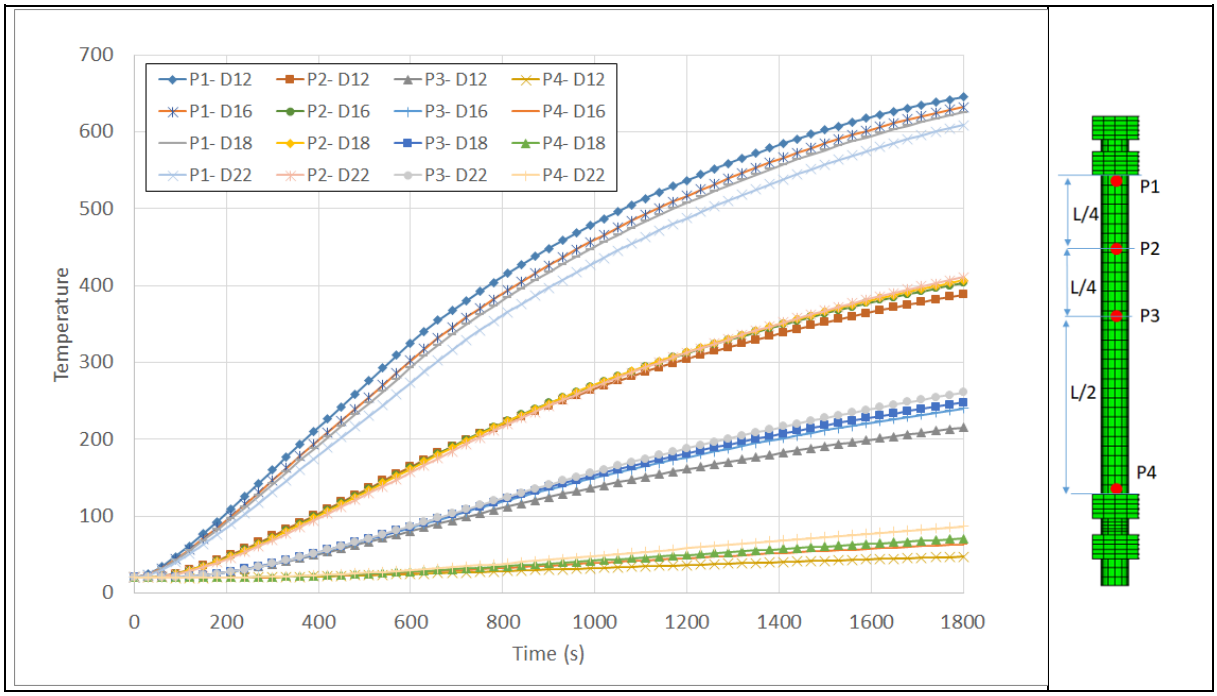

Figure 3.21: Time-temperature curves calculated in 175mm steel rods long for the third fusible link solution according to the rod diameter

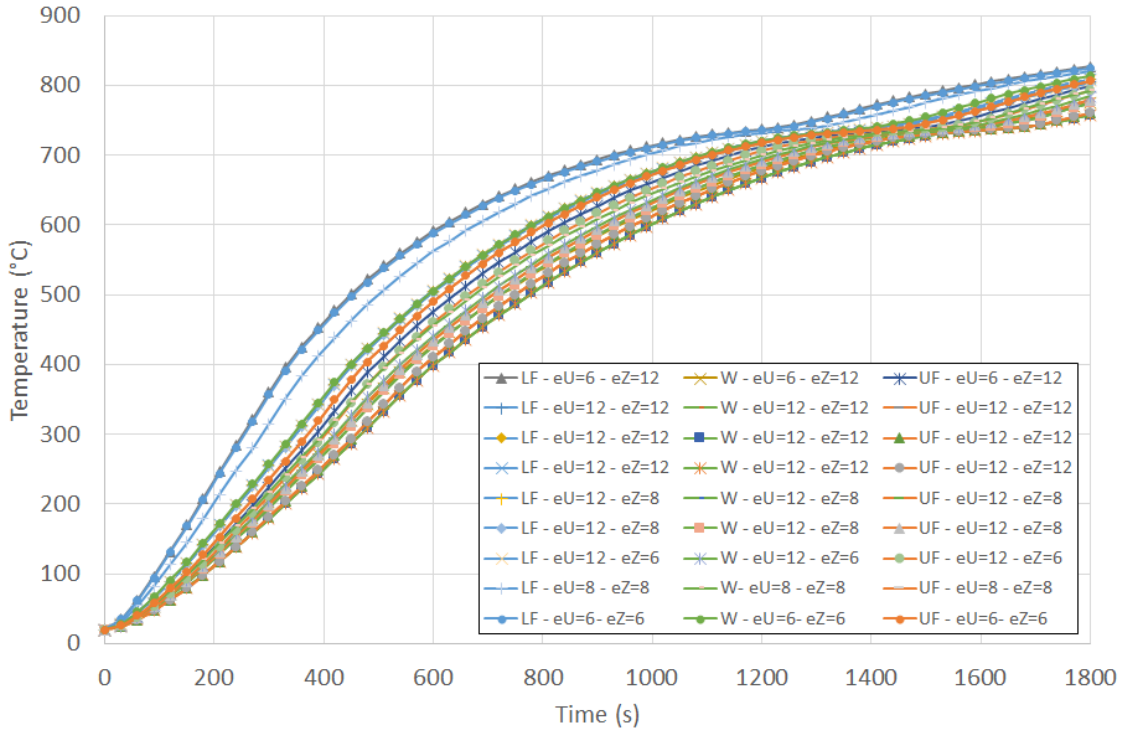

Figure 3.22: Time-temperature curves calculated in the U-shaped steel profile for the first fusible link solution according to the profile thicknesses

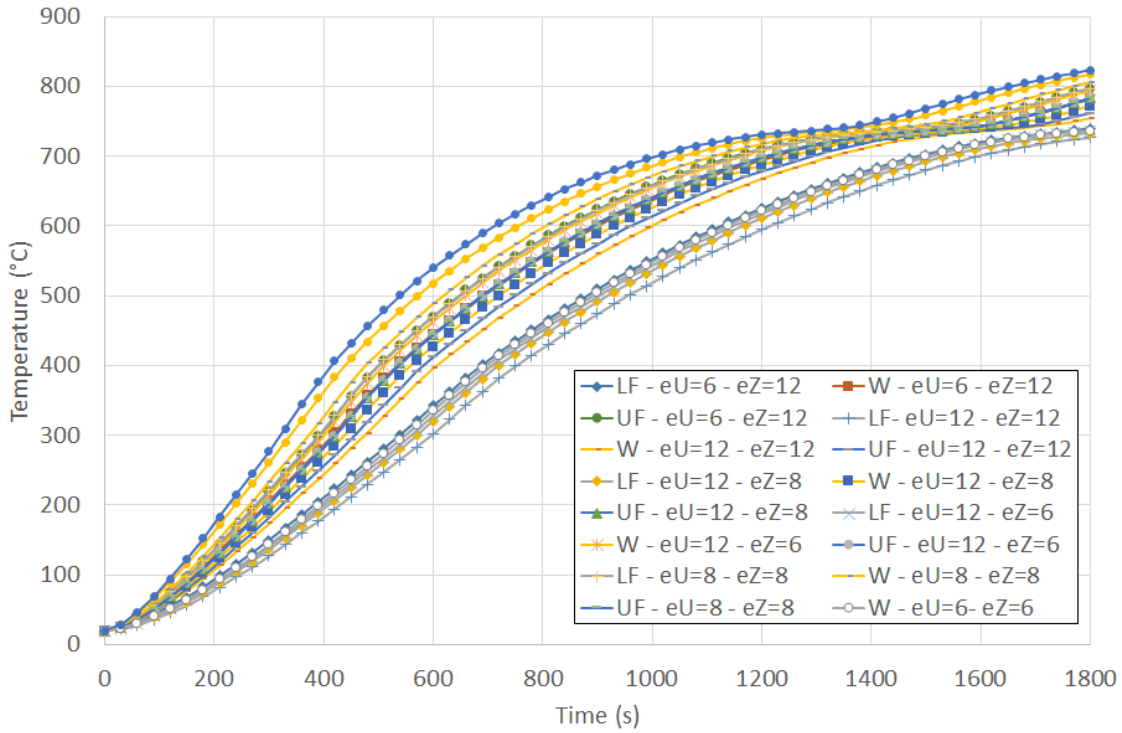

Figure 3.23: Time-temperature curves calculated in the Z-shaped steel profile for the first fusible link solution according to the profile thicknesses

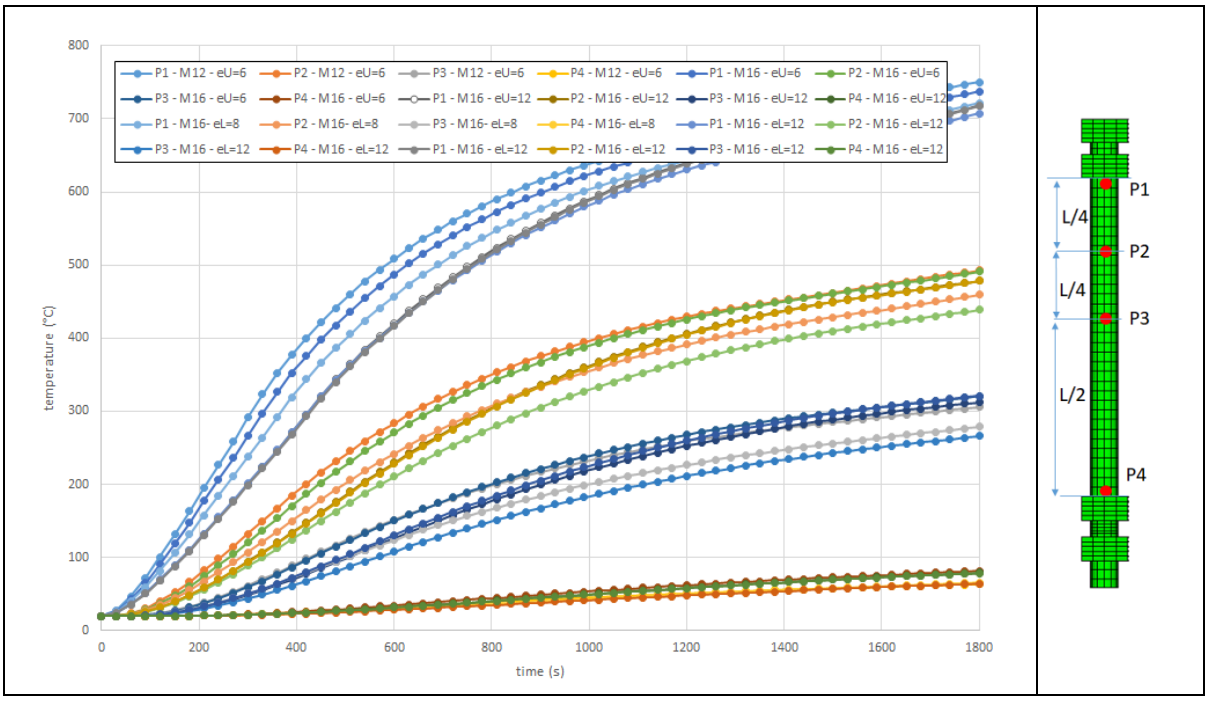

Figure 3.24: Time-temperature curves calculated in 175mm steel rods long for the first fusible link solution according to the rod diameter and the U-shaped profile thickness

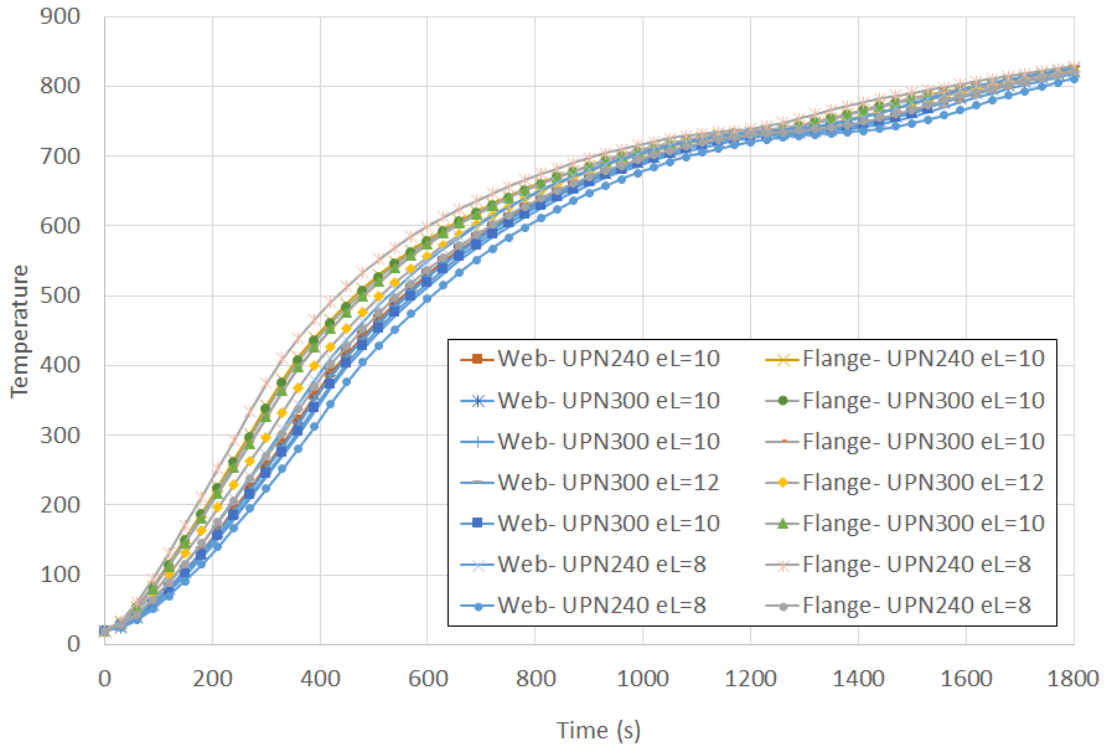

Figure 3.25: Time-temperature curves calculated in the L-shaped steel profile for the second fusible link solution, according to the profile thickness

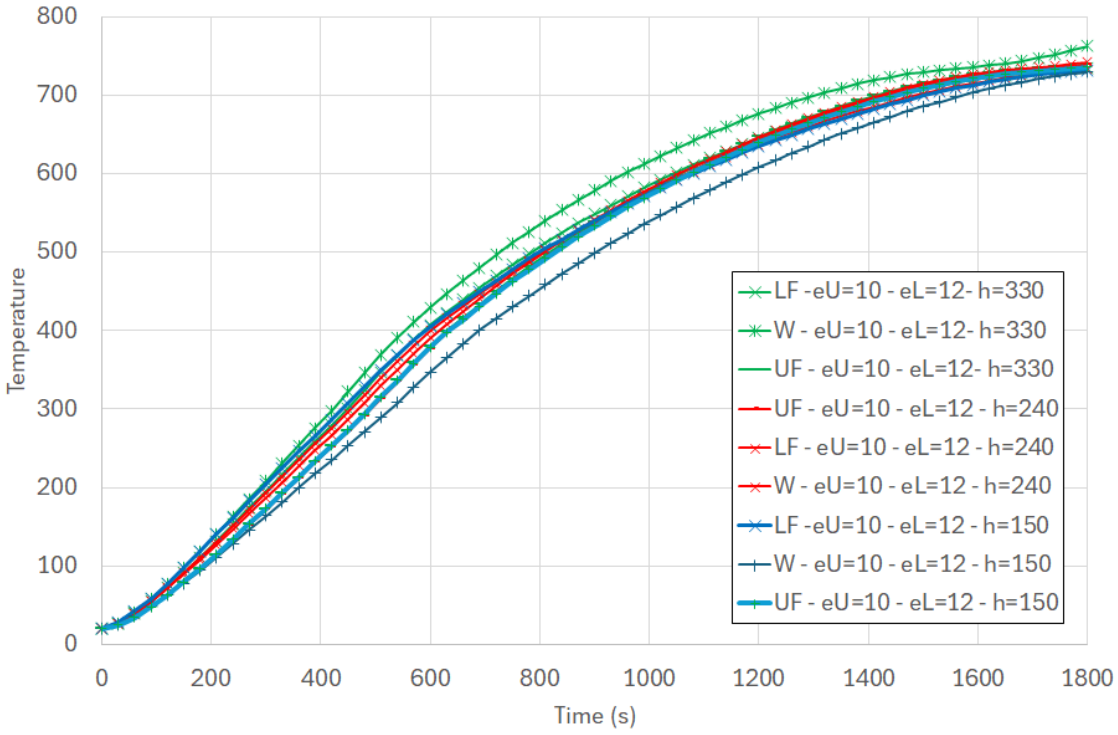

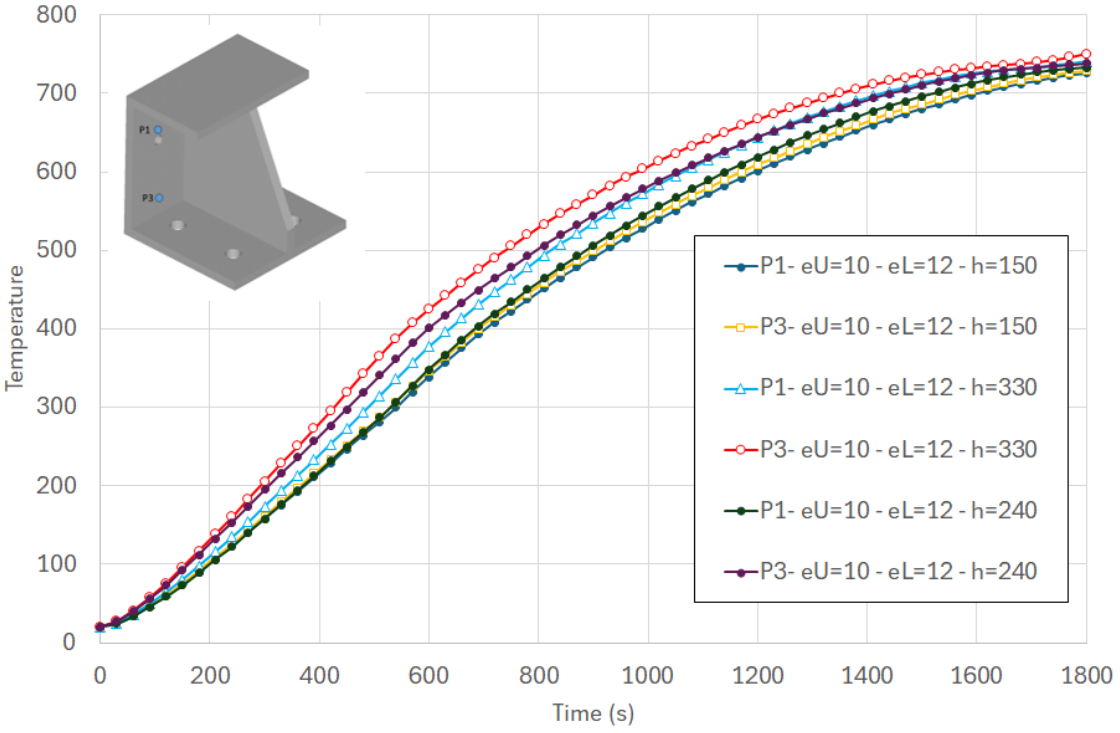

Figure 3.26: Temperature rises calculated in the U-shaped steel profile according to profile size

3.3.2 Mechanical analyses

As with the thermal analyses, only the results of the mechanical analyses for the studied fusible links that were considered representative are presented in this section. Thus, detailed results are provided for just three cases, one for each of the three configurations of fusible link studied. The results from numerical analyses are shown in terms of time-displacement curves, Von Mises strain distribution and time-reaction curves. Then, all the failure modes predicted for the studied fusible links are also presented and discussed.

3.3.2.1 Example case for the first fusible link solution

The results of the mechanical analysis for the selected fusible link case are summarised in Figure 3.27 to Figure 3.30. The model predicted a load-bearing capacity of approximately 74 kN in compression at normal temperature for this link. The results are presented according to the applied load level $N_{fi,Ed}/N_{Rd}$. Figure 3.28 illustrates the Von Mises plastic strain distribution predicted at the time of failure of the link. Figure 3.29 shows the vertical Uz displacement curves of the lower flange of the modelled column section over time, while Figure 2.25 shows the evolution of the reaction/applied load ratio at the restrained end of the steel rods. The Uz displacement is in the direction parallel to the rods length. The asymptotic shape of the displacement curves reveals the failure time of the link, which ranges from approximately 757 to 1130 seconds depending on the load level. The higher the load level, the lower the fire resistance. The failure modes of the link can be identified by analysing the strain level reached by its components. Observing the distribution of the von Mises plastic strain predicted throughout the entire link shows that the failure modes vary according to the load level. At the lower load level of 0.3, the fusible link begins to fail when the rod section of the first row of rods yields, just below the nut exposed to fire. This is followed by the yielding of the rod section in the second row of rods as well as the tensile failure of the steel bolts due to the bending effects associated with the steel resistance loss at high temperatures. No rod buckling is observed in this case. At higher load levels, the failure of the link begins with the yielding of the rod section in the first row of rods. The steel rods then quickly undergo bending/buckling with the Z-shaped steel profile undergoing also large bending deformation. It should be noted that the predicted failure modes at elevated temperatures differ from that observed at normal temperature, which only involve rod buckling (see Figure 3.27). Moreover, it should be noted that, by avoiding steel bolt failure, the numerical results showed that the predicted failure mode of the fusible link at the lowest load level is similar to that observed at higher load levels.

The time-reaction curves calculated at the restrained end of the threaded rods (see Figure 3.30) show that, despite thermal expansion effects, the temperature rise does not significantly alter the axial forces supported by each threaded rod. It should be noted that these forces are symmetrical with respect to the plane of the U-section stiffener. They remain relatively constant until the link fails. However, it should be noted that the sum of the axial forces supported by the first rod row exceeds the applied compressive load. This is due to load eccentricity and the associated bending effect, which puts the first rod row under compression and the second under tension. In this case, the first row of rods supports 150% of the applied load.

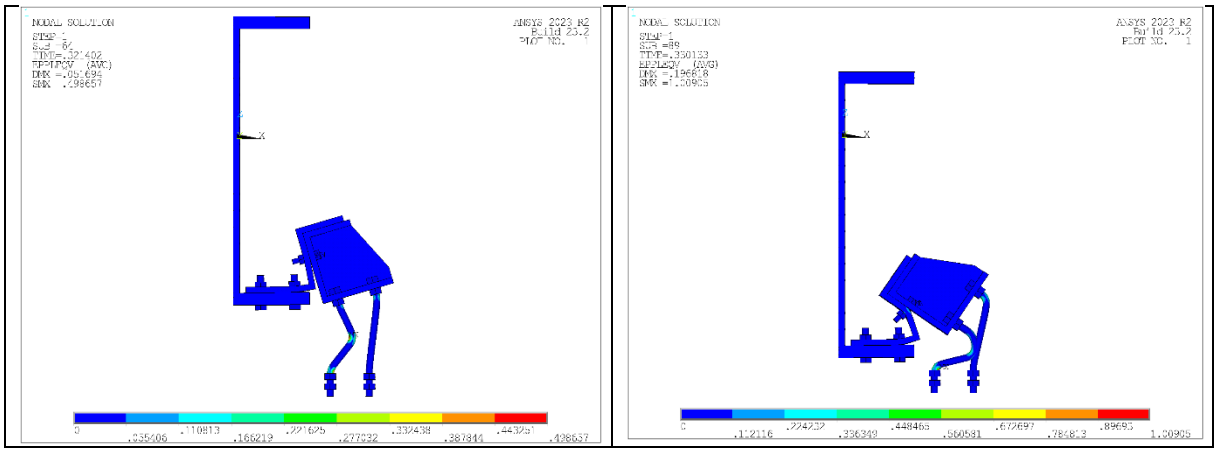

Figure 3.27: Von Mises plastic strain distribution at normal temperature predicted in the link corresponding to the second fusible link solution at failure

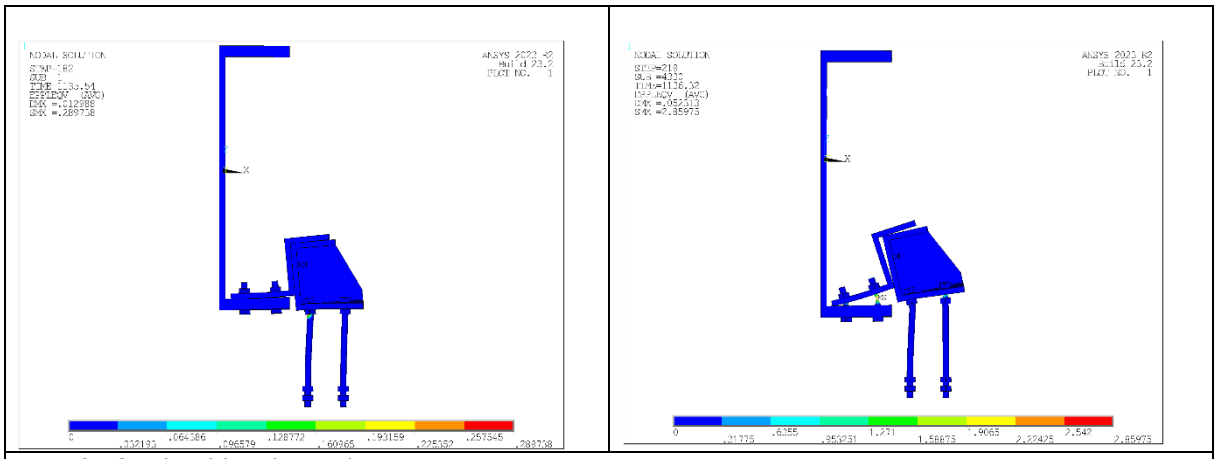

a) fire load level $N_{fi,Ed}/N_{Rd}=0.3$

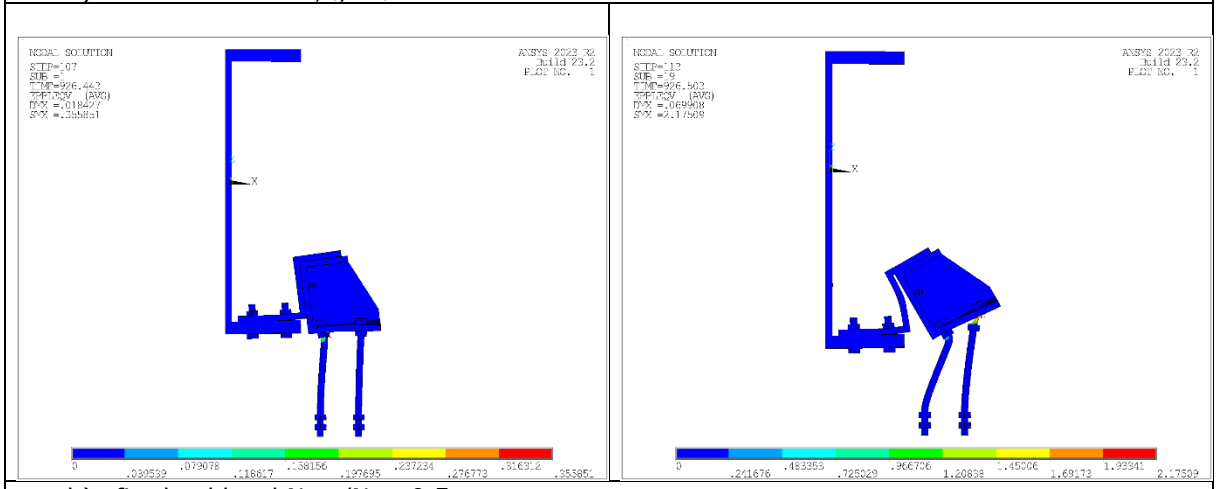

b) fire load level $N_{fi,Ed}/N_{Rd}=0.5$

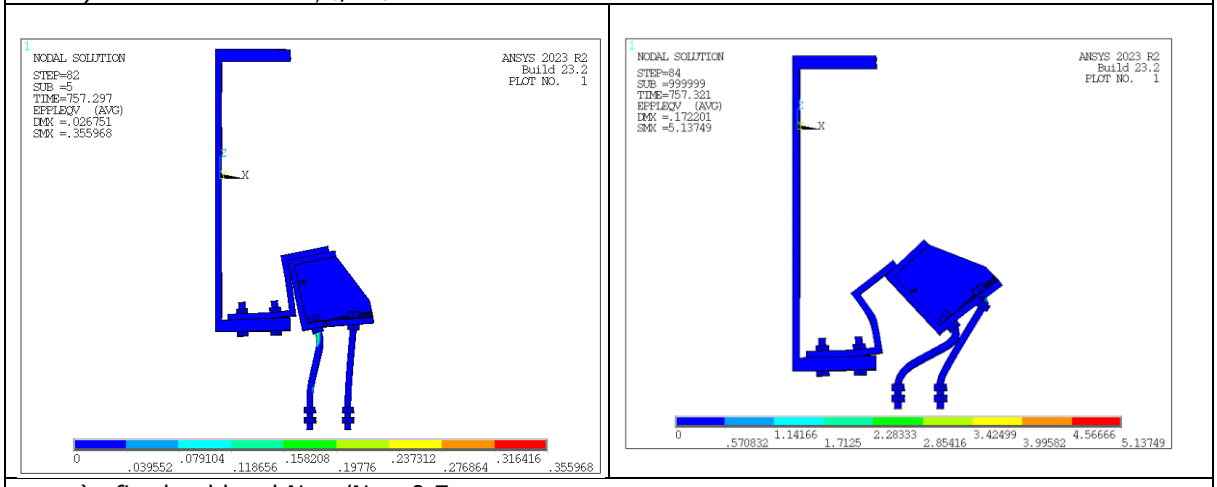

c) fire load level $N_{fi,Ed}/N_{Rd}=0.7$

Figure 3.28: Von Mises plastic strain distribution in the links corresponding to the first fusible link solution predicted at failure time according to the Nfi,Ed/NRd

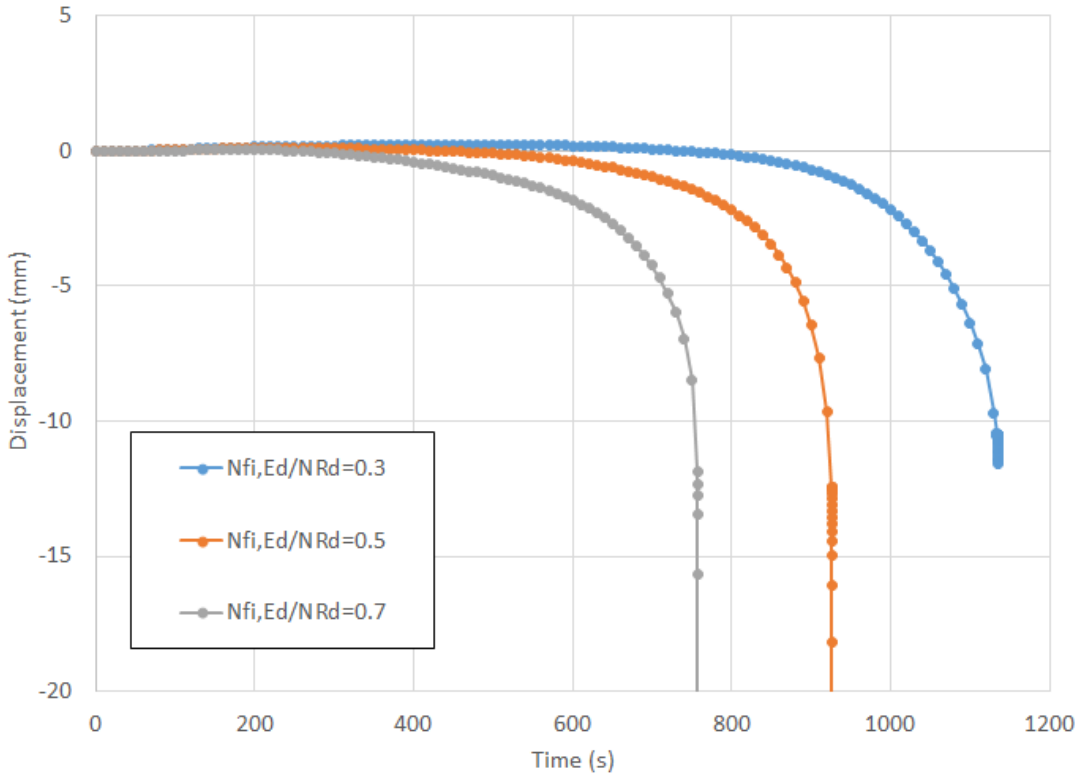

Figure 3.29: Time-vertical displacement curves calculated for the link corresponding to the first fusible link solution predicted at failure time according to the fire load level Nfi,Ed/NRd

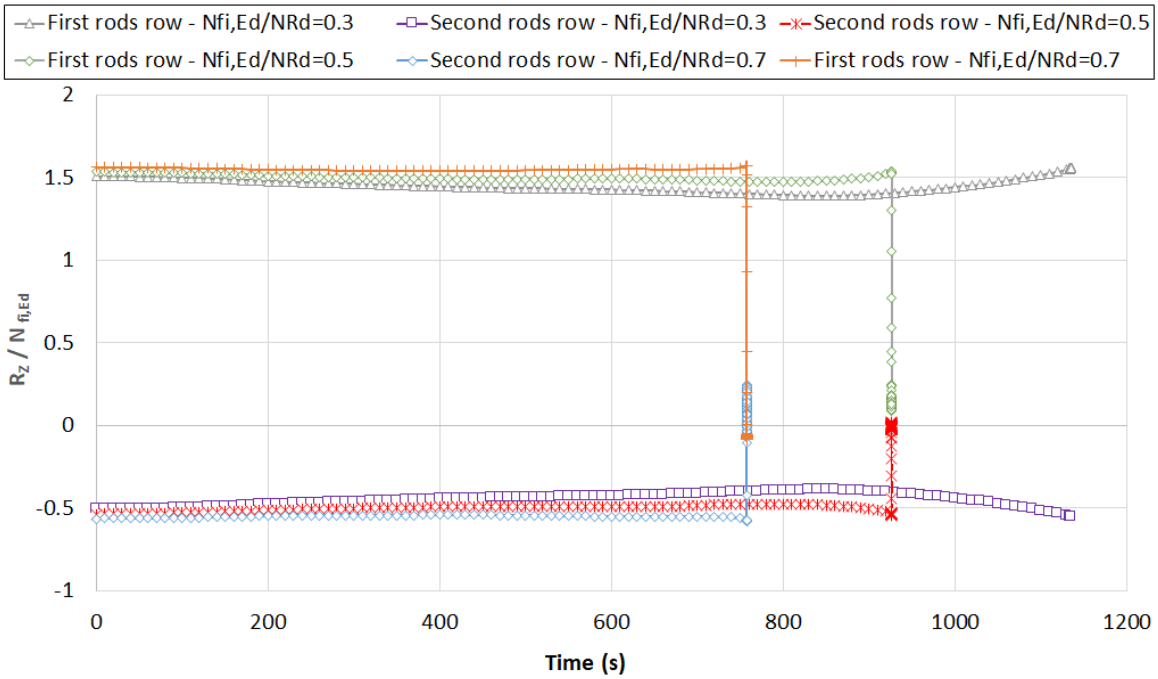

Figure 3.30: Evolution of the reaction/applied load ratio over time at the restrained end of the steel rods for the link corresponding to the first fusible link solution.

3.3.2.2 Example case for the second fusible link solution

Figure 3.31 to Figure 3.34 summarise the results of the mechanical analysis carried out for the selected fusible link case. The model predicted a load-bearing capacity of approximately 143 kN in compression at normal temperature for this link. The results are presented according to the applied load level $N_{fi,Ed}/N_{Rd}$. Figure 3.32 illustrates the Von Mises plastic strain distribution predicted at the time of failure of the link. Figure 3.33 shows the vertical Uz displacement curves of the lower flange of the modelled column section over time, while Figure 3.34 shows the evolution of the reaction/applied load ratio at the restrained end of the steel rods. The Uz displacement is in the direction parallel to the rods length. The asymptotic shape of the displacement curves reveals the failure time of the link, which ranges from approximately 500 to 1370 seconds depending on the load level. The higher the load level, the lower the fire resistance. The failure modes of the link can be identified by analysing the strain level reached by its components. Observing the distribution of the von Mises plastic strain predicted throughout the entire link shows that the failure modes vary according to the load level. At a lower fire load level of 0.3, the fusible link begins to fail when the rod section of the lower rod in the rod row closest to the column section (rod n°4 in the Figure 3.34) yields at the level of the nut exposed to fire. Localised plastic crushing of the rod occurs, but no buckling of the rod is observed. At higher load levels, the failure of the link begins with the yielding of the rod section in the lower row of rods (in contact with the UPN). The steel rods then quickly undergo bending. It can also be observed a flexural torsional buckling of the UPN associated as well as an important bending of the horizontal wall of the L-profile (bolted to the web of the UPN with the aluminium bolts). In the direction of gravity, perpendicular to the steel rods, the self-weight of the U-profile is supported by the stiffener welded between the flanges of the portal frame column and the vertical wall of the L-profile. The applied load is transmitted from the stiffener to the vertical web of the U-profile via three steel bolts and from the U-profile to the rods via aluminium bolts and a steel plate placed between the UPN flange and the rod head exposed to fire, as well as the L-profile. Due to the unsymmetrical nature of the connected steel elements, the existing eccentricity between the load applied to the stiffener plane and the support, which mainly mobilises the two lower threaded rods, causes the U-profile to rotate. This rotation is initially prevented by the stiffener welded to the column and the vertical wall of the L-profile. However, the combination of these effects with the temperature rise in the fire-exposed members and the corresponding loss of steel resistance leads progressively to flexural-torsional buckling of the UPN, and then to bending of the steel rods. It should be noted that the predicted failure modes at elevated temperatures differ slightly from that observed at normal temperatures. The latter mainly involve rods buckling (see Figure 3.31).

The time-reaction curves calculated at the restrained end of the threaded rods (see Figure 3.34) show that the axial forces supported by the threaded rods differ, that there is no uniform redistribution of the applied load effects and that these forces change progressively and noticeably with temperature rise in the link. Overall, the lower rod row is under compression and the upper rod row under tension throughout the fire exposure. Regarding the lower rod row, the axial force on rod n°4 increases progressively during the early stage of fire exposure and then decreases as failure approaches. The opposite trend is observed for rod n°3. These differences in the axial reactions of the threaded rods can be explained by the eccentricity of the load along the axis parallel to the UPN, as well as by the UPN's progressive deformation due to the temperature increase. Due to the combined effect of rotation around its weak axis and bending around its strong axis, the UPN exerts greater compression on the lower rod row, particularly on rod n°4. When the temperature of the steel rods rises and the corresponding steel resistance losses become too high, there is a progressive redistribution of the compression force between the two lower rods, until they bend and fail, resulting in failure of the fusible link. It should be noted that, as failure approaches, the reaction/applied load ratios of the steel rods are close to those observed at the beginning of the fire exposure.

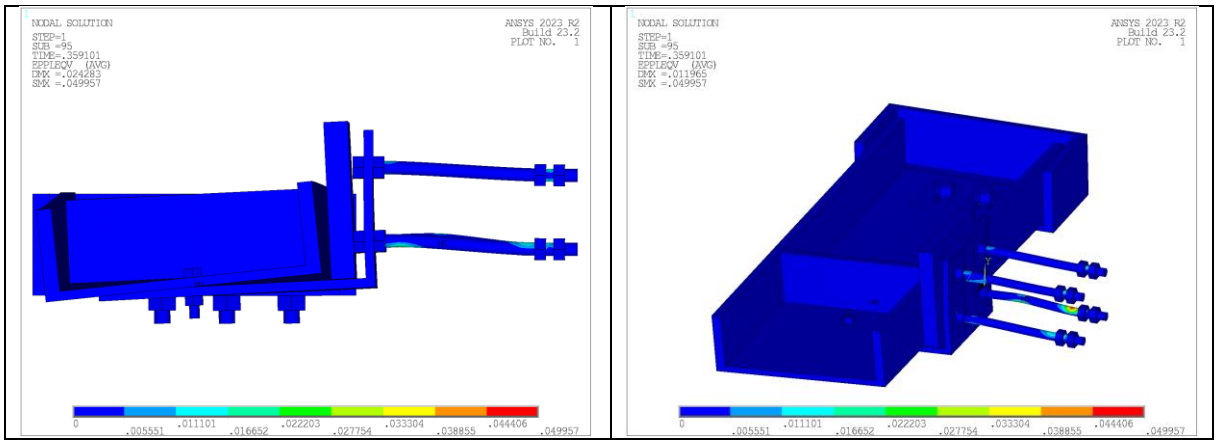

Figure 3.31: Von Mises plastic strain distribution at normal temperature predicted in the link corresponding to the second fusible link solution at failure

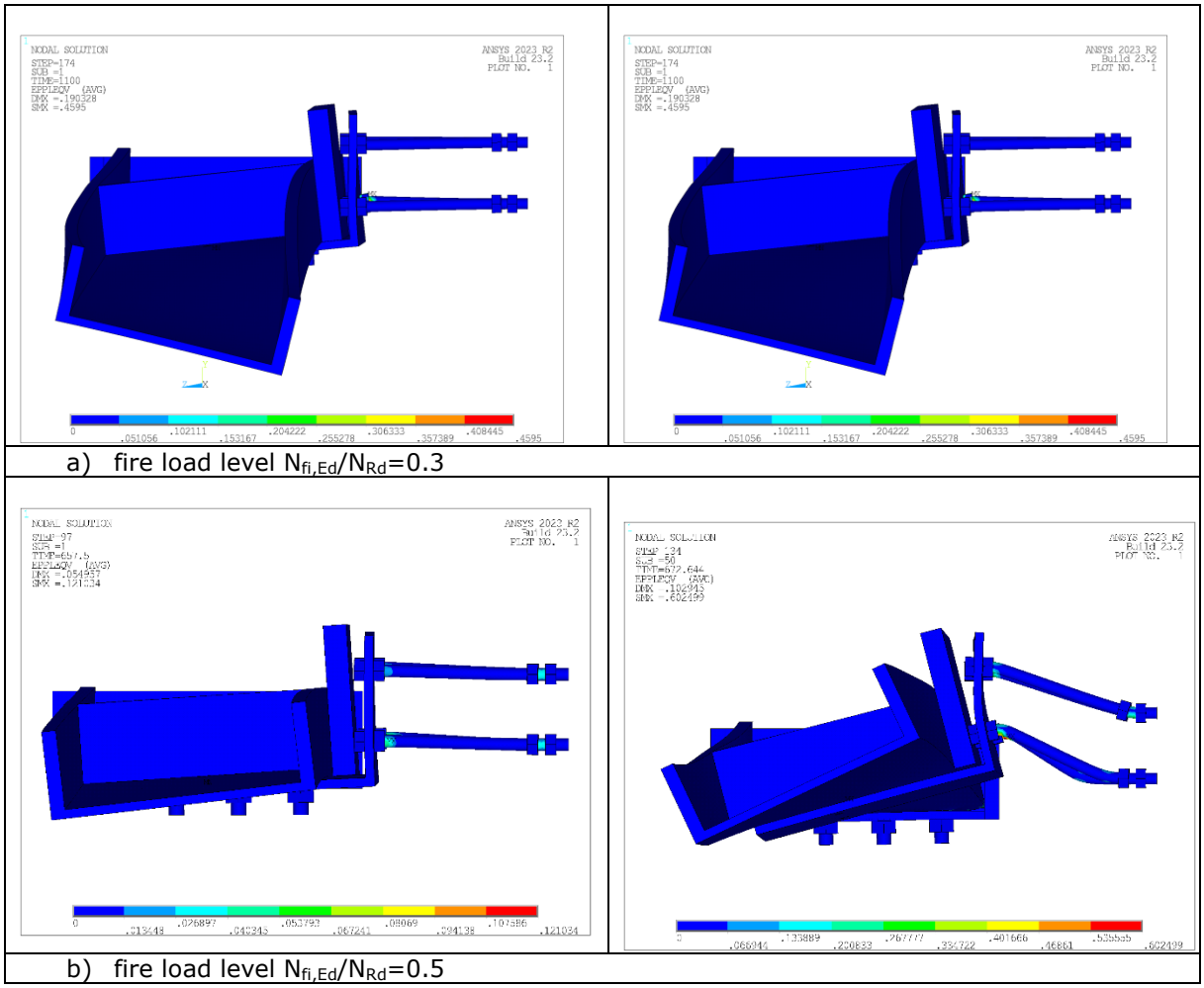

a) fire load level $N_{fi,Ed}/N_{Rd}$=0.3

b) fire load level $N_{fi,Ed}/N_{Rd}$=0.5

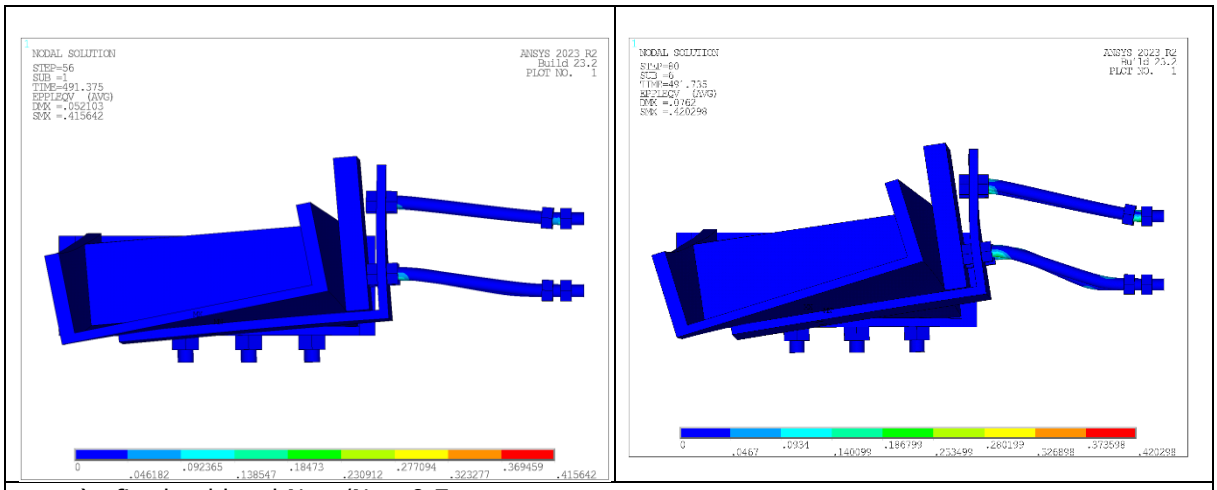

c) fire load level $N_{fi,Ed}/N_{Rd}$=0.7

Figure 3.32: Von Mises plastic strain distribution in the link corresponding to the second fusible link solution predicted at failure time according to the fire load level $N_{fi,Ed}/N_{Rd}$

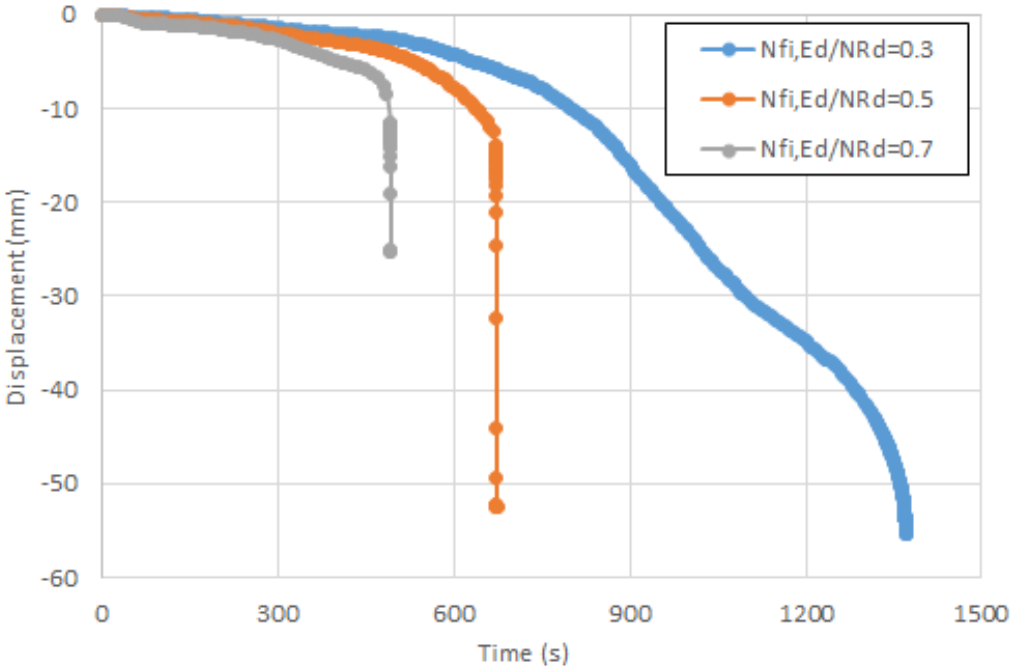

Figure 3.33: Time-vertical displacement curves calculated for the link corresponding to the second fusible link solution predicted at failure time according to the fire load level Nfi,Ed/NRd

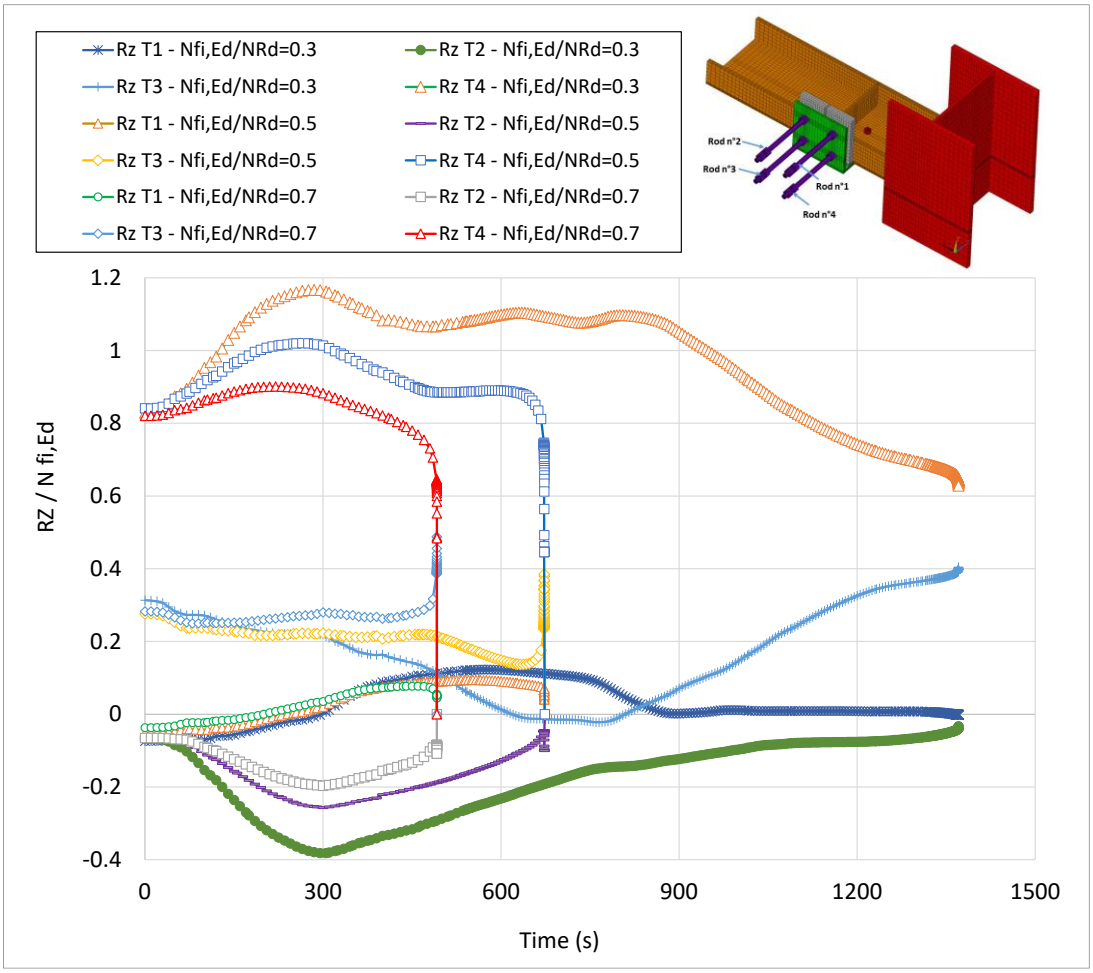

Figure 3.34: Evolution of the reaction/applied load ratio over time at the restrained end of the steel rods for the link corresponding to the second fusible link solution.

3.3.2.3 Example case for the third fusible link solution

The results of the mechanical analysis for the selected fusible link case are summarised in Figure 3.35 to Figure 3.38. The model predicted a load-bearing capacity of approximately 162 kN in compression at normal temperature for this link. The results are presented according to the applied load level $N_{fi,Ed}/N_{Rd}$. Figure 3.34 illustrates the Von Mises plastic strain distribution predicted at the time of failure of the link. Figure 3.36 shows the vertical Uz displacement curves of the lower flange of the modelled column section over time, while Figure 3.37 shows the evolution of the reaction/applied load ratio at the restrained end of the steel rods. The Uz displacement is in the direction parallel to the rods length. The asymptotic shape of the displacement curves reveals the failure time of the link, which ranges from approximately 850 to 1400 seconds depending on the load level. The higher the load level, the lower the fire resistance. The failure modes of the link can be identified by analysing the strain level reached by its components. Observing the distribution of the von Mises plastic strain predicted throughout the entire link shows that the failure modes are similar whatever the load level. The fusible link fails when the lower flange of the U-profile undergoes excessive local bending, which is followed by bending or buckling of the threaded rods in their upper part. It should be noted that the predicted failure modes at elevated temperatures are similar to those observed at normal temperature (see Figure 3.35).

The time-reaction curves calculated at the restrained end of the threaded rods (see Figure 3.38) show that they are all in compression, but with different load levels according to the rod row considered. It should be noted that these forces are symmetrical with respect to the plane of the U-section stiffener. These differences in loading between rod rows can be explained by the eccentricity of the loading, which is due to the offset of the U-section's centre of gravity from the plane of symmetry between the two rows of rods. This offset is probably affected by temperature increases

and the corresponding resistance losses. It should also be noted that the compression forces change progressively and noticeably with an increase in temperature in the link. For the rod row with the highest loading (closest to the column section), there is a progressive decrease in compression until approximately 500 s, followed by a progressive increase until the link fails. The opposite trend is observed for the second rod row. The first stage could be explained by the thermal expansion of the link components alone, since the temperature in the link does not exceed 400°C during 500 seconds of fire exposure, and at this temperature, there is no reduction in the yield strength of steel. The second stage could be explained by the progressive deformation of the lower flange of the U-profile, which influences the resulting bending moment exerted on the U-profile, and consequently the axial forces on the threaded rods, until failure occurs. In addition to the axial forces acting on the steel rods, there is a progressive increase in the horizontal forces exerted at the heads of the steel rods due to the progressive deformation of the U-profile, even if limited compared to the axial forces. It should be noted that, as failure approaches, the reaction/applied load ratios of the steel rods are slightly higher to those observed at the beginning of the fire exposure.

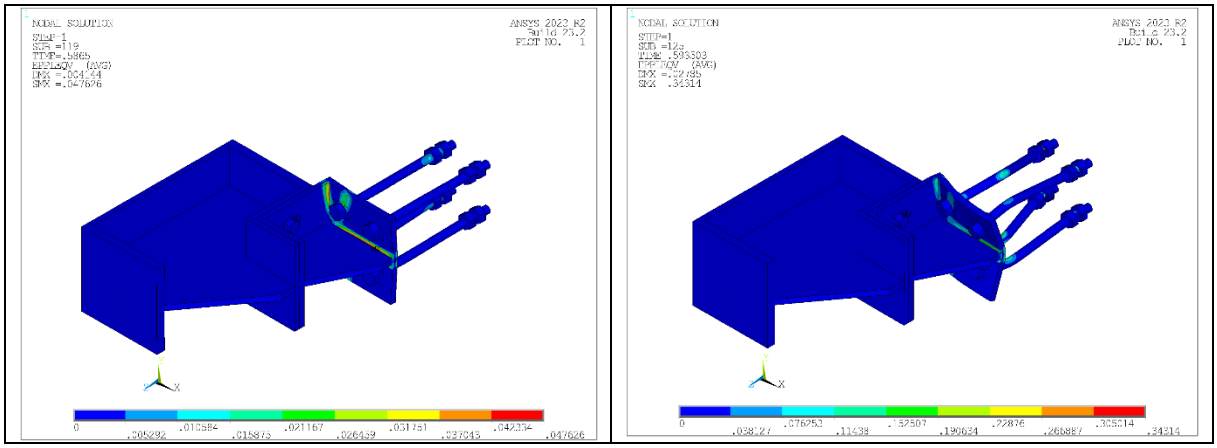

Figure 3.35: Von Mises plastic strain distribution at normal temperature predicted in the link corresponding to the third fusible link solution at failure

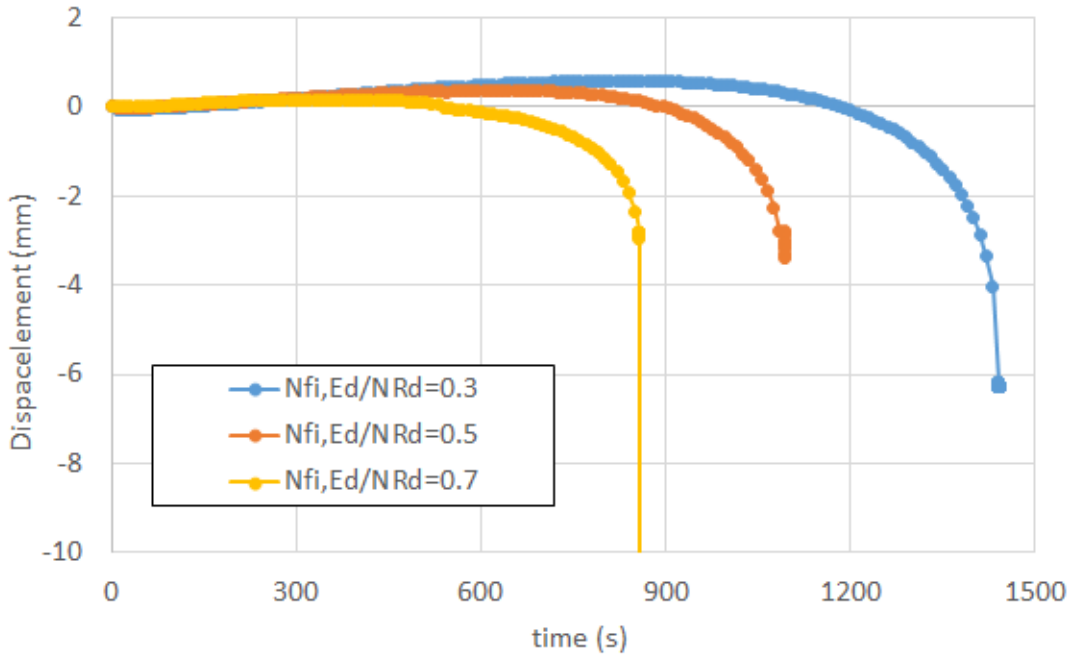

Figure 3.36: Time-vertical displacement curves calculated for the link corresponding to the third fusible link solution predicted at failure time according to the fire load level Nfi,Ed/NRd

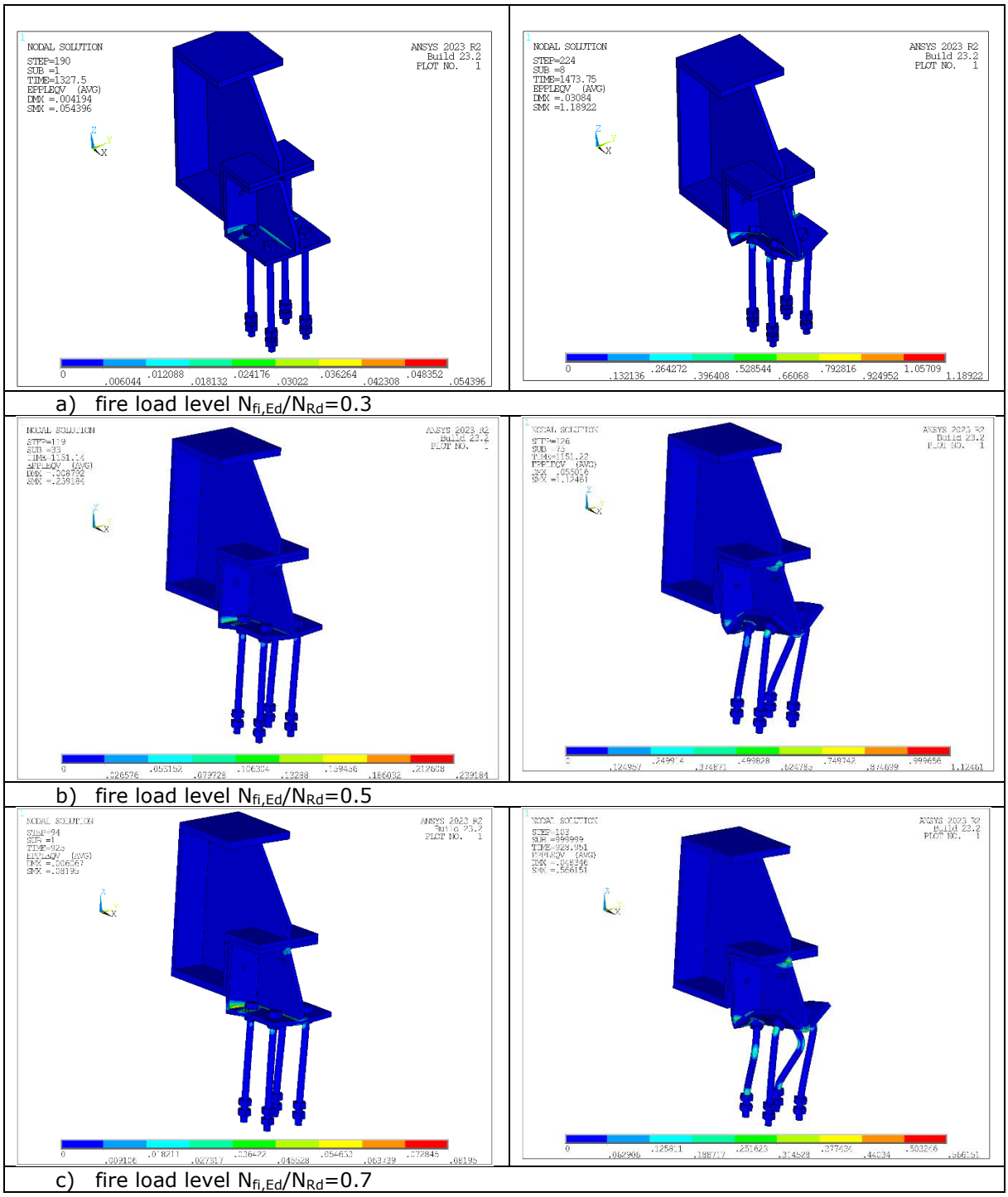

Figure 3.37: Von Mises plastic strain distribution in the link corresponding to the third fusible link solution predicted at failure time according to the fire load level $N_{fi,Ed}/N_{Rd}$

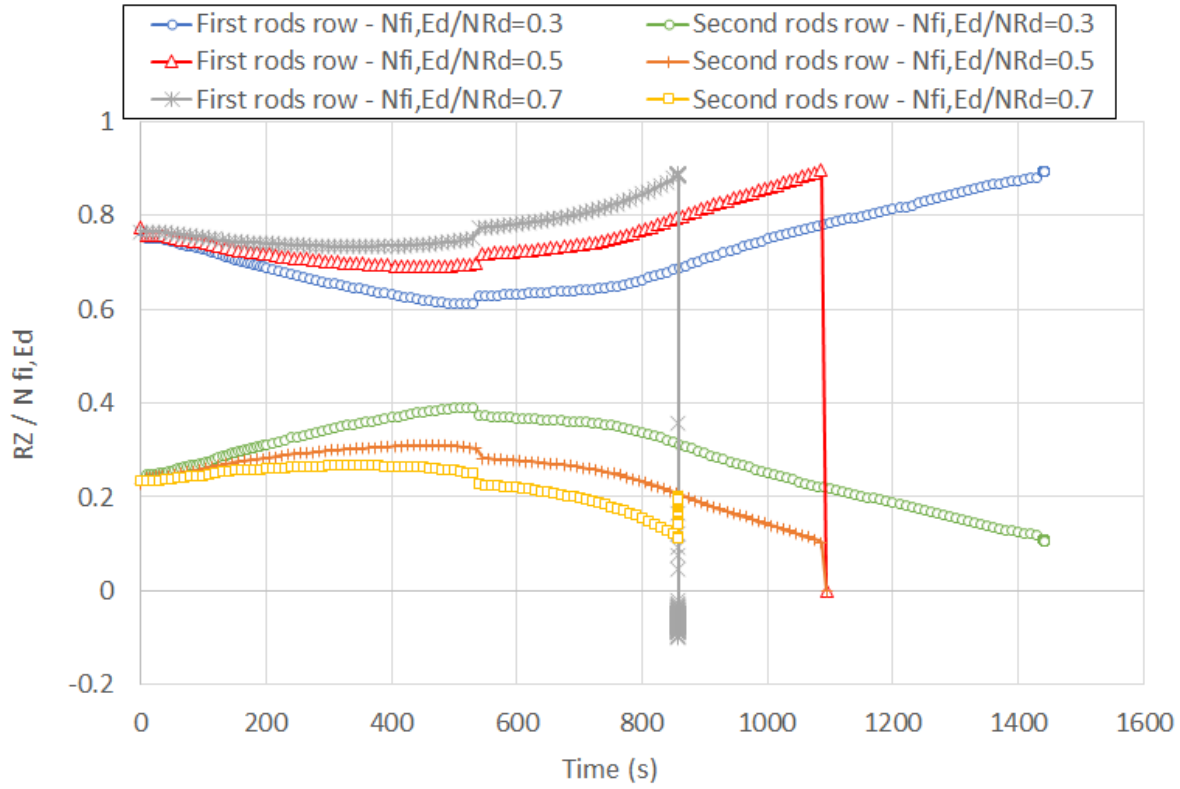

Figure 3.38: Evolution of the reaction/applied load ratio over time at the restrained end of the steel rods for the link corresponding to the second fusible link solution.

3.3.3 Summary results

3.3.3.1 Failure modes

Different failure modes were obtained for the fusible link configuration investigated. Although the bolts could fail in a brittle manner, the overall links response was ductile in most cases, with significant plastic deformation developing in the other components of the link (profile flange, steel rods, UPN profile, etc.).

Regarding the third fusible link solution, except for the yielding failure of the U-profile stiffener, which was not accounted in simulations, the following failure modes have been identified (see Figure 3.39):

- The threaded rod buckling, in many cases starting with that of the first row of rods (closest to the column section), followed by that of the rods in the second row. At normal temperature, the buckling involves all the steel rods when the rods are the weakest component of the link.
- The transverse bending failure of the lower U-section flange for the thinnest profiles (thicker than 10 mm for the parameter range considered herein), followed by bending/buckling of the rods when their slenderness ratio is sufficiently high. In contrast, rod cross-section yielding occurs just below the nut exposed to fire when the rod slenderness is low (i.e. small rod length and/or large rod diameter) and the exposure time to fire is significant. Increasing the flange thickness beyond a certain value (12 mm for the parameter range considered herein) results in less pronounced bending of the lower U-section flange.

It should be noted that in many cases, it was difficult to accurately identify t elevated temperatures the dominant failure mode of fusible links due to the simultaneous failure of various components. The transverse bending deformation of the upper flange of the U-profile undoubtedly affects the yielding/buckling of the steel rods, and vice versa. It is difficult to determine with certainty whether the progressive bending of the lower U-section flange leads to the buckling of rods or whether the progressive bowing of the upper part of the rods increases the effect of the transverse bending of the lower flange, leading to excessive flange yielding.

Regarding the buckling of threaded rods, it should be noted that this phenomenon can occur in different places. It can occur in the middle of the rods, or more frequently in the upper part (i.e. over half their length on the side exposed to fire), depending on the exposure time. This is due to differences in the longitudinal rigidity of the threaded rods, which varies according to the importance of the temperature gradient along them and the exposure time to fire. Additionally, the local bending of the bottom flange affects both rod failure and buckling length.

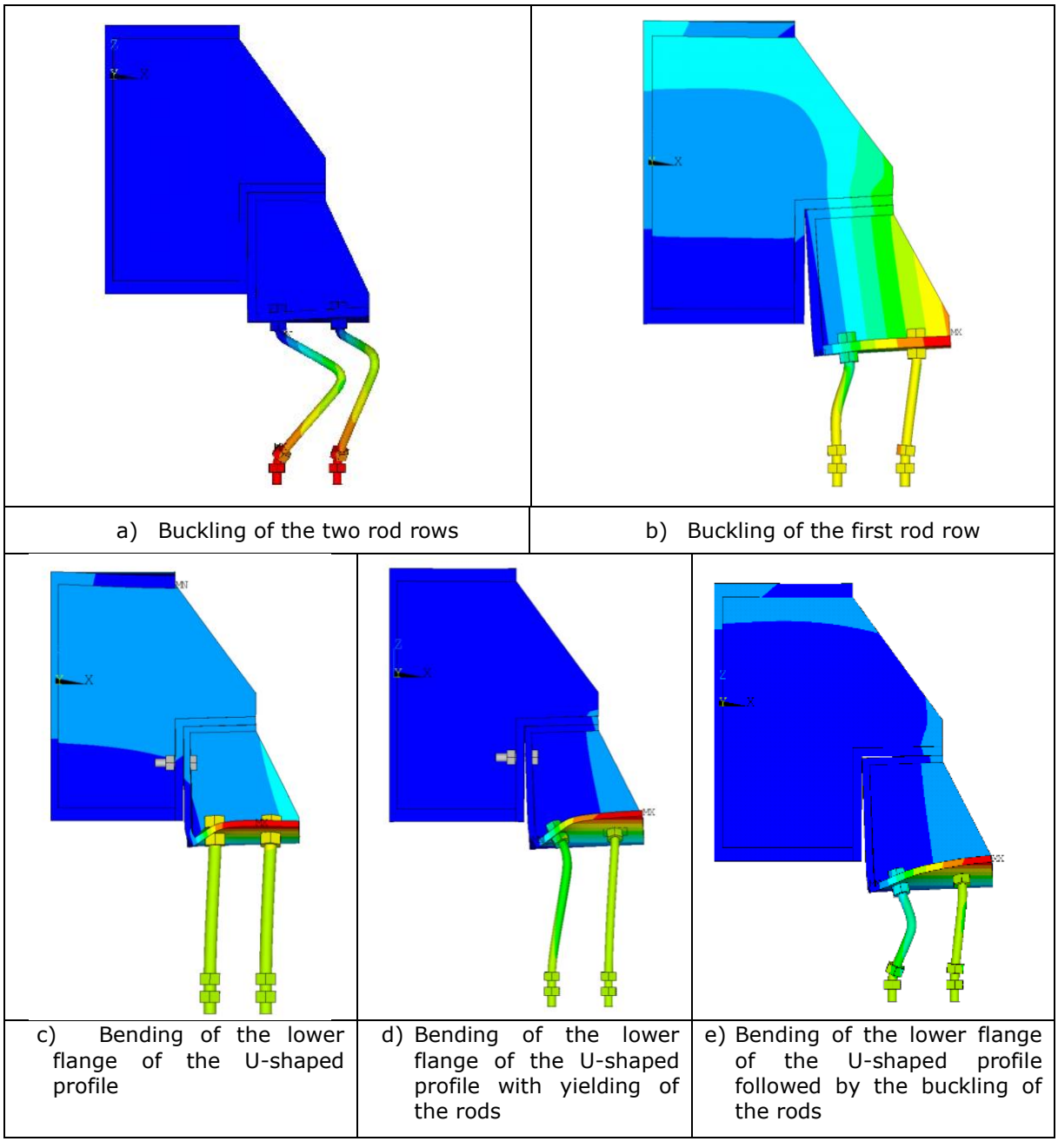

a) Buckling of the two rod rows

b) Buckling of the first rod row

c) Bending of the lower flange of the U-shaped profile

d) Bending of the lower flange of the U-shaped profile with yielding of the rods

e) Bending of the lower flange of the U-shaped profile followed by the buckling of the rods

Figure 3.39: Failure modes predicted for the third fusible link solution

Regarding the second fusible link solution, fusible links were found to fail more frequently by lateral torsional buckling of the UPN profile and rods bending or buckling, except for the shear failure of the steel bolts or bearing failure of the column stiffener, which was not accounted for in the simulations (see Figure 3.40). These failure modes were mainly observed at the two higher the fire load level $N_{fi,Ed}/N_{Rd}$ of 0.5 and 0.7. For the lower load level (e.g. 0.3), regardless of the characteristics of the rods (diameter and length) within the parameter range considered in the parametric study, the first failure occurs when the lower rod in the rod row closest to the column section yields at the level of the nut exposed to fire. Localised plastic crushing of the rod occurs, but no buckling of the rod is

observed. There is also significant bending of the horizontal wall of the L-profile (bolted to the web of the UPN with aluminium bolts), but these deformations have no real effect on the fire behaviour of the fusible links. Furthermore, it should be noted that, despite the lateral torsional buckling of the UPN profile, the fusible links can withstand the applied compressive forces until the failure of other components. Additionally, the UPN profile deforms on the side opposite the wall, thereby avoiding damage to the sandwich panels that constitute the fire wall.

Additionally, it should be noted that in some cases the bolt holes in both the UPN profile and the column stiffener exhibited permanent bearing deformations. However, this had no significant impact on the failure mode of the link.

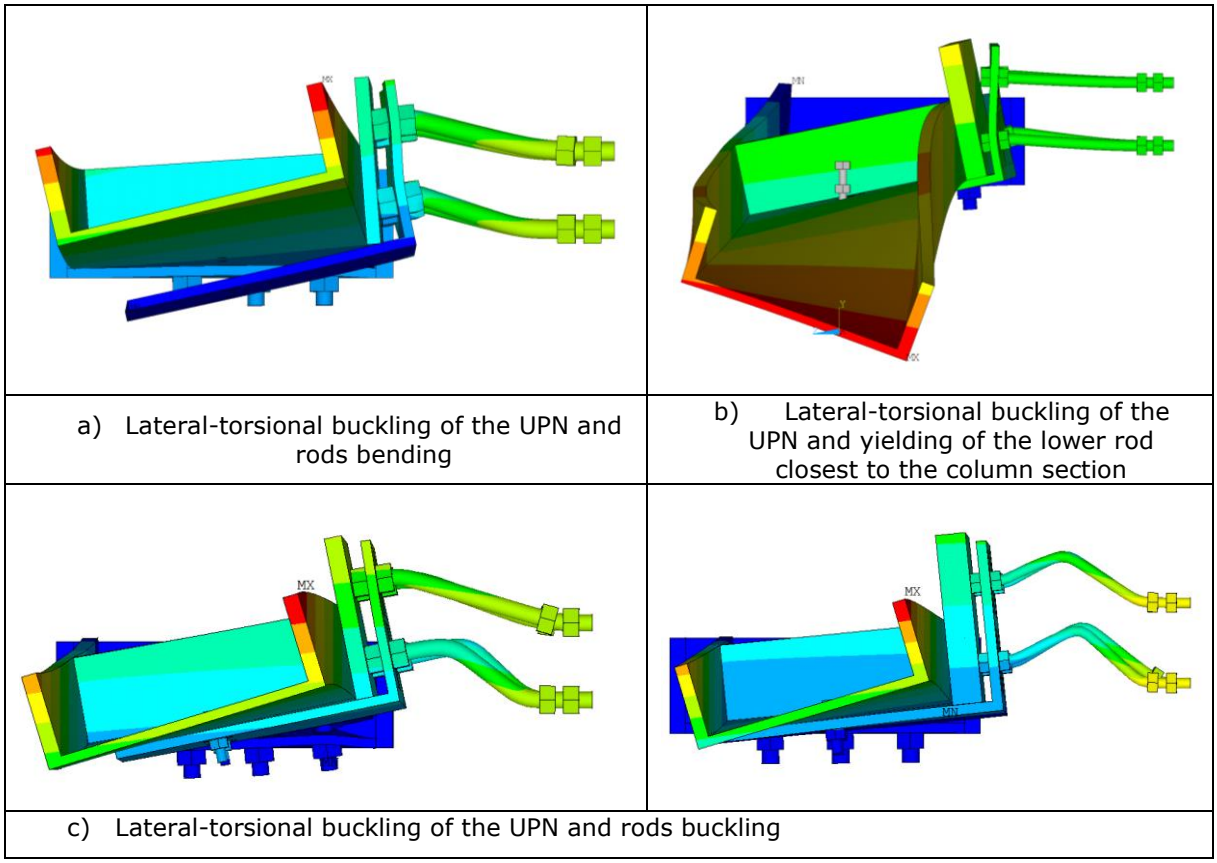

a) Lateral-torsional buckling of the UPN and rods bending

b) Lateral-torsional buckling of the UPN and yielding of the lower rod closest to the column section

c) Lateral-torsional buckling of the UPN and rods buckling

Figure 3.40: Failure modes predicted for the second fusible link solution

Finally, for the first fusible link solution, except for the yielding failure of the U-profile stiffener and the steel bolts failures, which was not accounted in simulations, the following potential failure modes were established (see Figure 3.41):

- Buckling or yielding of the threaded rod. Buckling often starts with the first row of rods (the ones closest to the column section), followed by the second row. Buckling always occurs at normal temperatures. Alternatively, the cross-section of the rods yields at elevated temperatures, just below the nut on the side exposed to the fire. In some cases, yielding is followed by buckling of the rods.
- For the thinnest Z-section thicknesses, the bending failure of the lower Z-section flange.
- For the thinnest U-section thicknesses, failure first occurs in the lower U-section flange, followed by bending of the Z-section and yielding of the rods if their resistance to compression is insufficient (due to small rod diameter), associated in some cases to the bending of the rods.

It should be noted that, unlike the third-link solution, there are fewer cases of rod buckling at elevated temperatures (at least when the failure mode was clearly identified as buckling). This is because the link is flexible thanks to its Z-profile. Furthermore, the failure mode is less affected by the duration of exposure to fire.

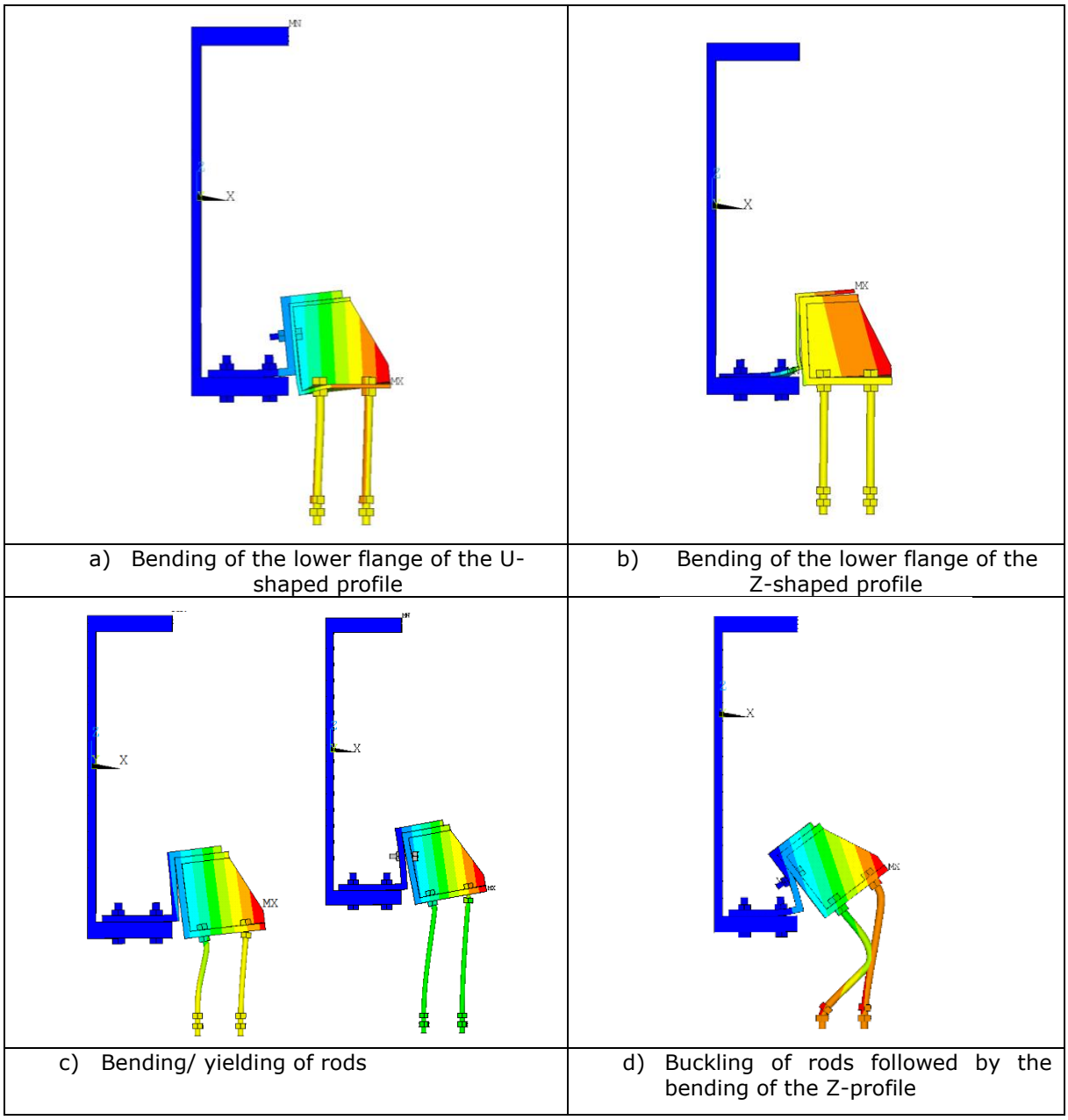

a) Bending of the lower flange of the U-shaped profile

b) Bending of the lower flange of the Z-shaped profile

c) Bending/ yielding of rods

d) Buckling of rods followed by the bending of the Z-profile

Figure 3.41: Failure modes predicted for the first fusible link solution

Another interesting result for the future development of simplified methods for calculating the fire resistance of the studied fusible links is an understanding of the load redistribution between the four rods. The Figure 3.42 to Figure 3.50 illustrate this, showing the ratio of the axial force to the applied load for the steel rods according to the considered link and the fire load level. As previously mentioned, the axial forces supported by the steel rods vary and can change progressively and significantly with an increase in temperature in the links. There is no uniform redistribution of the applied load. It should be noted that:

- For the first fusible link solution, the first rod row (closest to the column section) is under compression and supports approximately 150% of the applied compression load in all cases. The second rod row is in traction.
- For the third fusible link solution, the axial forces change progressively and noticeably with an increase in temperature in the link. As failure approaches, the load ratio ranges between 80% and 90% for the first rod row and between 10% and 20% for the second.
- In the second fusible link solution, a single rod (the lower rod in the rod row closest to the column section) takes most of the compressive load. As failure approaches, the load ratio of this steel rod ranges between 110% and 120%, regardless of the case considered.

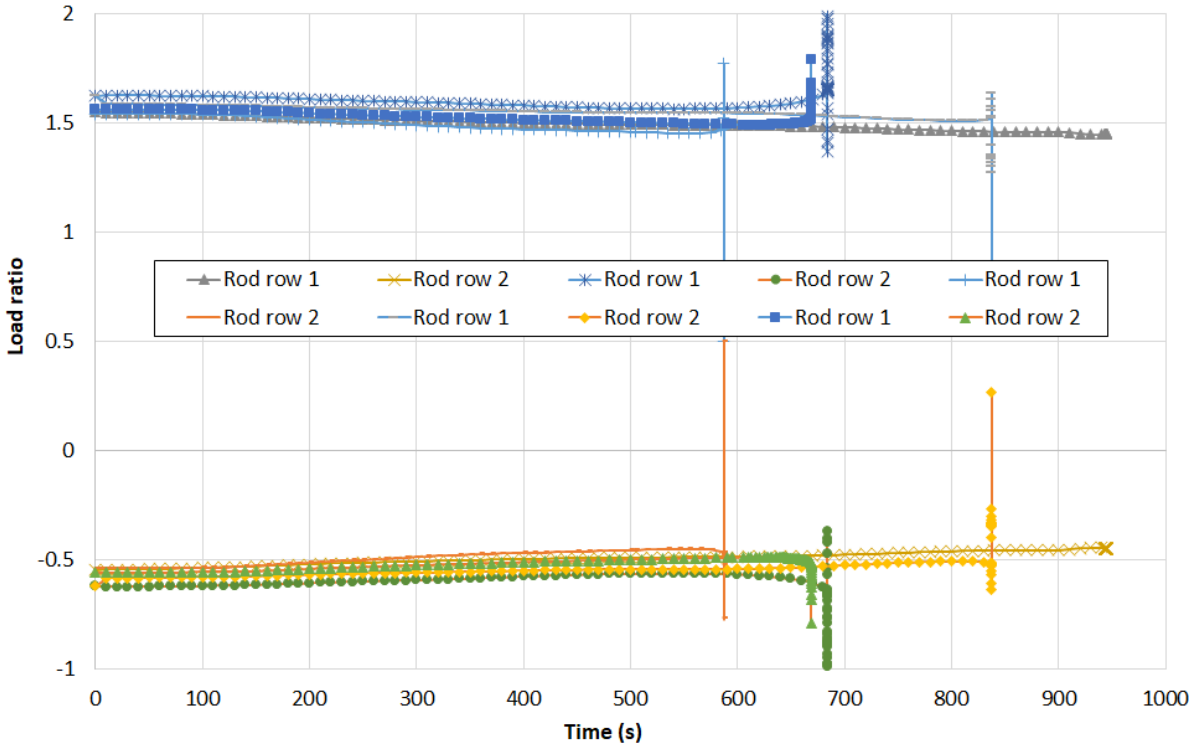

Figure 3.42: Evolution versus time of the axial force / applied load ratio of steel rods calculated for link cases corresponding to the first fusible link solution, with a fire load level $N_{fi,Ed}/N_{Rd}$ of 0.7

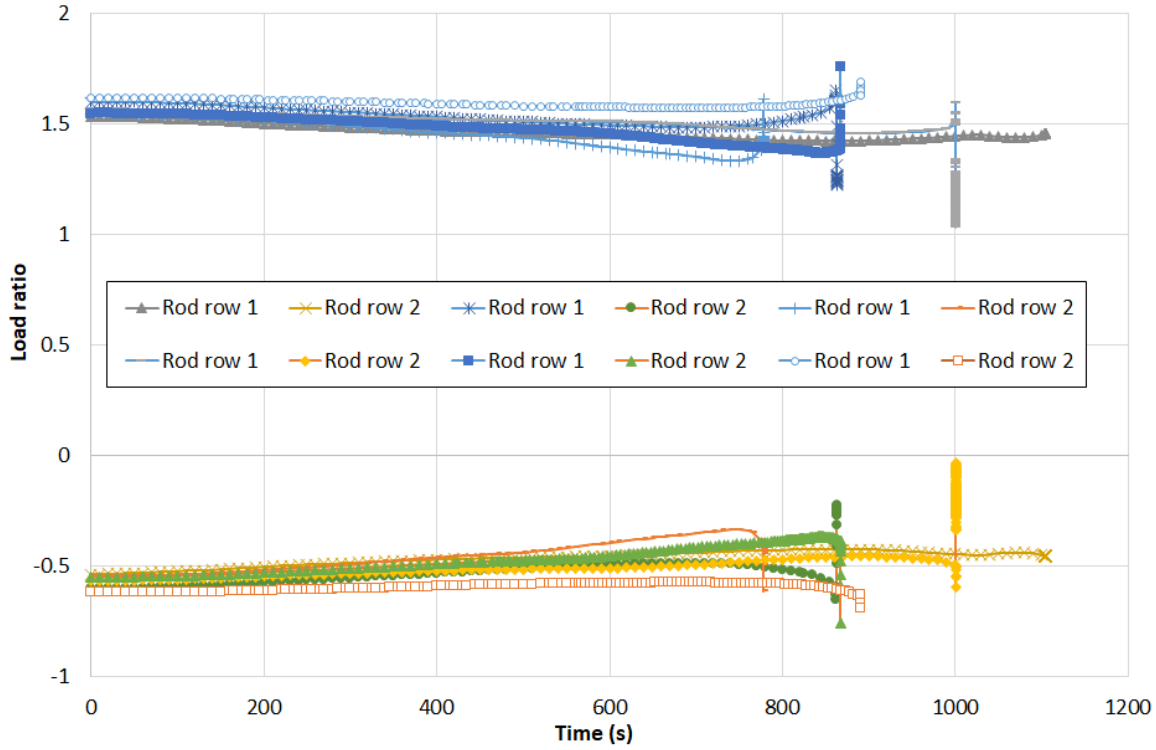

Figure 3.43: Evolution versus time of the axial force / applied load ratio of steel rods calculated for link cases corresponding to the first fusible link solution, with a fire load level $N_{fi,Ed}/N_{Rd}$ of 0.5

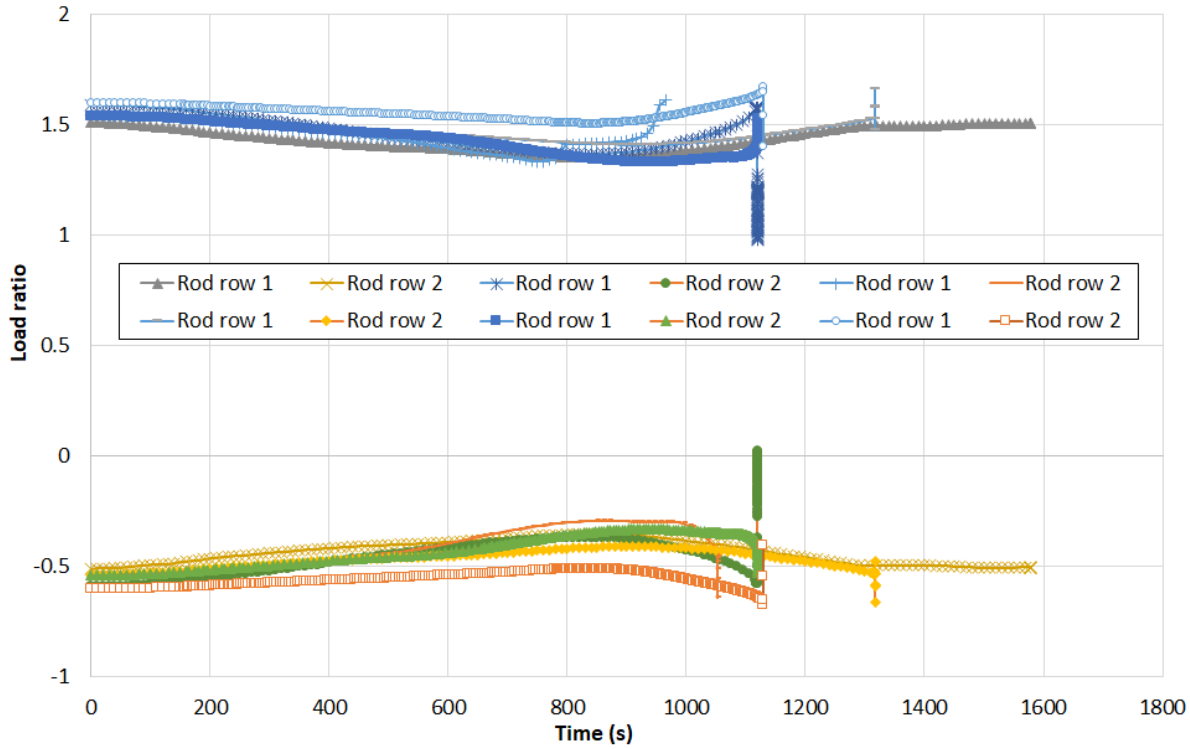

Figure 3.44: Evolution versus time of the axial force / applied load ratio of steel rods calculated for link cases corresponding to the first fusible link solution, with a fire load level $N_{fi,Ed}/N_{Rd}$ of 0.3

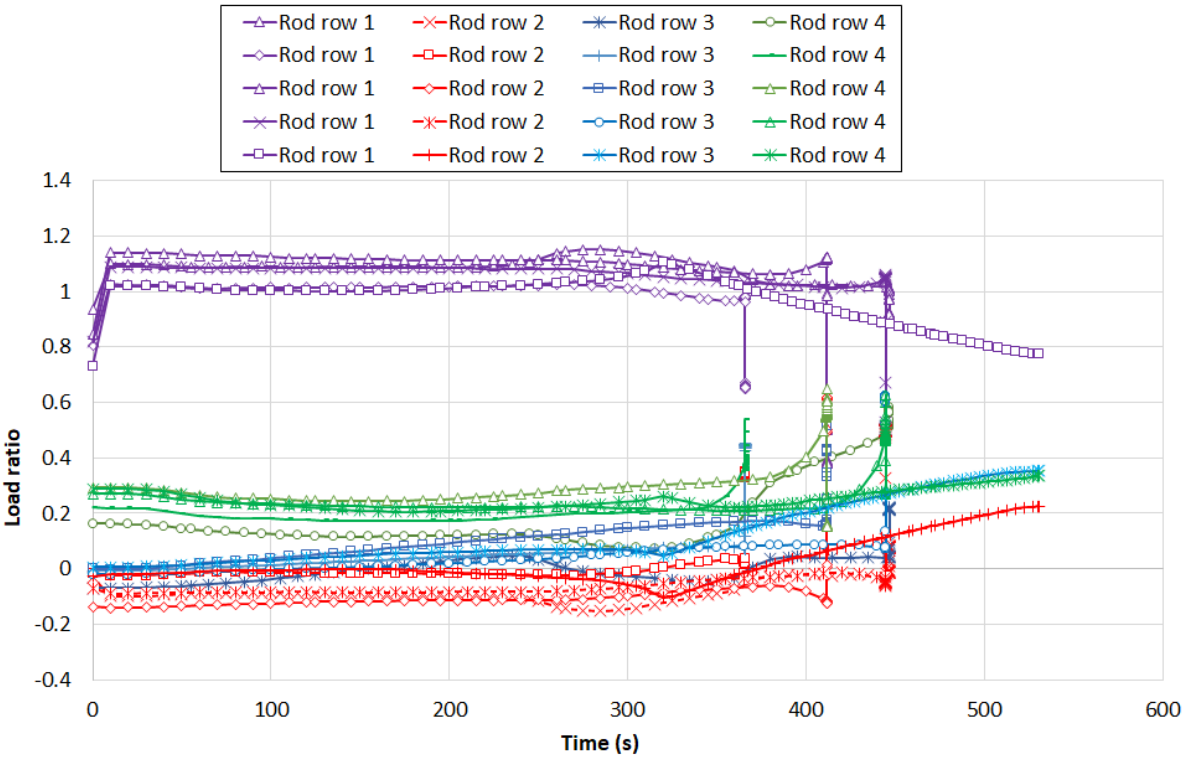

Figure 3.45: Evolution versus time of the axial force / applied load ratio of steel rods calculated for link cases corresponding to the second fusible link solution, with a fire load level $N_{fi,Ed}/N_{Rd}$ of 0.7

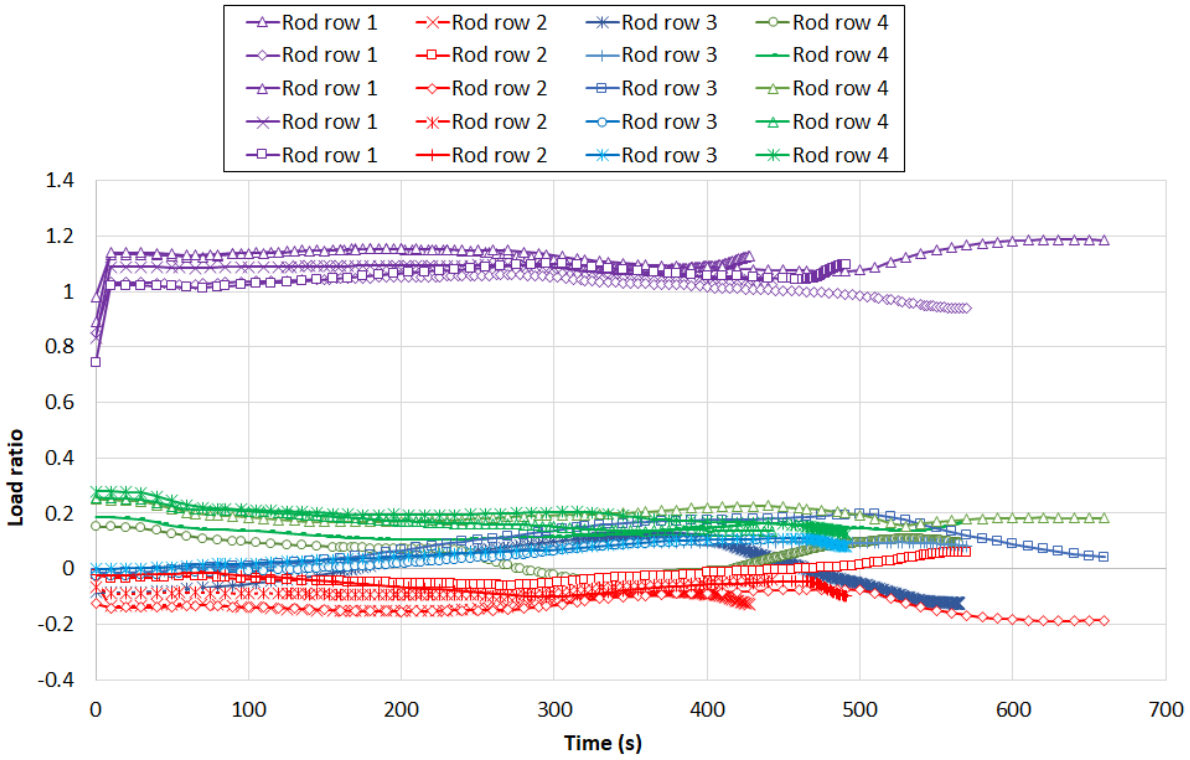

Figure 3.46: Evolution versus time of the axial force / applied load ratio of steel rods calculated for link cases corresponding to the second fusible link solution, with a fire load level $N_{fi,Ed}/N_{Rd}$ of 0.5

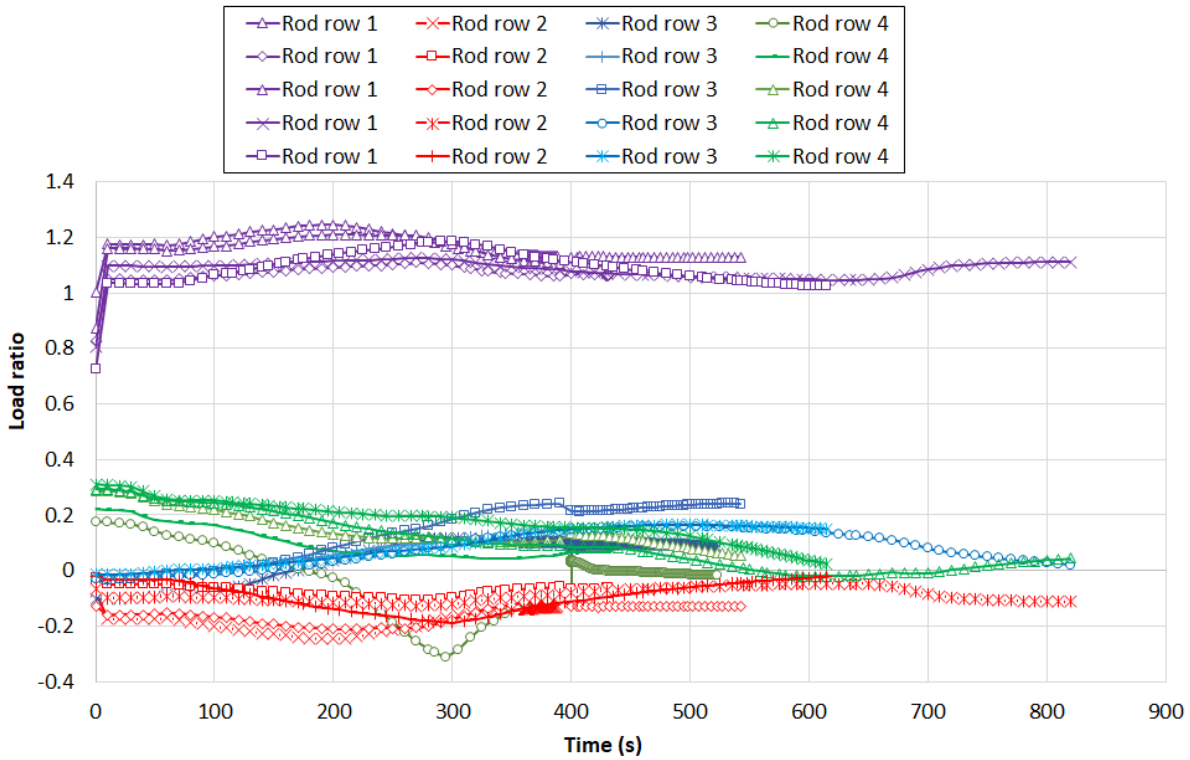

Figure 3.47: Evolution versus time of the axial force / applied load ratio of steel rods calculated for link cases corresponding to the second fusible link solution, with a fire load level $N_{fi,Ed}/N_{Rd}$ of 0.3

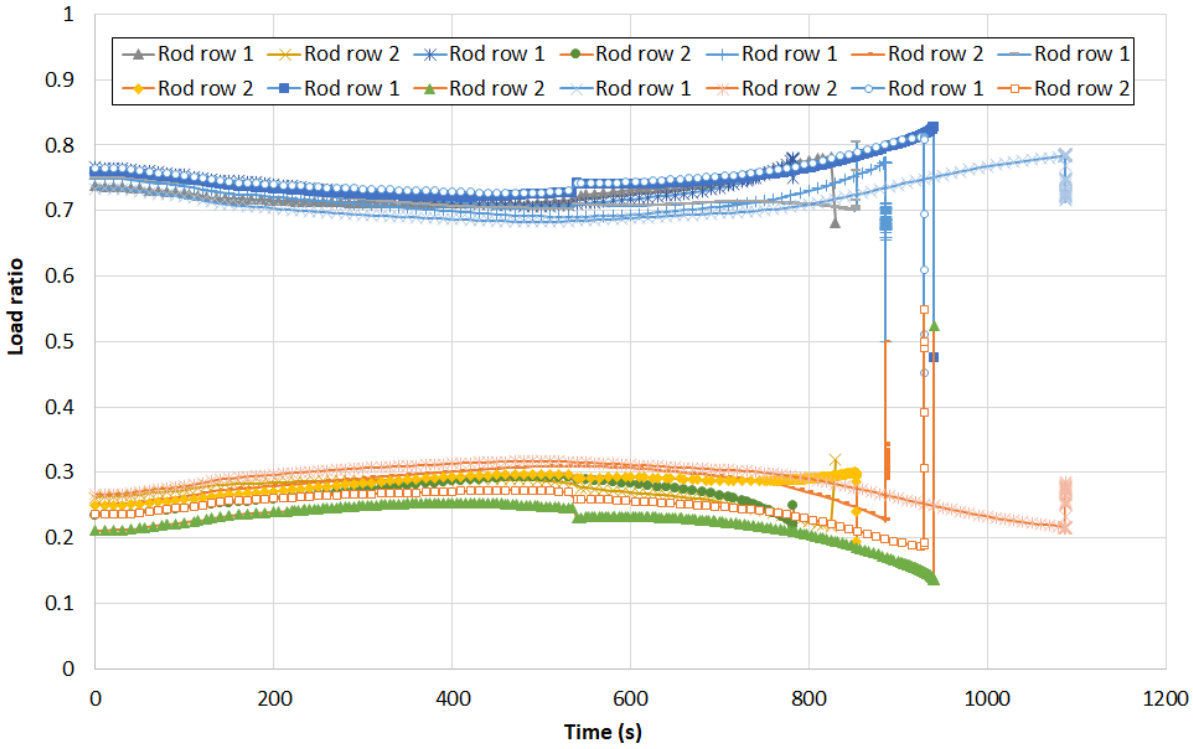

Figure 3.48: Evolution versus time of the axial force / applied load ratio of steel rods calculated for link cases corresponding to the third fusible link solution, with a fire load level $N_{fi,Ed}/N_{Rd}$ of 0.7

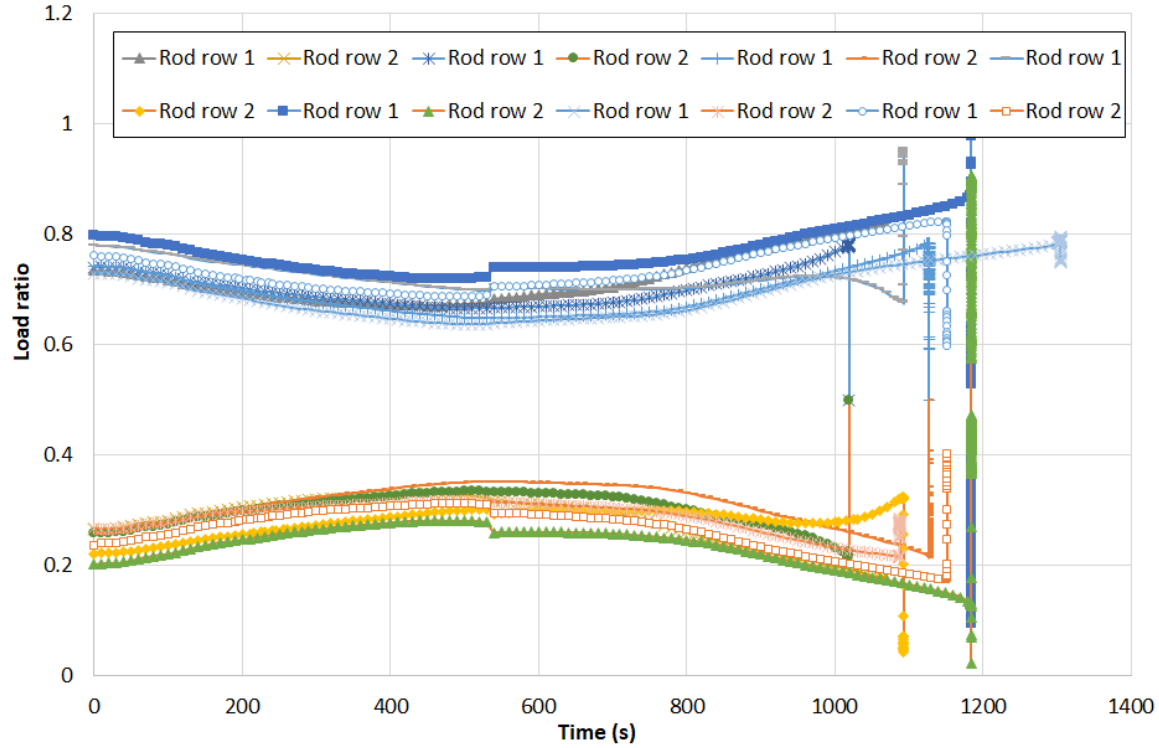

Figure 3.49: Evolution versus time of the axial force / applied load ratio of steel rods calculated for link cases corresponding to the third fusible link solution, with a fire load level $N_{fi,Ed}/N_{Rd}$ of 0.5

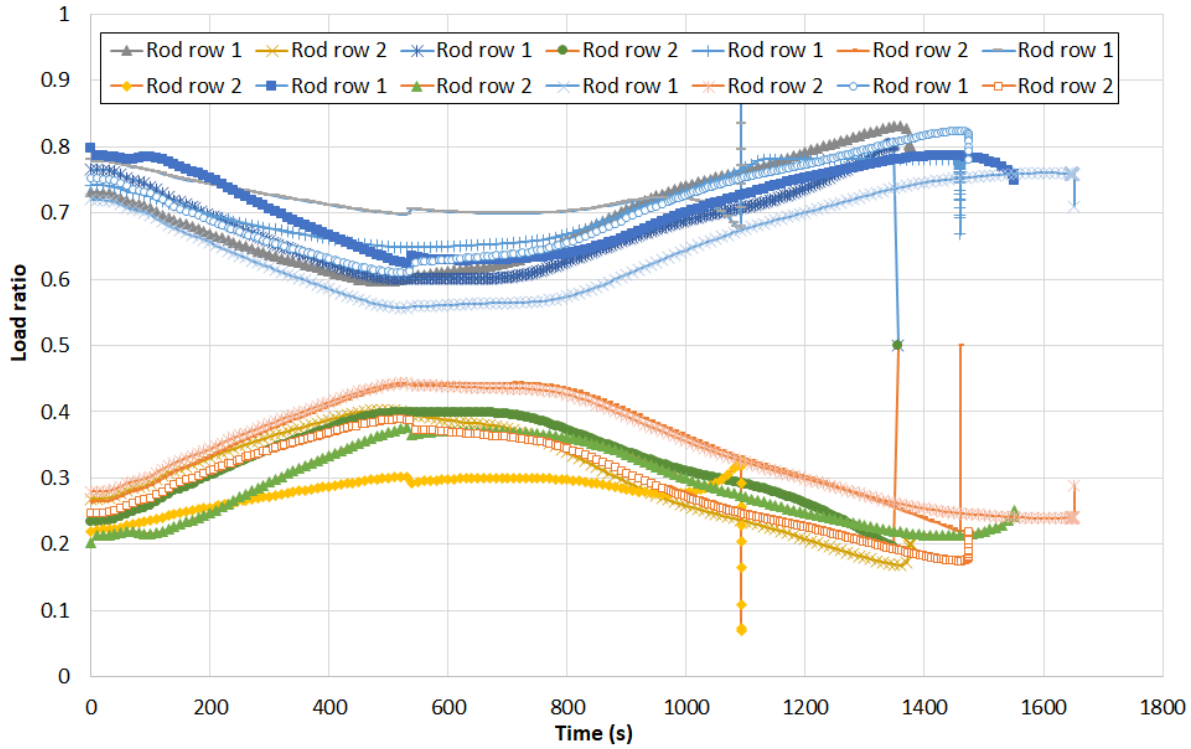

Figure 3.50: Evolution versus time of the axial force / applied load ratio of steel rods calculated for some link cases corresponding to the third fusible link solution, with a fire load level $N_{fi,Ed}/N_{Rd}$ of 0.3

3.3.3.2 Fire resistance time

The following tables show the predicted fire resistance times for the various defined cases of fusible links, as calculated by the numerical models. This data, along with the failure modes, has been used to develop simplified design methods for evaluating the load-bearing capacity of the investigated fusible links at elevated temperatures. These methods are described in the deliverable D5.2 [23].

Table 14 : Fire resistance times calculated for the link cases related to the 3rd fusible link solution

Case	Nfi,Ed (KN)	Time (s)	Case	Nfi,Ed (KN)	Time (s)
30%_M12_L100_eU6_mx29_p70_m35	29.4	1259	50%_M12_L175_eU8_mx27_p70_m35	62.5	1067
50%_M12_L100_eU6_mx29_p70_m35	49	950	70%_M12_L175_eU8_mx27_p70_m35	87.5	830
70%_M12_L100_eU6_mx29_p70_m35	68.1	760	R30_M12_L175_eU8_mx27_p70_m35	83.6	900
70%_M12_L100_eU10_mx25_p70_m35	125.3	803	30%_M14_L100_eU8_mx27_p70_m35	50.7	1220
50%_M12_L100_eU10_mx25_p70_m35	89.5	1061	50%_M14_L100_eU8_mx27_p70_m35	84.5	1015
30%_M12_L175_eU10_mx25_p70_m35	43.8	1350	70%_M14_L100_eU8_mx27_p70_m35	118.3	780
50%_M12_L175_eU10_mx25_p70_m35	73	1060	30%_M14_L175_eU8_mx27_p70_m35	45.6	1330
70%_M12_L175_eU10_mx25_p70_m35	105	858	50%_M14_L175_eU8_mx27_p70_m35	76	1047
30%_M12_L175_eU12_mx23_p70_m35	48.3	1453	70%_M14_L175_eU8_mx27_p70_m35	107.8	830
50%_M12_L175_eU12_mx23_p70_m35	85.5	1127	30%_M16_L100_eU10_mx25_p70_m35	79.2	1460
70%_M12_L175_eU12_mx23_p70_m35	119.7	808	50%_M16_L100_eU10_mx25_p70_m35	132	1079
50%_M12_L175_eU14_mx21_p70_m35	88	1120	70%_M16_L100_eU10_mx25_p70_m35	184.8	813
30%_M12_L175_eU14_mx21_p70_m35	51.3	1453	50%_M16_L175_eU6_mx29_p70_m35	67	960
70%_M12_L175_eU14_mx21_p70_m35	123	730	70%_M16_L175_eU6_mx29_p70_m35	93.8	740
70%_M12_L240_eU10_mx25_p70_m35	88.2	748	50%_M16_L175_eU10_mx25_p70_m35	117	1151
30%_M12_L240_eU10_mx25_p70_m35	37.8	1250	70%_M16_L175_eU10_mx25_p70_m35	163.8	925
50%_M16_L175_eU6_mx29_p70_m35	67	916	R30_M16_L175_eU10_mx25_p70_m35	160	900
30%_M16_L175_eU6_mx29_p70_m35	40.2	1220	R30_M16_L175_eU10_mx25_p70_m35	172	900
70%_M16_L175_eU6_mx29_p70_m35	93.8	730	30%_M18_L175_eU10_mx25_p70_m35	63.6	1640
70%_M16_L240_eU12_mx23_p70_m35	169.4	824.4	50%_M18_L175_eU10_mx25_p70_m35	106	1300
30%_M16_L240_eU12_mx23_p70_m35	72.6	1608	70%_M18_L175_eU10_mx25_p70_m35	148.4	1087
50%_M12_L175_eU6_mx29_p70_m35	44.45	900	50%_M20_L100_eU12_mx23_p70_m35	190	1152
70%_M12_L175_eU6_mx29_p70_m35	62.3	630	70%_M20_L100_eU12_mx23_p70_m35	266	887
50%_M12_L175_eU8_mx27_p70_m35	62	900	0.8_M20_L100_eU12_mx23_p70_m35	304	736
70%_M12_L175_eU8_mx27_p70_m35	86.8	790	0.65_M20_L175_eU12_mx33_p70_m35	231	940
50%_M12_L175_eU10_mx25_p50_m35	80	1020	70%_M20_L175_eU12_mx33_p70_m35	260	829
70%_M12_L175_eU10_mx25_p50_m35	112	816	R30_M20_L100_eU12_mx33_p70_m35	249	900
70%_M12_L175_eU10_mx25_p55_m35	105	760	30%_M20_L175_eU12_mx23_p70_m35	99	1400
50%_M12_L175_eU10_mx25_p55_m35	75	1050	50%_M20_L175_eU12_mx23_p70_m35	165	1182
30%_M12_L175_eU10_mx25_p50_m35	48	1350	70%_M20_L175_eU12_mx23_p70_m35	231	950
50%_M16_L175_eU10_mx25_p70_m35	117	1045	30%_M22_L175_eU12_mx23_p70_m35	102.9	1380
70%_M16_L175_eU10_mx25_p70_m35	163.8	830	50%_M22_L175_eU12_mx23_p70_m35	171.5	1200
30%_M16_L175_eU10_mx25_p70_m35	70.2	1416	70%_M22_L175_eU12_mx23_p70_m35	240.1	1000
30%_M12_L175_eU8_mx27_p70_m35	37.5	1370			

Table 15 : Fire resistance times calculated for the link cases related to the 2nd fusible link solution

Case	Nfi,Ed (KN)	Time (s)	Case	Nfi,Ed (KN)	Time (s)
70%-M16_L175_UPN240_eL10_p180_DX400	86	380	30%-M16_L175_UPN240_eL15_p180_DX200	860	46
50%-M16_L175_UPN240_eL10_p180_DX400	550	62	70%-M16_L100_UPN240_eL10_p180_DX400	440	98
30%-M16_L175_UPN240_eL10_p180_DX400	881	39	50%-M16_L100_UPN240_eL10_p180_DX400	580	70
70%-M16_L175_UPN240_eL10_p180_DX200	385	109	70%-M16_L175_UPN240_eL10_dy120_DX200	440	102
50%-M16_L175_UPN240_eL10_p180_DX200	550	78	50%-M16_L175_UPN240_eL10_dy120_DX200	680	72
30%-M16_L175_UPN240_eL10_p180_DX200	750	46	30%-M16_L175_UPN240_eL10_dy120_DX200	870	40
70%-M20_L175_UPN240_eL10_p180_DX200	295	155	70%-M16_L175_UPN240_eL10_dy50_DX200	433	102
50%-M20_L175_UPN240_eL10_p180_DX200	620	110	50%-M16_L175_UPN240_eL10_dy50_DX200	638	73
30%-M20_L175_UPN300_eL10_p180_DX200	565	113	50%-.M20_L175_UPN300_eL10_p180_DX200	600	142.2
70%-M16_L175_UPN300_eL10_p180_DX200	500	112	30%-M12_L175_UPN240_eL10_p180_DX200	900	24.45
30%-M16_L175_UPN300_eL10_p180_DX200	800	48	50%-M12_L175_UPN240_eL10_p180_DX200	700	35.75
70%-M16_L100_UPN240_eL10_p180_DX200	430	126	70%-M12_L175_UPN240_eL10_p180_DX200	510	57.05
50%-M16_L100_UPN240_eL10_p180_DX200	600	91	30%-M12_L175_UPN240_eL10_p180_DX400	950	19.5
70%-M16_L240_UPN240_eL10_p180_DX200	445	95	50%-M12_L175_UPN240_eL10_p180_DX400	660	32.5
50%-M16_L240_UPN240_eL10_p180_DX200	580	68	70%-M12_L175_UPN240_eL10_p180_DX400	500	45.5
30%-M16_L240_UPN240_eL10_p180_DX200	840	41	30%-M16_L175_UPN300_eL10_p180_DX400	960	42.9
70%-M20_L240_UPN240_eL10_p180_DX200	450	175	50%-M16_L175_UPN300_eL10_p180_DX400	670	71.5
50%-M20_L240_UPN240_eL10_p180_DX200	600	125	70%-M16_L175_UPN300_eL10_p180_DX400	490	100.1
30%-M20_L240_UPN240_eL10_p180_DX200	800	75	70%-M16_L175_UPN300_eL10_p180_DX200	490	112.7
70%-M16_L175_UPN240_eL8_p180_DX200	366	107	30%-M20_L175_UPN300_eL12_p180_DX200	900	88.5
70%-M16_L175_UPN240_eL15_p180_DX200	412	113	50%-M20_L175_UPN300_eL12_p180_DX200	640	147.5
50%-M16_L175_UPN240_eL15_p180_DX200	650	80	70%-M20_L175_UPN300_eL12_p180_DX200	450	206.5

Table 16 : Fire resistance times calculated for the link cases related to the 1th fusible link solution

Case	Nfi,Ed (KN)	Time (s)	Case	Nfi,Ed (KN)	Time (s)
70%-M16_L175_eU12_hU150_eZ8_mx23_p80_m65	78.0	750	70%-M16_L175_eU8_hU150_eZ8_mx27_p80_m65	71.2	600
50%-M16_L175_eU12_hU150_eZ8_mx23_p80_m65	56.0	900	50%-M16_L175_eU8_hU150_eZ8_mx27_p80_m65	50.9	750
30%-M16_L175_eU12_hU150_eZ8_mx23_p80_m65	33.6	1070	30%-M16_L175_eU8_hU150_eZ8_mx27_p80_m65	30.5	1050
70%-M16_L175_eU12_hU300_eZ12_mx23_p80_m65	85.0	683	R30-M16_L175_eU8_hU150_eZ8_mx27_p80_m65	38.0	900
50%-M16_L175_eU12_hU300_eZ12_mx23_p80_m65	59.0	890	70%-M16_L240_eU12_hU150_eZ12_mx23_p80_m65	76.3	837
70%-M16_L175_eU6_hU150_eZ12_mx29_p80_m65	65.0	450	50%-M16_L240_eU12_hU150_eZ12_mx23_p80_m65	54.5	1000
50%-M16_L175_eU6_hU150_eZ12_mx29_p80_m65	46.0	640	30%-M16_L240_eU12_hU150_eZ12_mx23_p80_m65	32.7	1315
70%-M12_L150_eU12_hU150_eZ12_mx29_p80_m65	45.0	850	50%-M16_L175_eU12_hU150_eZ6_mx23_p80_m65	61.0	890
50%-M12_L150_eU12_hU150_eZ12_mx23_p80_m65	35.0	910	30%-M16_L175_eU12_hU150_eZ6_mx23_p80_m65	36.6	1050
30%-M12_L150_eU12_hU150_eZ12_mx23_p80_m65	24.0	1060	R30-M16_L175_eU12_hU150_eZ6_mx23_p80_m65	62.0	900
70%-M16_L240_eU6_hU150_eZ12_mx29_p80_m65	56.0	400	70%-M12_L175_eU6_hU150_eZ12_mx29_p80_m65	36.9	570
50%-M16_L240_eU6_hU150_eZ12_mx29_p80_m65	40.0	682	50%-M12_L175_eU6_hU150_eZ12_mx29_p80_m65	18.9	800
30%-M16_L240_eU6_hU150_eZ12_mx29_p80_m65	20.0	1001	30%-M12_L175_eU6_hU150_eZ12_mx29_p80_m65	15.3	900
70%-M16_L175_eU6_hU150_eZ6_mx29_p80_m65	44.0	550	70%-M20_L240_eU10_hU150_eZ10_mx25_p80_m65	98.7	700
50%-M16_L175_eU6_hU150_eZ6_mx29_p80_m65	32.0	700	50%-M20_L240_eU10_hU150_eZ10_mx25_p80_m65	70.5	850
30%-M16_L175_eU6_hU150_eZ6_mx29_p80_m65	19.0	900	30%-M20_L240_eU10_hU150_eZ10_mx25_p80_m65	42.3	1080
30%-M16_L175_eU6_hU150_eZ12_mx29_p80_m65	28.0	870	30%-M16_L175_eU10_hU150_eZ10_mx25_p80_m65	34.2	1000
70%-M12_L240_eU12_hU150_eZ12_mx23_p80_m65	38.1	940	50%-M16_L175_eU10_hU150_eZ10_mx25_p80_m65	57.0	845
50%-M12_L240_eU12_hU150_eZ12_mx23_p80_m65	27.2	1100	70%-M16_L175_eU10_hU150_eZ10_mx25_p80_m65	79.8	663
30%-M12_L240_eU12_hU150_eZ12_mx23_p80_m65	16.3	1400	30%-M16_L175_eU14_hU150_eZ14_mx21_p80_m65	38.1	1300
30%-M16_L100_eU12_hU150_eZ8_mx23_p80_m65	41.0	1085	30%-M16_L175_eU14_hU150_eZ14_mx21_p80_m65	63.5	1030
70%-M16_L100_eU12_hU150_eZ8_mx23_p80_m65	95.6	680	30%-M16_L175_eU14_hU150_eZ14_mx21_p80_m65	88.9	900

4 GLOBAL ANALYSES OF STEEL STRUCTURES ASSOCIATED WITH PARTITION FIRE WALLS USING "FUSIBLE" LINKS

3D global structural analyses were performed to investigate the mechanical response of steel structures associated with firewalls using 'fusible' links under realistic fire conditions, and to check that the behaviour of the fusible links is appropriate when they are designed according to the design provisions proposed within the project. This involves ensuring that fusible links on the fire-exposed side can withstand the pushing phase. If the structure exposed to fire should collapse, fusible links located on the fire-exposed side must also fail first during the tensile phase.

The structural analyses were carried out on steel-framed buildings. These are based on one of the four reference buildings defined in deliverable D1.1 [21]. The fire scenarios were selected from those presented in deliverable D1.2 according to the selected reference buildings [22], for which the fire simulation software FDS was used.

4.1 Study cases

Due to the time-consuming nature of the required numerical simulations under real fire scenarios and the relatively large amount of computing power they require, it was not possible to study all the reference buildings defined in deliverable D1.1. Therefore, it was decided to perform the global analysis on steel-framed buildings based on reference building n°2 only. The buildings are divided into two or three fire compartments with an identical floor area, which are structurally independent and separated by fire walls with fusible link systems, as illustrated in Figure 4.1 and Figure 4.2. The fire walls are made of 175 mm-thick sandwich panels that provide an EI120 fire resistance performance. They are perpendicular or parallel to the steel portal frame. The steel structure of each fire compartment is the same for each case study and corresponds to that of the corresponding reference building. A schematic of the corresponding steel structures is shown in Figure 4.3. Detailed information is provided in deliverable D1.1.

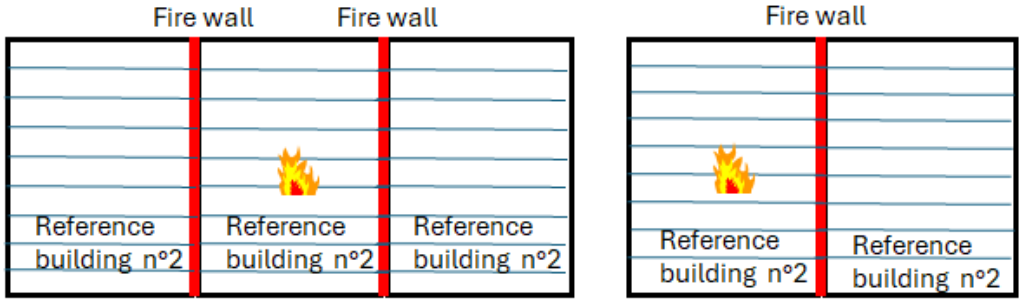

Figure 4.1: Studied building configurations - Fire wall perpendicular to steel portal frames

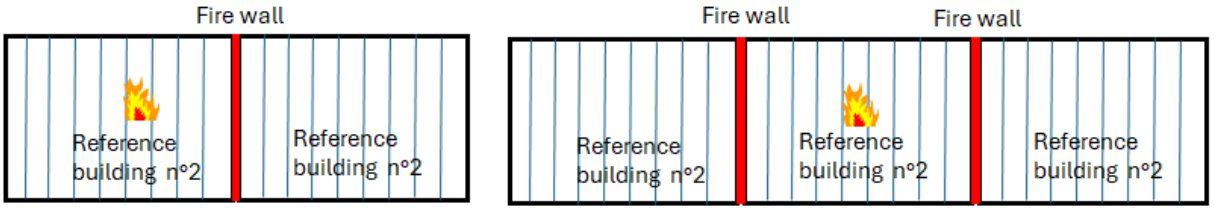

Figure 4.2: Studied building configurations - Fire wall parallel to steel portal frames

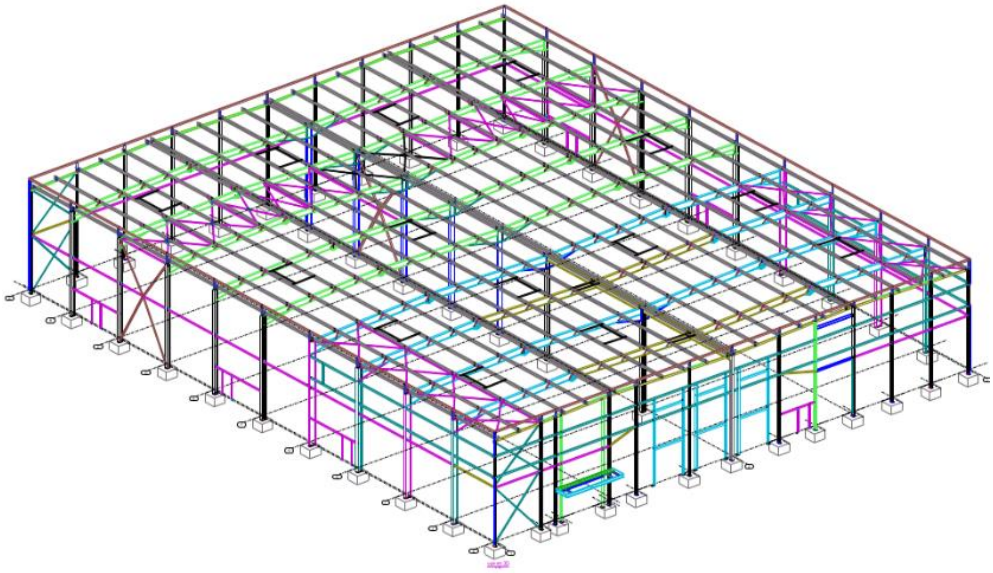

Figure 4.3: Perspective view of the reference building n°2

Three fire scenarios have been selected from those investigated in deliverable D1.2, according to the reference building considered. They are underlined in Table 17. These scenarios were chosen to cover all possible fire developments, from localised to fully engulfed fires.

Table 17: Detail of fire scenarios analysed

Fire scenario	Building	Occupancy type	Location of the fire source
W.2.3	2	Warehouse (rack storage)	In the middle of the central double row rack
S.2.3	2	Supermarket (shelf storage)	In the middle of the central double row shelf
I.2.2	2	Industrial building (bulk storage)	In a bulk storage near one of the shorter compartment sides

Finally, the details of the studied cases are reported in Table 18. They are deemed sufficient to meet the objectives of the numerical study.

Table 18: Summary of the studied cases

Case	Compartment number	Fire wall implementation	Reference building	Fire scenario
1	2	perpendicular	2	W.2.3
2	3	perpendicular	2	W.2.3
3	2	parallel	2	W.2.3
4	3	parallel	2	W.2.3
5	2	perpendicular	2	S.2.3
6	3	perpendicular	2	S.2.3
7	2	parallel	2	S.2.3
8	3	parallel	2	S.2.3
9	2	perpendicular	2	I.2.2
10	3	perpendicular	2	I.2.2
11	2	parallel	2	I.2.2
12	3	parallel	2	I.2.2

4.2 Fire behavior Modelling of the studied cases

The fire behaviour of building steel structures is analysed according to the calculation procedure of the fire part of Eurocode 1 [5] and the calculation methods of the fire part of Eurocode 3 [7]. For each selected design fire scenario, numerical analyses are performed in two successive steps:

- First, a heat transfer analysis is performed using the code ANSYS [18] to estimate the distribution and the evolution versus time of temperatures reached by the structural members exposed to fire.
- Then, from the previously calculated temperature fields, the fire behaviour of the steel structure is analysed using the code Ls-dyna [19]. The numerical simulation approach that is used combines implicit and explicit calculation steps and allows to obtain very advanced deformed states of the studied structure.

4.2.1 Predesign of fusible links

To achieve the requirements asked in terms of overall structural behaviour, i.e. avoid any progressive collapse in the case of compartmented buildings, the fusible links must be designed to withstand the compressive forces induced by the thermal expansion of the steel structure in the event of a fire, while also breaking adequately on the side exposed to the fire under the tensile forces induced by the collapse of the structure, if it occurs.

Based on all the fire development simulations performed for this project, it was believed that the first requirement could be met by designing the fusible links to achieve an R15 fire resistance rating under the standard fire curve. The exception to this is aluminium bolts, which do not contribute to the compression resistance of the links. The second requirement should be met by designing the fusible links at normal temperature to withstand the tensile forces resulting from the collapse of the structure exposed to fire. Due to the fusible link solutions developed, the resistance is mainly provided by the shear resistance of the aluminium bolts.

These design assumptions have been verified using the results of the global analyses carried out, which are presented below.

The design forces to be considered in the fire design of fusible links can be easily calculated using the simple rules developed in an earlier RFSC project [17], as reported in Appendix C. Once all the calculations have been made, the resulting, the resulting design forces are reported in the following tables, according to the study cases: fire walls parallel or perpendicular to steel portal frames and buildings divided into two or three fire compartments.

Table 19: Pushing forces F_p calculated at the top of end columns of steel portal frames – fire wall perpendicular to steel portal frames

Case	Fire location	c_{th}	K_1 (kN/m)	K_2 (kN/m)	n	L (m)	F_p (KN)
1	Building end	0.011	463.2	60.2	2	25	26.7
2	Middle of building	0.011	463.2	463.2	2	25	115.8
5	Building end	0.011	463.2	60.2	2	25	26.7
6	Middle of building	0.011	463.2	463.2	2	25	115.8
9	Building end	0.011	463.2	60.2	2	25	26.7
10	Middle of building	0.011	463.2	463.2	2	25	115.8

With:
- $q_{fi,Ed}$: uniformly distributed design load applied on beam portal frames
- L: span of beam portal frame
- n: total number of heated portal frame spans
- K_1, K_2: equivalent lateral stiffnesses of the structures

Table 20: Tensile forces calculated at the top of end columns of steel portal frames – fire wall perpendicular to steel portal frames

Case	Fire location	C_p	n_{eff}	L (m)	$q_{fi,Ed}$ (kN/m)	F_t (KN)
1	Building end	1.19	1	25	4.14	123.2
2	Middle of building	1.19	2	25	4.14	246.33
5	Building end	1.19	1	25	4.14	123.2
6	Middle of building	1.19	2	25	4.14	246.33
9	Building end	1.19	1	25	4.14	123.2
10	Middle of building	1.19	2	25	4.14	246.33

With:
- $q_{fi,Ed}$: uniformly distributed design load applied on beam portal frames
- n_{eff}: design number of heated portal frame spans
- L: span of beam portal frame

Table 21: Design forces calculated at the top of the boundary columns– fire wall parallel to steel portal frames

Case	$q_{fi,Ed}$ (kN/m)	L (m)	n	F_t or F_p (KN)
3	1.48	6.3	2.5	27.8
4	1.48	6.3	2.5	27.8
7	1.48	6.3	2.5	27.8
8	1.48	6.3	2.5	27.8
11	1.48	6.3	2.5	27.8
12	1.48	6.3	2.5	27.8

With:
- $q_{fi,Ed}$: uniformly distributed design load applied on purlins
- n: number of purlins
- L: span of purlins

Once the design forces calculated, the design of fusible links can be carried out by comparing these forces with the design resistance calculated using the simple rules developed as far of the project [23]. For all cases studied, it was assumed that the fusible links used with the fire wall were based on the first solution, with geometric dimensions indicated in the Figure 4.4. The Table 22 shows the fire design resistance to compression of the considered fusible link, according to the thickness of the U-shaped profile and the characteristics of the threaded rods, once all calculations have been performed. Table 23 gives the design resistance to traction according to the characteristics of aluminium bolts. Based on these design resistances, the fusible links finally selected for each case study are reported in
Table 24.

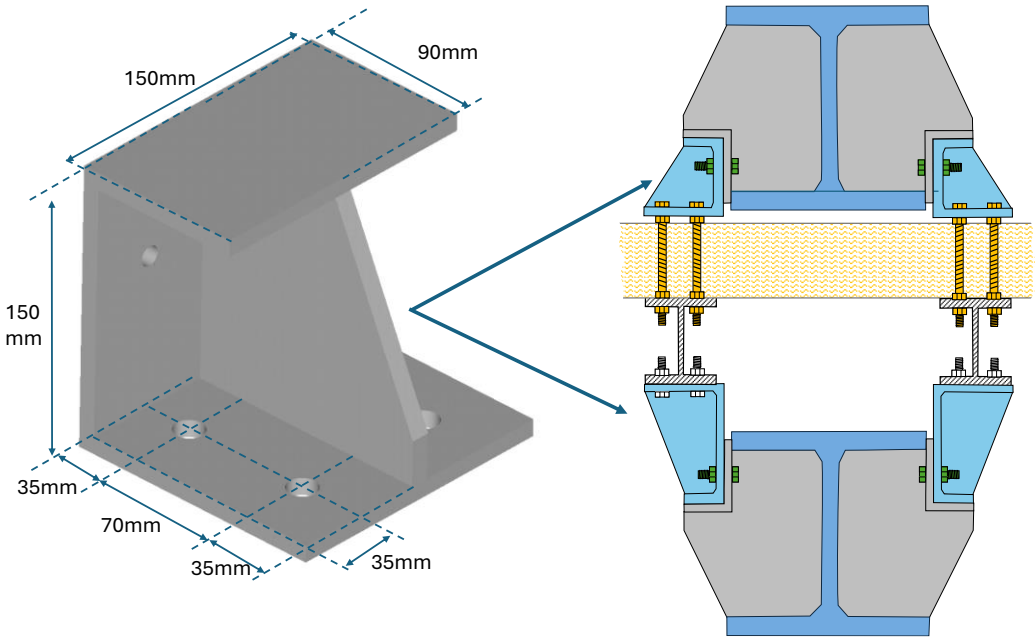

Figure 4.4: Geometrical characteristics of considered fusible links

Table 22: Fire design resistance to compression of the fusible link

Detail	U-shaped steel profile		Steel rods		$N_{Rd,fi,c}$ (KN)
	Thickness (mm)	steel grade	Diameter	steel grade	
1	7	S275	M12	8.80	33
2	8	S275	M12	8.80	45.9
3	9	S275	M12	8.80	64.2
4	10	S275	M12	8.80	86.9
5	12	S275	M12	8.80	96.6
6	12	S275	M14	8.80	131.8
7	14	S275	M12	8.80	101.2
8	16	S355	M22	10.90	454.9

Table 23: Shear resistance of aluminium bolts at normal temperature

Diameter	Yield strength (N/mm²)	Tensile strength (N/mm²)	As (mm²)	Bolt number	α_v	γ_{M2}	$F_{V,rd}$ (KN)
12	420	490	84.3	2	0.5	1	41.3
12	420	490	84.3	4	0.5	1	82.6
12	420	490	84.3	6	0.5	1	123.9
12	420	490	84.3	8	0.5	1	165.2
16	420	490	157	2	0.5	1	76.9
16	420	490	157	4	0.5	1	153.8
16	420	490	157	6	0.5	1	230.7
16	420	490	157	8	0.5	1	307.7

Table 24: Fusible link solutions

Case	F_p (KN)	Ft (KN)	Fusible link
1	26.7	123.2	Detail 1 with 2M16
2	115.8	246.3	Detail 3 with 4M16
3	27.8	27.8	Detail 1 with 1M16
4	27.8	27.8	Detail 1 with 1M16
5	26.7	123.2	Detail 1 with 2M16
6	115.8	246.3	Detail 3 with 4M16
7	27.8	27.8	Detail 1 with 1M16
8	27.8	27.8	Detail 1 with 1M16
9	26.7	123.2	Detail 1 with 2M16
10	115.8	246.3	Detail 3 with 4M16
11	27.8	27.8	Detail 1 with 1M16
12	27.8	27.8	Detail 1 with 1M16

4.2.2 Thermal analysis

For the building structure, heat transfer analyses have been performed using a coupling procedure for the CFD code FDS and the FEM code ANSYS, which was developed at CTICM [20]. This coupling procedure enables the thermal actions received by structural members in real fire conditions to be obtained with accuracy. Therefore, the amount of heating depends not only on the relative position of the analysed steel member with respect to the fire source, taking shadow effects into account, but also on the section factors of this steel member. A key feature of this procedure is that modelling of the structural members in the FDS domain is not required. Data on thermal actions (temperature and radiation) are recorded separately and then used in the coupling procedure.

Heat transfer analyses are carried using the following assumptions:

- In order to reduce calculation time while maintaining accuracy, heat transfer analyses are carried out using two-dimensional finite element models of cross-sections of various structural members. Calculations are performed at multiple positions along the considered members, and temperature gradients are recreated by assuming linear temperature variation between successive sections.

- Four-node surface elements (Plane55) and linear elements (Surf152) are used, on the one hand to represent the cross sections of the studied members, and on the other hand to apply thermal actions.
- The thermal properties of steel are those given in EN 1993-1-2 [7].
- All structural members are exposed to fire on four sides.
- In order to calculate the heat fluxes transmitted to the surface of the structural members, values for the convective coefficient, the fire emissivity and the steel surface emissivity must be introduced into the analysis. The values adopted are those given in EN 1991-1-2:
    - Emissivity of fire $\varepsilon_m = 1.0$,
    - Emissivity of carbon steel $\varepsilon_m = 0.7$,
    - Convective coefficient $\alpha_c = 35$ W/m^2 K ;

Regarding the fusible links, an accurate prediction of their heating should necessitate the use of detailed 3D numerical models, such as those developed in the project. These models allow shadow effects created by structural members and the lower level of thermal radiation received by the shadowed parts of members' profiles to be considered. However, using these models at an overall structural level is prohibitively expensive. Consequently, the heating of the fusible links has been calculated using the simplified method proposed in deliverable D5.2. This method is based on the analytical approach given in EN 1993-1-2, using the appropriate section factor A_m/V value for the part forming the fusible link. Moreover, the link heating has been calculated by considering the hot gas temperature predicted in the vicinity of the considered fusible link by the FDS fire simulations carried out in the project [22]. To verify the accuracy and relevance of this approach in real fire conditions, Apppendix B summarises a comparison of the calculated fusible link temperatures using 3D finite element (FE) models with those predicted using the simplified method.

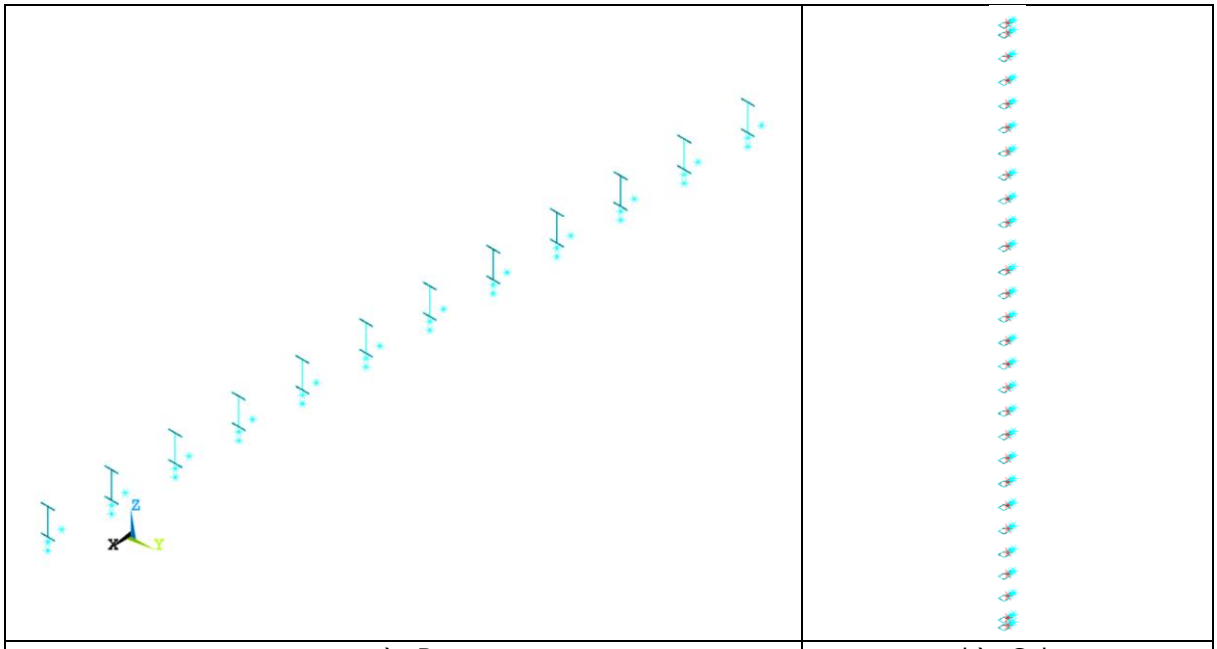

a) Beam b) Column

Figure 4.5: Modelling of steel members in thermal analysis

4.2.3 Mechanical analysis

The mechanical behaviour of the studied structure at elevated temperatures was investigated by considering the heating of its various members. The numerical simulation combines implicit and explicit calculation phases, allowing advanced deformation states of the structure to be obtained in the progressive collapse phase following loss of members resistance due to elevated temperatures.

The following assumptions have been adopted:

- The structure has been modelled using the Hughes-Liu beam finite elements.
- Although thermal analysis provides information on the temperature gradients occurring on the cross-sections of structural members, to reduce calculation time, the temperature applied to each cross-section corresponds to the maximum temperature calculated for that section in the heat transfer analysis.
- The mechanical properties of steel at elevated temperatures, including reduction factors for characteristic strengths, stress-strain laws and the thermal expansion coefficient, are those specified in EN 1993-1-2 [7]. For this purpose, temperature-dependent material model MAT202 was used.
- All profiles are made of S275 or S355 steel grade. The mechanical properties of the steel at normal temperatures are as follows:
    - yield strength: f_y = 275 or 355 MPa;
    - Young's modulus: E = 210,000 MPa.
- The base of the columns is hinged.
- The support conditions are assumed to remain unchanged throughout the fire exposure.
- As is generally assumed in fire calculations, the possible horizontal stabilisation effect of the building envelope on the structure is neglected.
- The fire wall and its supporting columns are not modelled.
- Fusible links are assumed to be subject to axial forces only, either traction or compression. Each fusible link is modelled as a combination of two series of beam and uniaxial spring elements arranged in parallel, as shown in Figure 4.6. Each beam-spring series accounts for the resistance of the fusible link under compression or tension, with the corresponding uniaxial spring acting only in the relevant direction. A linear elastic–perfectly plastic material model is assigned to each beam element. For the beam element dedicated to traction recovery, the yield stress was calibrated to reproduce the shear resistance of aluminium bolts at elevated temperatures (these bolts provide the traction resistance of the fusible links). Thus, the model can be used to predict the failure of the fusible links directly. Regarding compression, to avoid duplicating the simulations, it is assumed that the corresponding beam element is fully resistant at all temperatures. Therefore, once the simulation has finished, the adequate compression resistance of the fusible link at elevated temperatures must be verified by comparing it with the internal forces acting on the corresponding beam.
- The steel structures not exposed to fire are modelled as springs that are assembled in parallel configurations to represent a structure's equivalent stiffness. The stiffness of each spring was determined using preliminary 3D analyses of the steel structure, which was assumed to be subjected to lateral loads.
- In addition to the structure's own weight, a uniformly distributed load is applied to each purlin and column supporting the façade elements (see Table 18). These loads remain constant throughout fire exposure. They were calculated using the relevant load combinations for the fire situation, in accordance with EN 1990 [4] and EN 1991-1-2 [5] and their French national annexes. In principle, the fire stability of any building structure should be verified using load combinations that account for the effects of wind and snow loads. However, this parametric study only considers load combinations accounting for snow loads, as these usually have the greatest impact on fire resistance. Consequently, following load combinations were considered only:
    - $G + 0{,}9\ Q$,
    - $G + 0{,}8\ Q + 0{,}2\ W$,

Where, *G* are the permanent loads, *Q* are the live loads and S are the snow loads. The characteristic values of these loads are reported in Table 25.

It can be noted that aluminium bolts are unlikely to regain their initial strength after heating. In the absence of precise data on this subject, some numerical simulations were carried out to study the effect of such irreversibility. For these simulations, it was assumed that the fusible links would retain the same temperature after reaching the maximum temperature calculated for the relevant fire scenario until the end of the simulations.

Moreover, 2D structural analyses of isolated steel portal frames were also carried out, considering the most heated steel portal frame for each of the three fire scenarios related to reference building No. 2.

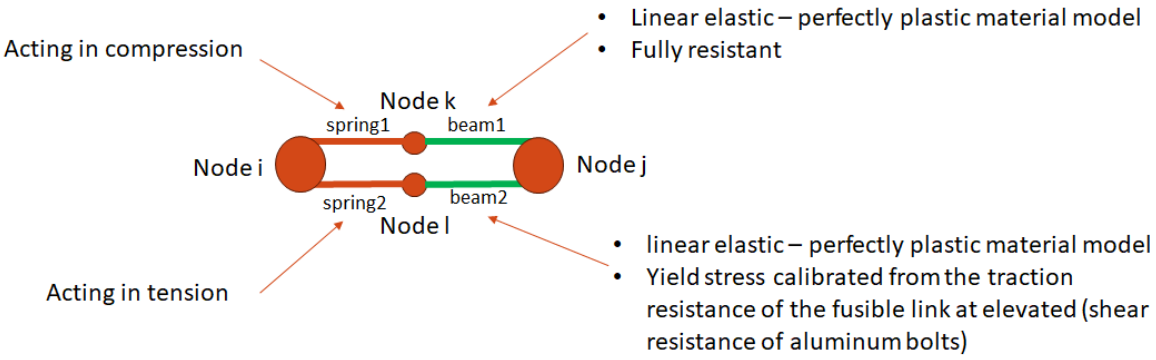

Figure 4.6: FE modelling of fusible links

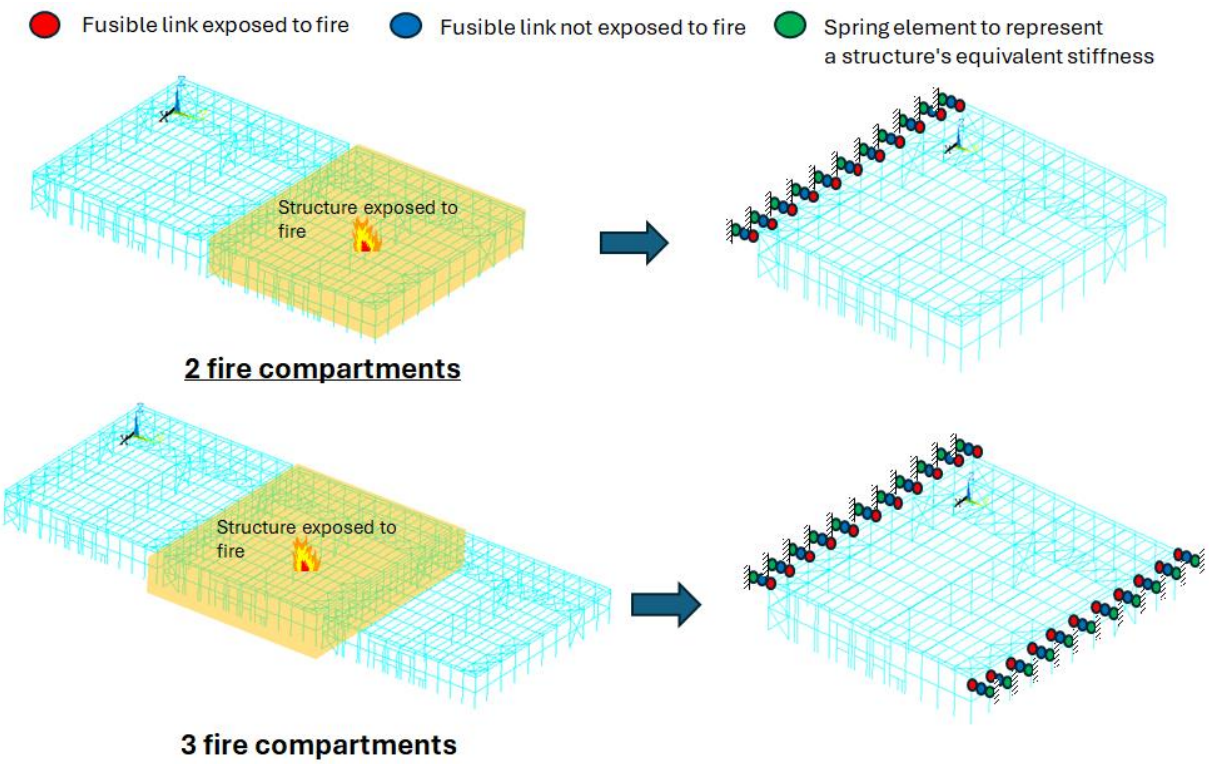

Figure 4.7: FE modelling principle of the investigated study case

Table 25 : Characteristic values of loads considered in the buildings design [21]

Load type	load value
Permanent loads	Roof panels: 30 kg/m² Façade elements: 25 kg/m² Other accessories: 5 kg/m²
Snow loads	S = 45 kg/m²

Table 26 : Uniformly distributed load (KN/m) applied in the structural modelling

Load type	Reference building N°2
purlin	1.60
Column	1.44

4.3 Numerical results

4.3.1 Thermal analyses results

Figure 4.8 to Figure 4.12 show the temperatures reached by the structural elements under consideration at different times of exposure to fire, according to the fire scenario concerned.

It should be noted that:

- For fire scenarios S.2.3 and I.2.2, fire effects remain localised. The structural members located closest to the initial source of the fire heat up much faster than the rest of the structure. The resulting temperature increases are very high locally (in the internal column of the most heated portal frame), with maximum temperatures more than 800°C. However, the highly heated zone of the structure is not extensive, and the maximum temperature reached by structural members more than ten metres from the fire's source does not exceed 400°C in any of these fire scenarios (see Figure 4.10 and Figure 4.12). In addition, the member's heating undergoes a decay phase when the gas temperature decreases after the combustible material has been consumed. It should also be noted in scenario S.2.3 that the fire travels along the most heated portal frame, which results in a delay between the heating and cooling of the portal frame sections (see Figure 4.10).
- For fire scenarios W.2.3 (related to fires involving rack pallets), the fire's effects remain localised to the structural members closest to the initial source for the first few minutes. Then, as the fire spreads, the heated zone gradually spreads throughout the building. After 20 minutes in scenario W.2.3, the heated members are at very high temperatures, with maximum temperatures more than 900°C in most parts of the roof structure and the upper part of the columns.

The temperatures calculated for the aluminium bolts of the considered fusible links if they were placed at the top end of each column located at the periphery of the studied structure are illustrated in Figure 4.13 to Figure 4.12. As with the structural members, it can be noted that the temperatures reached in each link in scenario W.2.4 are very high, well above 500°C (the melting temperature of aluminium), suggesting that these links will all fail during a fire. Due to the rapid spread of the fire, the temperature rises of the aluminium bolts are very close together. In the other two scenarios involving localised fires, the temperatures reached in the fusible links are much lower, depending on whether they are near or far from the initial fire source. In addition, the links heating undergoes also a decay phase. The maximum temperatures vary between 170 and 275 °C in scenario S.2.3, depending on the link. The maximum temperatures in scenario I.2.2 range from 120 to 370°C. For this fire scenario, the differences in temperature rise are more pronounced.

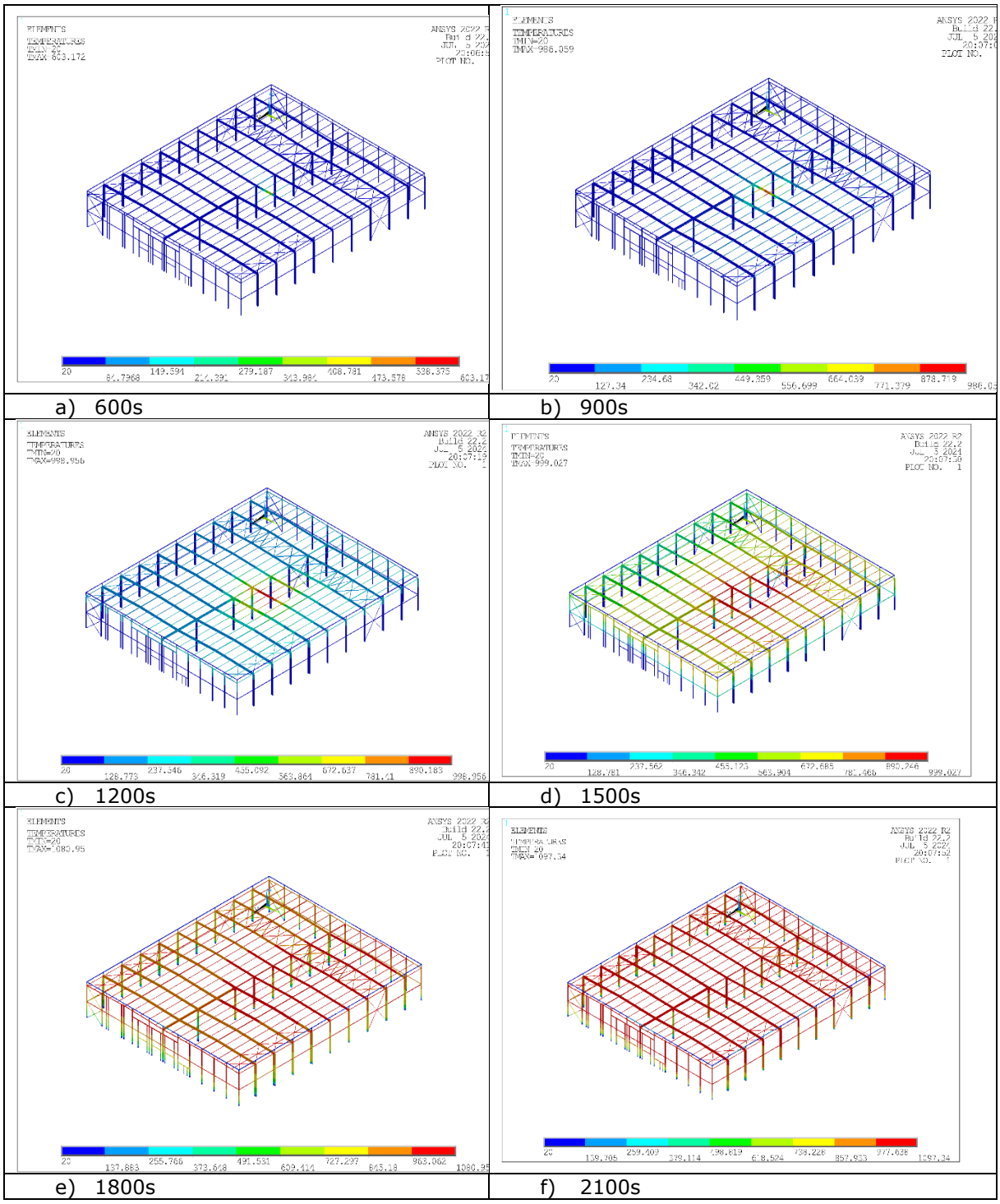

a) 600s b) 900s

c) 1200s d) 1500s

e) 1800s f) 2100s

Figure 4.8: Heating of the steel structure of reference building No. 2 at different fire exposure times in scenario W.2.3 (°C)

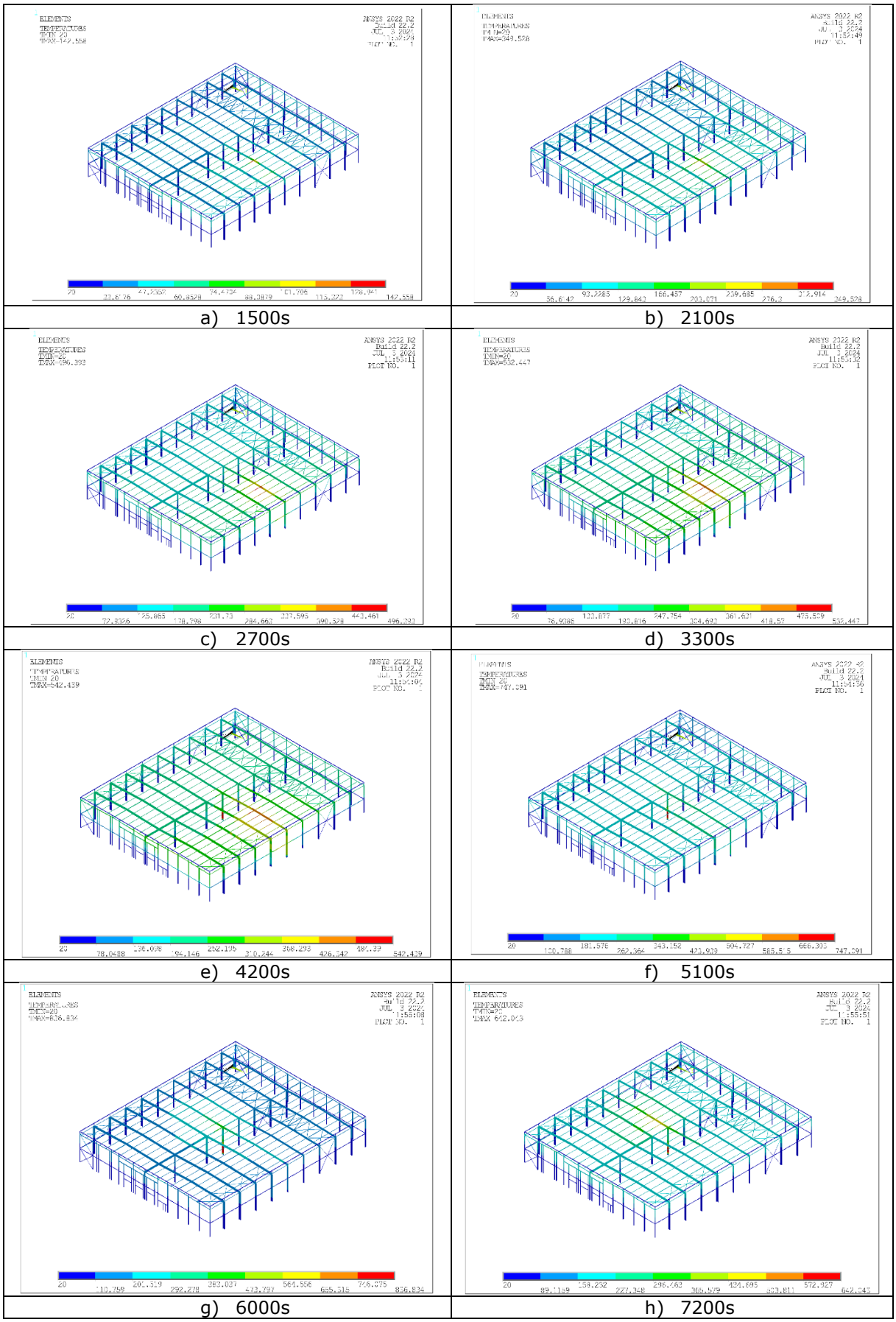

a) 1500s | b) 2100s

c) 2700s | d) 3300s

e) 4200s | f) 5100s

g) 6000s | h) 7200s

Figure 4.9: Heating of the steel structure of reference building No. 2 at different fire exposure times in scenario S.2.3 (°C)

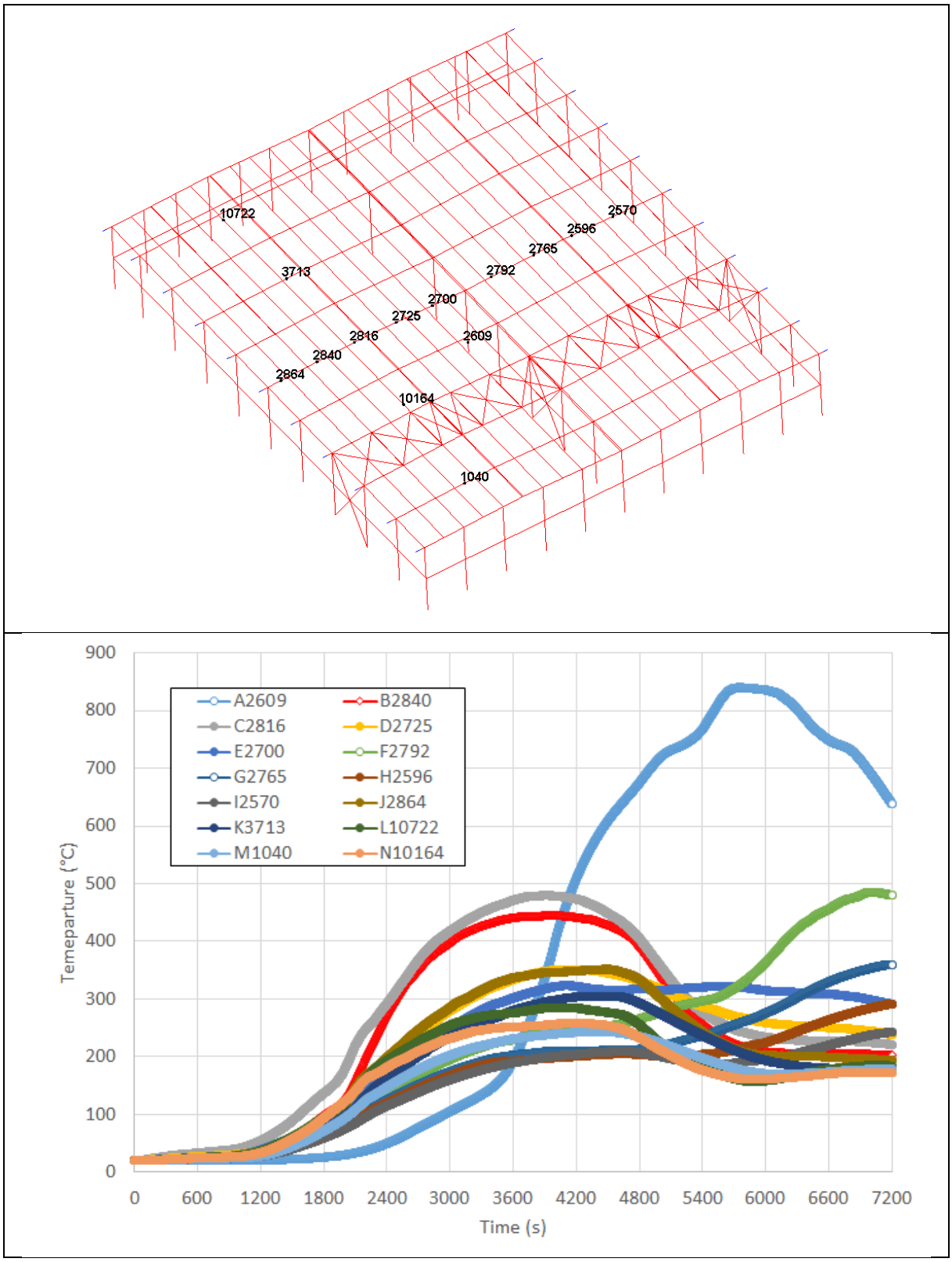

Figure 4.10: Temperature-histories in some points of the steel structure in scenario S.2.3

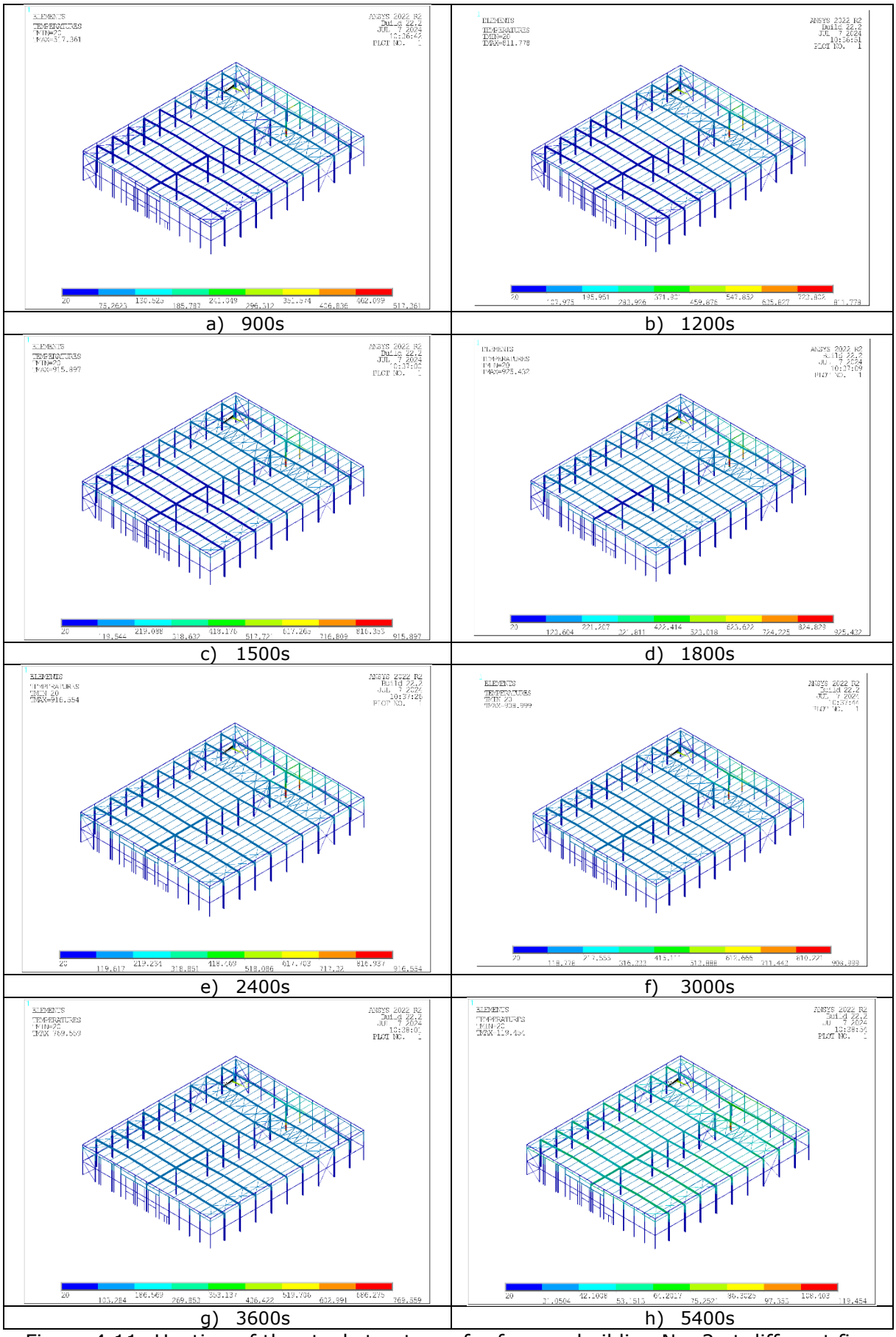

a) 900s | b) 1200s

c) 1500s | d) 1800s

e) 2400s | f) 3000s

g) 3600s | h) 5400s

Figure 4.11: Heating of the steel structure of reference building No. 2 at different fire exposure times in scenario I.2.2 (°C)

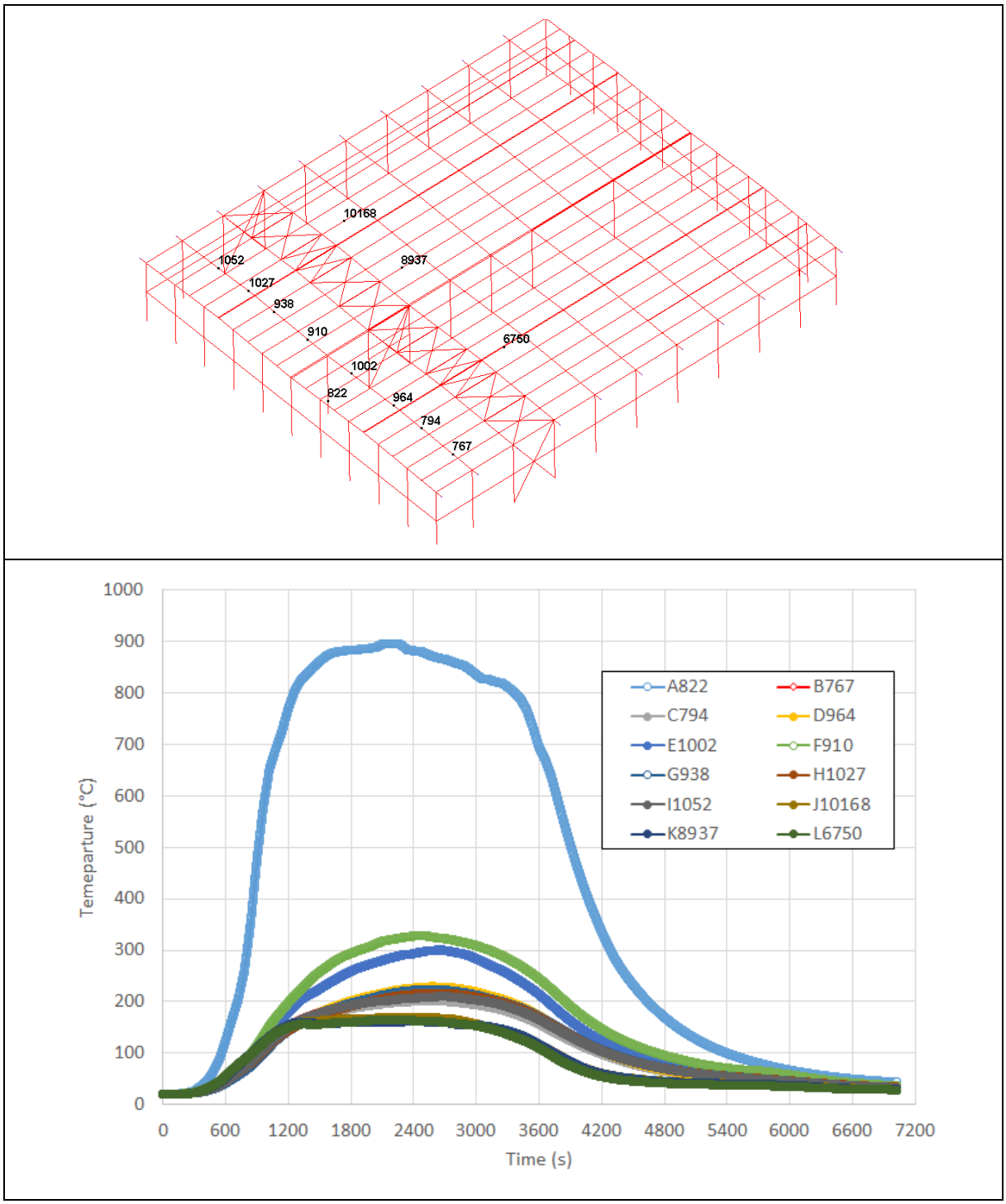

Figure 4.12: Temperature-histories in some points of the steel structure in scenario I.2.2

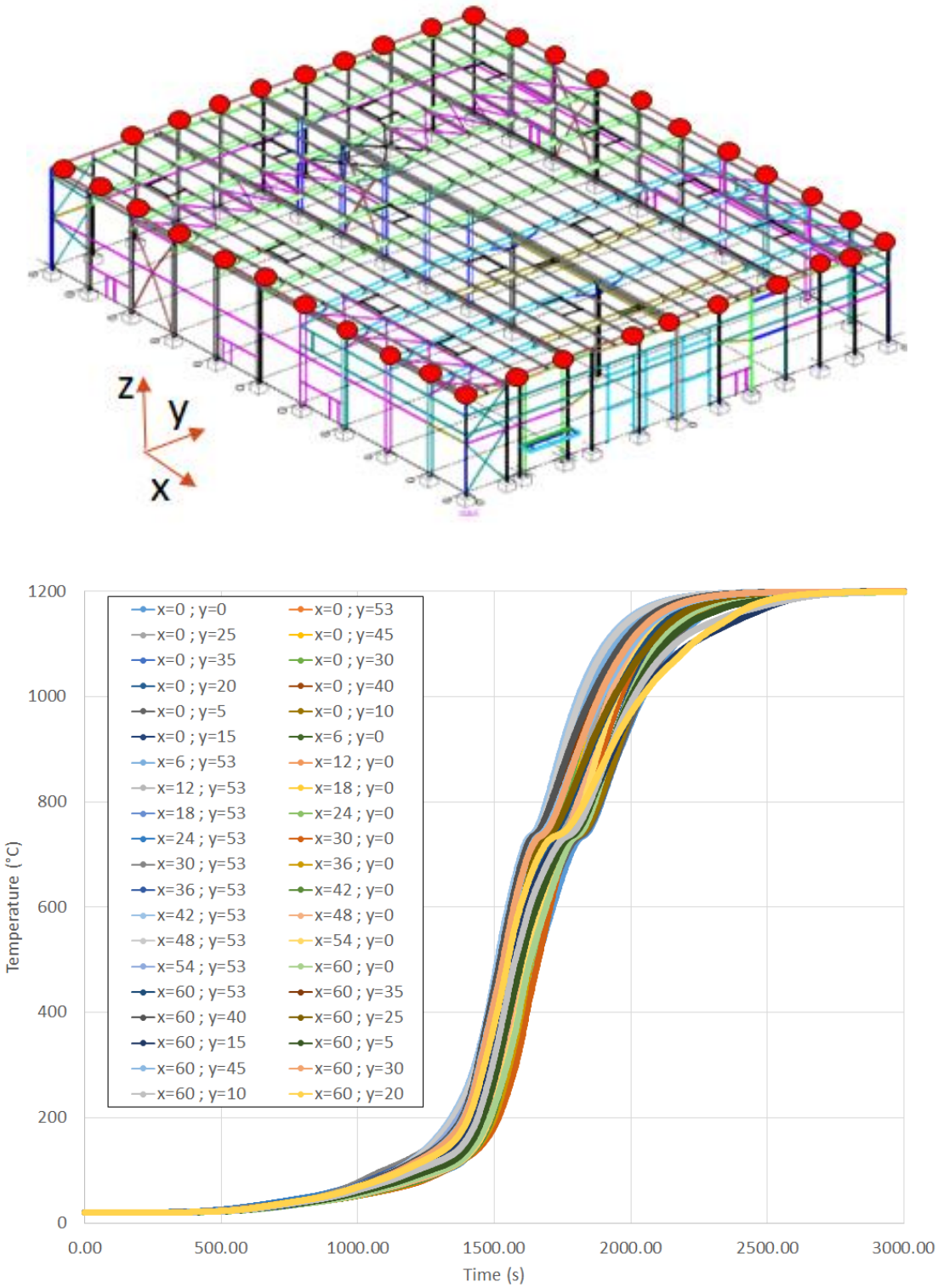

Figure 4.13: Temperature rises predicted in the aluminium bolts of fusible links located in the reference building N°2 for the fire scenario W.2.3

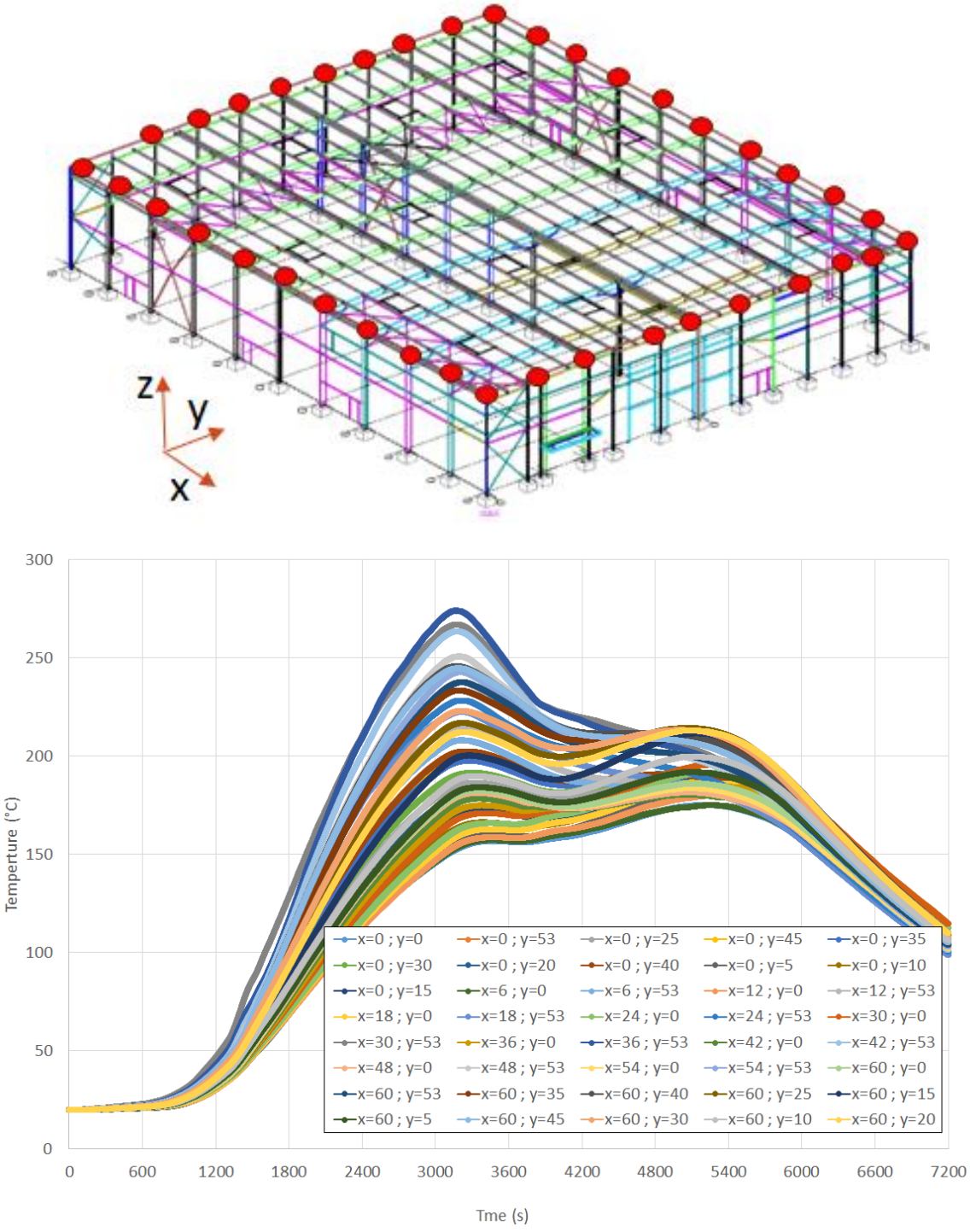

Figure 4.14: Temperature rises predicted in the aluminium bolts of fusible links located in the reference building N°2 for the fire scenario S.2.3

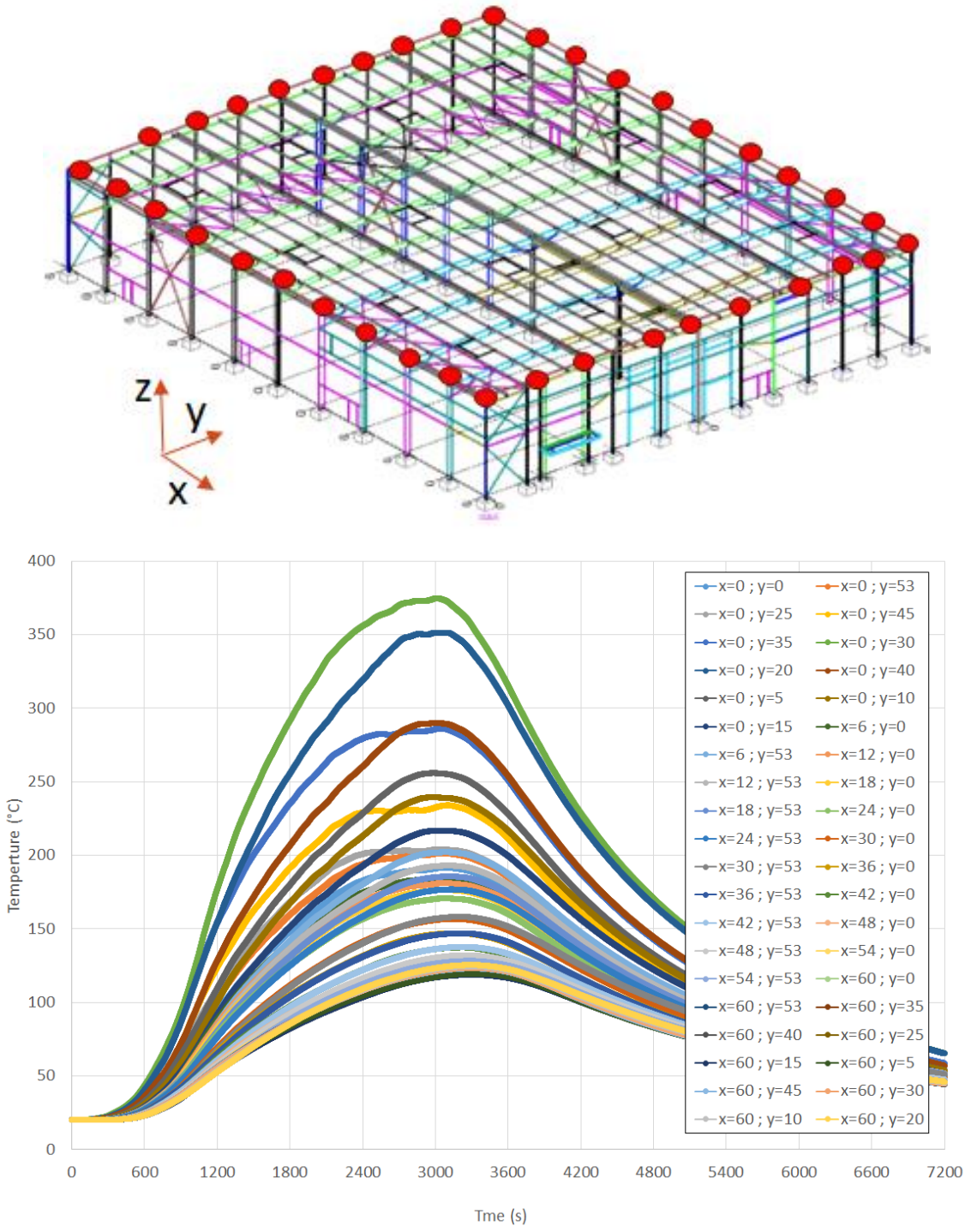

Figure 4.15: Temperature rises predicted in the aluminium bolts of fusible links located in the reference building N°2 for the fire scenario I.2.2

4.3.2 Mechanical results

4.3.2.1 2D structural analyses

The following figures summarise the numerical results obtained from the 2D analyses performed on the most heated steel portal frame for the three selected fire scenarios related to the reference building n°2. It provides: The vertical displacement history at the mid-span of the beams, the horizontal displacement history at the top end of the edge columns, the temperature history in the fusible links (aluminium bolts), the axial forces acting on the fusible links during the fire, and the deformed shape of the steel portal frame at the end of the simulation.

Let's start with the results for the fire scenario W.2.3 given in Figure 4.16. It can be noted that the horizontal displacements predicted at the top of the columns gradually increase towards the outside of the fire compartment during the first few minutes of fire exposure due to the thermal expansion of the beams. Then, the movement reverses and the columns move rapidly inwards due to the combined effect of temperatures, corresponding steel strength losses and applied loads, resulting in the failure of the portal frame beams. Thus, portal frame failure occurs inwards, thereby avoiding the risk of fire wall damage. Regardless of the building configuration (divided into two or three fire compartments), it should be noted that the failure mode of the steel portal frame is similar, and the failure times are very close. However, failure occurs slightly earlier in the case of a building divided into three compartments (see Figure 4.19). This is simply due to the higher compression force developed in the beams, which is caused by axial restraint against thermal elongation induced by cold structures. Some figures illustrate the axial forces generated in the fusible links during the fire scenario. These are compared to the links' load-bearing capacities, considering their traction and compression resistances ($N_{Rd,fi,t}$ and $N_{Rd,fi,c}$). These resistances were calculated using simple design rules developed as part of the project, considering the calculated temperature rise for each fusible link in the fire scenario (which varies from link to link). There are also compared to the design pushing forces. At the beginning of fire exposure, compressive force is developed in the fusible(s) link(s) due to restrained thermal expansion. As the temperature increases, the stiffness and strength of the steel deteriorate. Therefore, the axial compressive force decreases progressively after 18 minutes of fire exposure approximately. After around 20 minutes, the force becomes tensile and catenary action develops. It should be noted that the numerical model predicts failure of the fusible link due to insufficient traction resistance after 22 minutes of fire exposure, as indicated by a sudden drop in force to zero. It should also be noted that the calculated compressive force never exceeds the design value ('SM' in the figures) or the resistance to compression of the fusible link at elevated temperatures ($N_{Rd,fi,c}$) throughout the entire duration of the fire.

Figure 4.19 to Figure 4.21 illustrate the results obtained for scenario S.2.3. As in the previous scenario, the thermal expansion of the portal frame causes the displacement of the edge-of-structure columns to gradually increase towards the outside during the first few minutes of fire exposure. This movement then reverses as the temperature in the portal frame increases progressively. In this scenario, the portal frame partially collapses around 97 minutes due to the buckling of the internal column, which is the structural member that has been most affected by the localised impact of the fire. In contrast, the FE model does not predict the breakage of the fusible links, as the tensile forces due to the cantilever action remain lower than the fusible link's traction resistance throughout the duration of the fire. This can be explained by a stabilisation effect, which is probably the result of a decrease in temperature when the bowed part of the column comes into contact with the ground. This result may seem unrealistic. It is more likely that the tensile forces will be more pronounced, leading to the breakage of the fusible link. As the portal frame is heated to a lesser extent than in the first scenario, the compressive force calculated in the fusible link is slightly lower. At no point during the fire does it exceed the design value ('SM' in the figures) or the resistance to compression at elevated temperatures ($N_{Rd,fi,c}$).

The same results are obtained with the fire scenario I.2.2 (see Figure 4.22 to Figure 4.24). The portal frame collapses after approximately twenty minutes following the failure of the internal column. However, in contrast to the previous scenario, the numerical model predicts failure of the fusible link(s) due to insufficient traction resistance after 32 to 38 minutes of fire exposure, depending on whether the building is divided into two or three fire compartments. This is indicated by a sudden drop in force to zero.

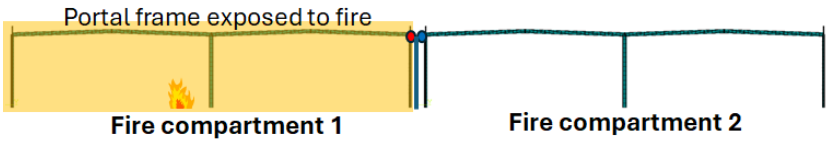

a) Studied building configuration

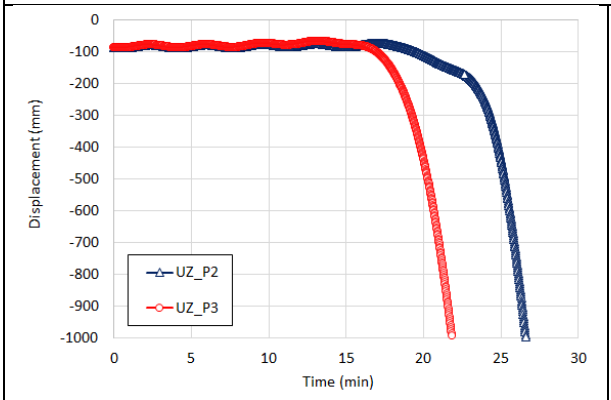

b) Vertical displacement at beams mid-span

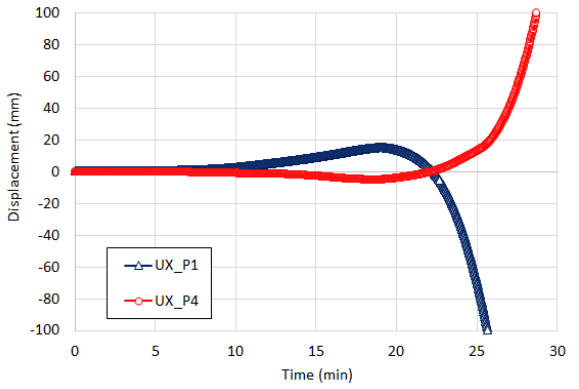

c) horizontal displacement at the top of end columns of steel portal frame

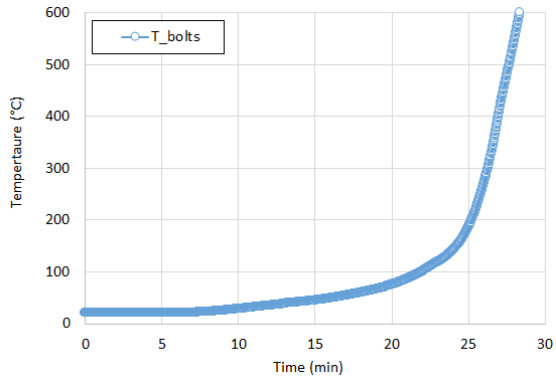

d) Temperature rise in aluminium bolts

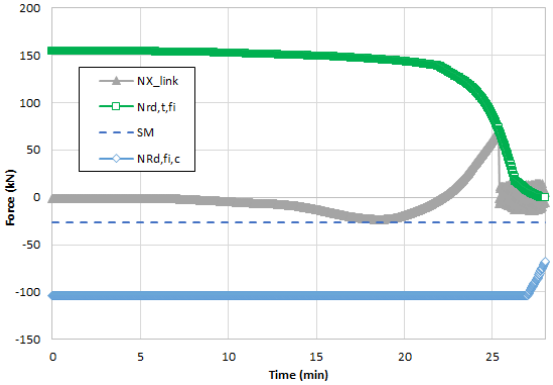

e) Axial force acting in the fusible link

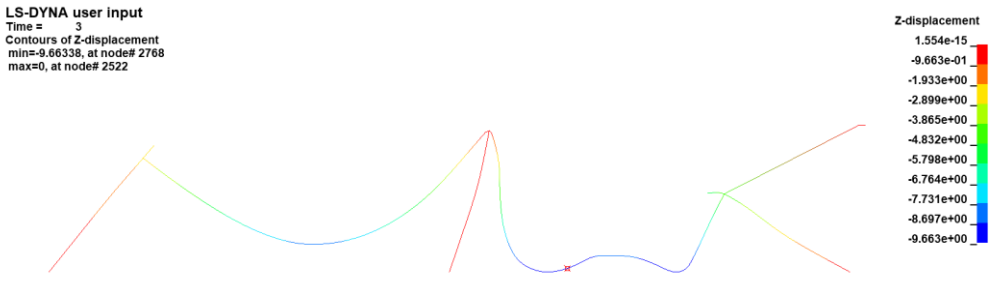

f) Deformed state of the steel portal frame at simulation end

Figure 4.16: Results of the study case n°1a

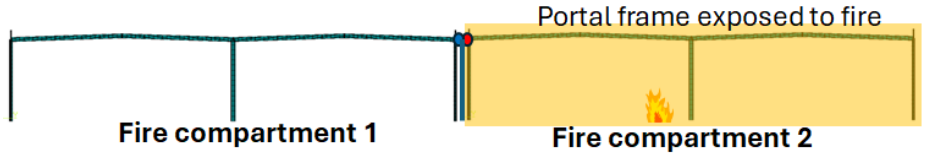

a) Studied building configuration

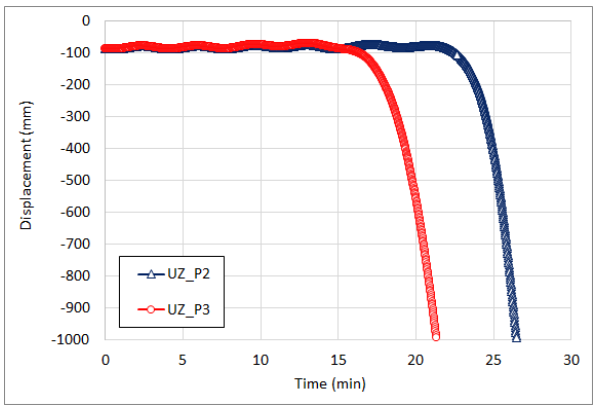

b) Vertical displacement at beams mid-span

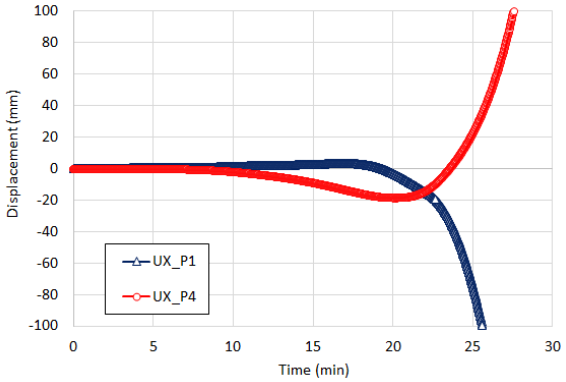

c) horizontal displacement at the top of end columns of steel portal frame

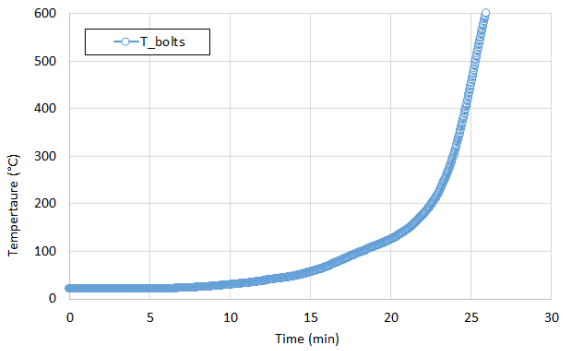

d) Temperature rise in aluminium bolts

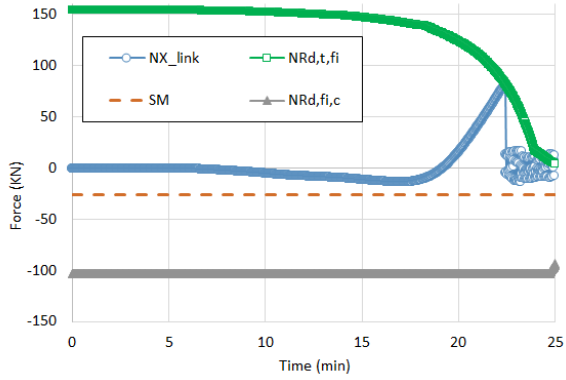

e) Axial force acting in the fusible link

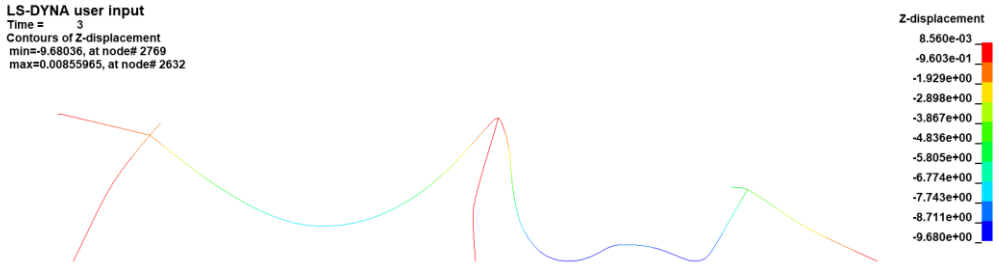

f) Deformed state of the steel portal frame at simulation end

Figure 4.17: Results of the study case n°1b

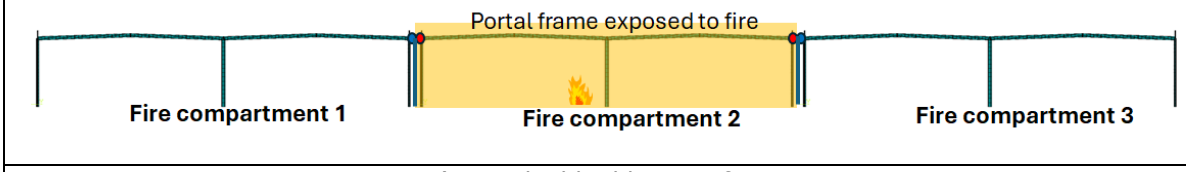

a) Studied building configuration

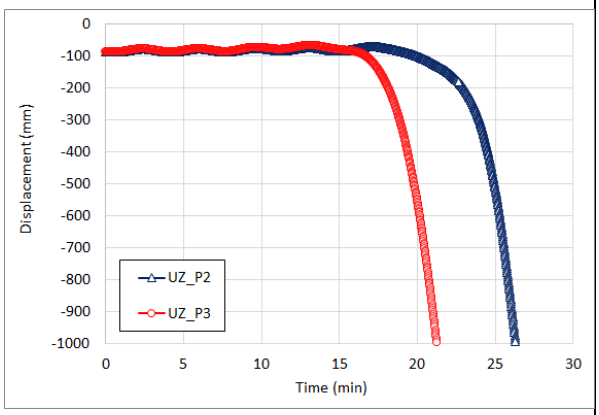

b) Vertical displacement at beams mid-span

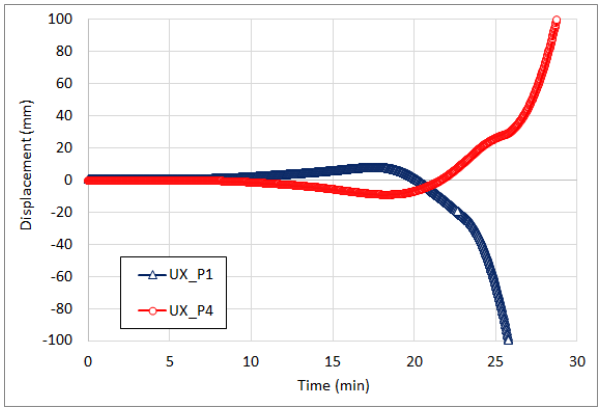

c) horizontal displacement at the top of end columns of steel portal frame

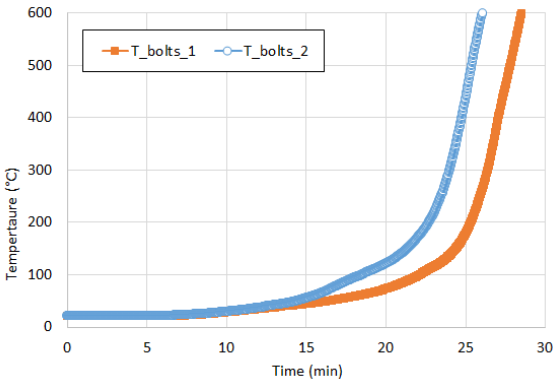

d) Temperature rise in aluminium bolts

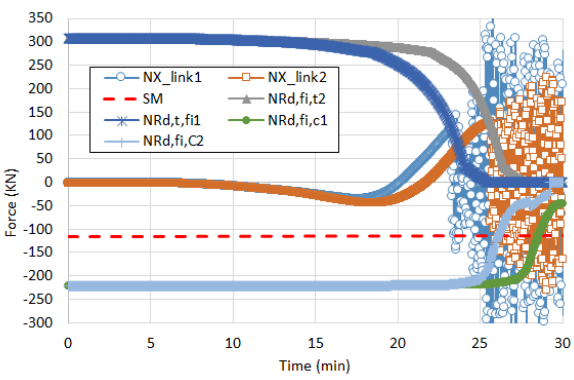

e) Axial force acting in the fusible link

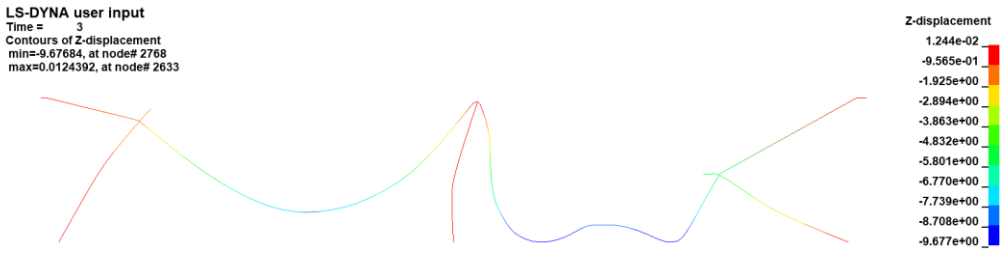

f) Deformed state of the steel portal frame at simulation end

Figure 4.18: Results of the study case n°2

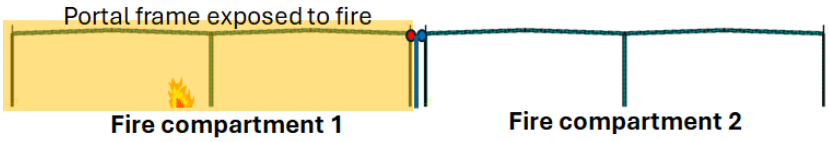

a) Studied building configuration

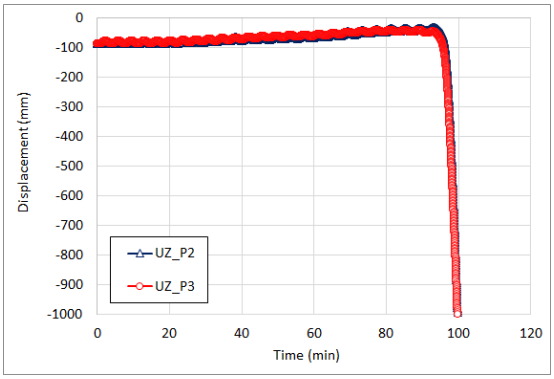

b) Vertical displacement at beams mid-span

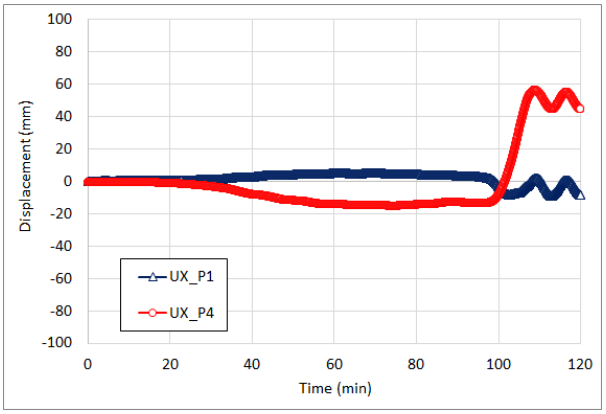

c) horizontal displacement at the top of end columns of steel portal frame

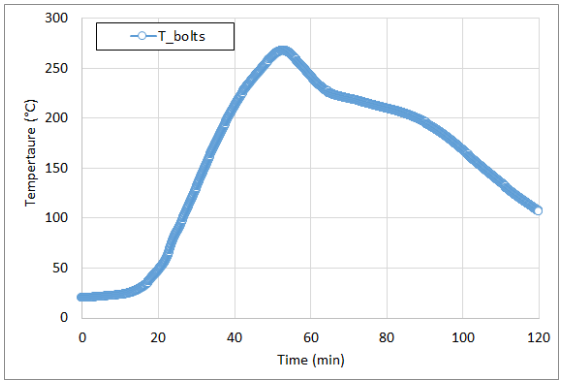

d) Temperature rise in aluminium bolts

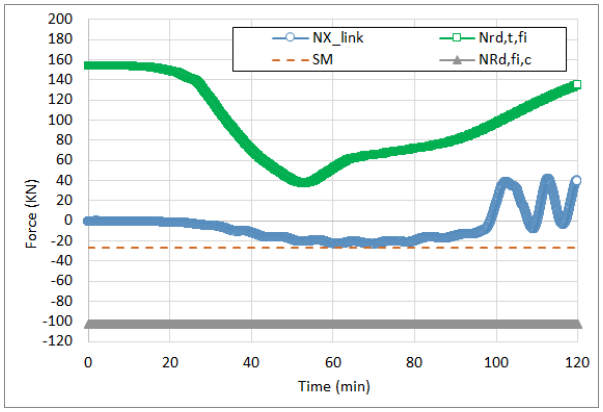

e) Axial force acting in the fusible link

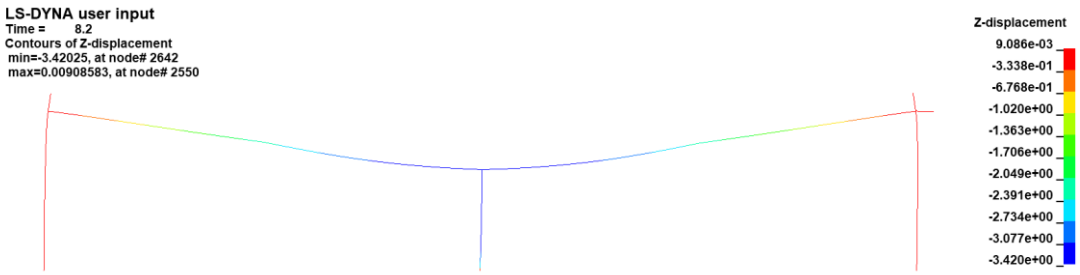

f) Deformed state of the steel portal frame at simulation end

Figure 4.19: Results of the study case n°5a

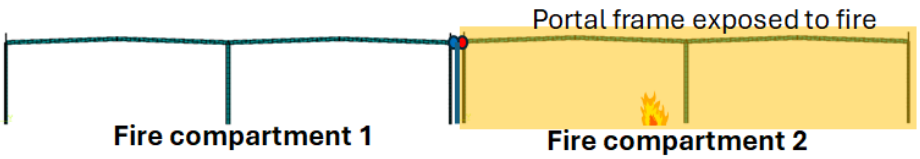

a) Studied building configuration

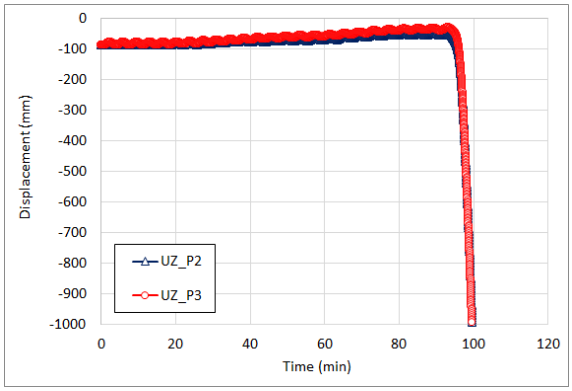

b) Vertical displacement at beams mid-span

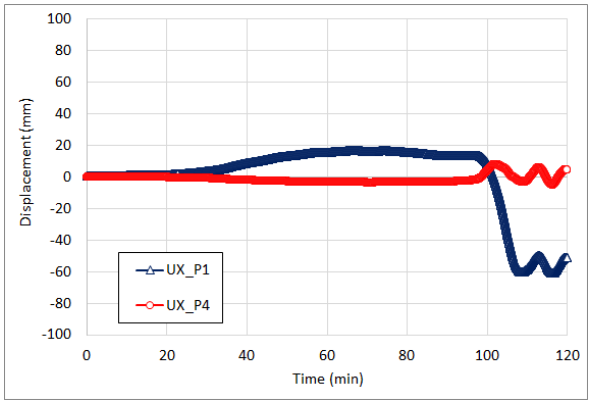

c) horizontal displacement at the top of end columns of steel portal frame

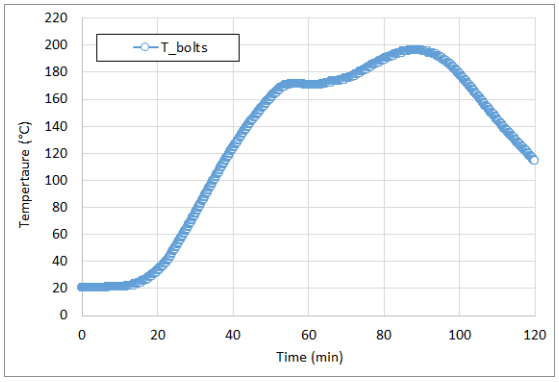

d) Temperature rise in aluminium bolts

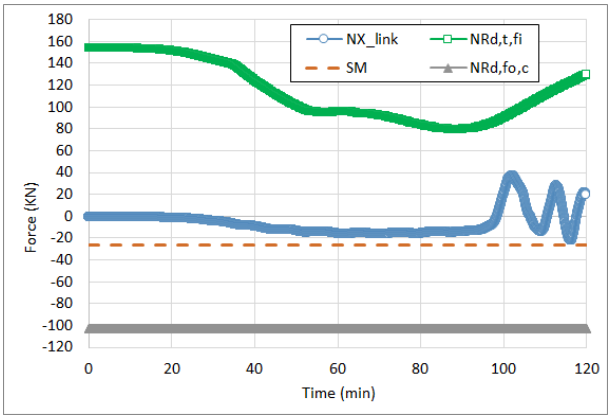

e) Axial force acting in the fusible link

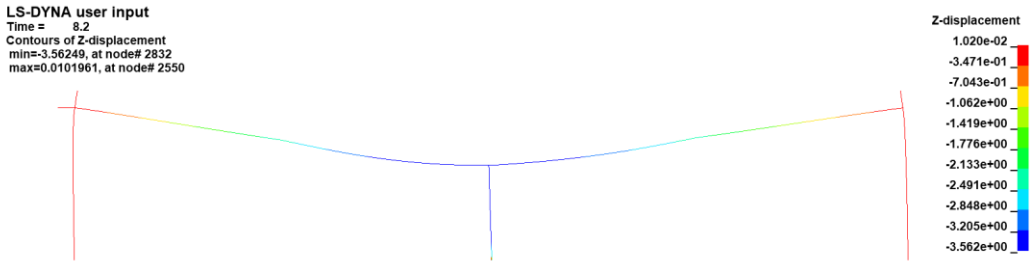

f) Deformed state of the steel portal frame at simulation end

Figure 4.20: Results of the study case n°5b

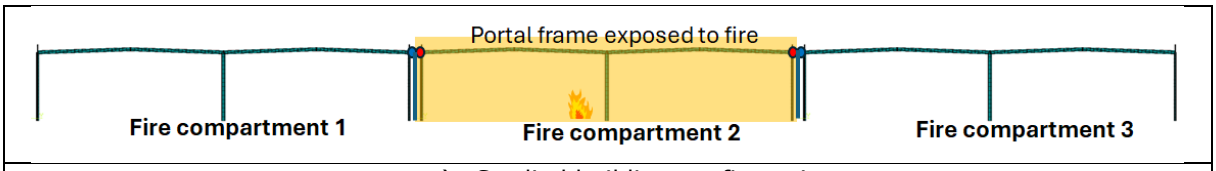

a) Studied building configuration

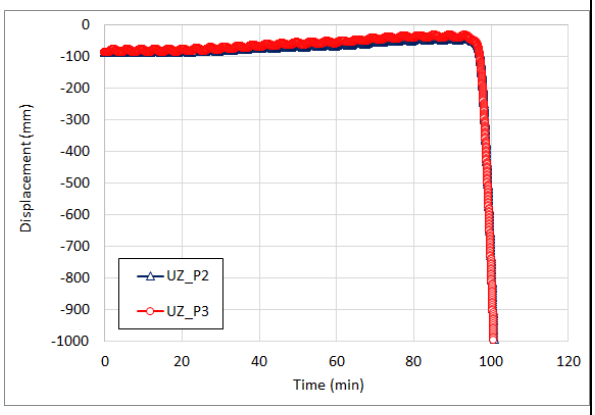

b) Vertical displacement at beams mid-span

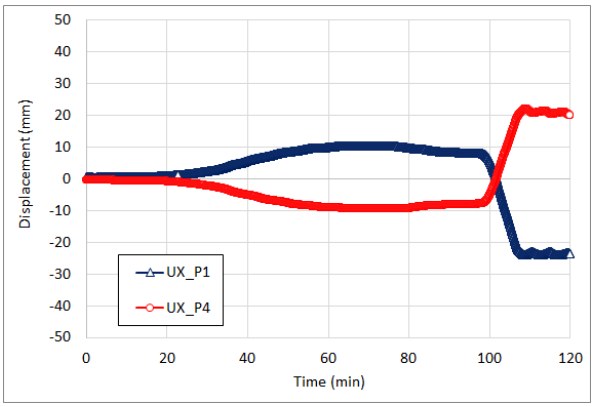

c) horizontal displacement at the top of end columns of steel portal frame

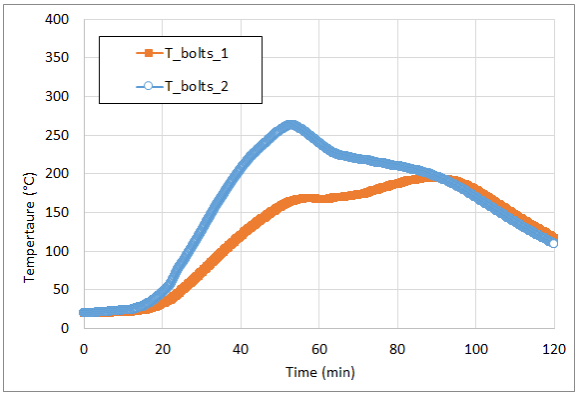

d) Temperature rise in aluminium bolts

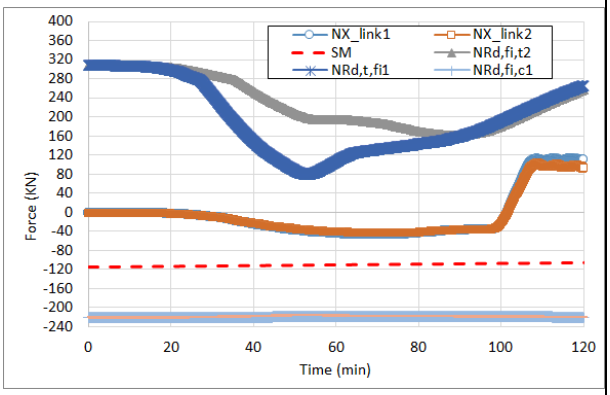

e) Axial force acting in the fusible link

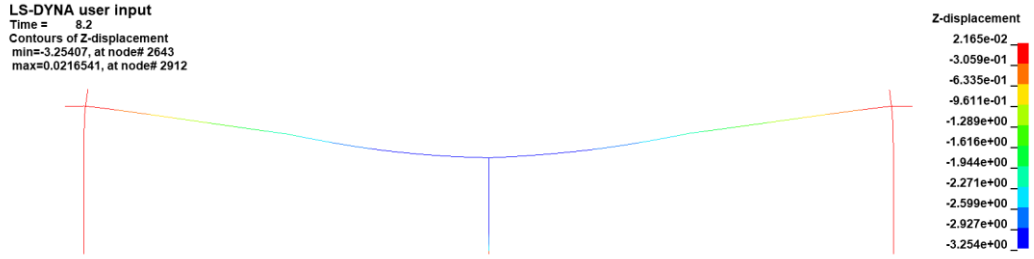

f) Deformed state of the steel portal frame at simulation end

Figure 4.21: Results of the study case n°6

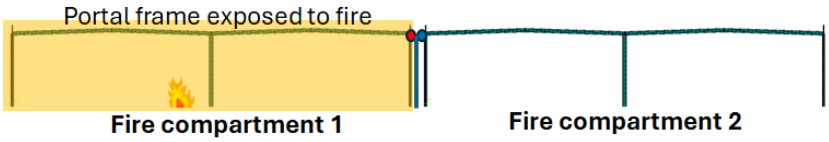

a) Studied building configuration

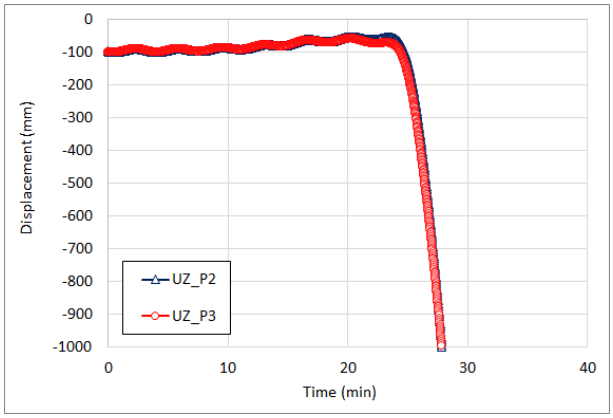

b) Vertical displacement at beams mid-span

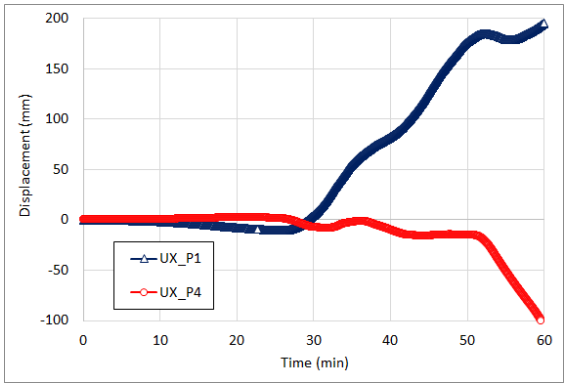

c) horizontal displacement at the top of end columns of steel portal frame

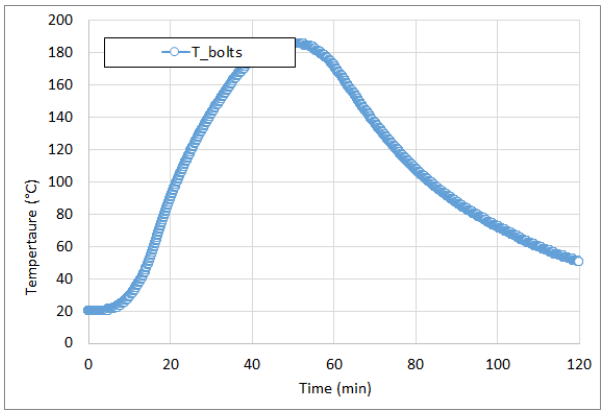

d) Temperature rise in aluminium bolts

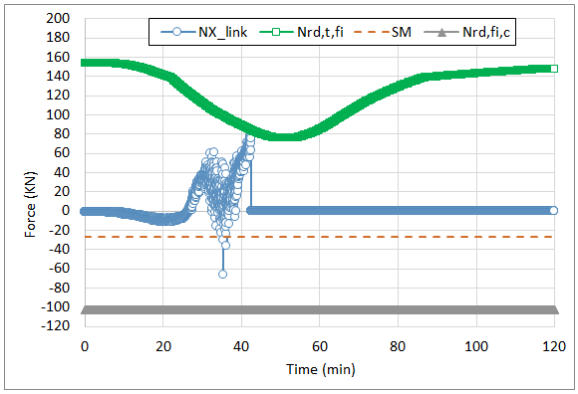

e) Axial force acting in the fusible link

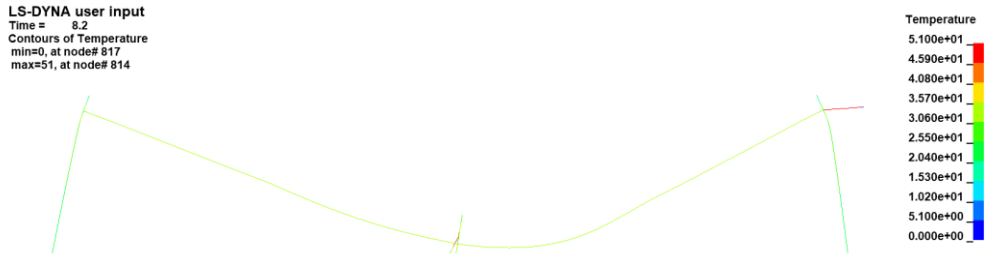

f) Deformed state of the steel portal frame at simulation end

Figure 4.22: Results of the study case n°4a

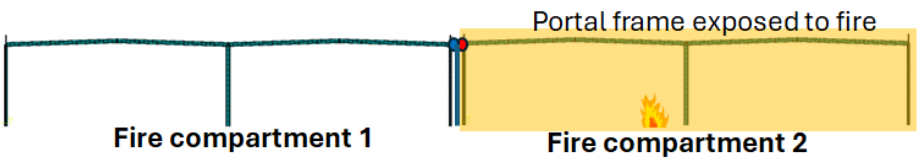

a) Studied building configuration

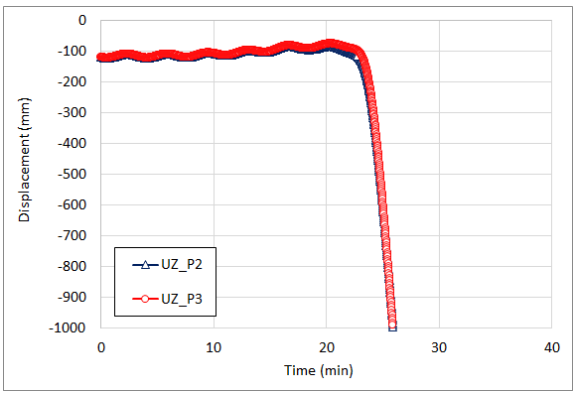

b) Vertical displacement at beams mid-span

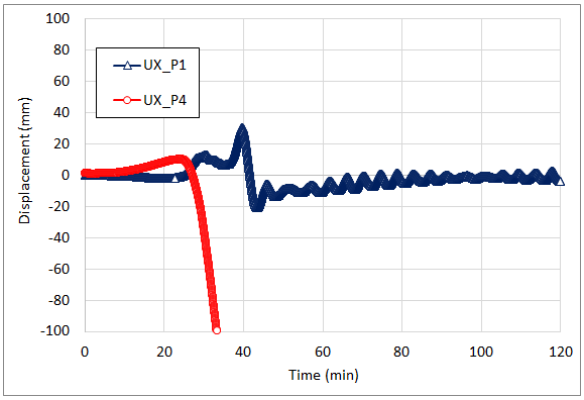

c) horizontal displacement at the top of end columns of steel portal frame

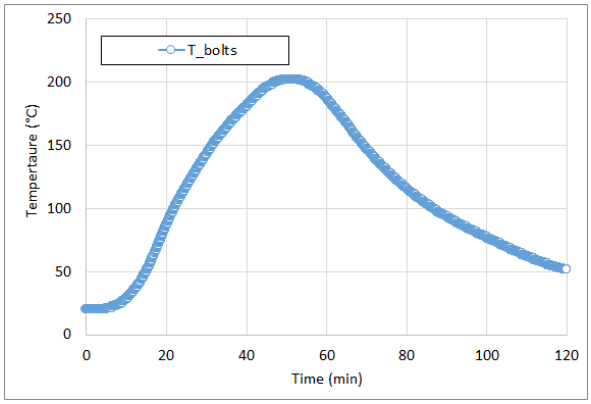

d) Temperature rise in aluminium bolts

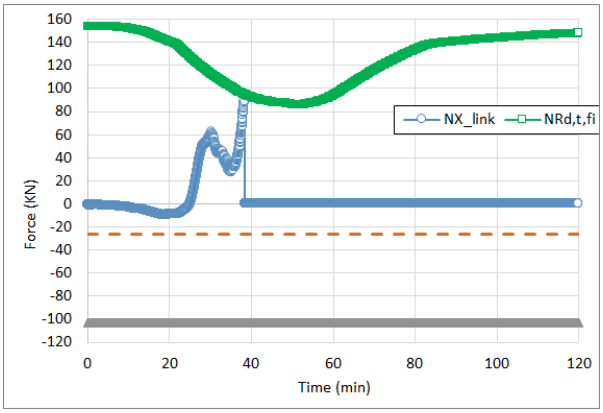

e) Axial force acting in the fusible link

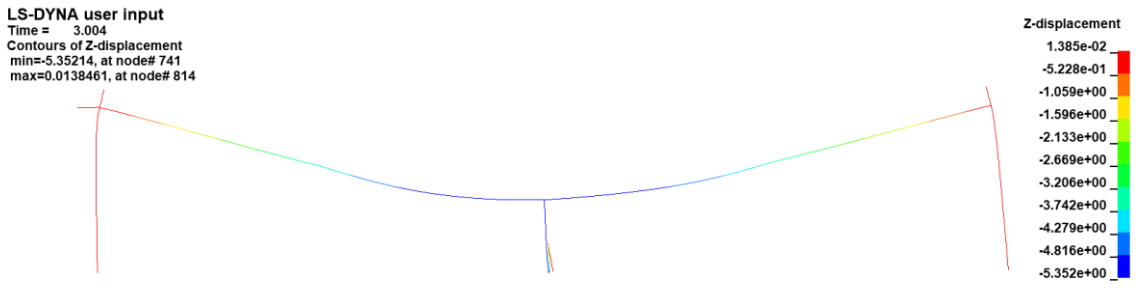

f) Deformed state of the steel portal frame at simulation end

Figure 4.23: Results of the study case n°4b

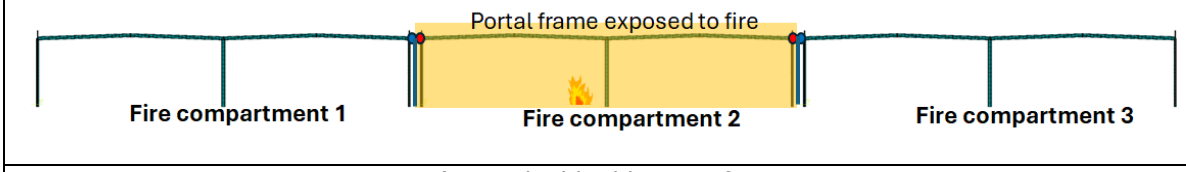

a) Studied building configuration

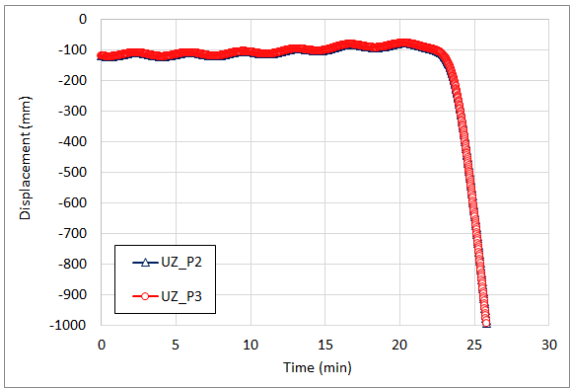

b) Vertical displacement at beams mid-span

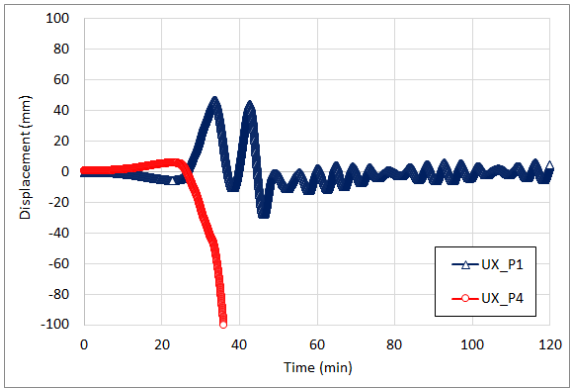

c) horizontal displacement at the top of end columns of steel portal frame

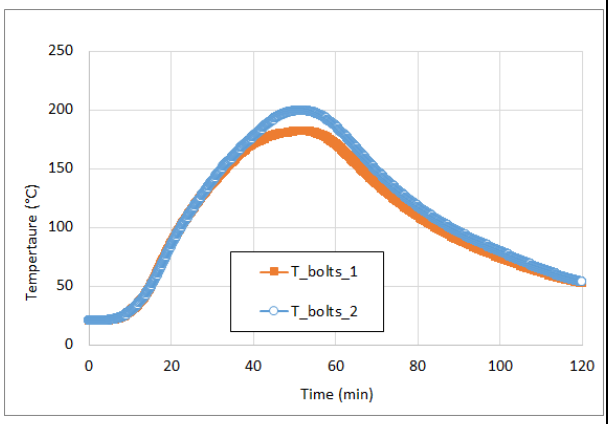

d) Temperature rise in aluminium bolts

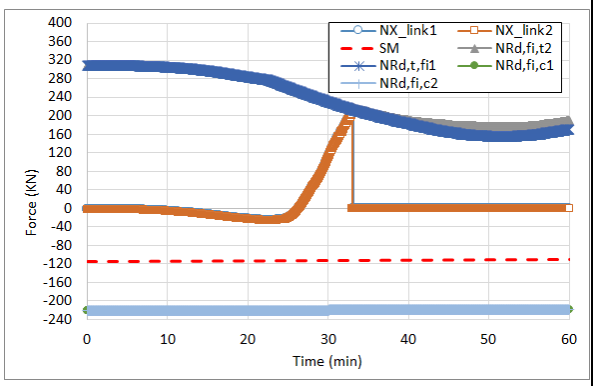

e) Axial force acting in the fusible link

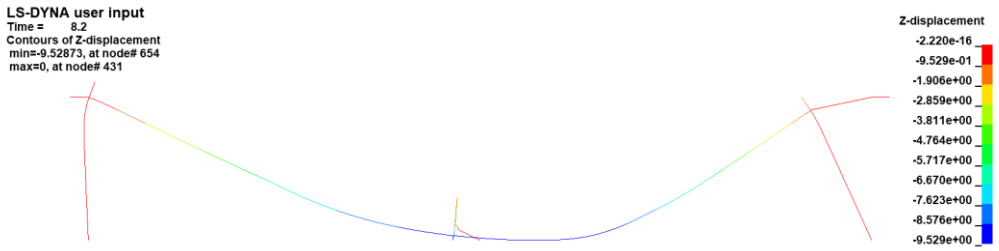

f) Deformed state of the steel portal frame at simulation end

Figure 4.24: Results of the study case n°5

4.3.2.2 3D structural analyses

The sections summarise the numerical results obtained from the 3D analyses performed on the entire steel structure for each of the defined study cases. The following are provided: the horizontal displacement history at three-quarters of the height of the columns with fusible links; the temperature history in the fusible links (aluminium bolts); the axial forces acting on the fusible links during the fire; and the deformed shape of the steel structure at different times during fire exposure.

4.3.2.2.1 Study cases 1 to 4

These case studies relate to buildings under fire scenario W.2.3 divided into two or three fire compartments, which are separated by fire walls that are either perpendicular or parallel to the steel portal frames. The steel structure of each fire compartment corresponds to that of reference building No. 2.

The simulation results for study Case n°1 can be found in Figure 4.25 and Figure 4.26. Figure 4.25 shows the deformation of the structure at different exposure times to fire. It illustrates the failure mode of the steel structure. The first signs of members failure appear in the roof structure (beams and purlins) around 20 minutes, close to the initial fire source. The failures then spread progressively to adjacent structural members as the heated part of the structure spread (as illustrated in Figure 4.8). This finally led to the structure's complete collapse after 30 minutes of fire exposure. At this point, most of the roof structure will have reached a temperature of at least 800°C. The collapse of the structure occurs towards the inside of the fire compartment. Figure 4.26b shows the axial forces developed in the fusible links during the fire. These are compared to the load-bearing capacities of the links, considering both their traction and compression resistances. These resistances were calculated using simple design rules developed as part of the project, considering the temperature rise calculated for each fusible link in the considered fire scenario (which differs from one link to another). As with the 2D analyses, compressive force is developed in fusible links due to restrained thermal expansion at the beginning of fire exposure. As the temperature increases, the stiffness and strength of the steel deteriorate. Consequently, the axial compressive forces decrease progressively, and the roof structure's members change from a combined compression and bending state to a simple tensile state. As successive members fail, catenary action develops throughout the structure and the axial force becomes tensile in each fusible link. The appearance of tensile forces in the fusible links occurs at different times, depending on the progression of the area of the structure affected by the fire and the collapse of the roof members. The first fusible link subjected to tensile forces was the one located at the end of the steel portal frame closest to the fire's source, i.e. the link n°6. This occurred around 17 minutes of exposure to the fire. Then, tensile forces progressively appear in the other fusible links until the structure completely collapses. The resistance to traction of fusible links decreases rapidly after 23 minutes of exposure to fire due to the high temperature rise in aluminium bolts (see Figure 4.26a). Consequently, the numerical model predicts failure of all fusible links due to insufficient traction resistance, as indicated by a sudden drop in forces to zero. It should also be noted that the maximum predicted compressive force in the fusible links is around 24.5 kN, which is slightly lower than the design value of 26.7 kN. Moreover, the fusible link's resistance to compression at elevated temperatures ($N_{Rd,fi,c}$) is never reached throughout the entire duration of the fire. Figure 4.26c shows the predicted horizontal displacement at three-quarters of the height of the columns associated with the fusible links in the plane of the portal frames. Negative values indicate movement towards the interior of the fire compartment. The displacement curves demonstrate the outward collapse of the steel structure. They also demonstrate that the displacements are sufficiently small as to not compromise the integrity of the fire wall.

The Figure 4.27 and Figure 4.28 summarise the simulation results obtained for case study n°2, in which fusible links are attached to the edge columns of the steel portal frames on both sides of the steel structure. The same observations regarding structural behaviour can be made as for the previous case. It should be noted that the numerical model predicts the failure of all fusible links due to insufficient traction resistance, as indicated by the sudden drop in forces to zero in Figure 4.28b. As the steel structure collapsed, the fusible links broke one after the other. Failure of the links occurred with a time lag between the two sides of the building, which can be explained by the links heating up more rapidly on the side closest to the initial fire source than on the other side (as illustrated in Figure 4.28a). It should also be noted that the maximum predicted compressive force in the fusible links is around 110 kN, which is slightly lower than the design value of 115 kN. Furthermore, the fusible links' resistance to compression at elevated temperatures (NRd,fi,c) is never reached throughout the entire fire duration.

The simulation results for the study case n°3 are reported in Figure 4.29 an Figure 4.30. In this case, there are fusible links on one side of the steel structure, which are attached to steel gable columns. The structure's behaviour remains unchanged, and the model predicts the failure of all the fusible links fail due to insufficient traction resistance at high temperatures. It should be noted that the initial traction resistance of the links is much lower in this case than when the wall is perpendicular to the portal frames. This resistance is provided by two M16 aluminium bolts only. It can also be noted that the maximum predicted compressive force in the fusible links is around 22 kN, which is slightly lower than the design value of 26.7 kN. Furthermore, the fusible links' resistance to compression at elevated temperatures ($N_{Rd,fi,c}$) is never reached throughout the duration of the considered fire scenario.

For study case n°4, where fusible links are attached to steel gable columns on both sides of the steel structure, the numerical model also predicts failure of the links (see Figure 4.31 and Figure 4.32). As in the previous three cases, the maximum predicted compressive force in the fusible links is slightly lower than the design value used for their design. Furthermore, the resistance of the fusible links to compression at elevated temperatures is never reached throughout the entire duration of the fire.

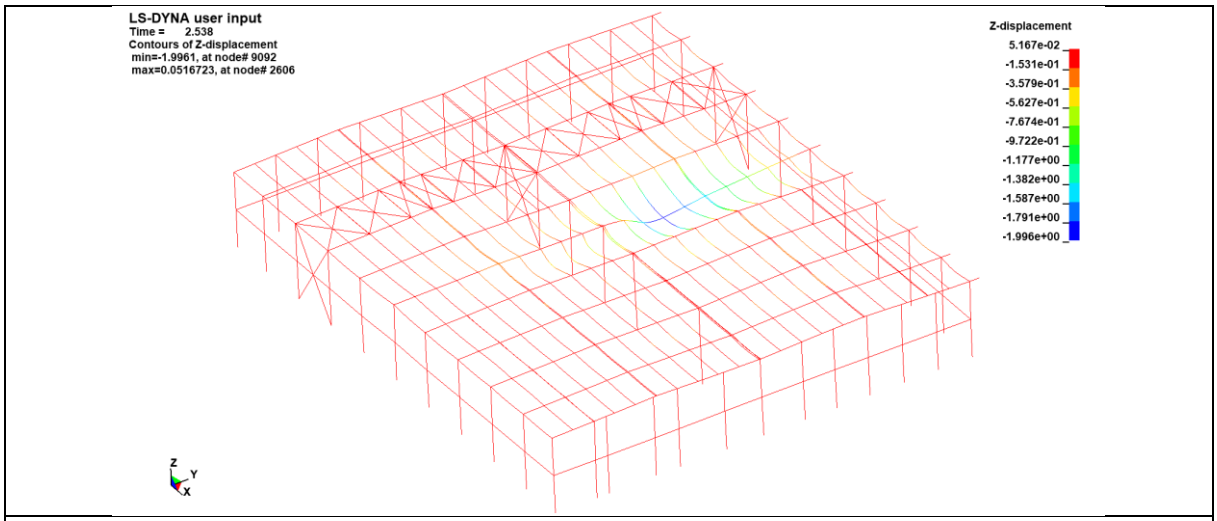

a) Deformed state after 20.3 minutes of exposure to fire

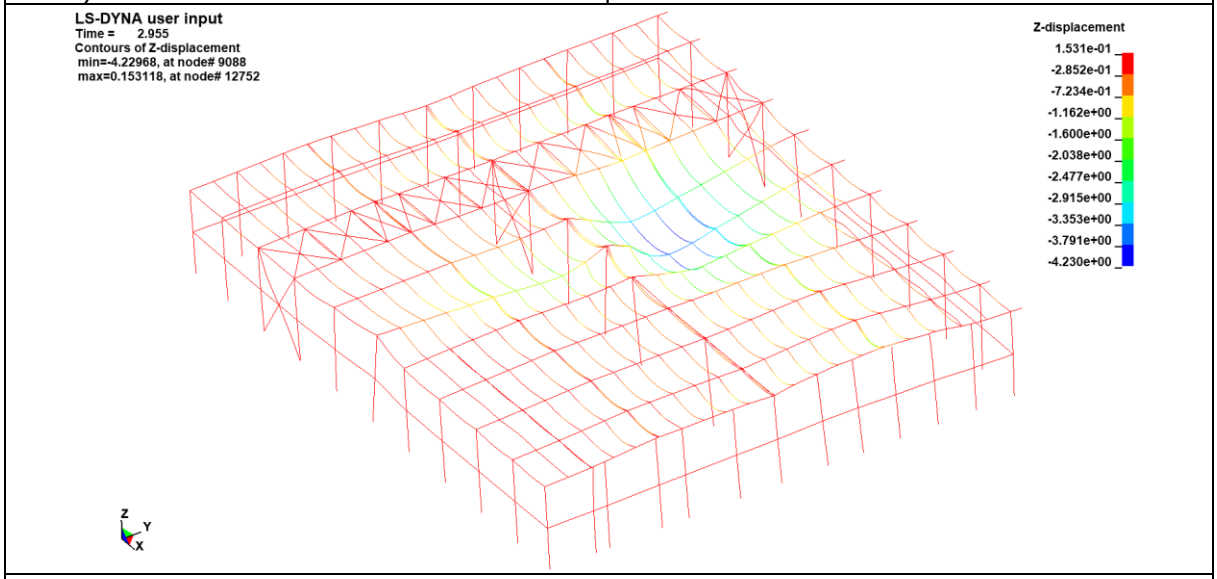

b) Deformed state after 24.5 minutes of exposure to fire

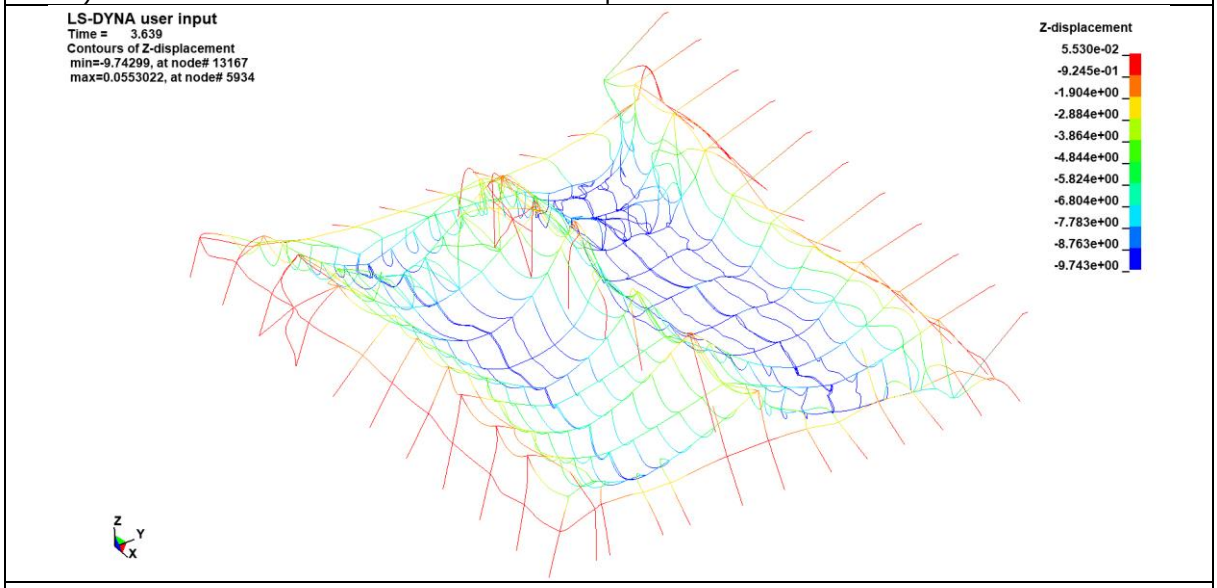

c) Deformed state after 31.4 minutes of exposure to fire

Figure 4.25: Deformed stated predicted for the fire exposed steel structure of the study case n°1

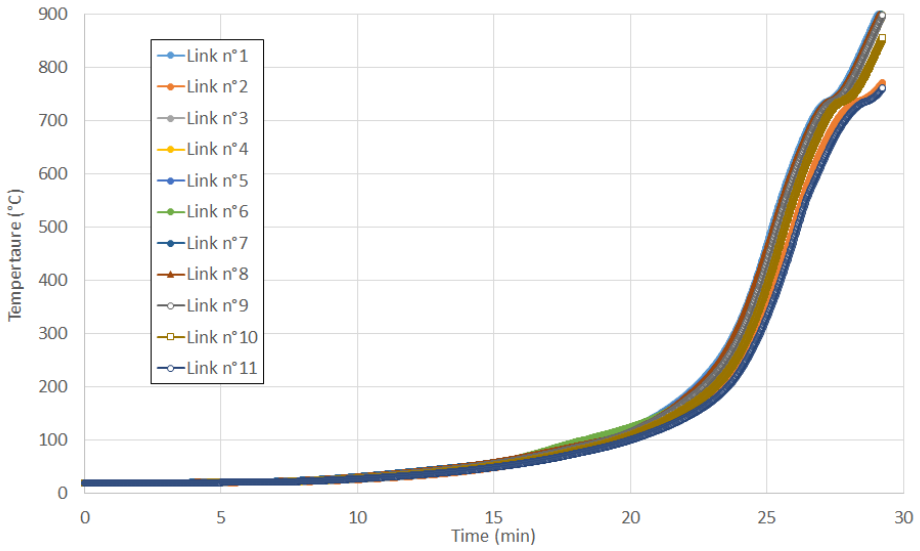

a) Temperature rise in aluminium bolts

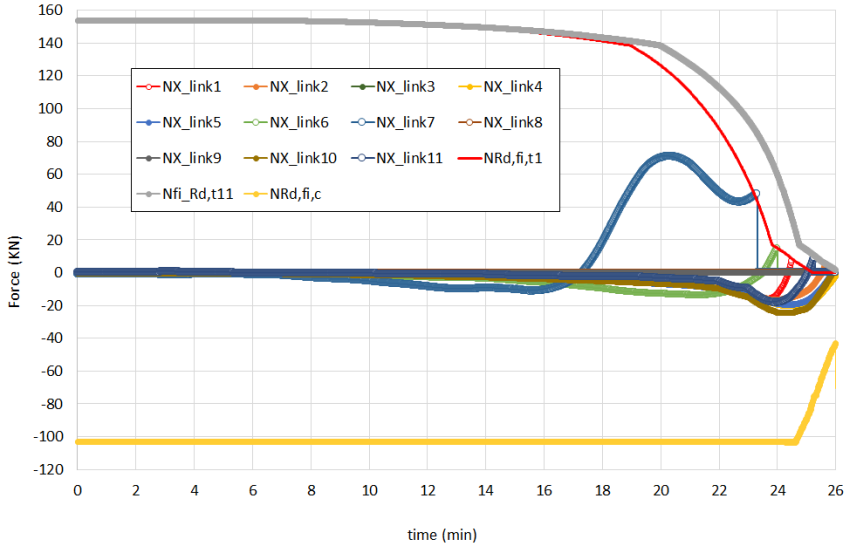

b) Axial force acting in the fusible links

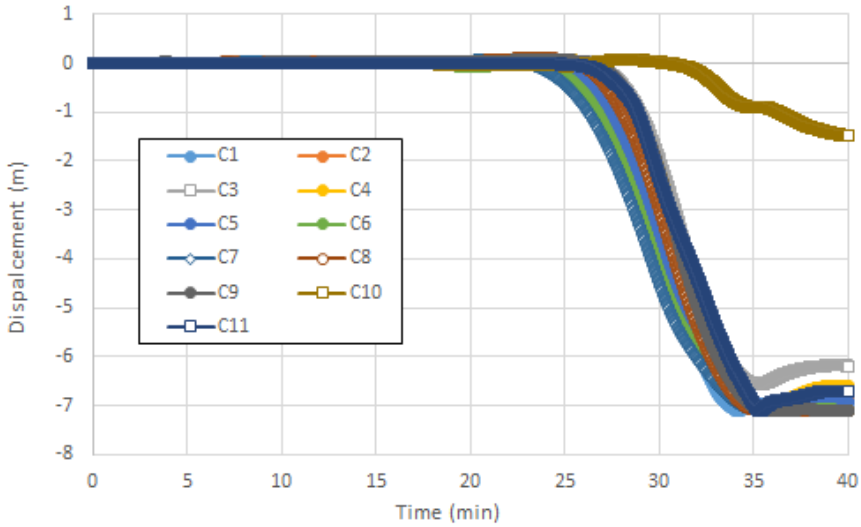

c) Horizontal displacement at three quarter of the height of the columns with fusible links

Figure 4.26: Temperatures, forces and displacements predicted for the study case n°1

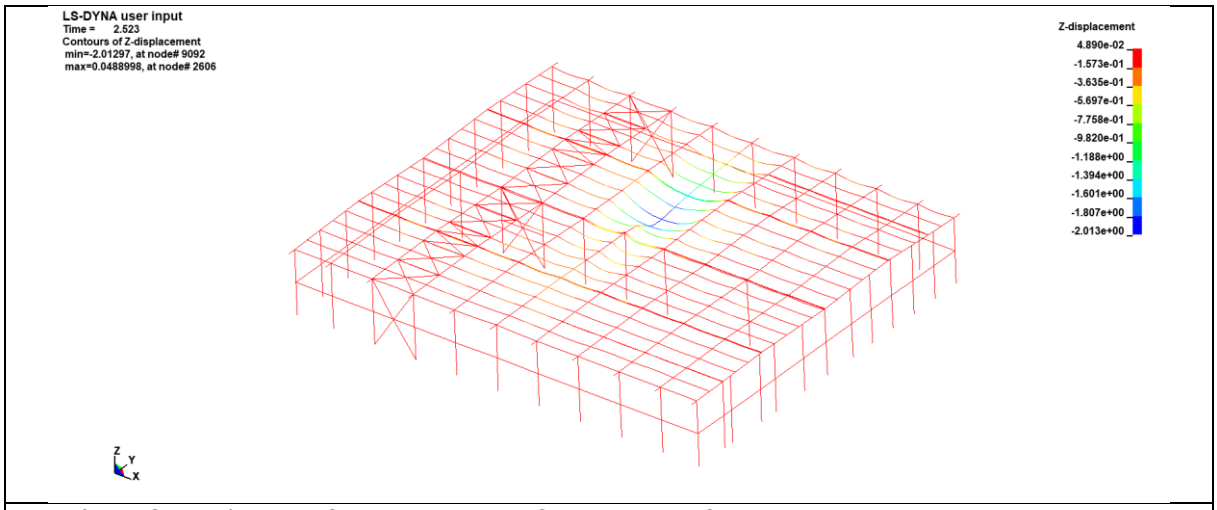

a) Deformed state after 20 minutes of exposure to fire

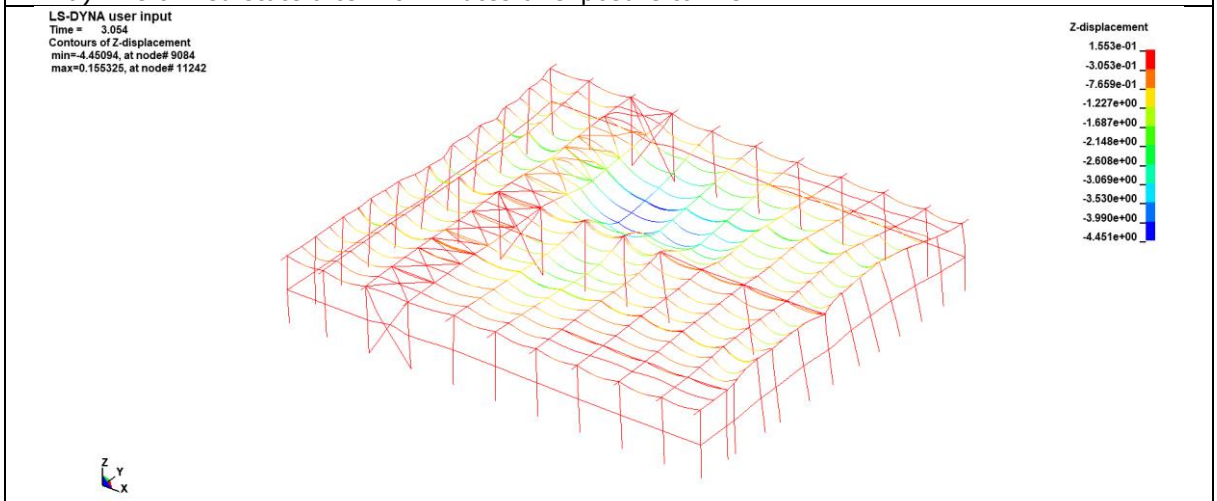

b) Deformed state after 25 minutes of exposure to fire

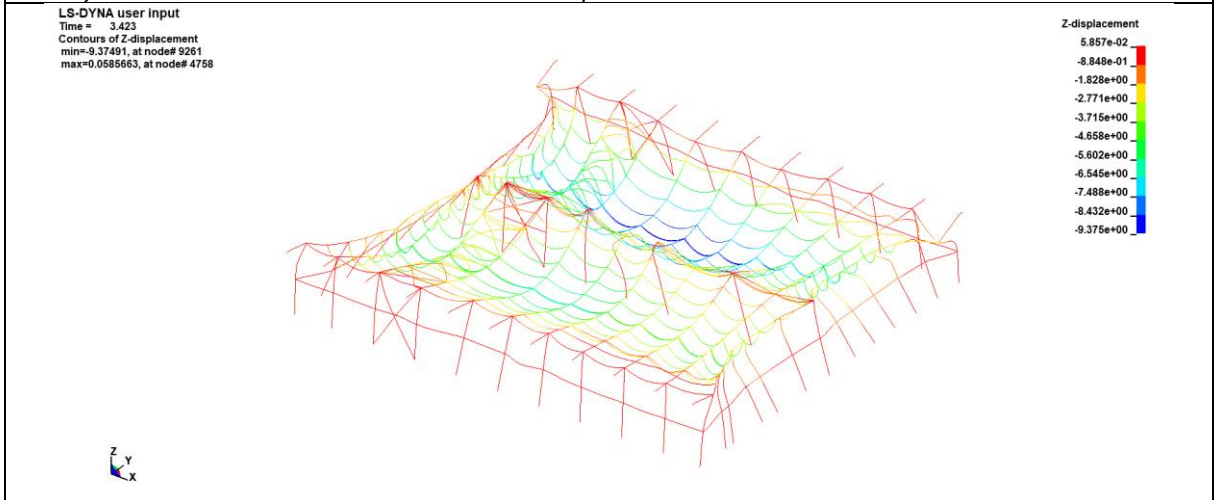

c) Deformed state after 29 minutes of exposure to fire

Figure 4.27: Deformed stated predicted for the fire exposed steel structure of the study case n°2

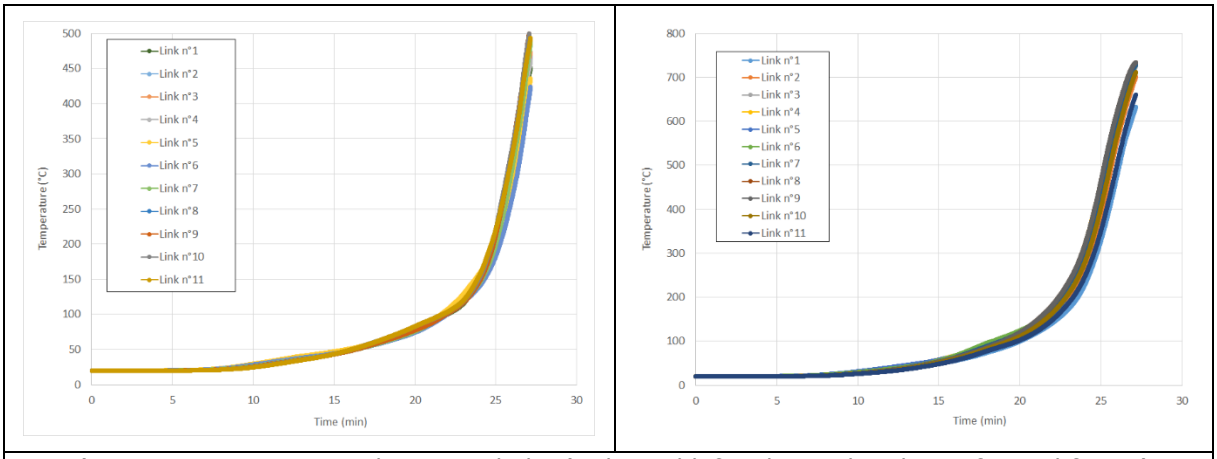

a) Temperature rise in aluminium bolts (right and left sides in the plane of portal frame)

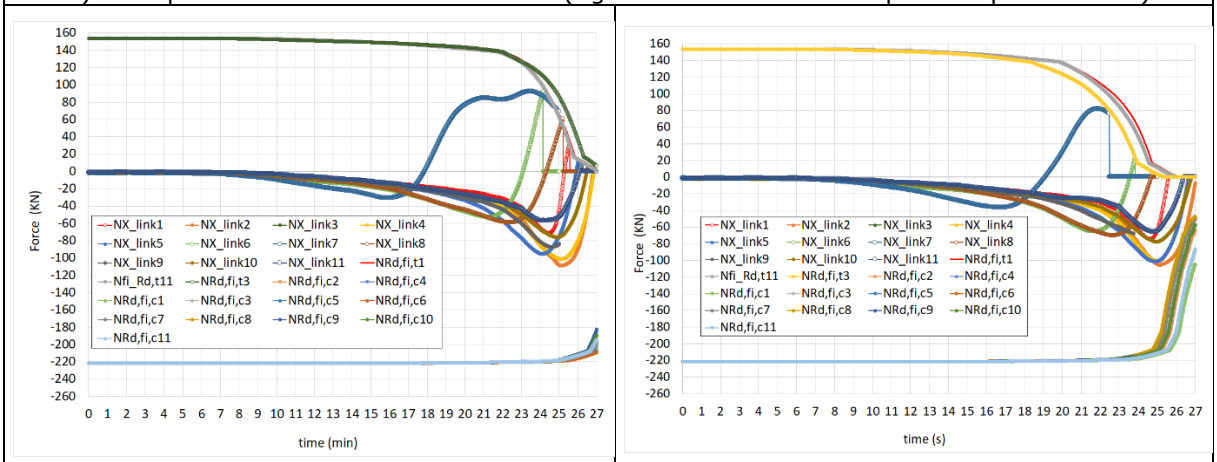

b) Axial force acting in the fusible link (right and left sides in the plane of portal frame)

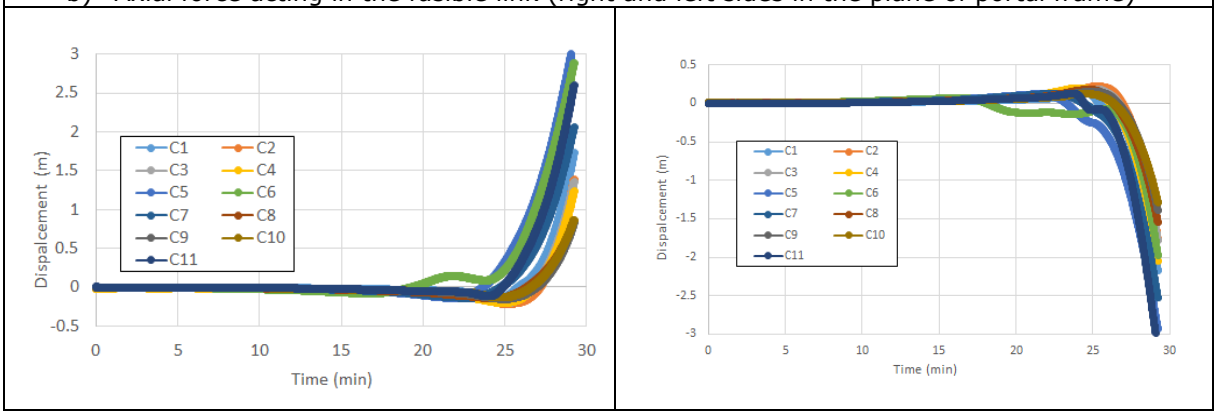

a) Horizontal displacement at three quarter of the height of the columns with fusible links (right and left sides in the plane of portal frame)

Figure 4.28: Temperatures, forces and displacements predicted for the study case n°2

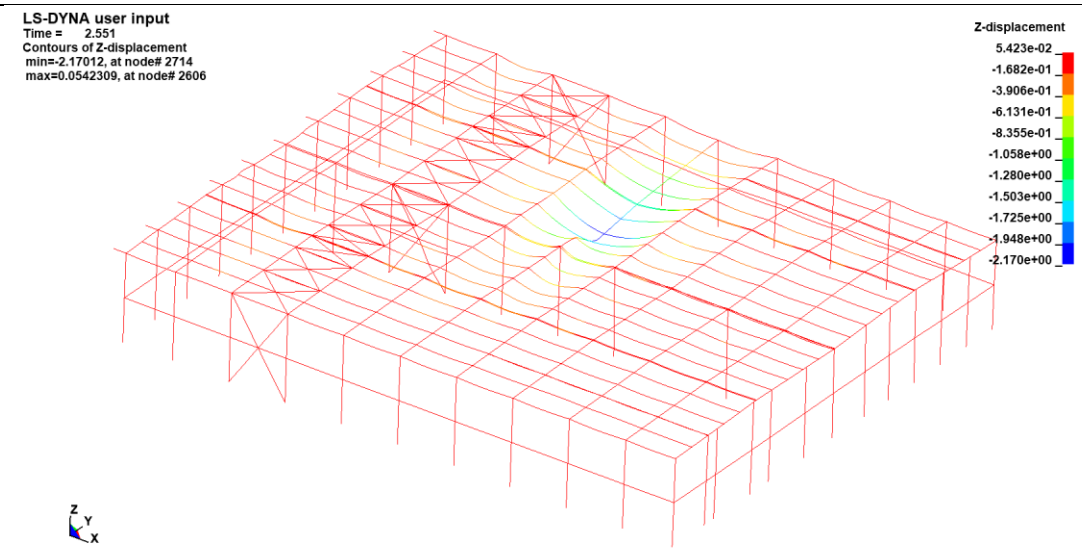

a) Deformed state after 20 minutes of exposure to fire

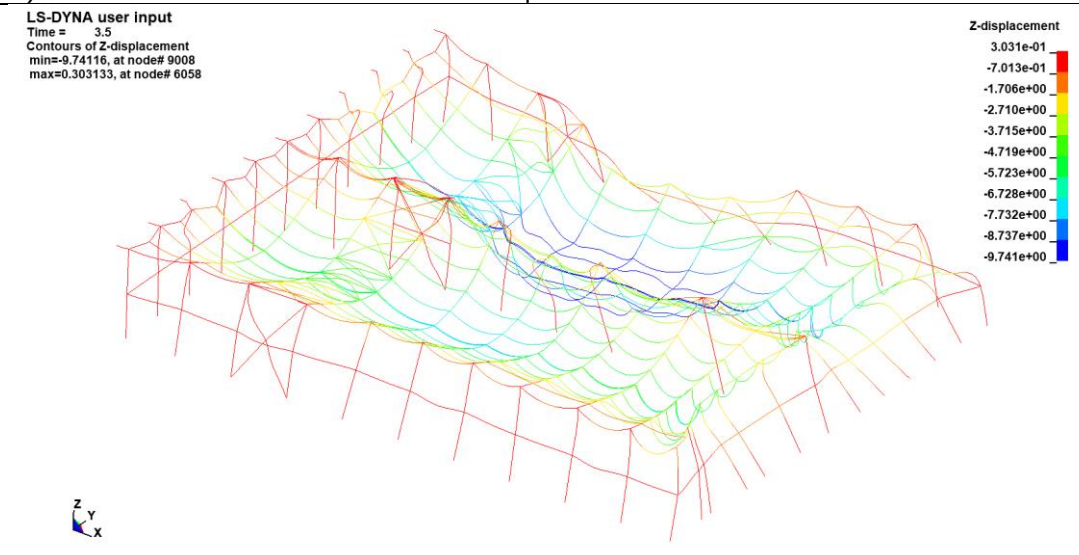

b) Deformed state after 30 minutes of exposure to fire

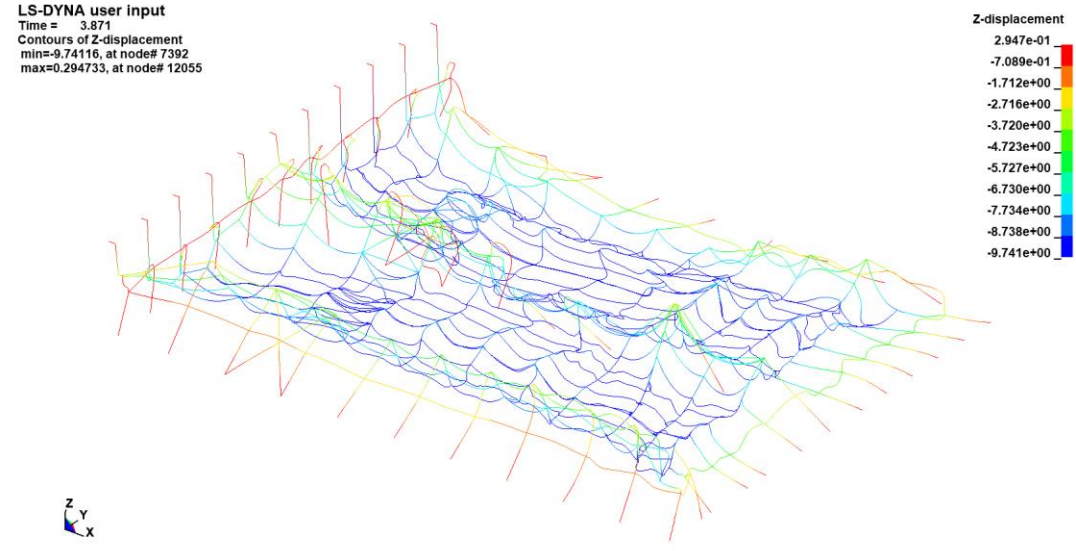

c) Deformed state after 33 minutes of exposure to fire

Figure 4.29: Deformed stated predicted for the fire exposed steel structure of the study case n°3

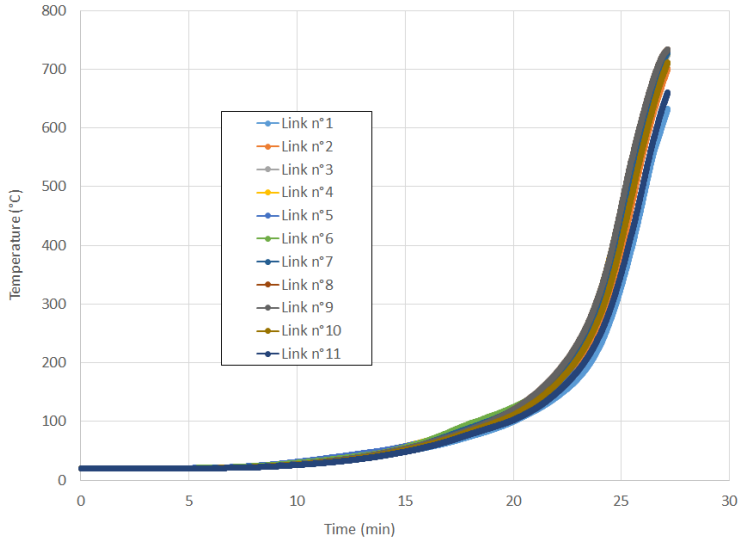

a) Temperature rise in aluminium bolts

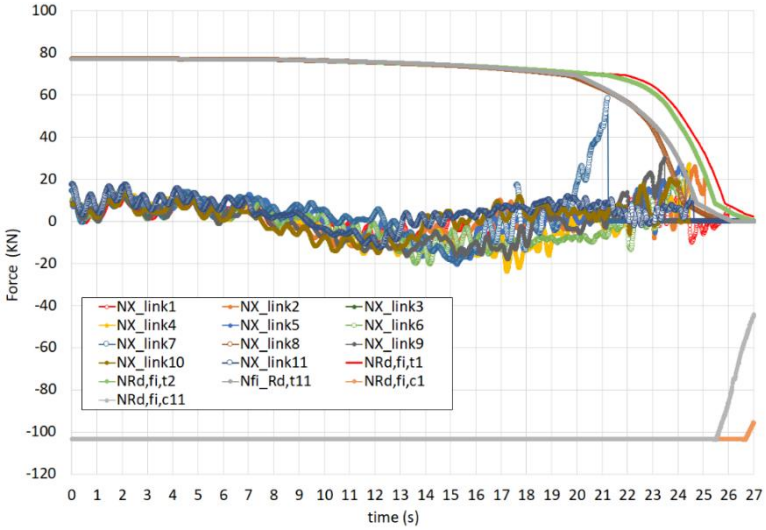

b) Axial force acting in the fusible link

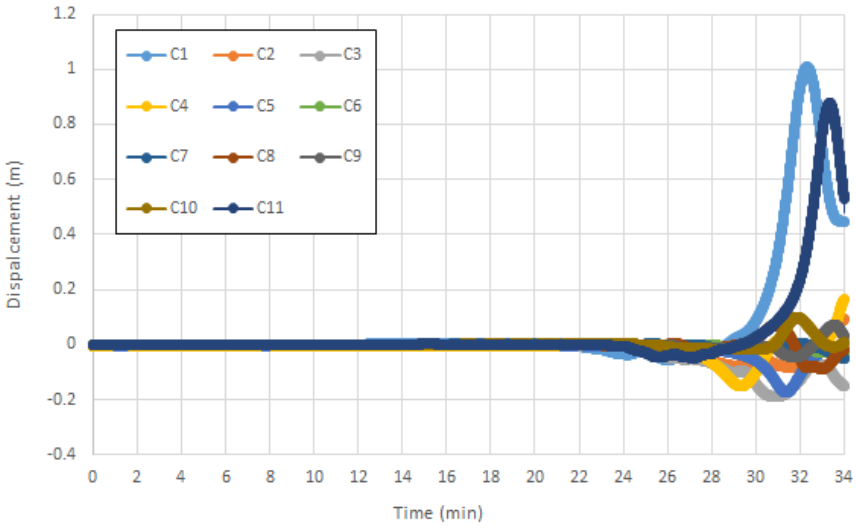

c) Horizontal displacement at three quarter of the height of the columns with fusible links

Figure 4.30: Temperatures, forces and displacements predicted for the study case n°3

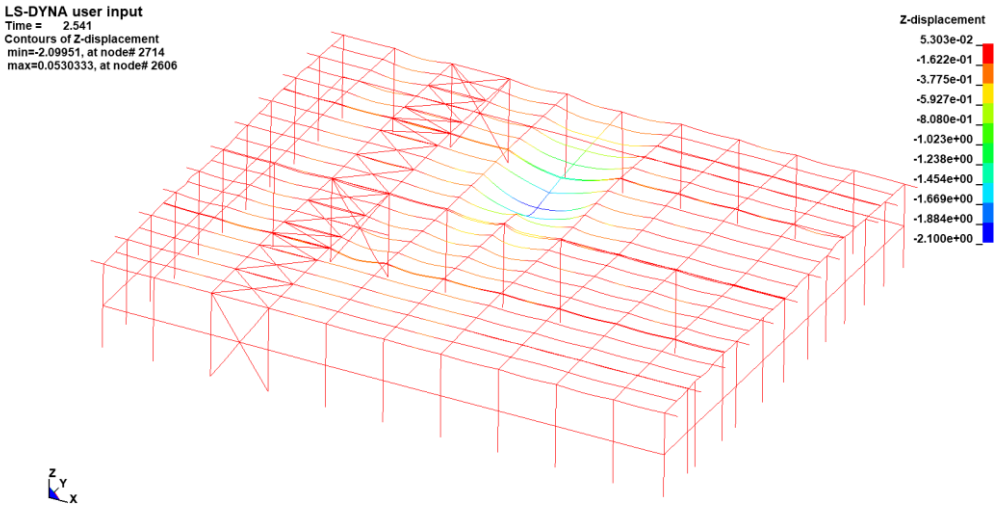

d) Deformed state after 20 minutes of exposure to fire

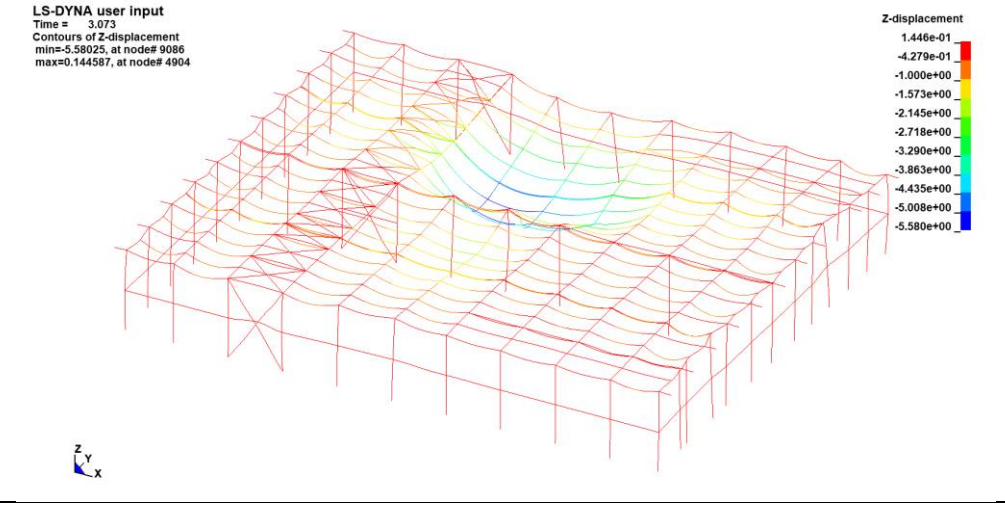

e) Deformed state after 25 minutes of exposure to fire

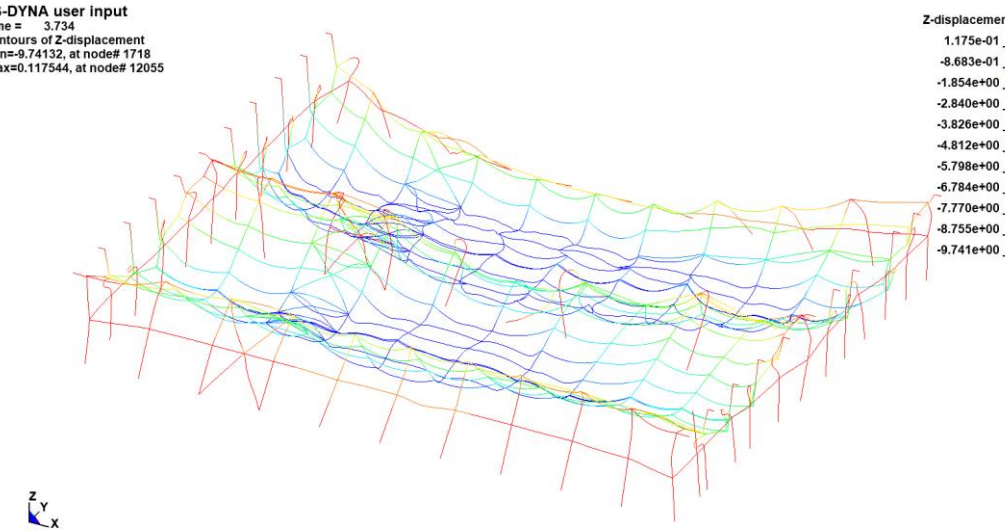

f) Deformed state after 32 minutes of exposure to fire

Figure 4.31: Deformed stated predicted for the fire exposed steel structure of the study case n°4

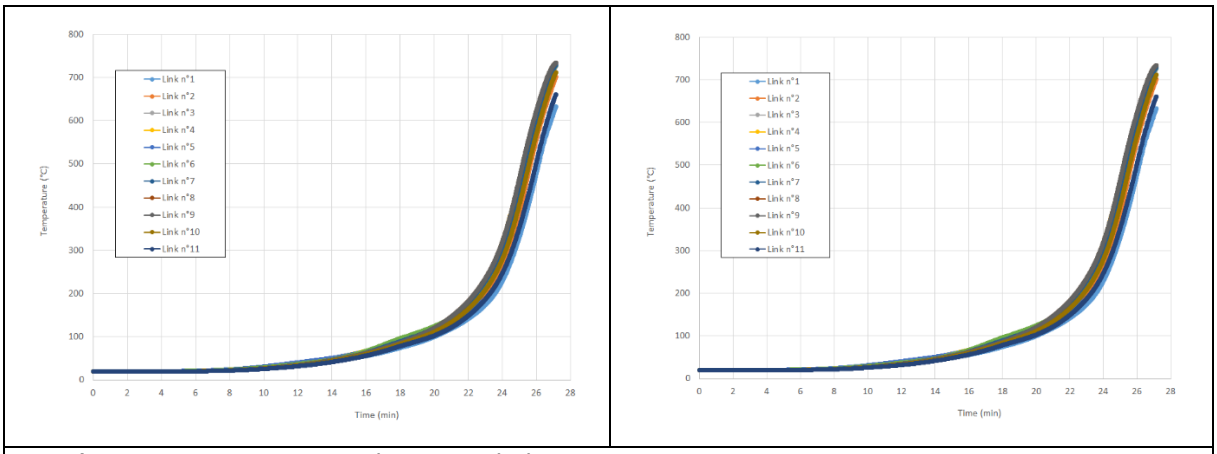

c) Temperature rise in aluminium bolts

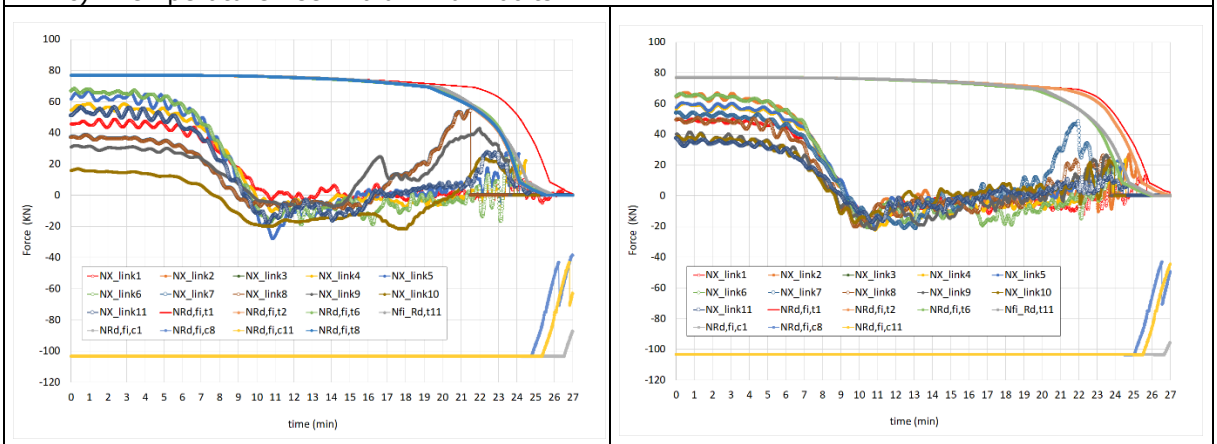

d) Axial force acting in the fusible link

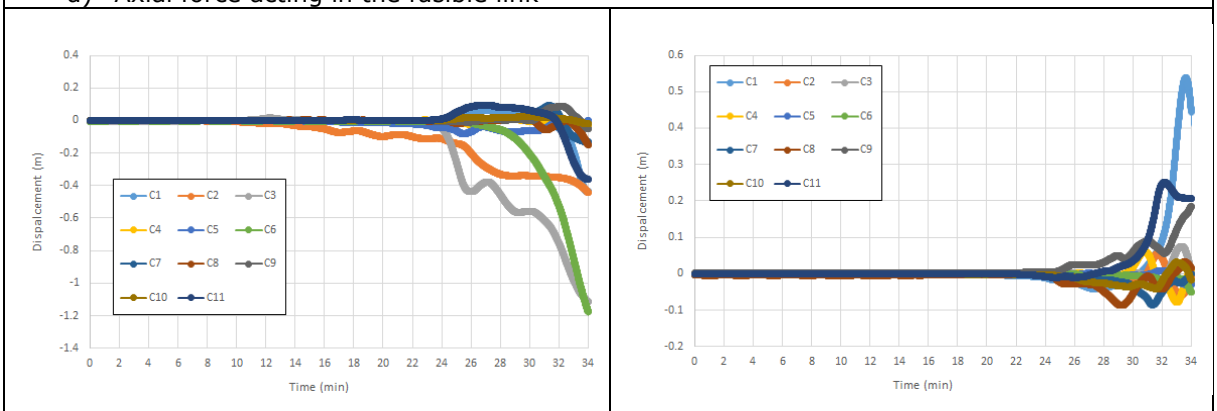

b) Horizontal displacement at three quarter of the height of the columns with fusible links

Figure 4.32: Temperatures, forces and displacements predicted for the study case n°4

4.3.2.2.2 Study cases 5 to 8

These case studies relate to buildings under fire scenario S.2.3 divided into two or three fire compartments, which are separated by fire walls that are either perpendicular or parallel to the steel portal frames. The steel structure of each fire compartment corresponds to that of reference building No. 2.

The simulation results for Study Case n°5 can be found in Figure 4.33 and Figure 4.34. In this case, there are fusible links on one side of the steel structure, attached to the edge columns of steel portal frames. Figure 4.33 illustrates the deformation of the structure when exposed to fire. It illustrates the failure mode of the steel structure. The first signs of failure in the steel portal frame appeared after 95 minutes, close to the initial fire source. As in the 2D analyses, failure begins with the buckling of the internal column, the structural member most affected by the localised impact of the fire. This is followed by the progressive collapse of part of the steel structure, primarily due to the catenary actions induced by the significant deformations of the collapsed structural members (portal frame and purlins). The temperatures reached in this part of the structure are insufficient to cause resistance losses in the roof members, resulting in the observed failure. Conversely, the other part of the structure is strong enough to resist tensile forces thanks to the bracing system and because the temperature of the members does not rise above 400 °C. Figure 4.33b shows the axial forces developed in the fusible links during fire exposure. These are compared to the load-bearing capacities of the links, considering their resistance to both traction and compression. As in the 2D analyses, compressive force is developed in the fusible links due to restrained thermal expansion at the start of the fire. As the temperature increases, the axial compressive forces in a large proportion of the fusible links decrease progressively and the axial force becomes tensile due to catenary action. All the fusible links attached to the columns of the collapsed part of the structure undergo traction, while the others remain in compression. The appearance of tensile forces in the fusible links varies depending on the collapse history of the steel structure. The first fusible link to be subjected to tensile forces was the one located at the end of the steel portal frame closest to the source of the fire, i.e. link n°6. This occurred after around 95 minutes of exposure to the fire. Then, tensile forces progressively appeared in the other fusible links until the end of the simulation. The maximum temperature reached by the fusible links (i.e. the aluminium bolts) ranges between 200 and 275°C. Fire decay occurs in scenario S.2.3. Consequently, the resistance of the fusible links decreases progressively as they heat up, reaching a minimum value after approximately 50 minutes. Then, their resistance increases during the decay phase. While the fusible links have regained some traction, the numerical model predicts that those located at the level of the collapsed structure will fail due to insufficient resistance. This is indicated by a sudden drop in forces to zero (see Figure 4.33b). It should also be noted that the maximum predicted compressive force in the fusible links is around 23 kN, which is slightly lower than the design value of 26.7 kN. Furthermore, the resistance of the fusible links to compression at elevated temperatures ($N_{Rd,fi,c}$) is never reached throughout the entire duration of the fire. In fact, the fusible links' resistance to compression is mainly provided by the steel components that make up the links. Since the temperature in the fusible links never exceeds 400°C, the threshold at which steel begins to lose strength, the fusible links maintain their initial resistance throughout the duration of the considered fire scenario. Figure 4.33c shows the predicted horizontal displacement at three-quarters of the height of the columns associated with the fusible links in the plane of the portal frames. Negative values indicate movement towards the interior of the fire compartment. The displacement curves demonstrate the outward collapse of the steel structure. They also show that the displacements are small enough not to compromise the integrity of the fire wall.

The Figure 4.36 and Figure 4.37 summaries the simulation results for the case study case n°6, where there are fusible links on both sides of the steel structure, attached to the edge columns of steel portal frames. In this case, it should be noted that the irreversibility of aluminium bolt resistance was considered by assuming that the temperature of the fusible links remained at the maximum level calculated for the relevant fire scenario until the end of the numerical simulations. The same observations can be made regarding the structural behaviour as for the previous case. However, it should be noted that, due to the presence of fusible links on both sides of the steel portal frame, the first member failure occurs slightly later. With regard to the fusible links (see Figure 4.36), the model predicts their failure around the collapsed part of the steel structure, but only on the side where they are heated the most. On the other side, no links break due to the temperature rise in the links being limited, and due to the fusible links having too much residual traction resistance. The maximum temperature reached by the fusible links (i.e. the aluminium bolts) is between 200 and 275°C on one side. On the other side, they range between 175 and 200°C. Note that aluminium bolts lose 25% of

their strength at 150°C and 50% at 200°C). It should also be noted that the maximum predicted compressive force in the fusible links is around 45 kN,

The Figure 4.38 and Figure 4.39 illustrate the fire behaviour of the study case n°7, where there are fusible links on one side of the steel structure, which are attached to steel gable columns. The structure's behaviour remains unchanged, and the model predicts that three-quarters of the links fail due to insufficient traction resistance at high temperatures. The maximum temperature reached by the fusible links (i.e. the aluminium bolts) is between 150 and 200°C.It should be noted that the initial traction resistance of the links is much lower in this case than when the wall is perpendicular to the portal frames. This resistance is provided by two M16 aluminium bolts only). It should also be noted that the maximum predicted compressive force in the fusible links is around 24 kN.

Then, for the study case n°8, in which there are fusible links on both sides of the steel structure, which are attached to steel gable columns, it can be noted that the numerical model predicts failure of most of the fusible links. Unlike the previous three cases, there is no progressive collapse of the steel structure due to the catenary action. Collapse remains localised to the portal frame and purlins near the initial fire source. It is believed that this is due to the presence of fusible links on both sides of the structure, which retain their tensile strength for long enough to prevent progressive collapse. The maximum temperature reached by the fusible links (i.e. the aluminium bolts) is between 225 and 300°C on one side. On the other side, they range between 150 and 200°C). It should also be noted that the maximum predicted compressive force in the fusible links is around 22 kN.

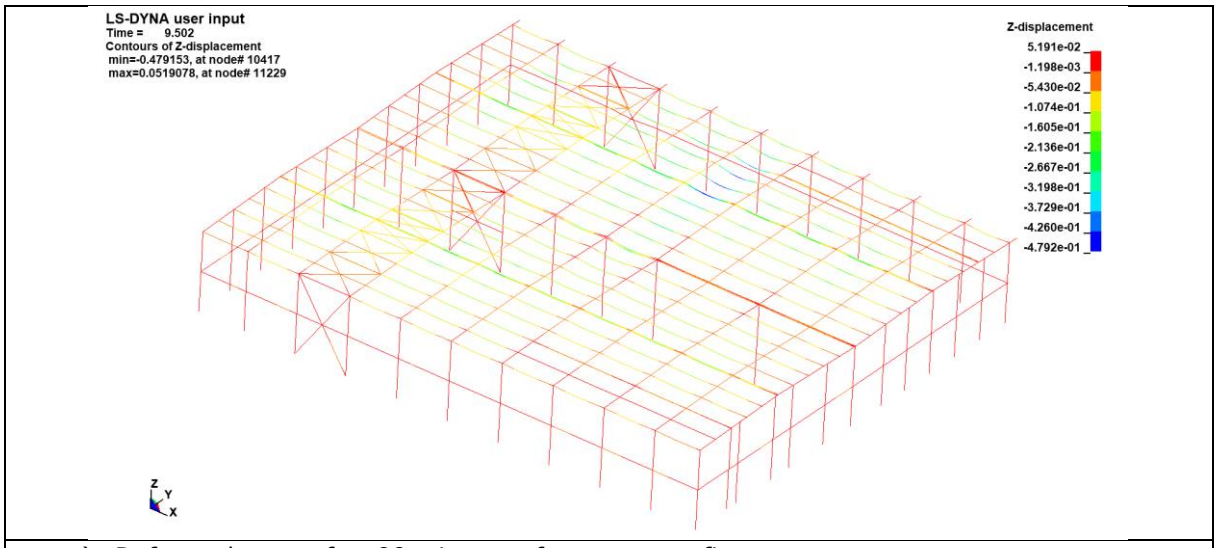

a) Deformed state after 90 minutes of exposure to fire

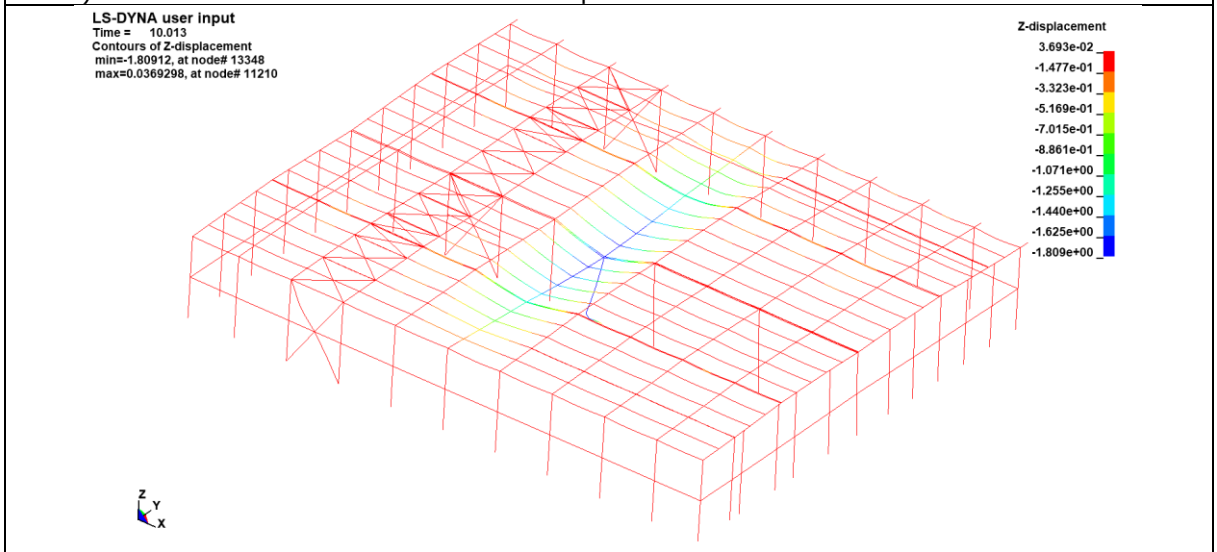

b) Deformed state after 95 minutes of exposure to fire

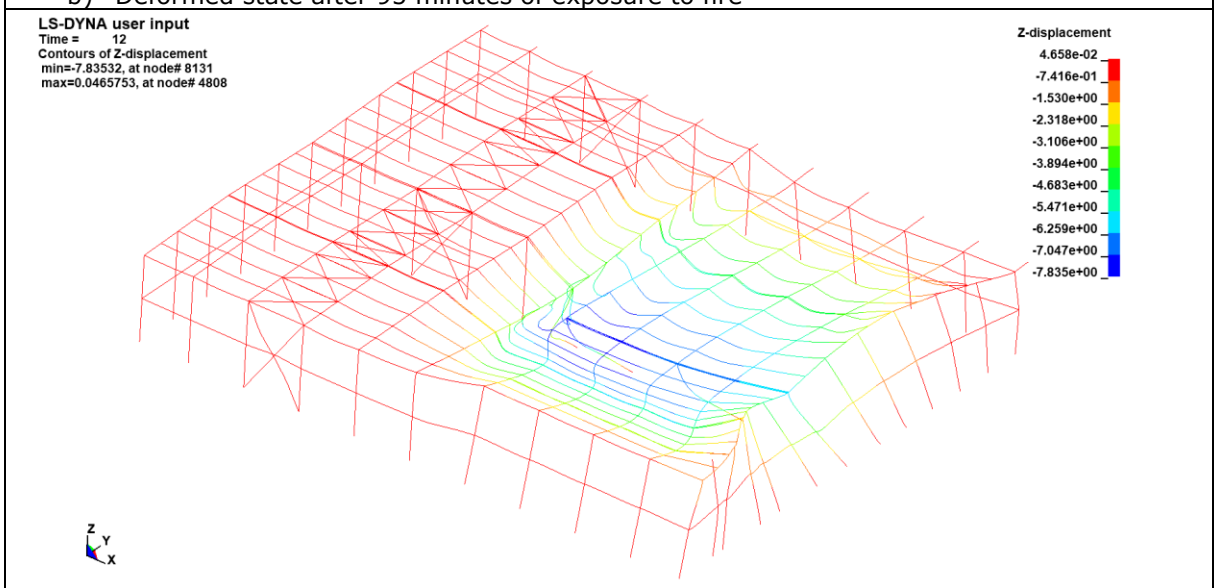

c) Deformed state after 115 minutes of exposure to fire

Figure 4.33: Deformed stated predicted for the fire exposed steel structure of the study case n°5

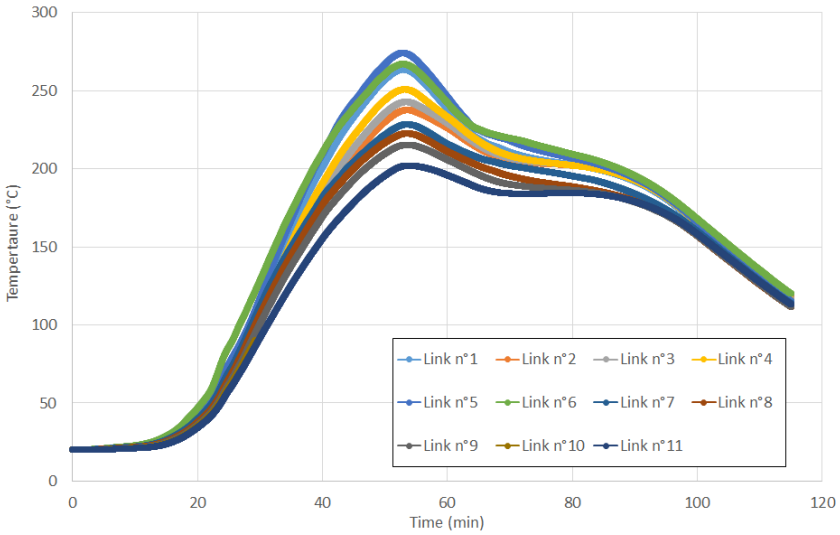

d) Temperature rise in aluminium bolts

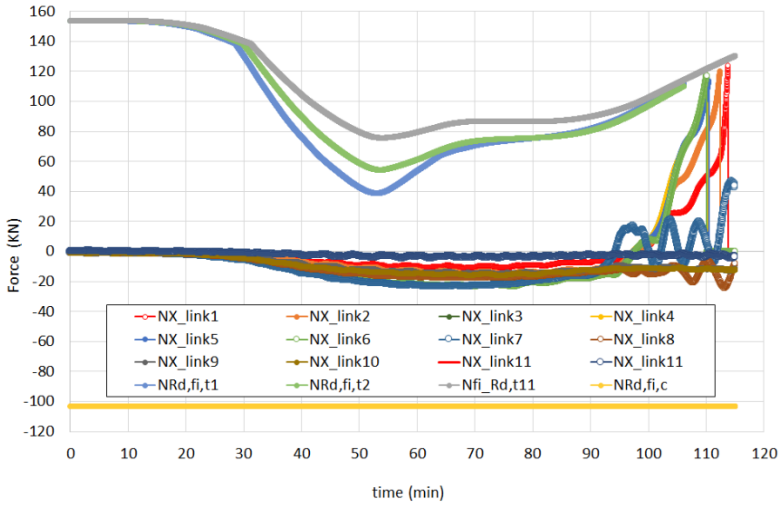

e) Axial force acting in the fusible link

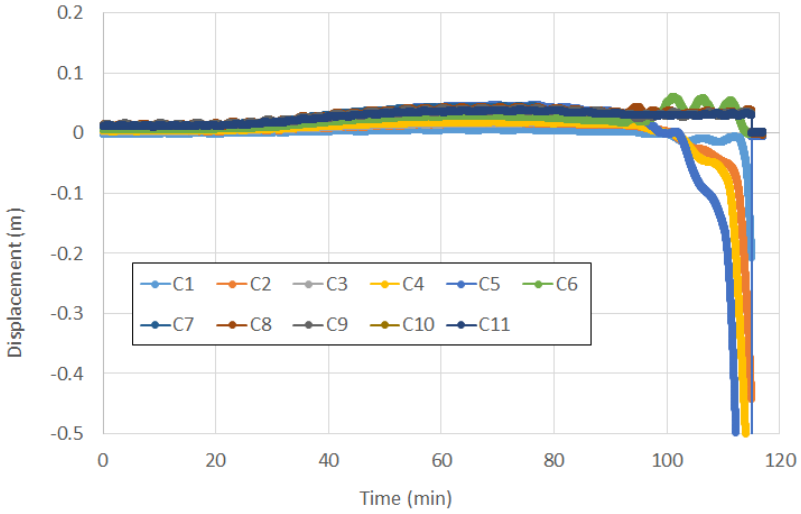

f) Horizontal displacement at three quarter of the height of the columns with fusible links

Figure 4.34: Temperatures, forces and displacements predicted for the study case n°5

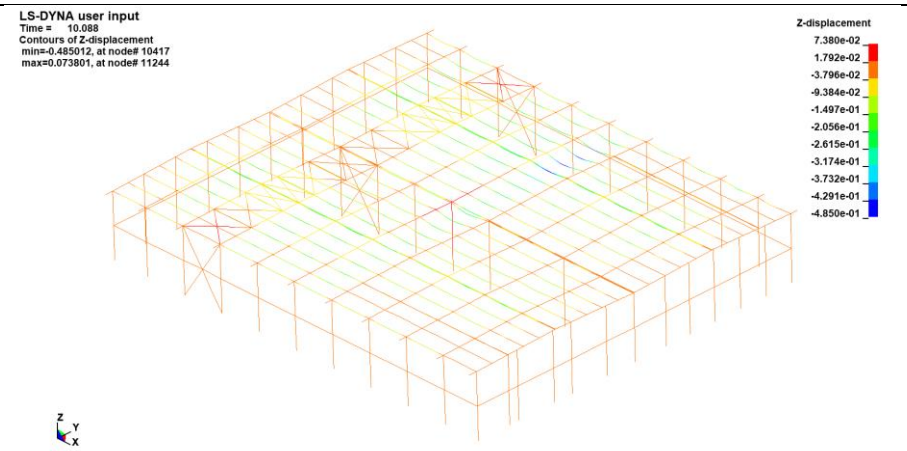

a) Deformed state after 95 minutes of exposure to fire

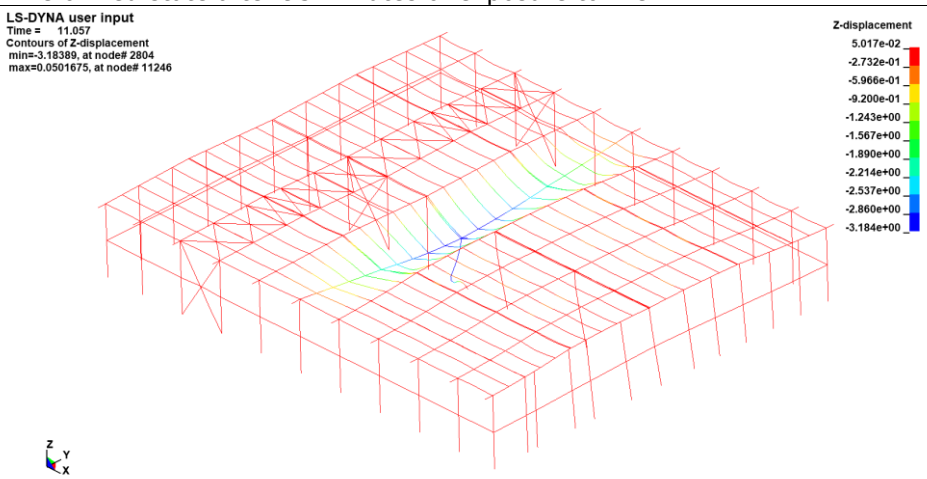

b) Deformed state after 105 minutes of exposure to fire

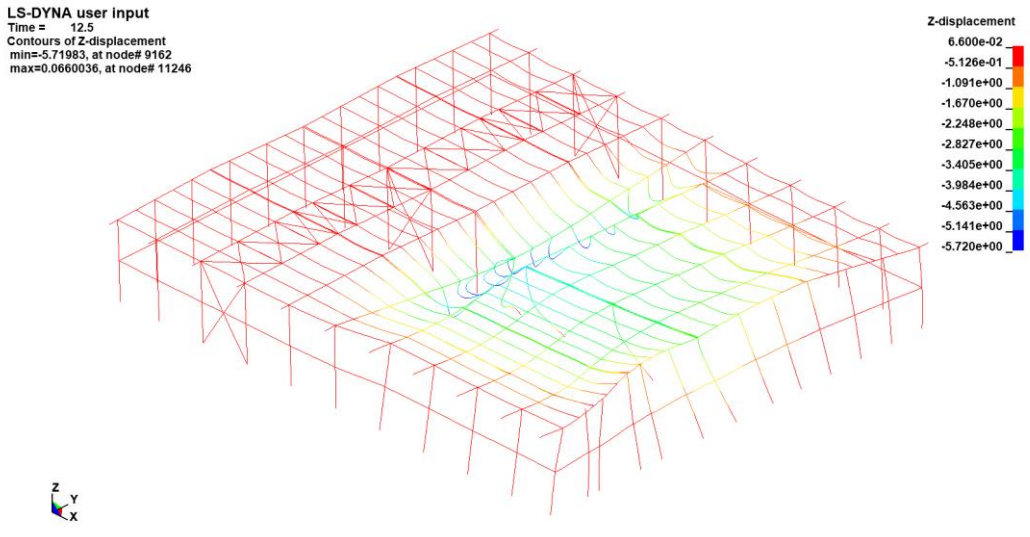

c) Deformed state after 115 minutes of exposure to fire

Figure 4.35: Deformed stated predicted for the fire exposed steel structure of the study case n°6

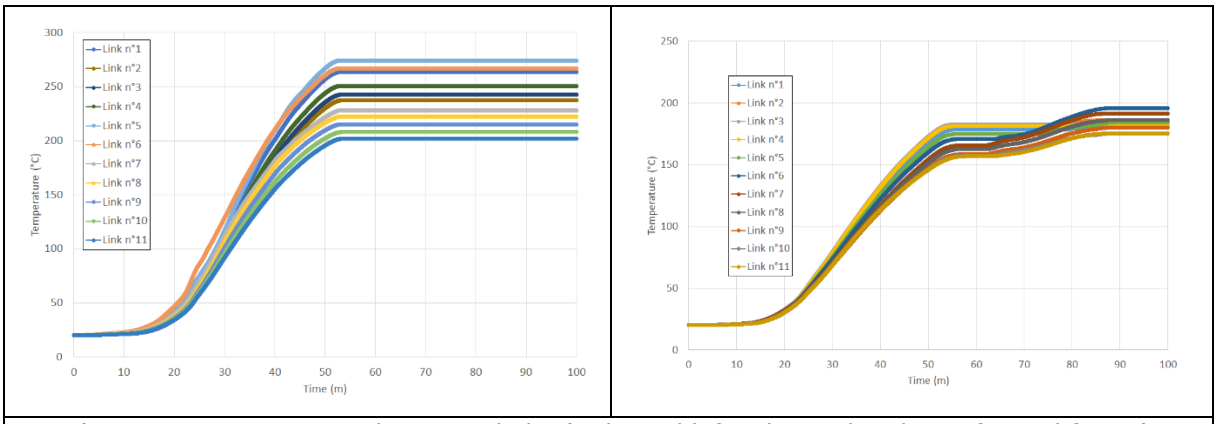

a) Temperature rise in aluminium bolts (right and left sides in the plane of portal frame)

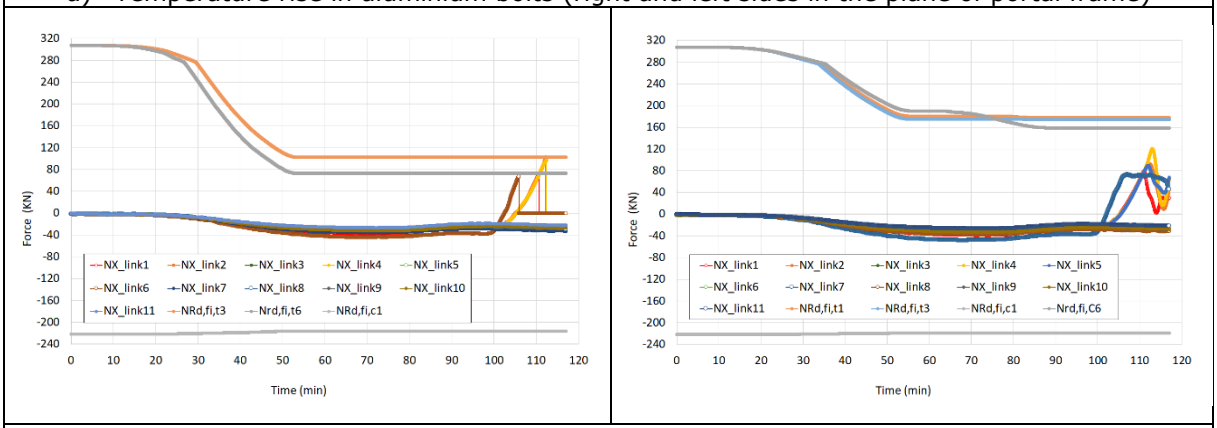

b) Axial force acting in the fusible link (right and left sides in the plane of portal frames)

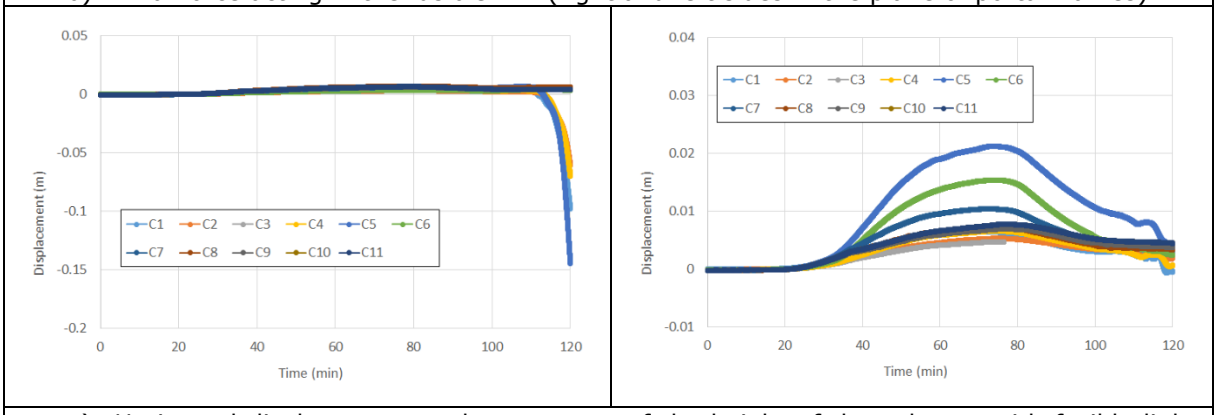

a) Horizontal displacement at three quarter of the height of the columns with fusible links (Right and left sides in the plane of portal frames)

Figure 4.36: Temperatures, forces and displacements predicted for the study case n°6

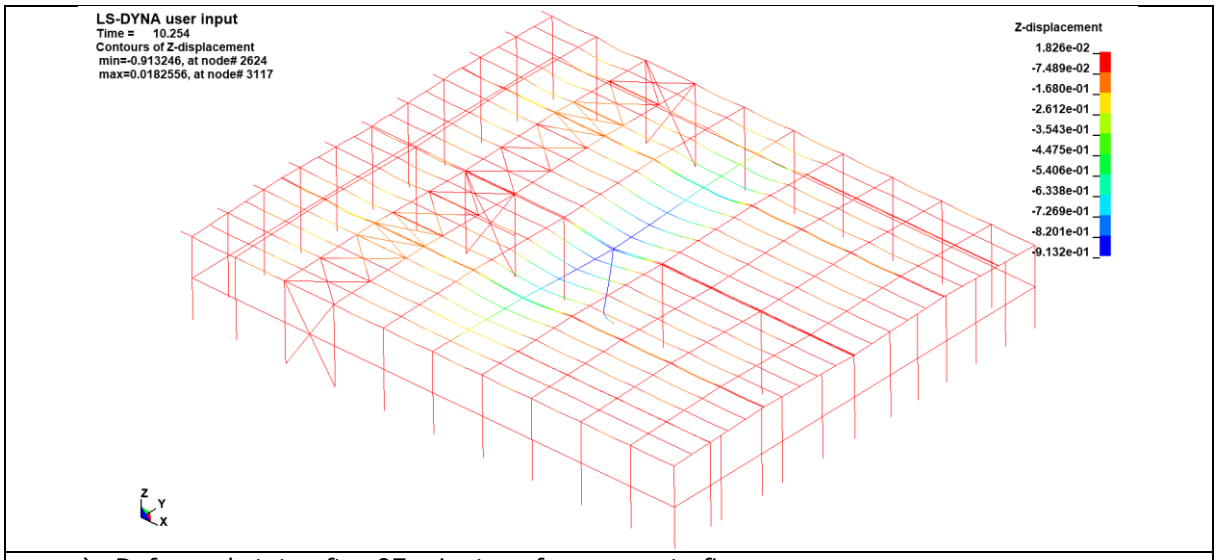

a) Deformed state after 97 minutes of exposure to fire

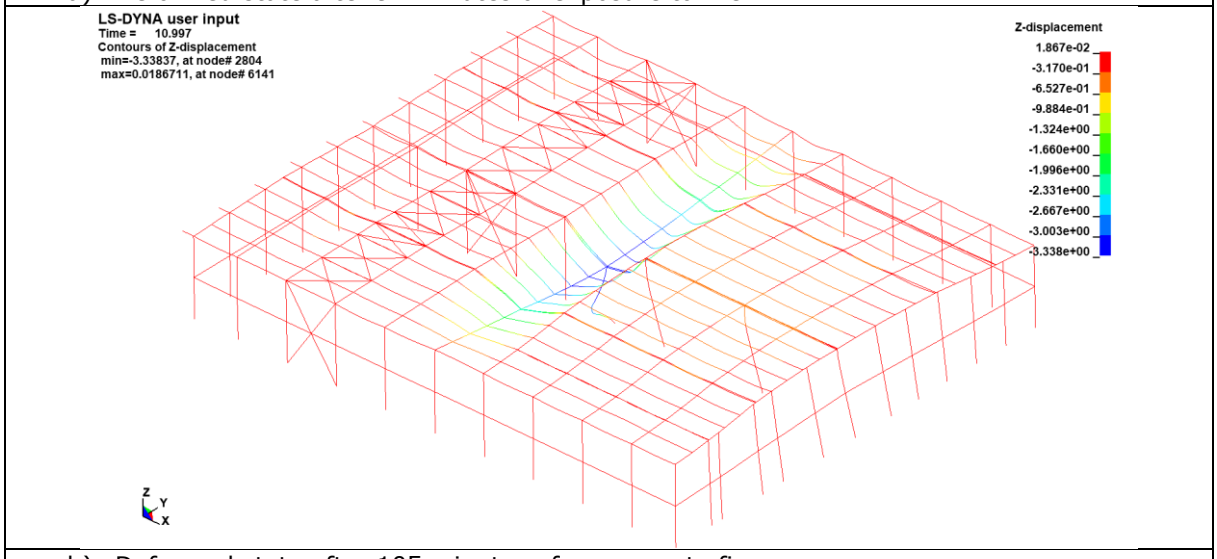

b) Deformed state after 105 minutes of exposure to fire

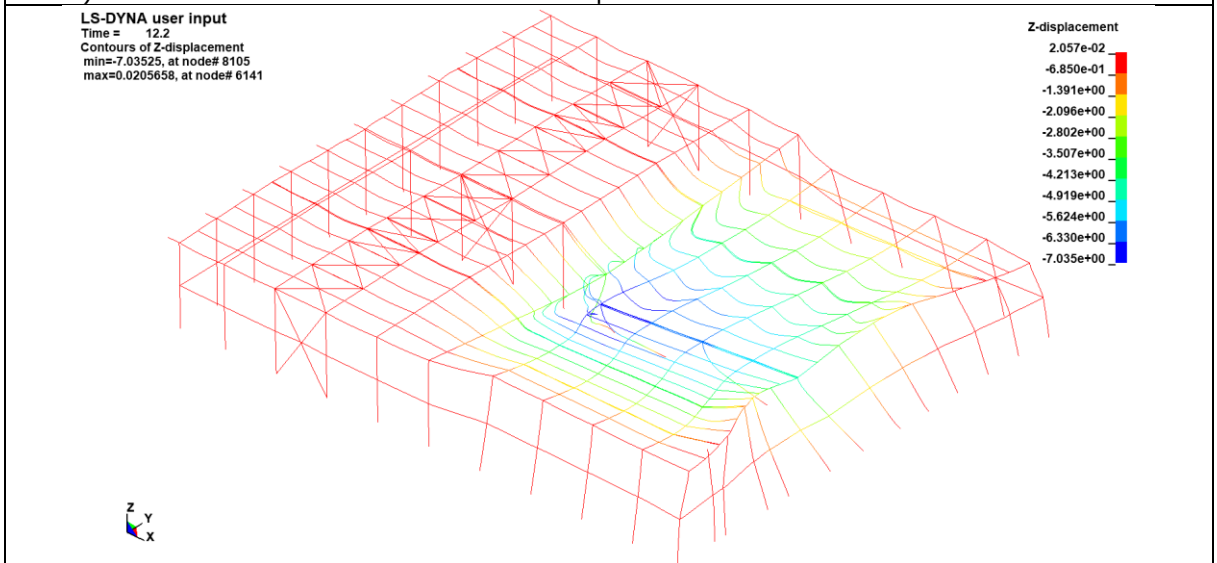

c) Deformed state after 115 minutes of exposure to fire

Figure 4.37: Deformed stated predicted for the fire exposed steel structure of the study case n°7

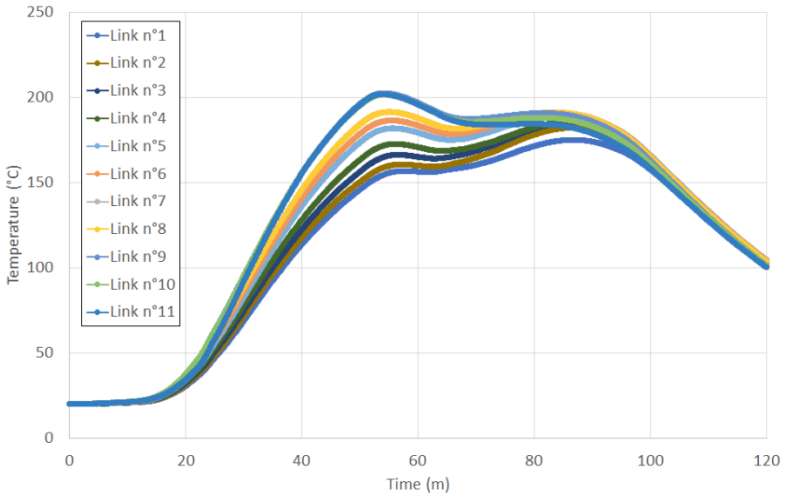

g) Temperature rise in aluminium bolts

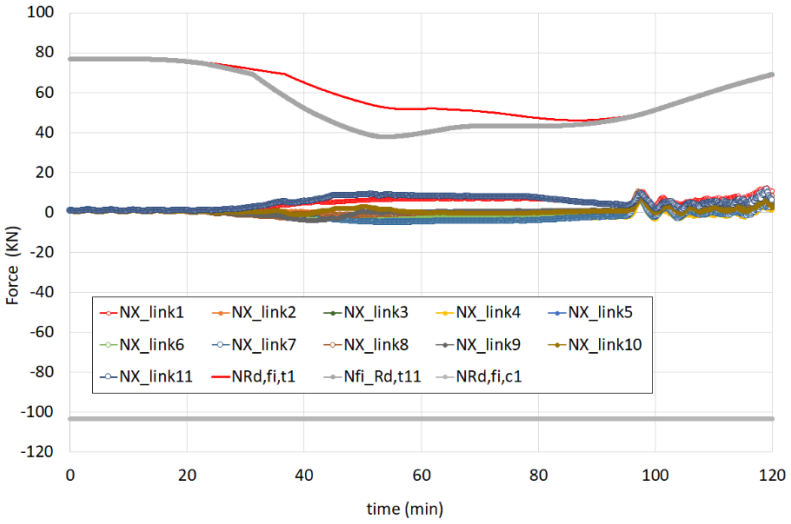

h) Axial force acting in the fusible link

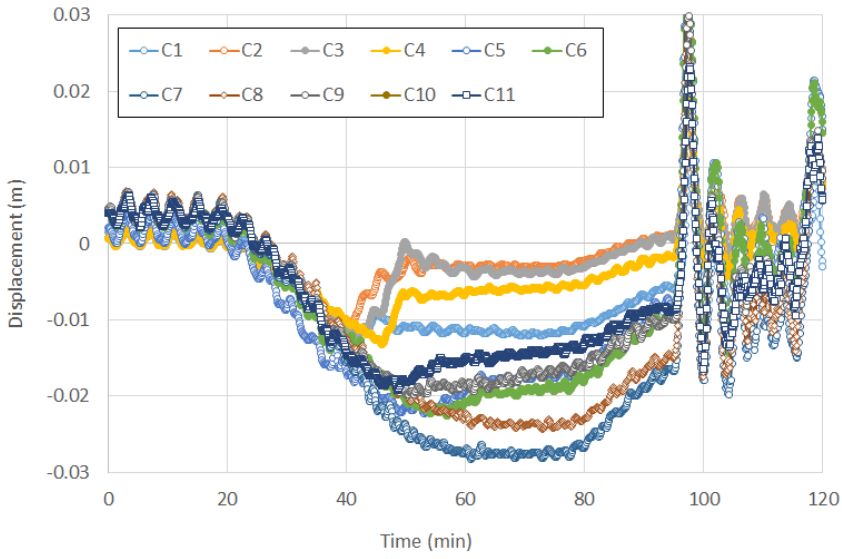

i) Horizontal displacement at three quarter of the height of the columns with fusible links

Figure 4.38: Temperatures, forces and displacements predicted for the study case n°7

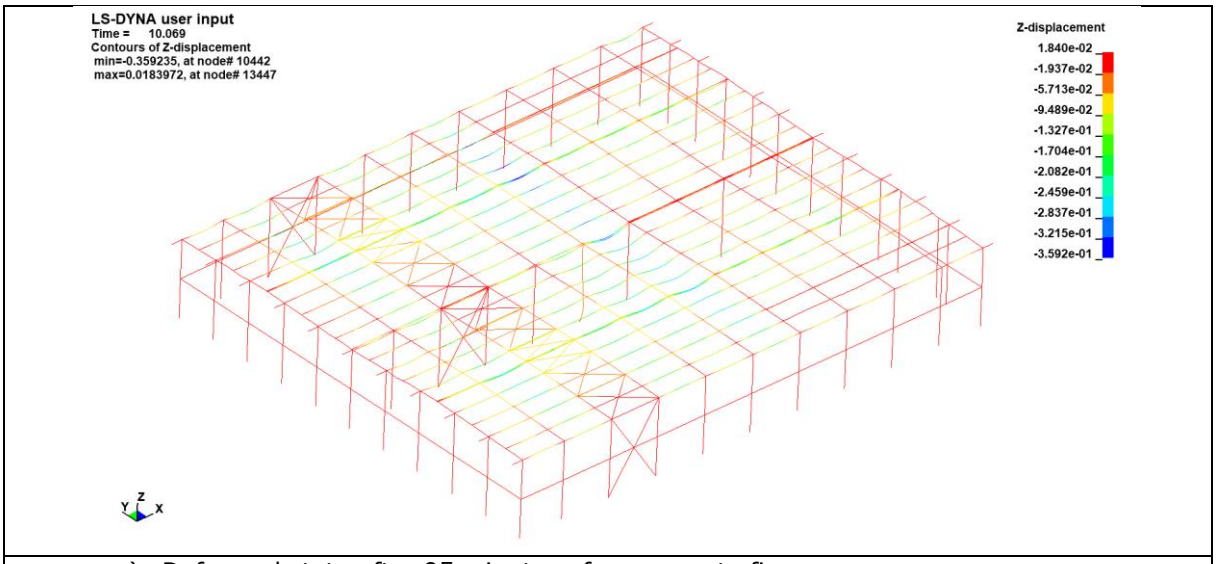

a) Deformed state after 95 minutes of exposure to fire

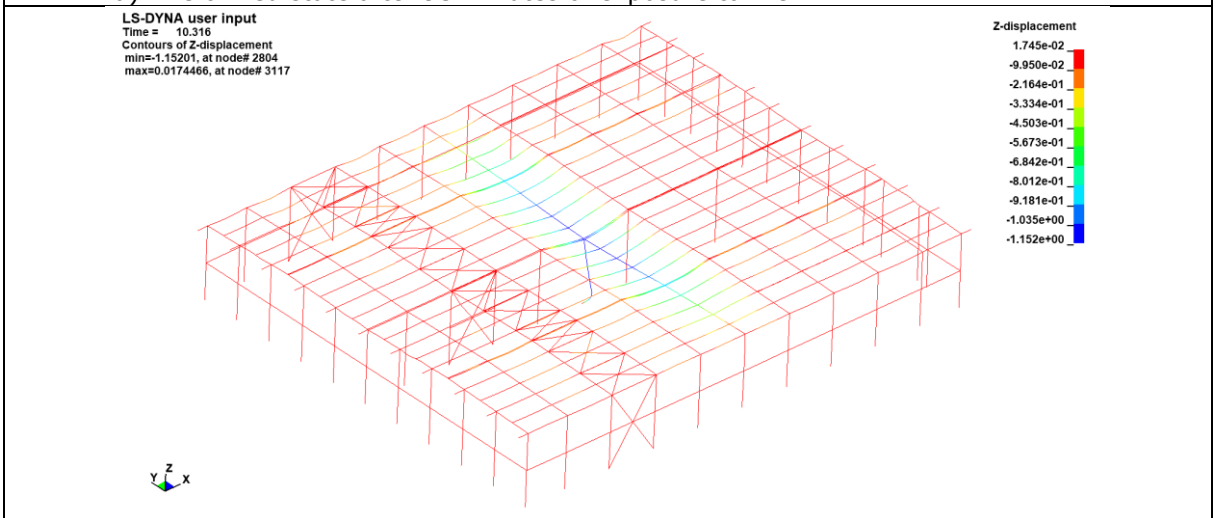

b) Deformed state after 98 minutes of exposure to fire

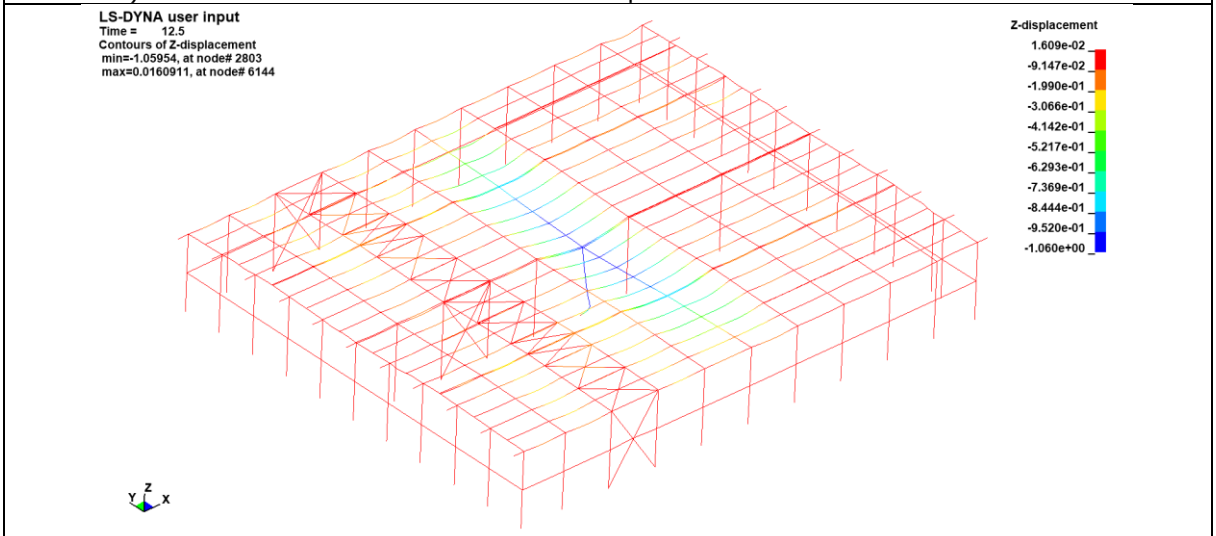

c) Deformed state after 115 minutes of exposure to fire

Figure 4.39: Deformed stated predicted for the fire exposed steel structure of the study case n°8

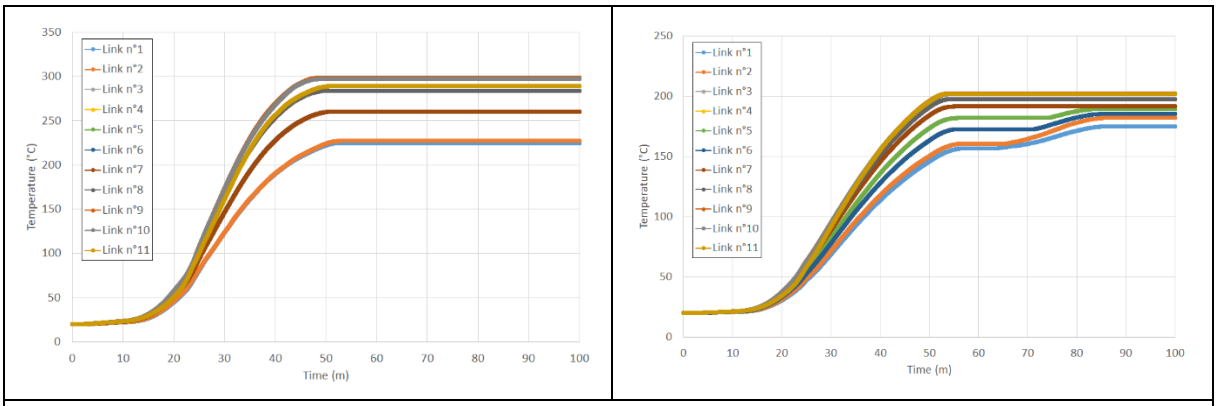

a) Temperature rise in aluminium bolts

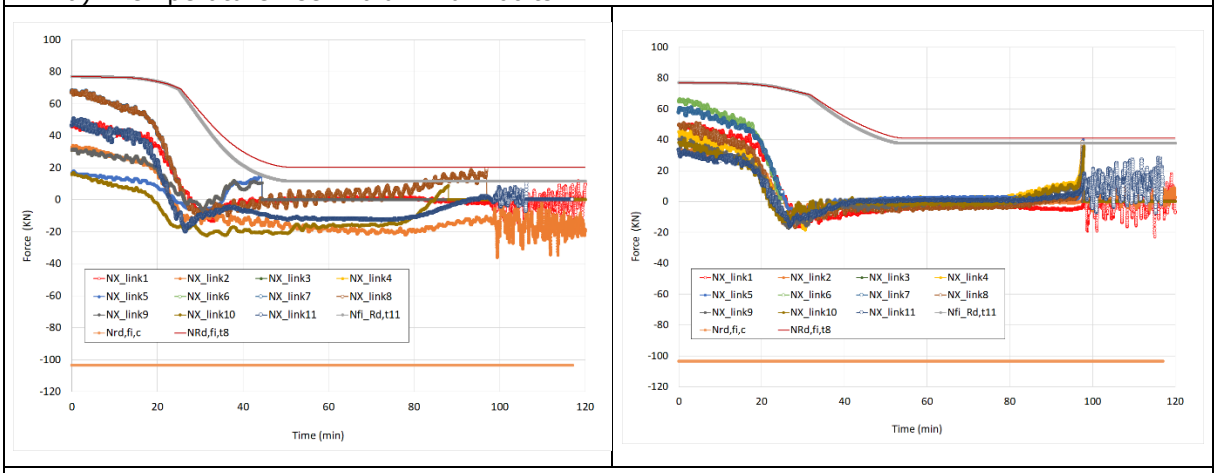

b) Axial force acting in the fusible link

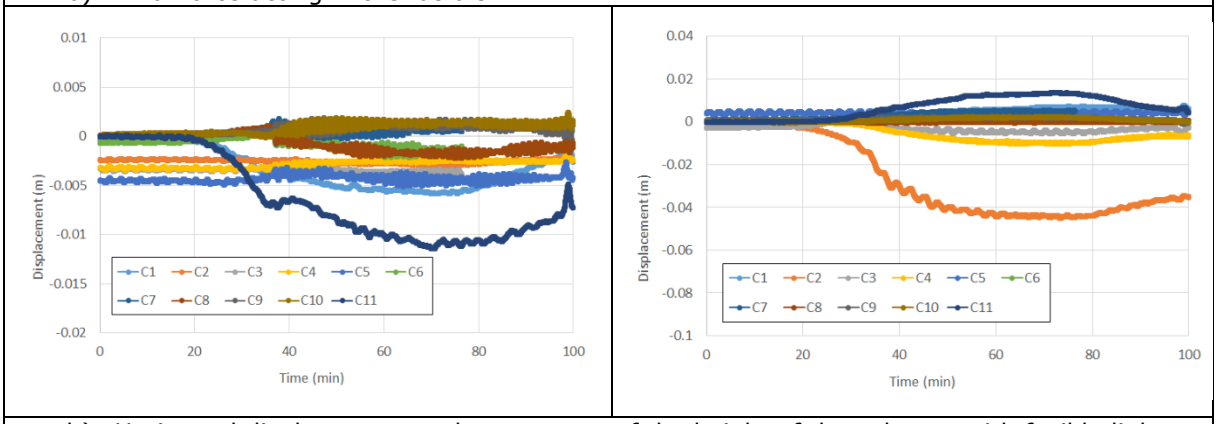

b) Horizontal displacement at three quarter of the height of the columns with fusible links

Figure 4.40: Temperatures, forces and displacements predicted for the study case n°8

4.3.2.2.3 Study cases 9 to 12

These case studies relate to buildings under fire scenario I.2.2 divided into two or three fire compartments, which are separated by fire walls that are either perpendicular or parallel to the steel portal frames. The steel structure of each fire compartment corresponds to that of reference building No. 2.

The simulation results for Study Case n°9 can be found in Figure 4.41 and Figure 4.42. In this case, there are fusible links on one side of the steel structure, attached to the edge columns of steel portal frames. Moreover, it should be noted that the irreversibility of aluminium bolt resistance was considered by assuming that the temperature of the fusible links remained at the maximum level calculated for the relevant fire scenario until the end of the numerical simulations. Figure 4.41 shows the deformation of the structure at different exposure times to fire. It illustrates the failure mode of the steel structure. A limited and localised collapse occurs in the part of the structure that is most heavily heated due to the combined effects of temperature, corresponding steel strength losses, and applied loads. The first signs of failure in the steel portal frame emerged after 25 minutes, close to the initial fire source. As in the 2D analyses, failure begins with the buckling of the internal column, which is the structural member most affected by the localised impact of the fire. Despite the significant vertical displacement of the collapsed part of the structure, no progressive structural collapse occurs during the considered fire scenario. The other part of the structure and the bracing system are strong enough to resist tensile forces, because the temperature of the members does not rise above 400°C. Figure 4.42b shows the axial forces developed in the fusible links during the fire exposure. These are compared to the load-bearing capacities of the links, considering both their traction and compression resistances. As with the 2D analyses, compressive force is developed in fusible links due to restrained thermal expansion at the beginning of fire exposure. After around 40 minutes, as the temperature first increases and then decreases, the axial compressive forces in the fusible links decrease progressively. However, due to the catenary action, the axial force in the two fusible links closest to the collapsed part of the steel structure becomes tensile. These two links are located between the end of the structure and the roof bracing system. Tensile forces occur after around 28 minutes of exposure to fire and progressively increase with the localised collapse of the roof structure until they exceed the traction resistance of the fusible link. The maximum temperature reached by the fusible links (i.e. the aluminium bolts) is between 125 and 200°C.The model predicts failure of the two fusible links at this time, which is indicated by a sudden drop in forces to zero (see Figure 4.42b). It can also be noted that the maximum predicted compressive force in the fusible links is around 11 kN, which is lower than the design value of 26.7 kN. Furthermore, the resistance to compression of the fusible link at elevated temperatures ($N_{Rd,fi,c}$) is never exceeded throughout the duration of the fire, as the temperature of the fusible links never exceeds 400°C. Figure 4.42c shows the predicted horizontal displacement at three-quarters of the height of the columns associated with the fusible links in the plane of the portal frames. Negative values indicate movement towards the interior of the fire compartment. The displacement curves demonstrate the outward collapse of the steel structure. They also demonstrate that the displacements are sufficiently small as to not compromise the integrity of the fire wall.

The Figure 4.43 and Figure 4.44 show the results for case study n°10, where fusible links are attached to the edge columns of steel portal frames on both sides of the steel structure. As in the previous case, irreversibility of aluminium bolt resistance was considered. The same observations can be made regarding the structural behaviour. The model predicts that the two fusible links closest to the collapsed part of the steel will break almost simultaneously on both sides. The maximum temperature reached by the fusible links (i.e. the aluminium bolts) is between 125 and 200°C. It can also be noted that the maximum predicted compressive force in the fusible links is around 60 kN, which is lower than the design value of 115.8 kN.

The simulation results for Study Case n°11 are shown in Figure 4.44 and Figure 4.45. In this case, there are fusible on one side of the steel structure, which are attached to steel gable columns. They are located on the structure side close to the fire source. The fire behaviour observed for the structure is slightly different, with less pronounced collapse of the most heated part of the structure than in the previous case. The model predicts that half of the fusible links (those in the middle of the gable frame, so the most heated) fail due to insufficient traction resistance at high temperatures, as opposed to catenary actions. By contrast, the other fusible links retain sufficient traction resistance to prevent the structure from collapsing further. It can also be noted that the maximum predicted compressive force in the fusible links is around 23.5 kN, which is lower than the design value of 26.7 kN.

The Figure 4.46 and Figure 4.47 show the results for case study n°11, where fusible links are attached to the edge columns of steel portal frames on both sides of the steel structure. It can be noted that the numerical model predicts all the fusible links fail along the gable frame closest to the fire source. Failure of the links starts in the middle of the building and gradually spreads towards the ends of the gable frame. This is due to the greater tensile forces generated at the centre of the gable frame than at its ends (due to the buckling of the central column of the most heated portal frame). Similarly, the fusible links are heated more at the centre due to their proximity to the initial fire source than at the edges of the gable frame. On the other side of the structure, the model predicts failure for all the links, except for two. However, it should be noted that the link failure occurs at relatively low temperatures, just over 100°C. Therefore, all the fusible links would fail in the event of a more severe fire. However, in this case, breaking of the links does not really matter on this side of the structure since there is no progressive structural collapse. It can also be noted that the maximum predicted compressive force in the fusible links is around 26 kN, which is lower than the design value of 26.7 kN.

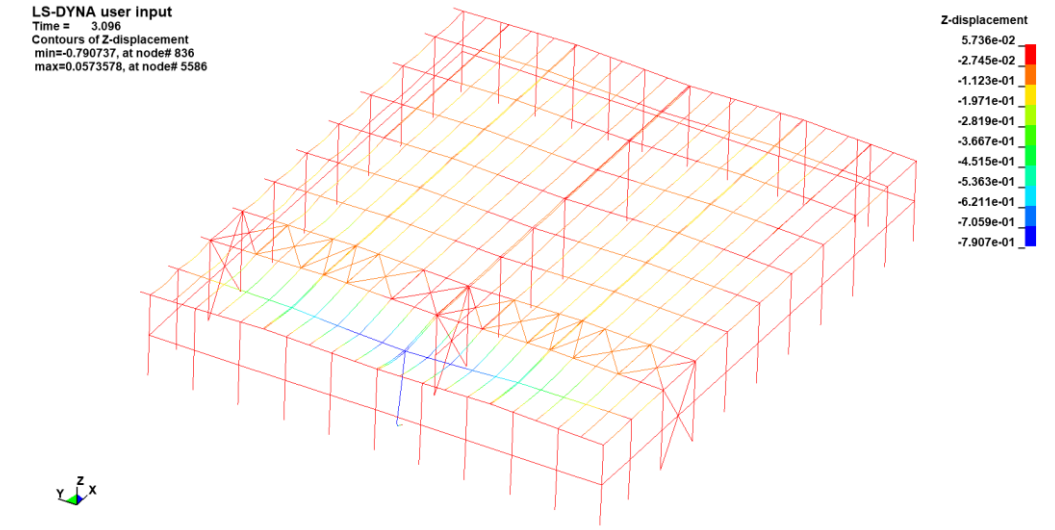

a) Deformed state after 25 minutes of exposure to fire

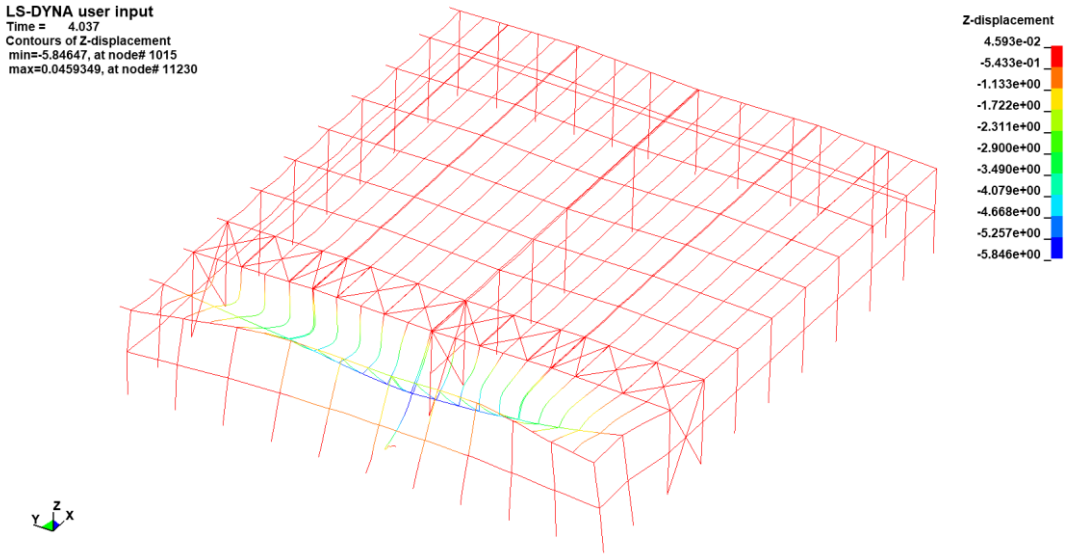

b) Deformed state after 35 minutes of exposure to fire

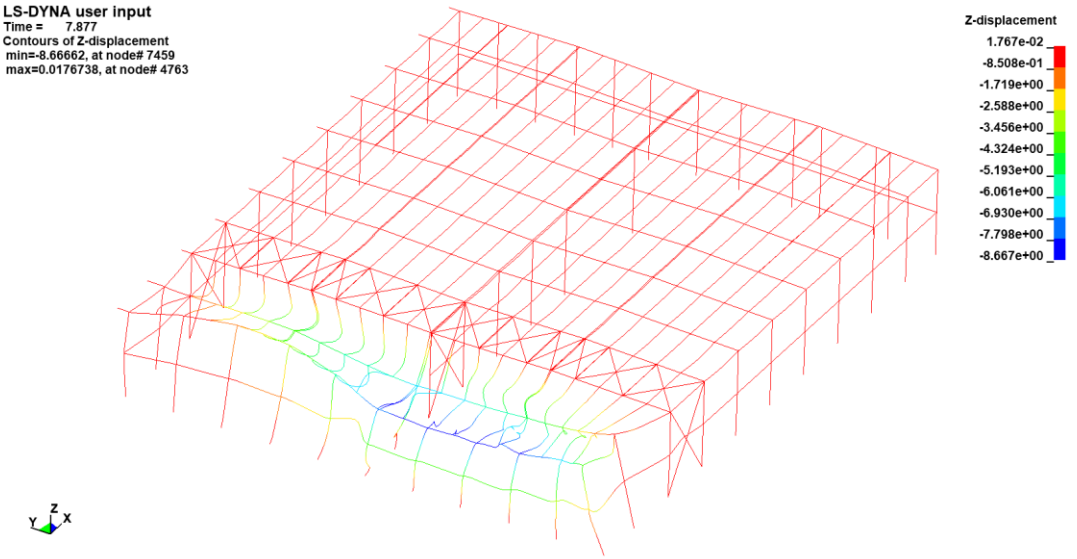

c) Deformed state after 73 minutes of exposure to fire

Figure 4.41: Deformed stated predicted for the fire exposed steel structure of the study case n°9

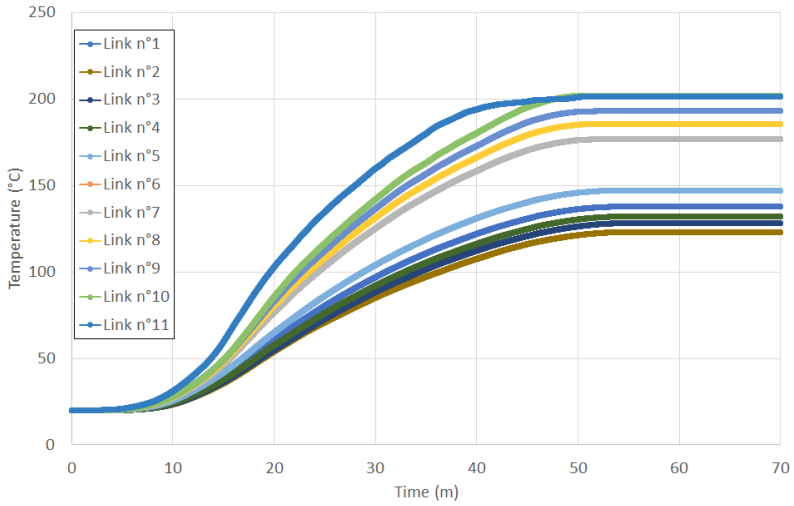

c) Temperature rise in aluminium bolts

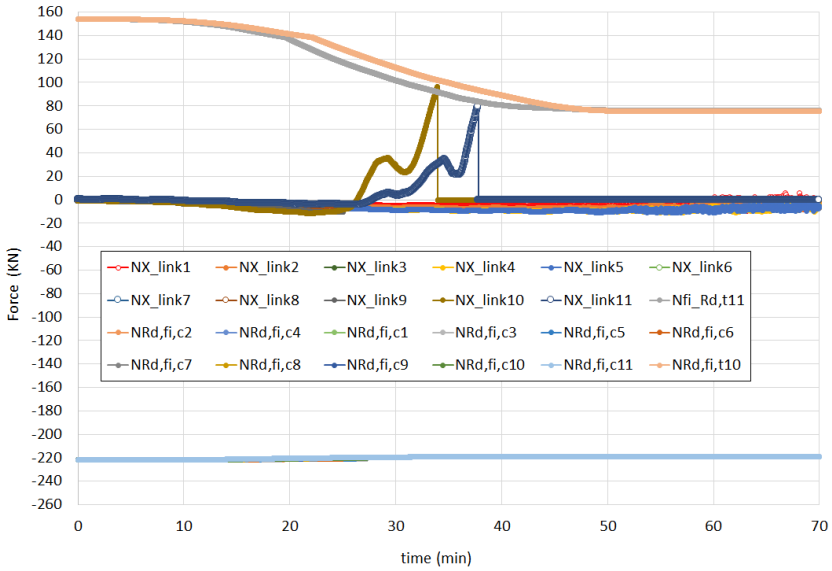

d) Axial force acting in the fusible link

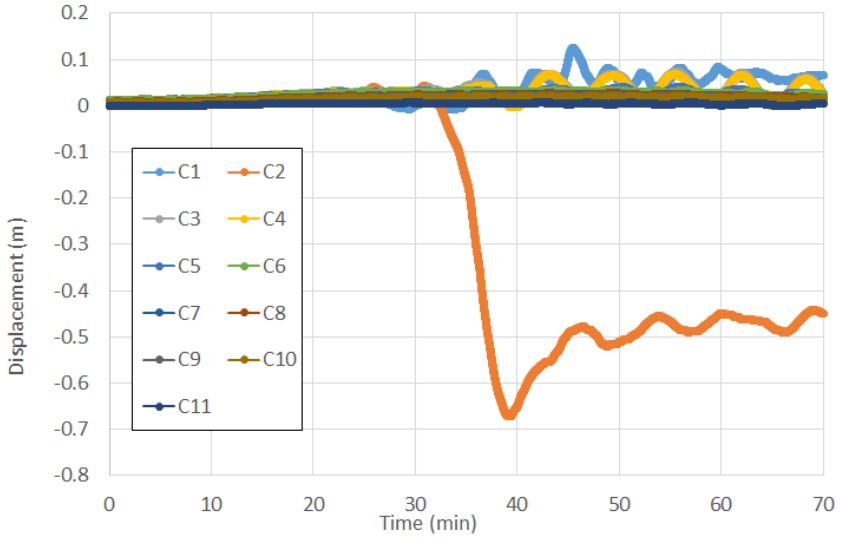

e) Horizontal displacement at three quarter of the height of the columns with fusible links

Figure 4.42: Temperatures, forces and displacements predicted for the study case n°9

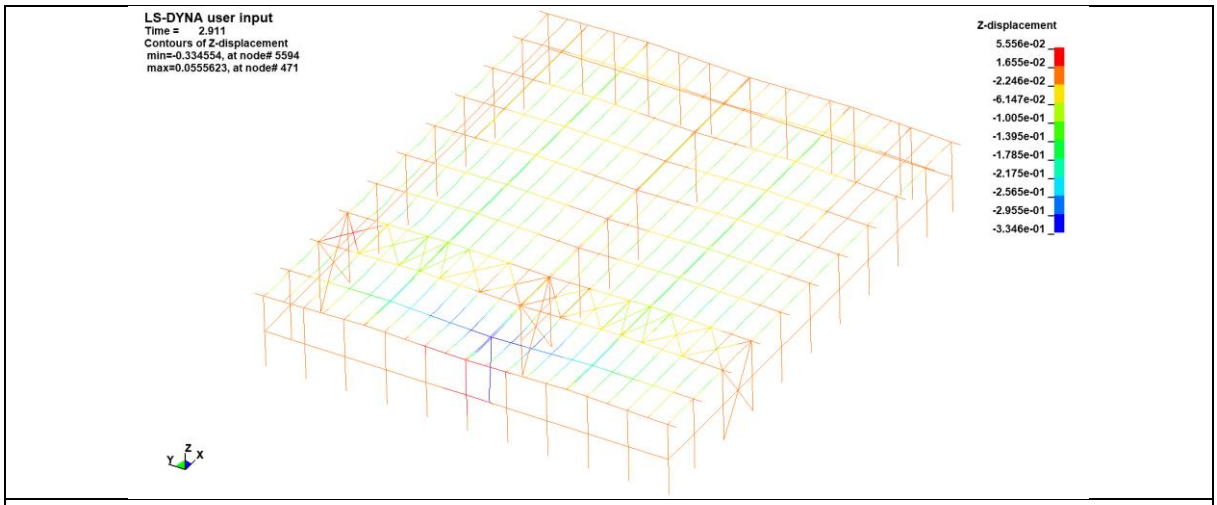

a) Deformed state after 24 minutes of exposure to fire

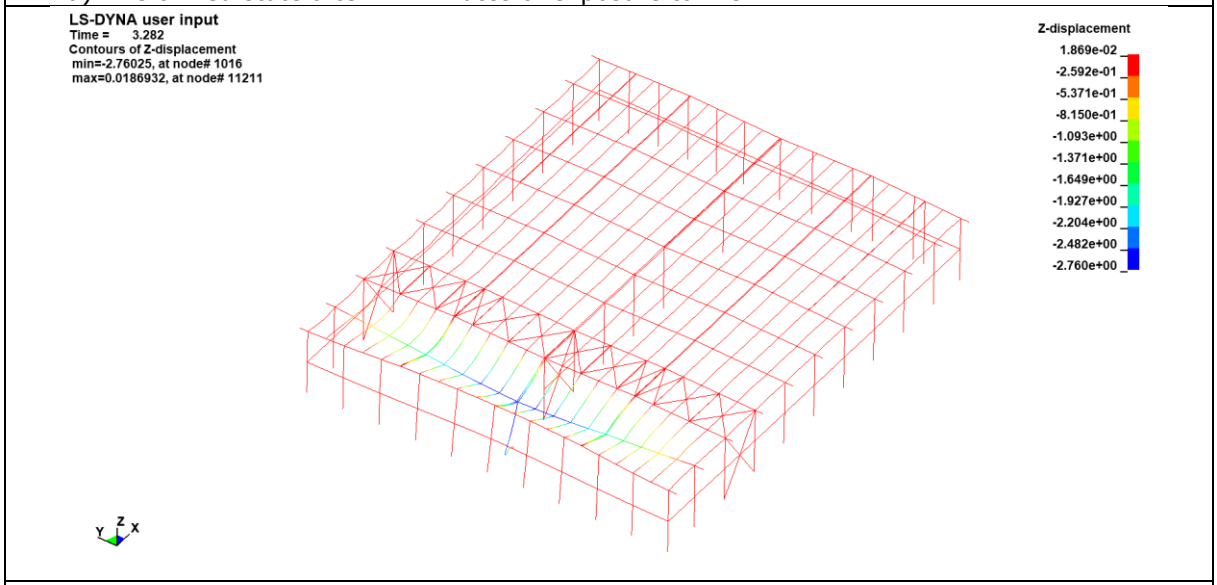

b) Deformed state after 28 minutes of exposure to fire

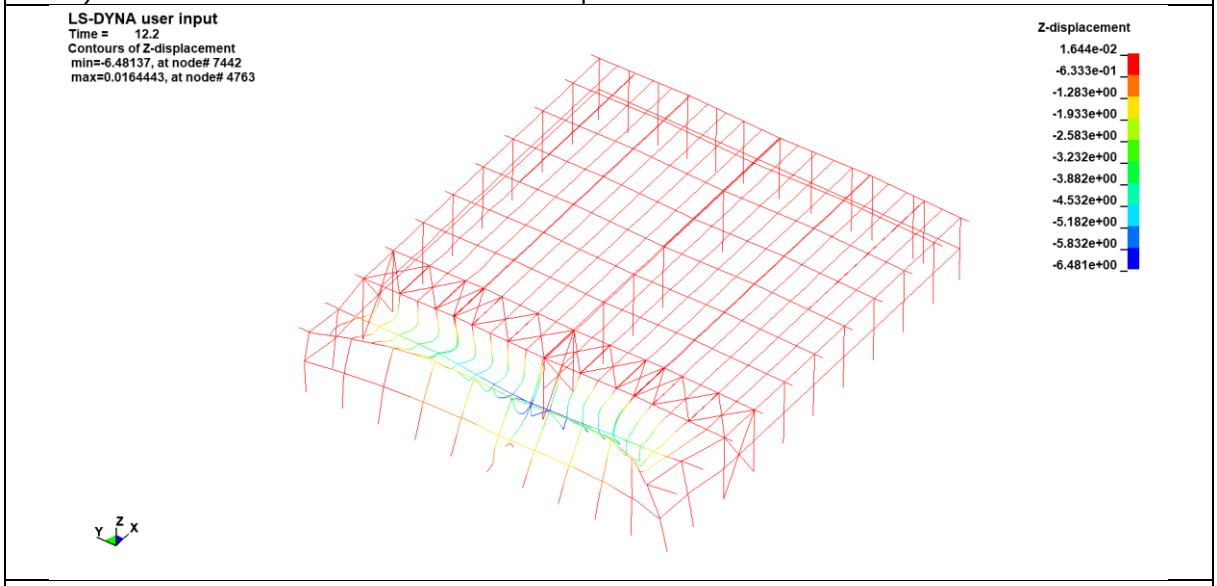

c) Deformed state after 117 minutes of exposure to fire

Figure 4.43: Deformed stated predicted for the fire exposed steel structure of the study case n°10

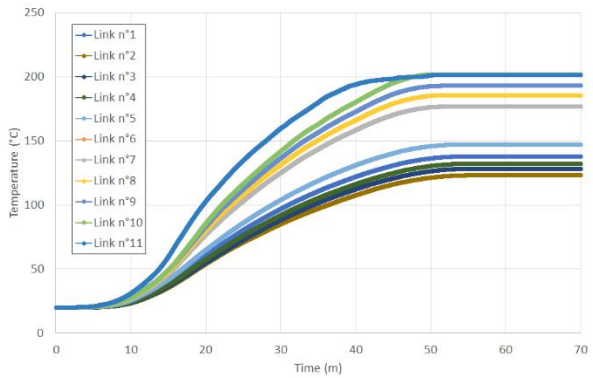

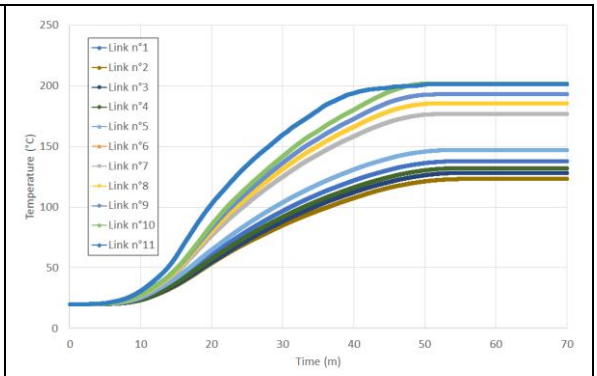

a) Temperature rise in aluminium bolts (Right and left sides in the plane of portal frames)

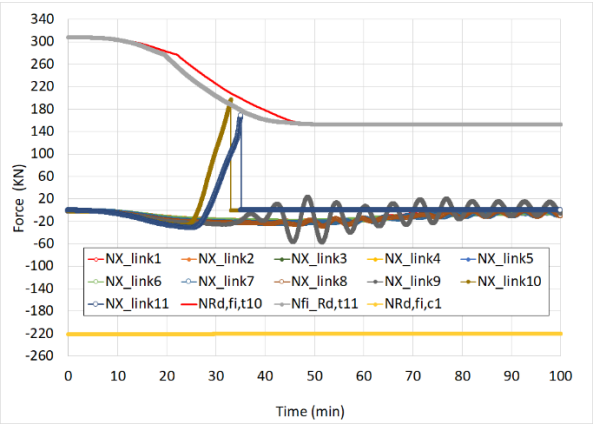

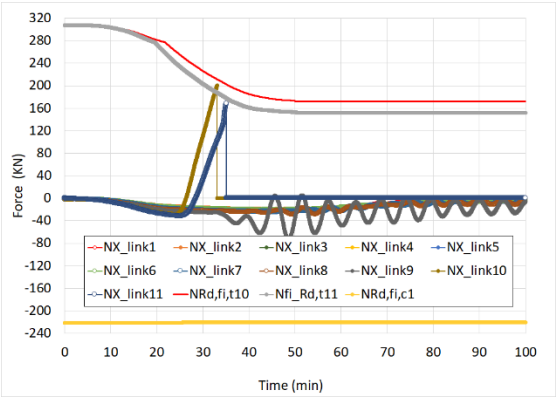

b) Axial force acting in the fusible link (Right and left sides in the plane of portal frames)

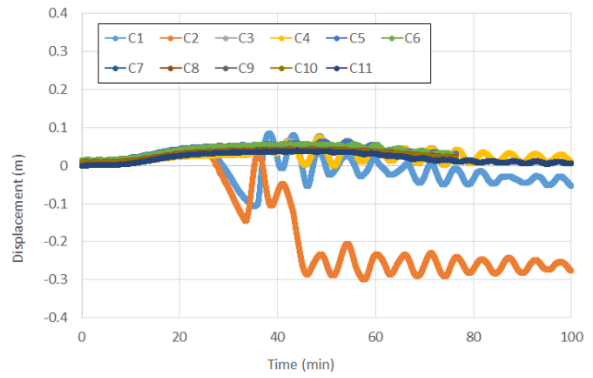

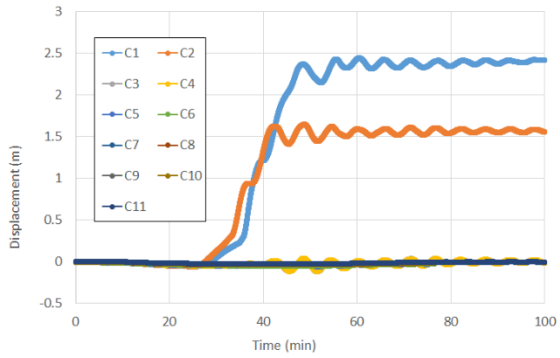

d) Horizontal displacement at three quarter of the height of columns with fusible links (Right and left sides in the plane of portal frames)

Figure 4.44: Temperatures, forces and displacements predicted for the study case n°10

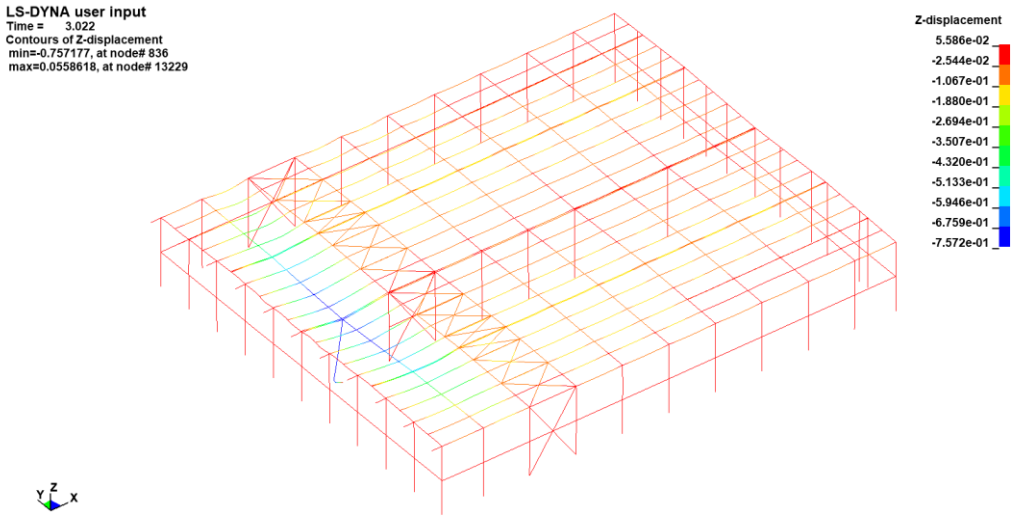

a) Deformed state after 25 minutes of exposure to fire

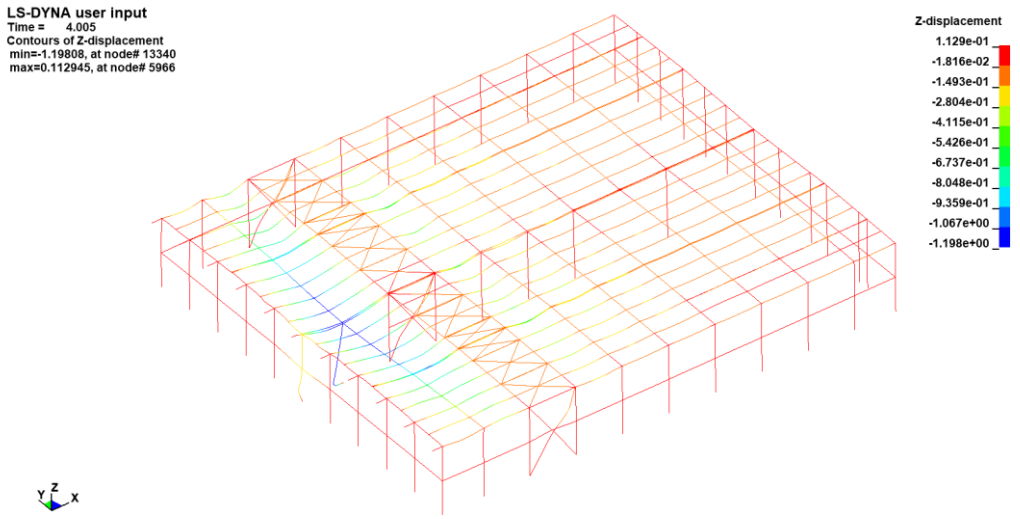

b) Deformed state after 35 minutes of exposure to fire

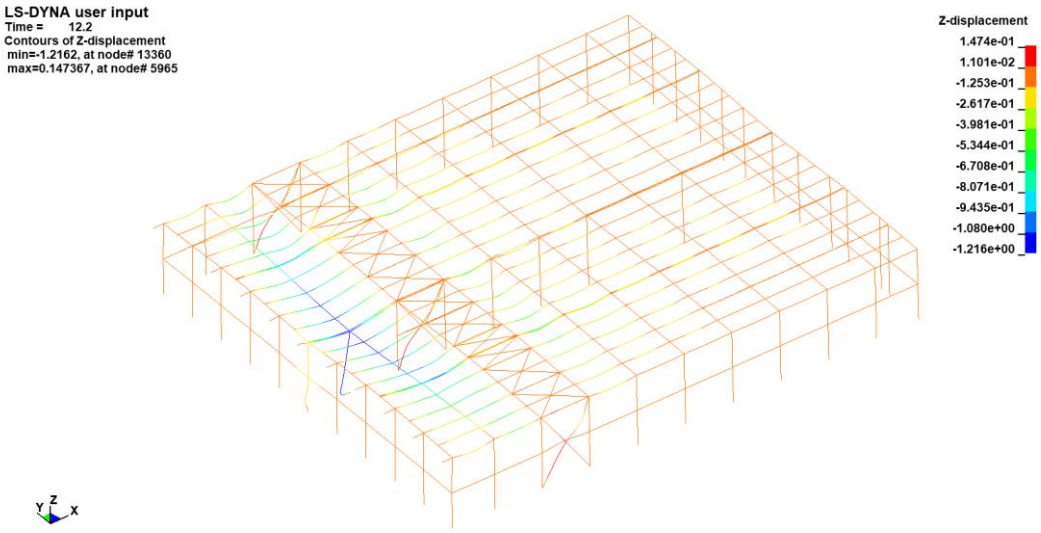

c) Deformed state after 115 minutes of exposure to fire

Figure 4.45: Deformed stated predicted for the fire exposed steel structure of the study case n°11

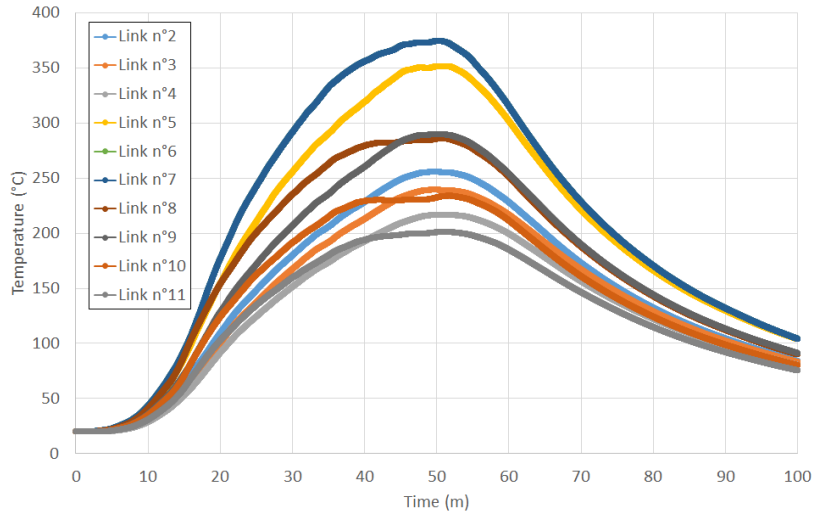

e) Temperature rise in aluminium bolts

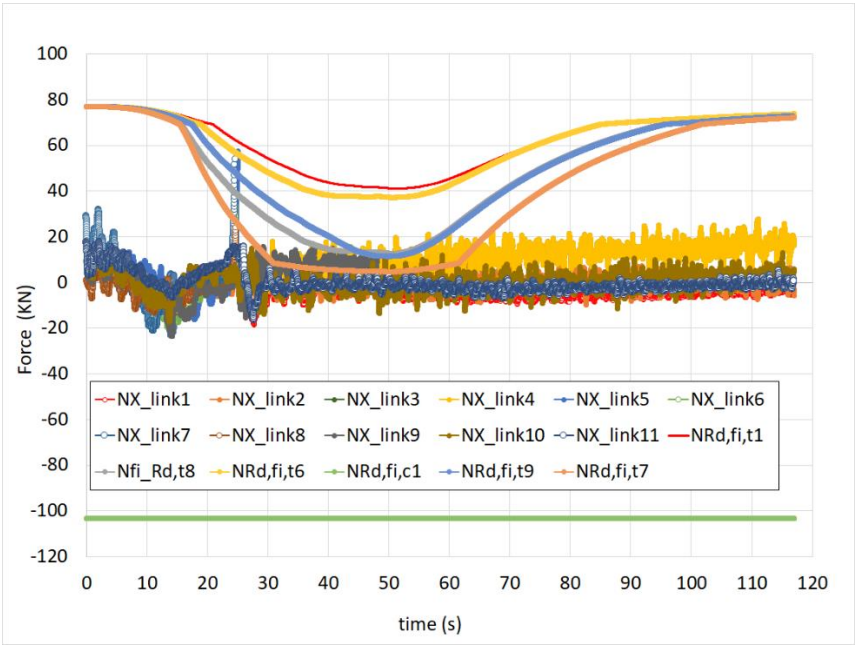

f) Axial force acting in the fusible link

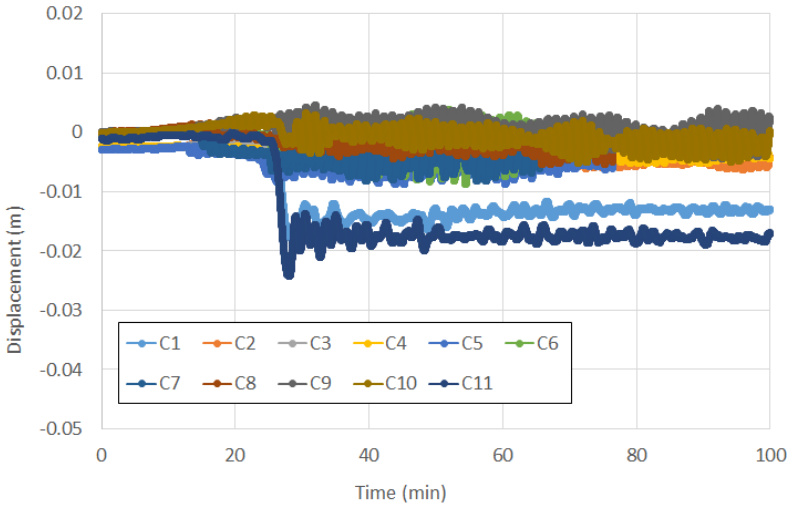

g) Horizontal displacement at three quarter of the height of columns with fusible links

Figure 4.46: Temperatures, forces and displacements predicted for the study case n°11

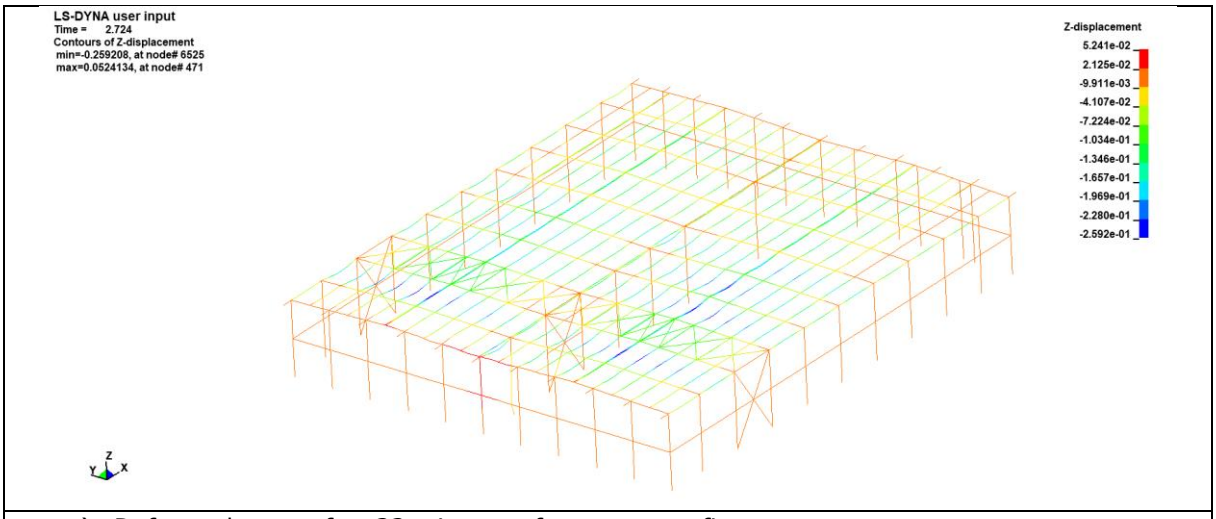

a) Deformed state after 22 minutes of exposure to fire

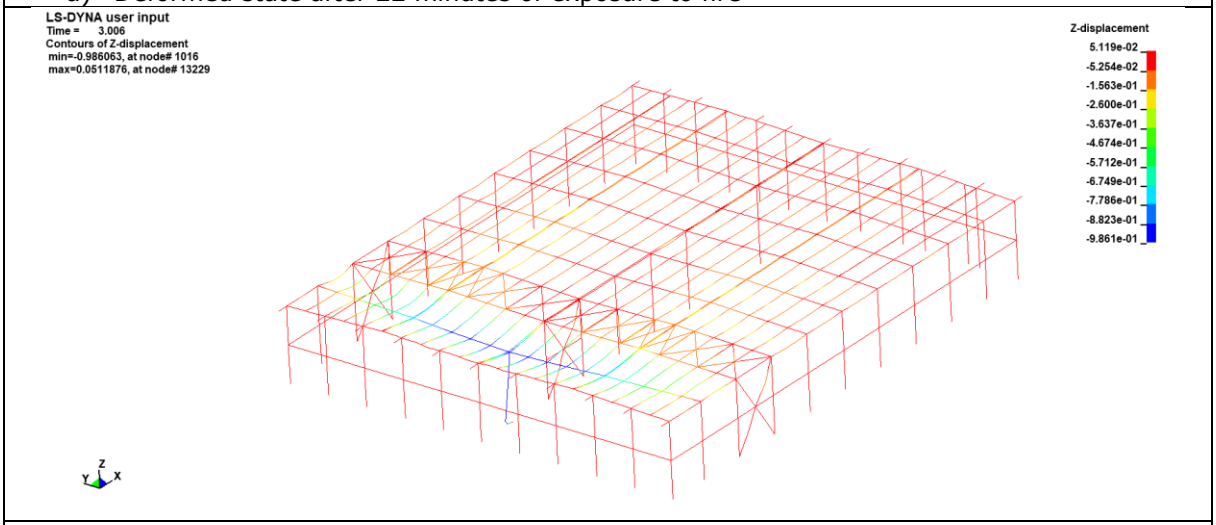

b) Deformed state after 25 minutes of exposure to fire

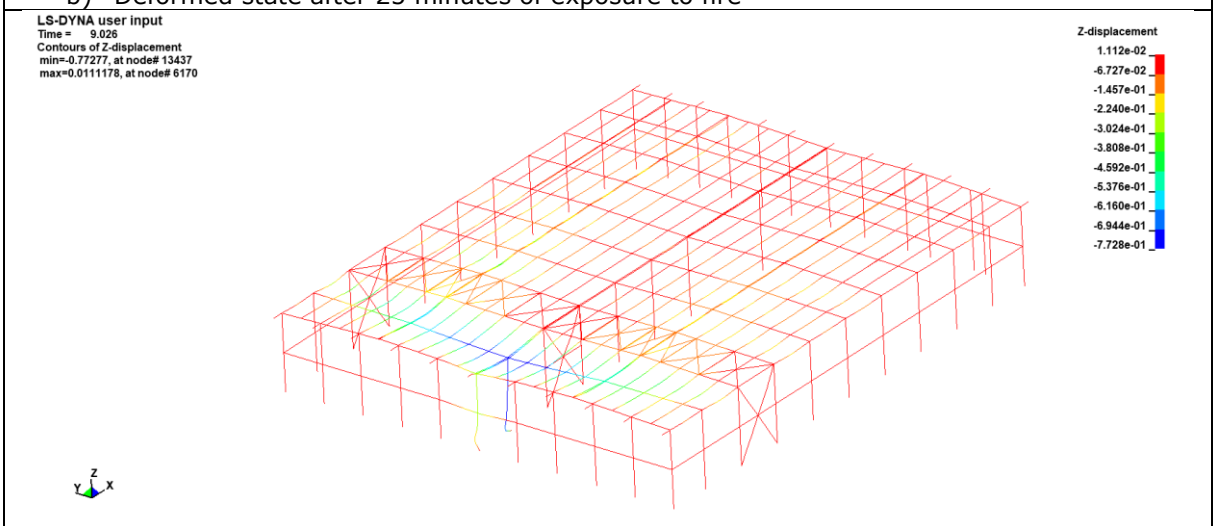

c) Deformed state after 85 minutes of exposure to fire

Figure 4.47: Deformed stated predicted for the fire exposed steel structure of the study case n°12

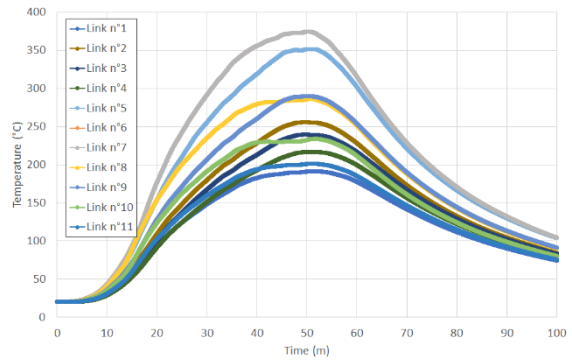

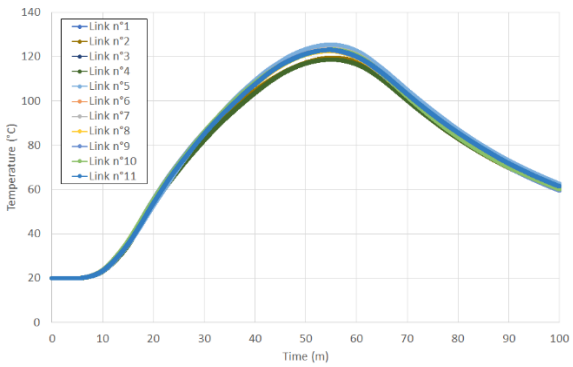

a) Temperature rise in aluminium bolts (Right and left sides in the plane of portal frames

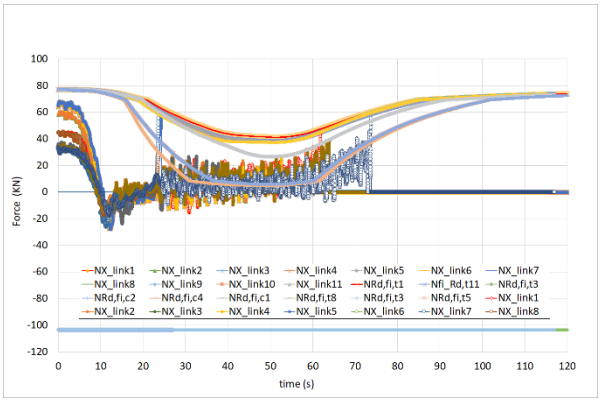

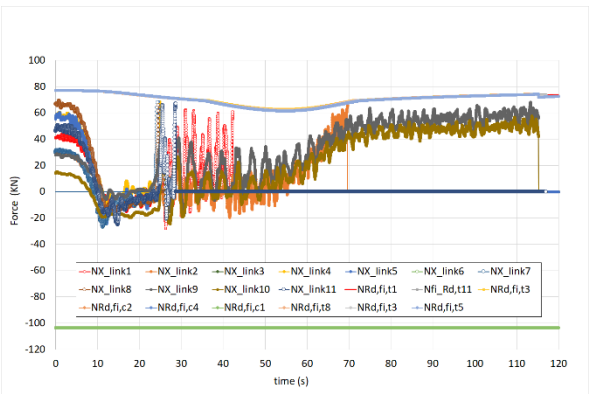

b) Axial force acting in the fusible link (Right and left sides in the plane of portal frames

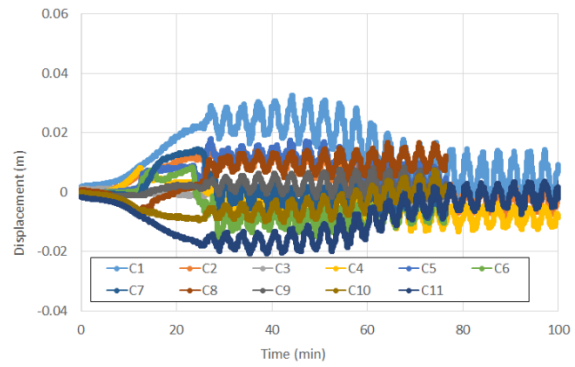

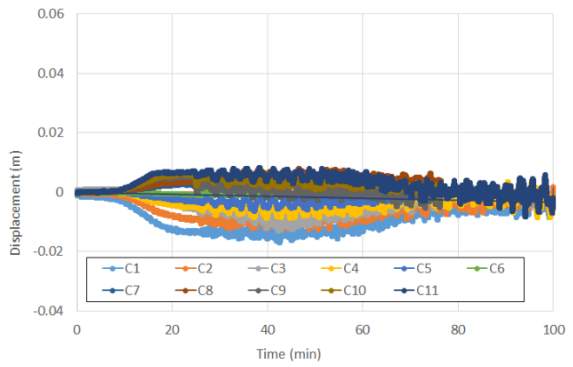

c) Horizontal displacement at three quarter of the height of columns with fusible links (Right and left sides in the plane of portal frames

Figure 4.48: Temperatures, forces and displacements predicted for the study case n°12

4.3.3 summary results

The main results of the 3D global structural analyses carried out on the study cases involving different fire scenario are summarised in the following table. The table indicates the failure mode of the steel structure (local or global), whether the fusible links broke, and the maximum value of the pushing forces acting on the fusible links.

Table 27: Summary of results of the ED global structural analyses

Case	Fire comp. number	Fire wall implementation	Maximum pushing force (KN)	Structure collapse	Fusible links breaks
1	2	perpendicular	24.5	Global	All
2	3	perpendicular	110	Global	All
3	2	parallel	22	global	All
4	3	parallel	23	global	All
5	2	perpendicular	23.5	Half of the structure	Fusible links at level of the collapsed part of the steel
6	3	perpendicular	45	Half of the structure	Fusible links at level of the collapsed part of the steel
7	2	parallel	24	Half of the structure	Fusible links at level of the collapsed part of the steel
8	3	parallel	22	Middle of the structure Localized to the most heated steel members: portal frame and purlins	Most of the fusible links
9	2	perpendicular	11	Structure edge impacted by fire	Two fusible links closest to the collapsed part of the steel
10	3	perpendicular	60	Structure edge impacted by fire	Two fusible links closest to the collapsed part of the steel on both side
11	2	parallel	23.5	Localized to the most heated steel members: portal frame and purlins	All
12	3	parallel	26.1	Localized to the most heated steel members: portal frame and purlins	All the fusible links along the gable frame closest to the fire source

5 CONCLUSION

The aim of this report is to present the results of parametric studies undertaken in a fire situation as part of the Fishwall project. Firstly, a parametric study was conducted on steel purlins passing through a fire wall made of sandwich panels, investigating purlin deformation in proximity to the fire wall and the impact of steel roof decking dimensions on purlin heating, particularly at the level of the purlin encasement. The results showed that an encasement system that only partially protects the purlin leads to a drastic decrease in the heating of the encased steel purlin parts, regardless of the dimensions of the steel sheets and whether the wave cavities are filled at the encasement level. The results also confirmed that, when the purlins fail, the purlin deformations are limited to the level of the encasement, with a plastic hinge forming at the end of the encasement, as observed experimentally. Based on these findings, it was recommended that the wall opening at the level of the purlins should be 100 mm larger than their cross-sectional dimensions. This should allow deformation of the purlins in and out of their plane to be absorbed without damaging the wall. It will also facilitate the passage of the purlins through the wall and the subsequent filling of the hole with mineral wool. As with the fire test, a mineral wool strip should be placed between the wall and the encasement system. A strip at least 50 mm thick is recommended. Then, the cover flashings enclosing the mineral wool strip should only be fixed to the wall panels.

Then, the results of the parametric study investigating the fire resistance of the three fusible links solution developed in the project were presented. This study aimed to create a database to develop simplified rules for determining the load-bearing capacity of the fusible links under standard fire conditions. The results allowed the different failure modes of the studied links, related to their components, to be identified, whether expected or not, and their complexity and interaction.

Finally, the results of 3D global structural analyses investigating the mechanical response of steel structures with fire walls and 'fusible' links under realistic fire conditions are presented. The main objective of these analyses was to verify the behaviour of the fusible links when designed in accordance with the design provisions proposed within the project. This involves ensuring that the fusible links on the fire-exposed side can withstand the pushing phase and, if the structure should collapse due to fire, that the fusible links on the fire-exposed side fail first during the tensile phase. The results showed that designing the fusible links to achieve a standard fire resistance of 15 minutes (R15) in compression ensures they can withstand the compressive forces induced by the thermal expansion of a steel structure exposed to fire, regardless of the fire scenario. The results also showed that not all of the fusible links necessarily broke during the tensile phase that characterise the collapse of the structure. This depended on the extent of the fire and collapse, as well as the temperatures reached by the links. If case of fully engulfed fires, all of the fusible links will heat up sufficiently and break due to insufficient traction resistance, disconnecting the fire-exposed structure from the firewalls and steel structures on the other side. For a localised fire, there are several possible scenarios: i) The fire remains localised and the structure is not damaged. It makes no difference whether the links break. ii) The fire remain remains localised and leads to a localised collapse of the structure. If this collapse occurs near a fire wall, the temperature in the compartment will be high enough to cause the links on the fire side to fail. Note that aluminium bolts lose 25% of their strength at 150°C and 50% at 200°C. However, if the fire is far from the wall, the links may not heat up much. In this case, designing the fusible links on the unexposed side to withstand the tensile forces induced by the collapse of the fire-exposed structure will ensure they remain sufficiently resistant on both sides of the wall. The study's results indicated that the existing rules for calculating tensile forces provide safe values for these forces.

6 REFERENCES

[1] Vaněk J., FISHWALL project, RFSC-2020, GAN 101034083, Work Package 3, Deliverable 3.3, Fire test report on fire wall connected to an unprotected steel structure by means of fusible links, 2023.

[2] Vaněk J., FISHWALL project, RFSC-2020, GAN 101034083, Work Package 3, Deliverable 3.2, Fire test reports on partition fire walls made of sandwich panels with large spans, 2023.

[3] Vijayakumar M., Kozich M. and Wald F. FISHWALL project, RFSC-2020, GAN 101034083, Work Package 3, Deliverable 3.1, Experimental analysis of mechanical behaviour of aluminium bolts at ambient and elevated temperature, 2022.

[4] EN 1990: Eurocode – Basis of structure design, Brussels, Belgium, CEN, 2003.

[5] EN 1991-1-2: Eurocode 1: Actions on structures - Part 1-2: General actions - Actions on structures exposed to fire, Brussels, Belgium, CEN, 2002.

[6] EN 1993-1-1: Eurocode 3: Design of steel structures. Part 1-1: General rules and rules for buildings, CEN, 2005.

[7] EN 1993-1-2: Eurocode 3: Design of steel structures – Part 1-2: General rules – Structural fire design, Brussels, Belgium, CEN, 2005.

[8] EN 1999-1-2, Eurocode 9: Design of aluminium structures - Part 1-2: Calculation of fire behaviour, Brussels, Belgium, CEN, 2007.

[9] ANSYS, ANSYS User's Manual for Revision 8.0 – Volume IV – Theory, Swanson Analysis LINK, INC., Houston USA, 1992.

[10] Vaněk J., FISHWALL project, RFSC-2020, GAN 101034083, Work Package 3, Deliverable 3.2, Fire test report on a fire wall solidly attached to an unprotected steel structure and penetrated by steel purlins, 2024.

[11] CTICM, Eurocodes – fire parts: Proposal for a methodology to check the accuracy of assessment methods, technical report MZE-99/83-JK/IM, 2014.

[12] Renaud C., FISHWALL project, RFSC-2020, GAN 101034083, Work Package 3, Deliverable 3.4, Development and validation of FE numerical models, 2025.

[13] Vaněk J., FISHWALL project, RFSC-2020, GAN 101034083, Work Package 3, Deliverable 3.3, Fire test report on fire wall connected to an unprotected steel structure by means of fusible links, 2023.

[14] Vijayakumar M., Kozich M. and Wald F. FISHWALL project, RFSC-2020, GAN 101034083, Work Package 3, Deliverable 3.1, Experimental analysis of mechanical behaviour of aluminium bolts at ambient and elevated temperature, 2022

[15] Vaněk J., FISHWALL project, RFSC-2020, GAN 101034083, Work Package 3, Deliverable 3.2, Fire test report on a fire wall solidly attached to an unprotected steel structure and penetrated by steel purlins, 2024.

[16] CTICM, EuroPratic Guide:Application guide for Eurocode 3. CTICM Edition, 2015.

[17] BRE, ARCELOR Profil Luxembourg, TNO Efectis, Université de Liège & CTICM, Final Report of RFCS Project FIRESTRUC - Integrating advanced three-dimensional modelling methodologies for predicting thermo-mechanical behaviour of steel and composite structures subjected to natural fires, Mars 2007.

[18] ANSYS, ANSYS User's Manual for Revision 8.0 – Volume IV – Theory, Swanson Analysis SYSTEM, INC., Houston USA, 1992.

[19] Ls-dyna, Theory and Keywords Manuals, 2018.

[20] Zhao B., Desanghere S., Darche J., CFD and FEM coupling with computer codes FDS and Ansys for fire resistance assessment, Interflam 2007, pp1461-1466.

[21] Henneton N. and Renaud C., FISHWALL project, RFSC-2020, GAN 101034083, Work Package 1, Deliverable D1.1, Current practice for single storey steel framed buildings and review of fire and seismic regulations, 2021.

[22] Henneton N. and Tramoni J-B., FISHWALL project, RFSC-2020, GAN 101034083, Work Package 1, Deliverable D1.2, Analysis of real fire development in typical single storey building, 2021.

[23] Renaud C., FISHWALL project, RFSC-2020, GAN 101034083, Work Package 5, Deliverable 5.2, Design guidance and constructional details for the investigated fire wall solution, 2025.

[24] Renaud C., FISHWALL project, RFSC-2020, GAN 101034083, Work Package 5, Deliverable 5.3, Design guide, 2025.

APPPENDIX A. TEMPERATURES PREDICTED FROM THE FE THERMAL MODELS ACCORDING TO THE STEEL DECK SIZES

A.1. Thermal analysis without additional wave cavity filling

A.1.1. Purlin with steel sheet JI-42-252-1010

This section shows the predicted temperature rises in the purlin that supports the JI-42-252-1010 type steel sheets.

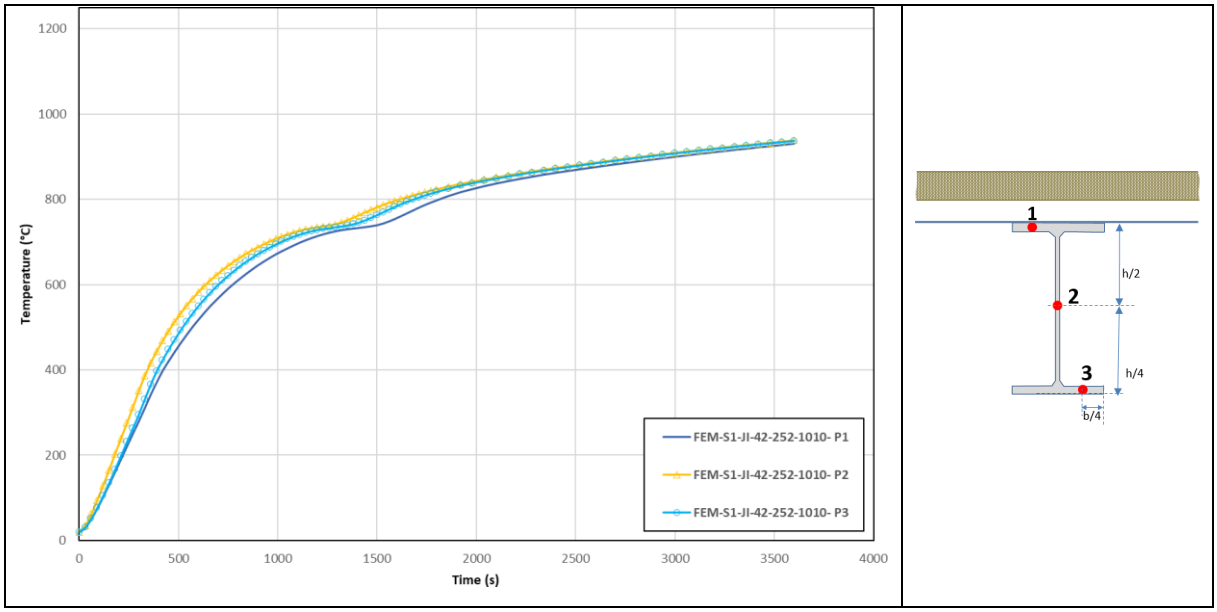

Figure A.1: Predicted temperatures in purlin cross-section S1

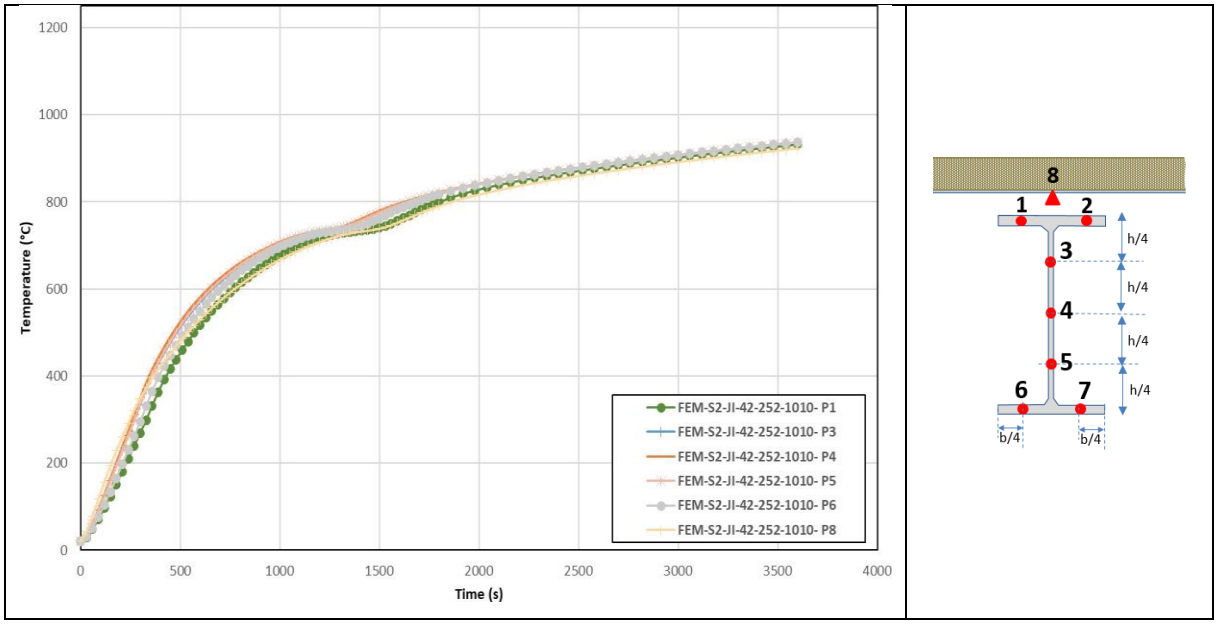

Figure A.2: Predicted temperatures in purlin cross-section S2

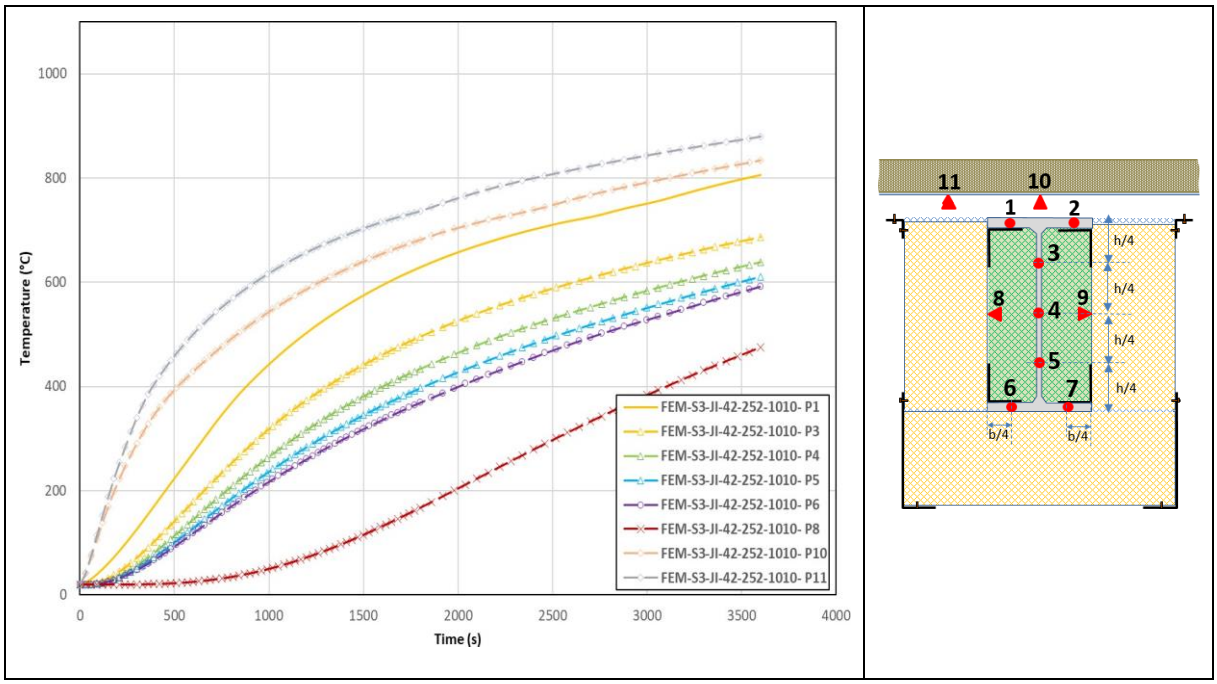

Figure A.3: Predicted temperatures in purlin cross-section S3

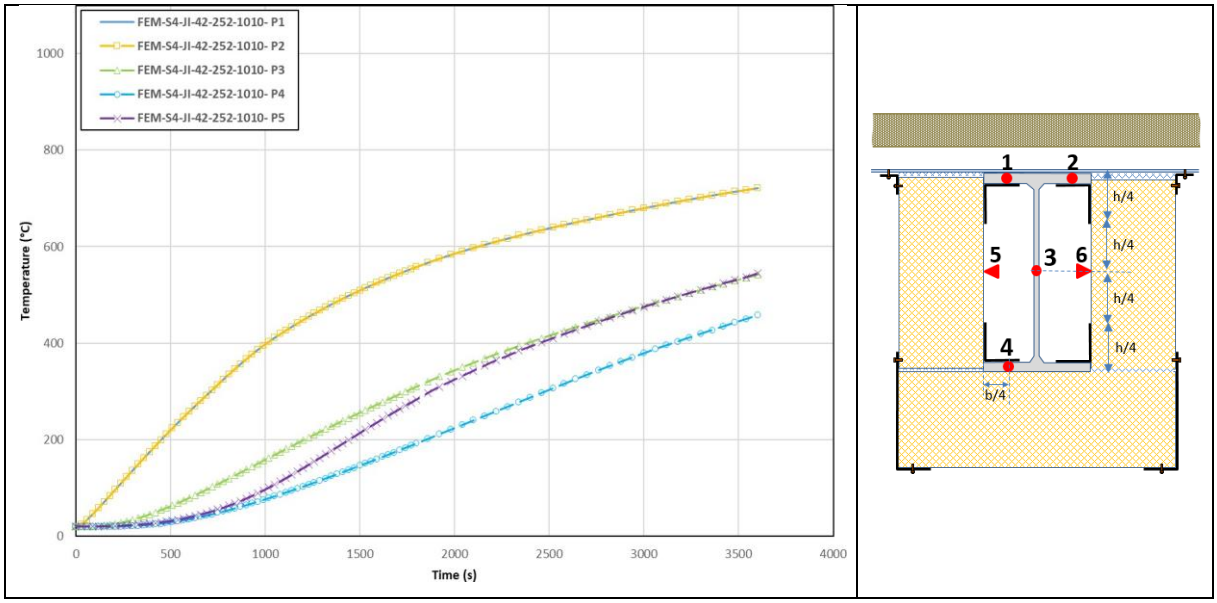

Figure A.4: Predicted temperatures in purlin cross-section S4

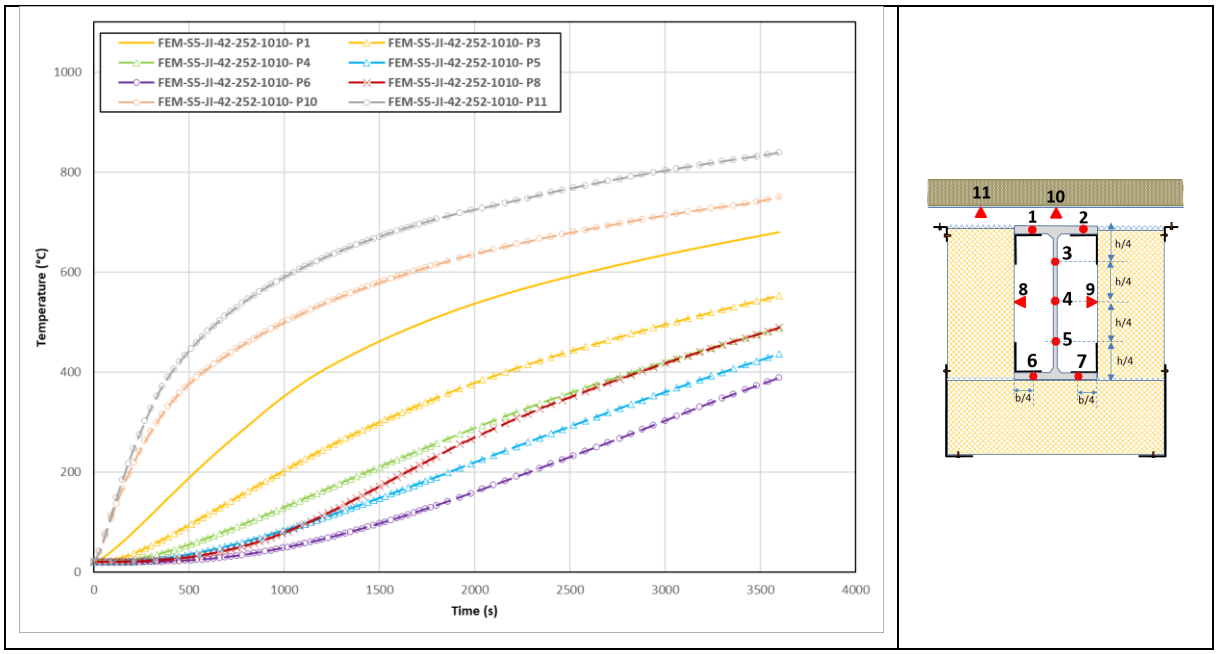

Figure A.5: Predicted temperatures in purlin cross-section S5

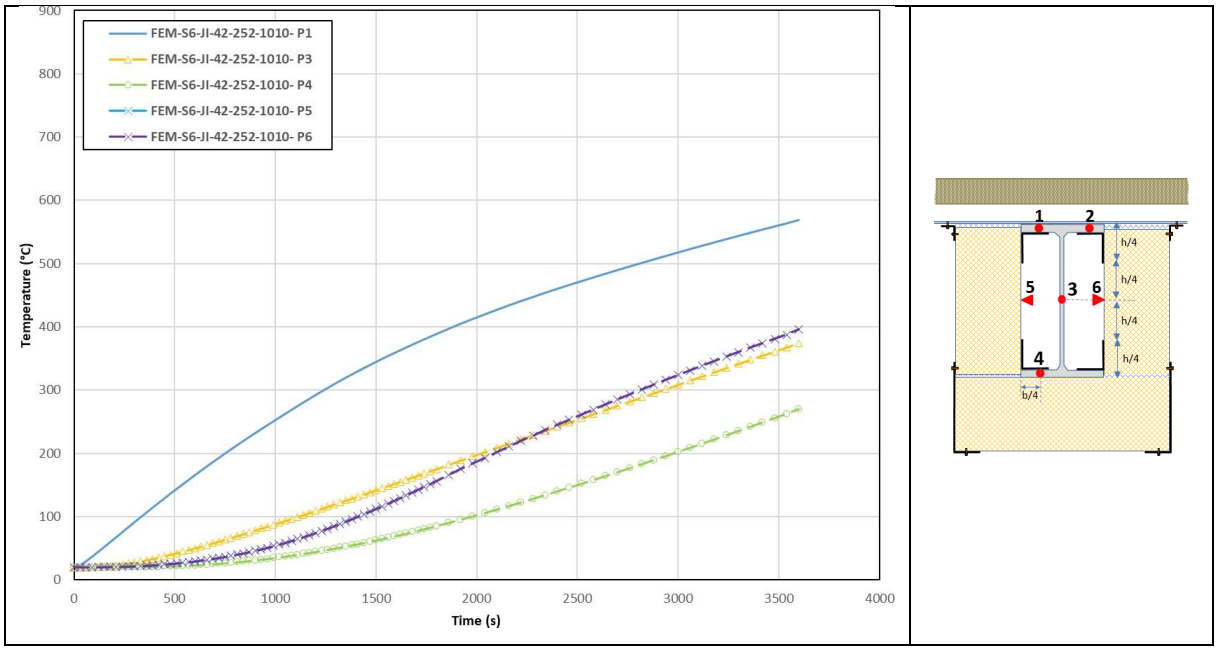

Figure A.6: Predicted temperatures in purlin cross-section S6

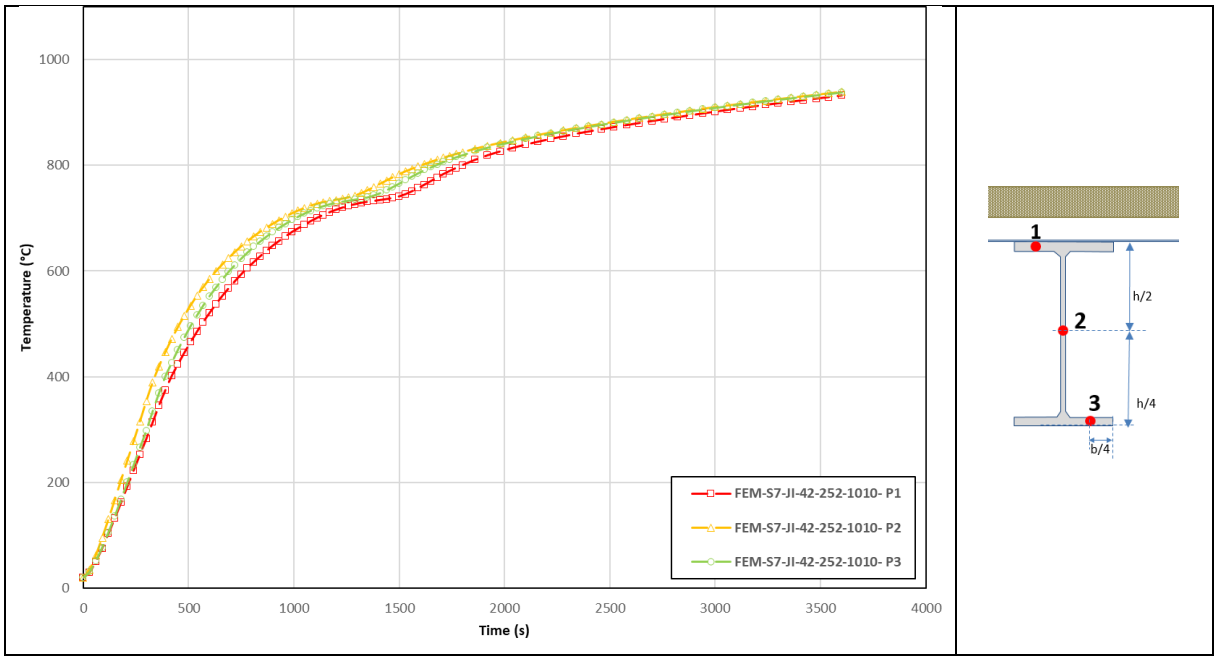

Figure A.7: Predicted temperatures in purlin cross-section S7

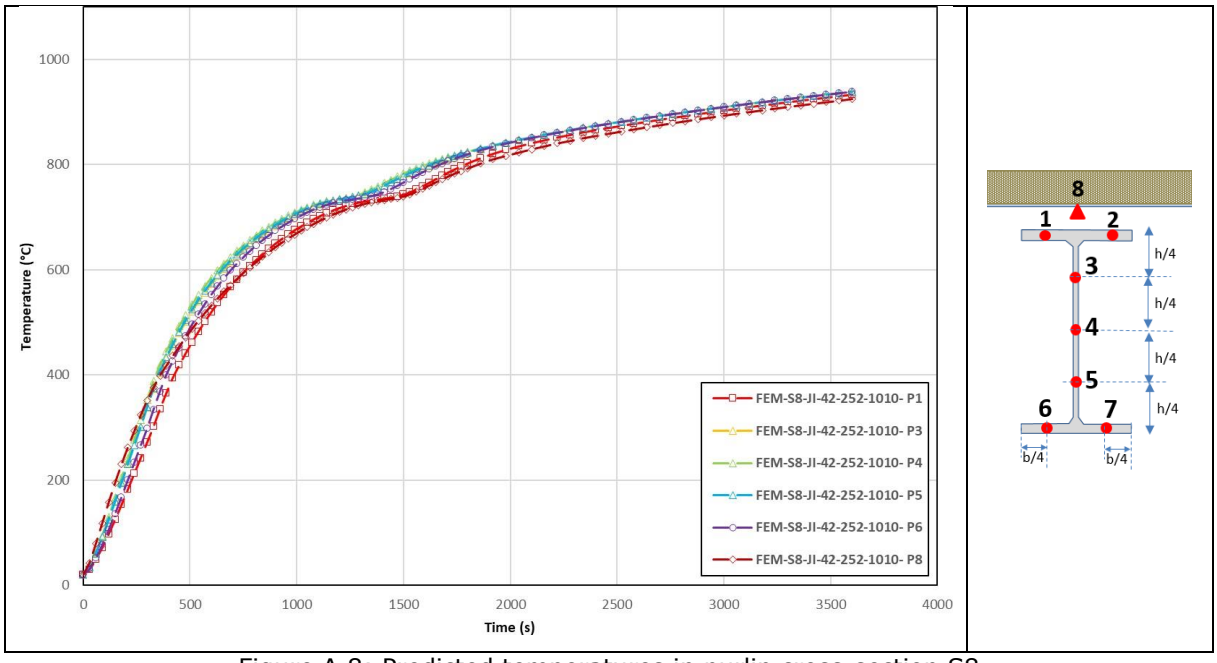

Figure A.8: Predicted temperatures in purlin cross-section S8

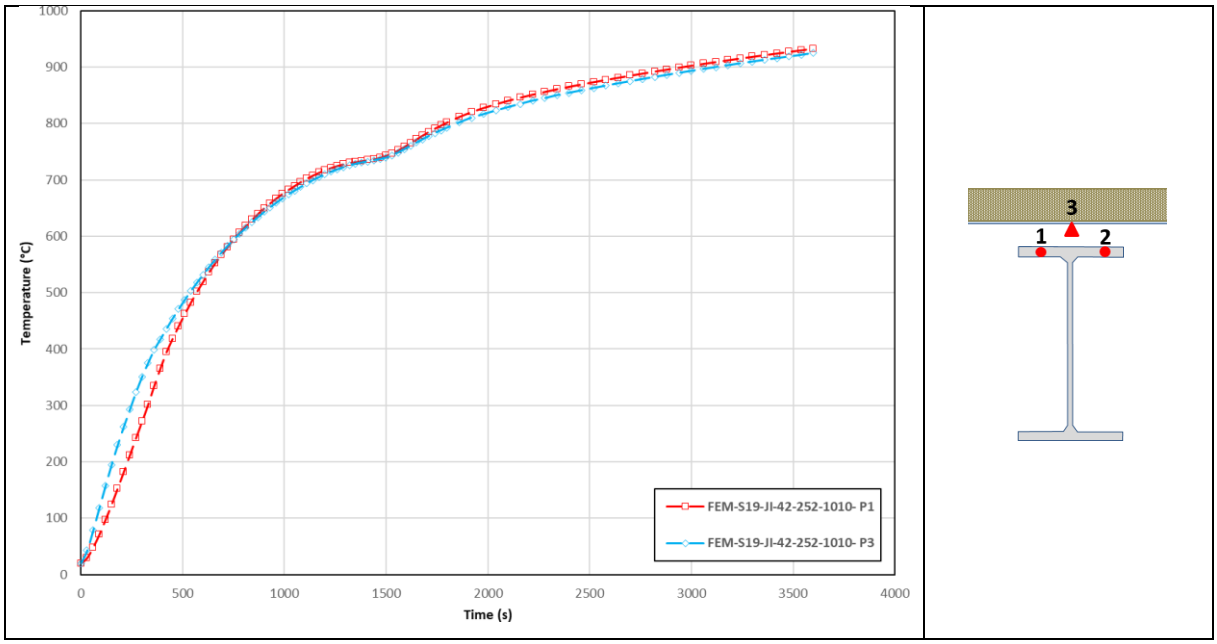

Figure A.9: Predicted temperatures in purlin cross-section S19

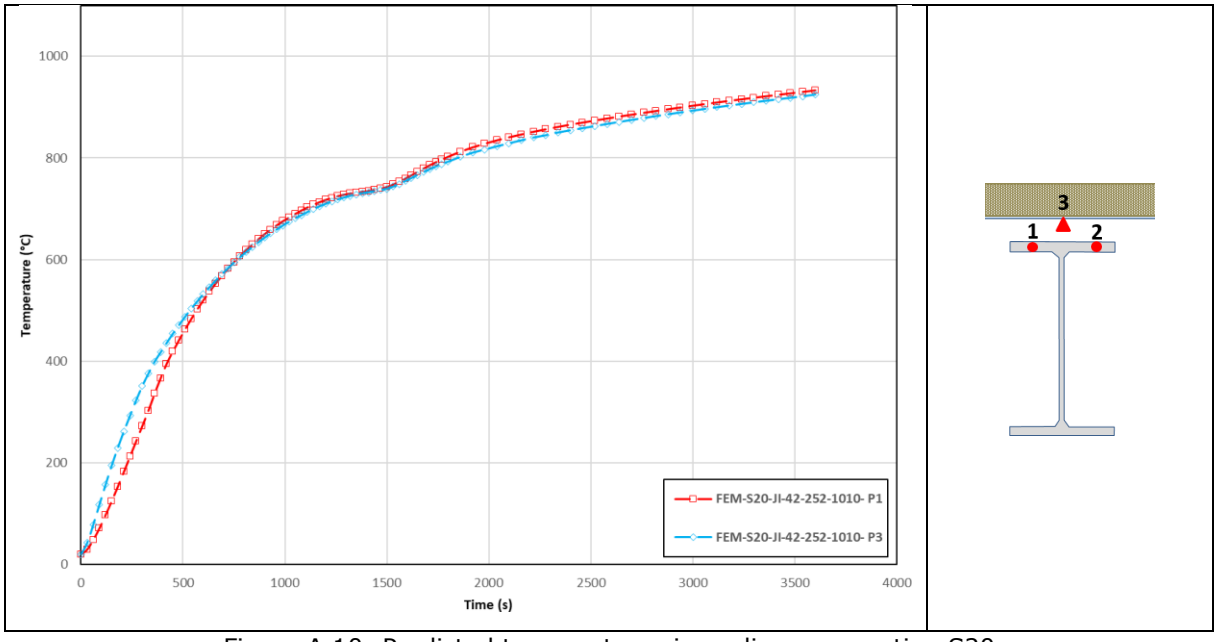

Figure A.10: Predicted temperatures in purlin cross-section S20

A.2. Purlin with steel sheet JI-73-195-780

This section shows the predicted temperature rises in the purlin that supports the JI-73-195-780 type steel sheets.

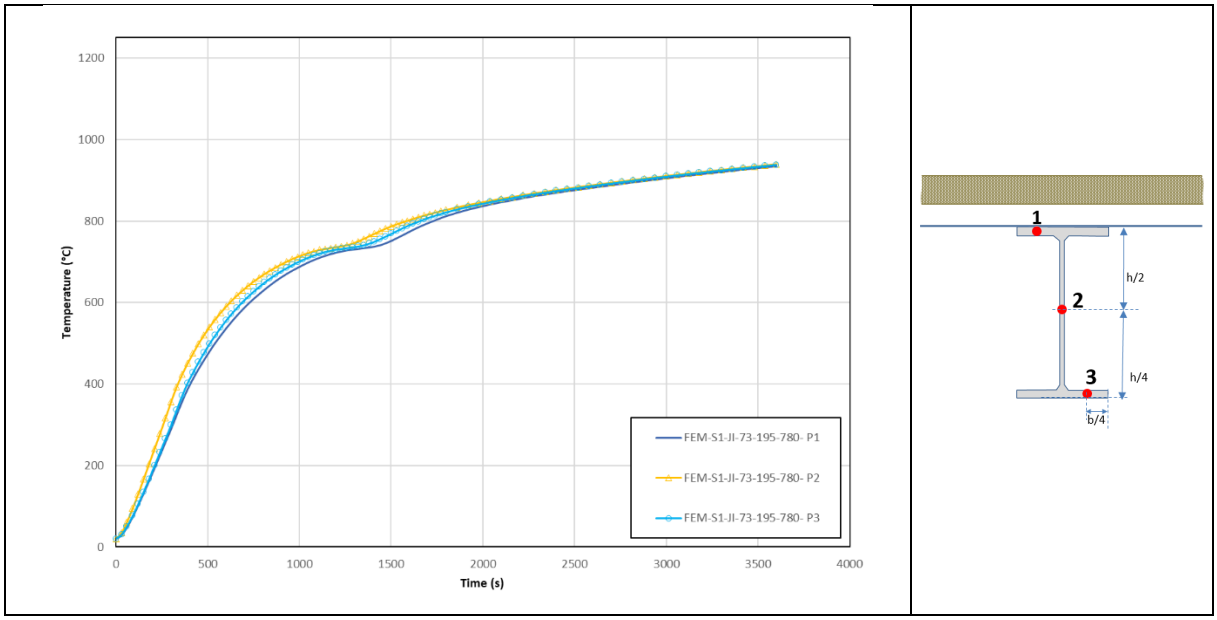

Figure A.11: Predicted temperatures in purlin cross-section S1

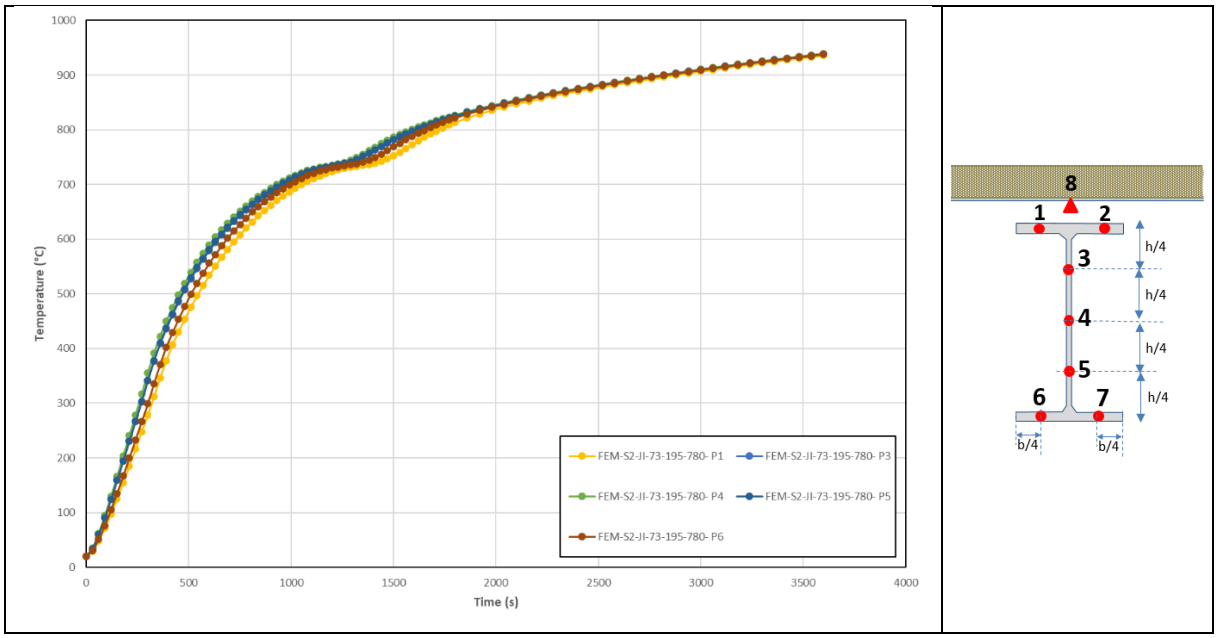

Figure A.12: Predicted temperatures in purlin cross-section S2

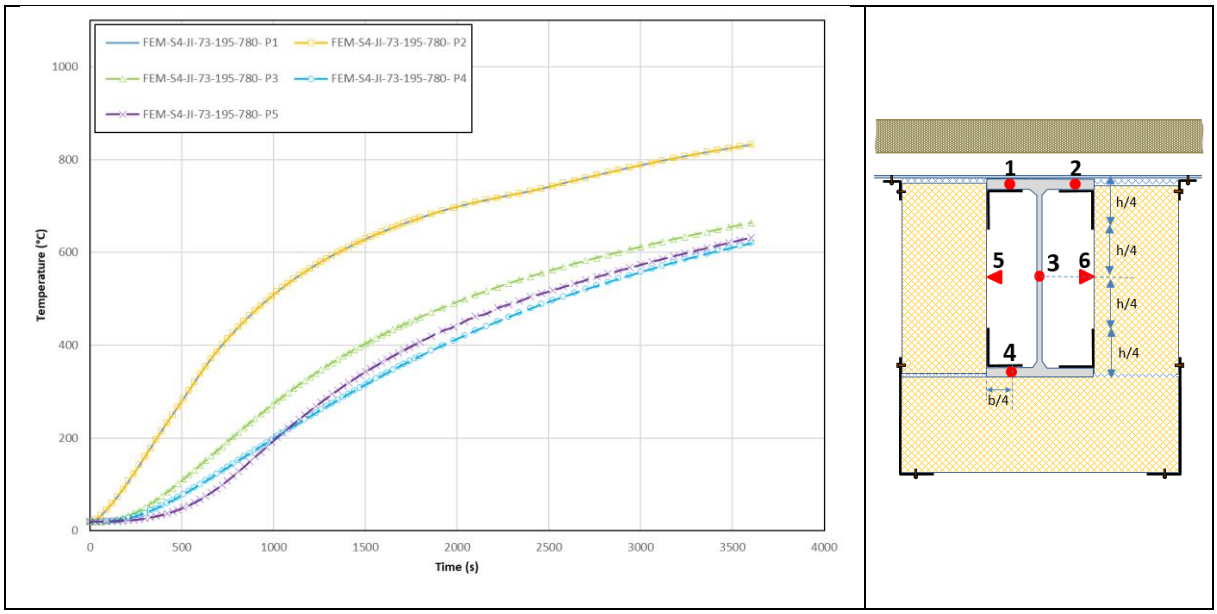

Figure A.13: Predicted temperatures in purlin cross-section S4

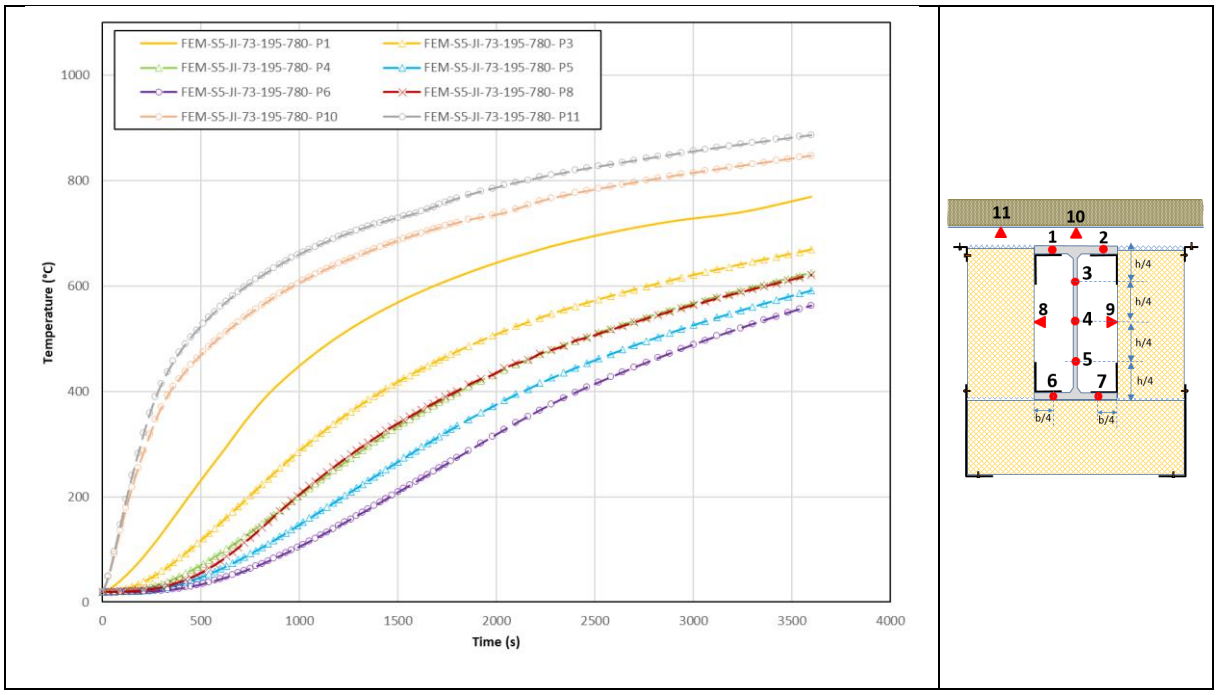

Figure A.14: Predicted temperatures in purlin cross-section S5

A.3. Purlin with steel sheet JI-113-320-960

This section shows the predicted temperature rises in the purlin that supports the JI-113-320-960 type steel sheets.

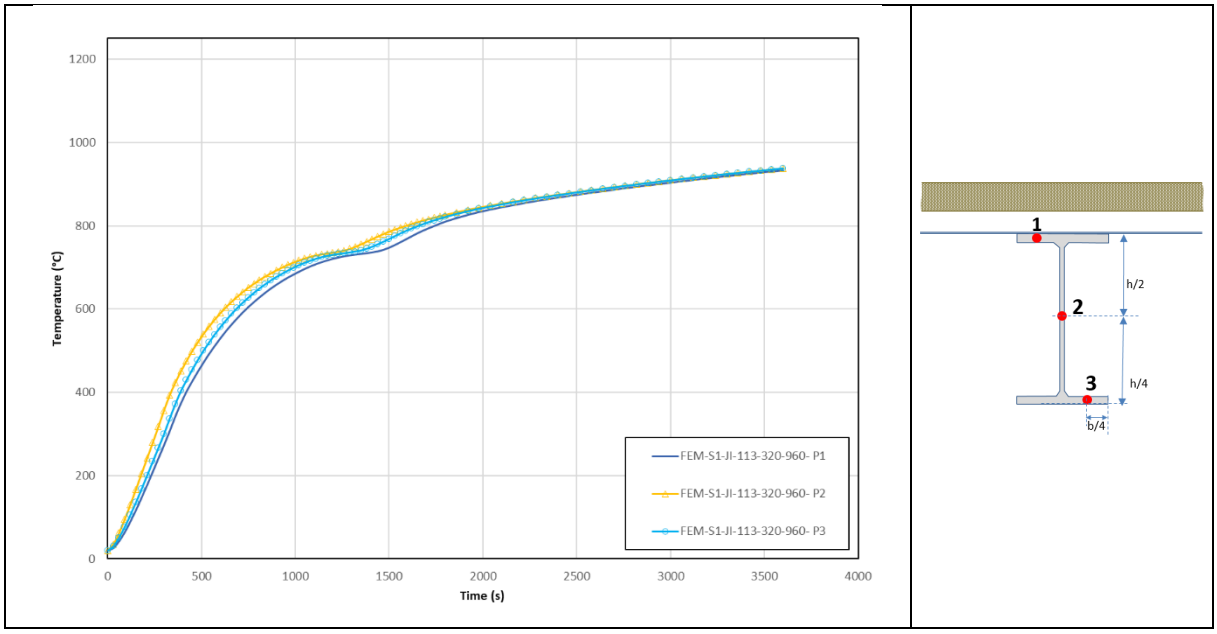

Figure A.15: Predicted temperatures in purlin cross-section S1

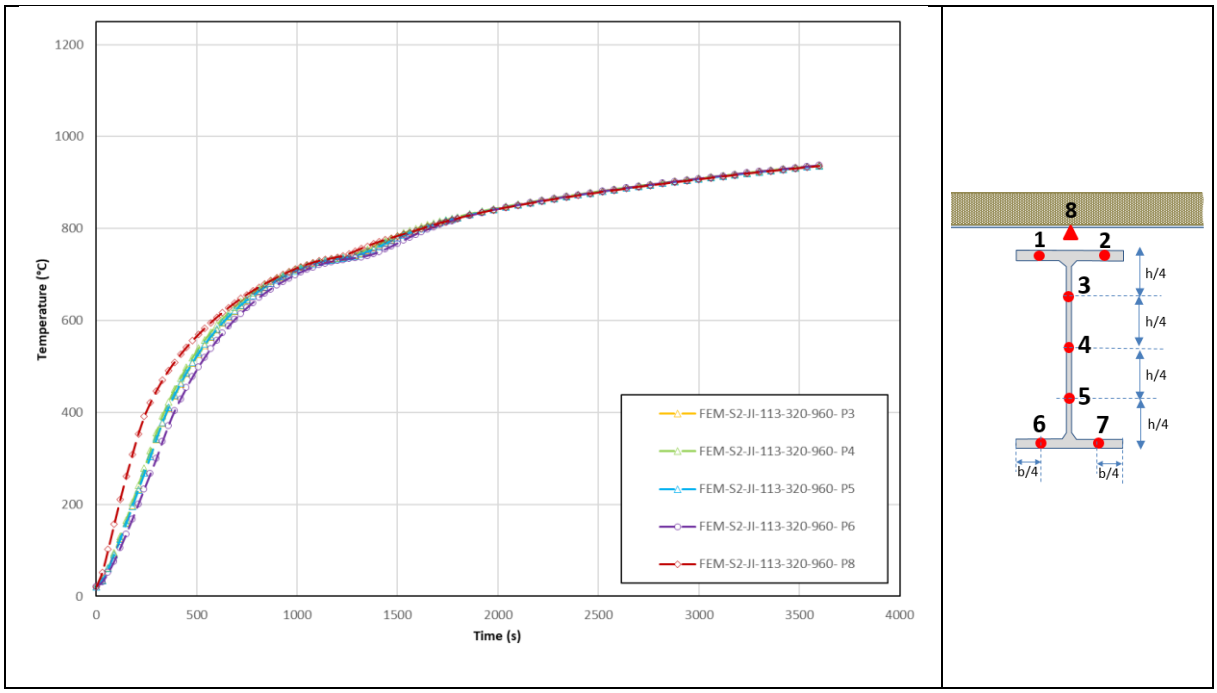

Figure A.16: Predicted temperatures in purlin cross-section S2

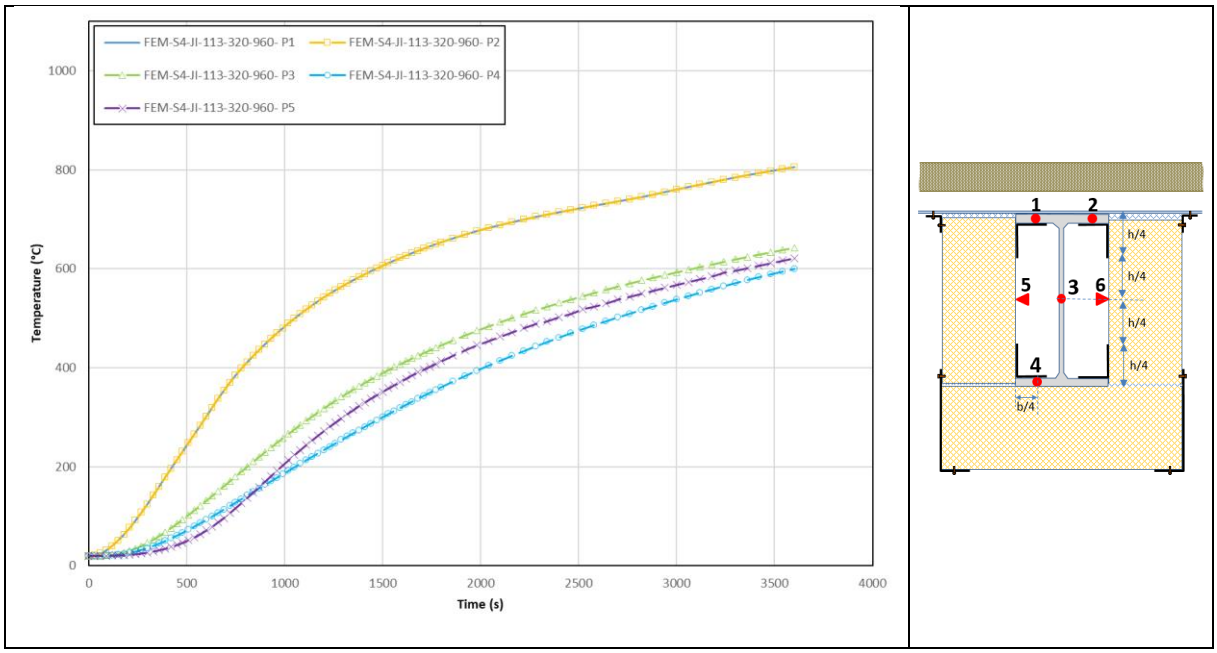

Figure A.17: Predicted temperatures in purlin cross-section S4

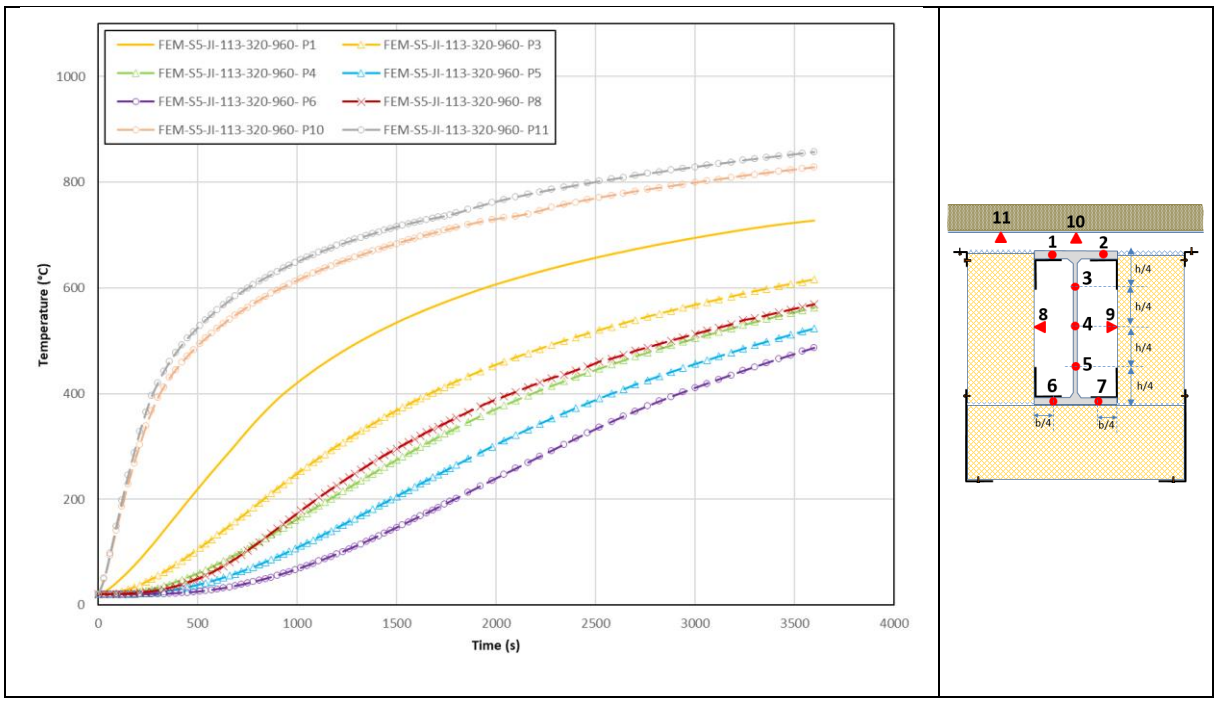

Figure A.18: Predicted temperatures in purlin cross-section S5

A.4. Purlin with steel sheet JID-137-310-930

This section shows the predicted temperature rises in the purlin that supports the JID-137-310-930 type steel sheets.

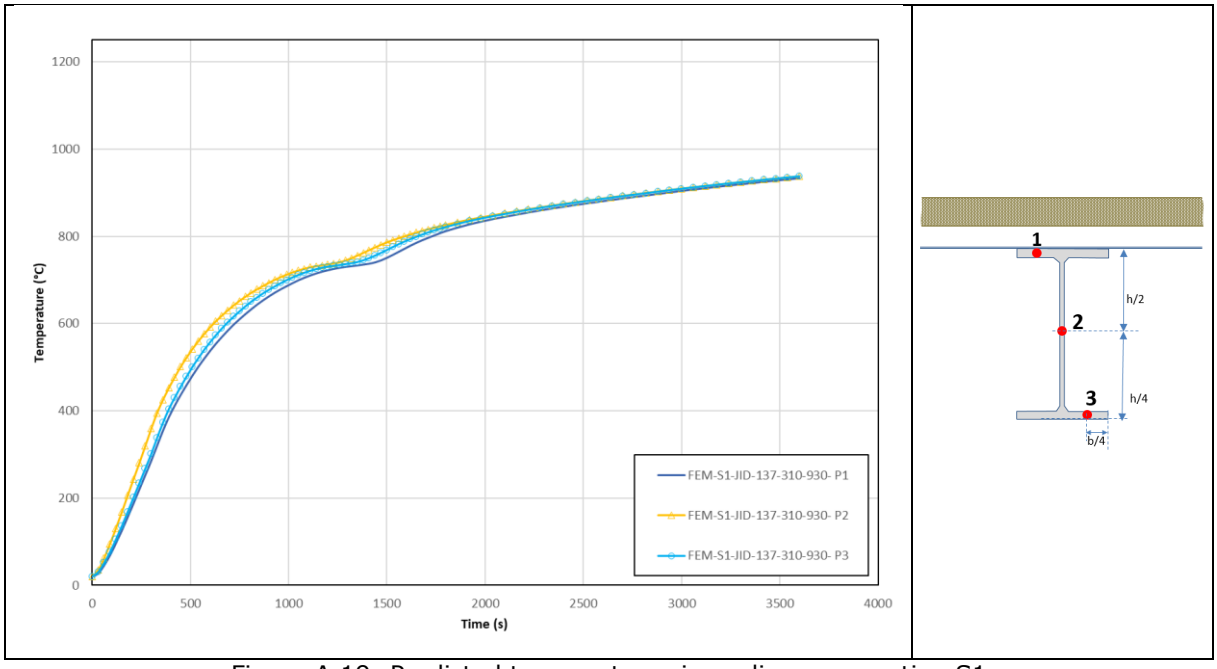

Figure A.19: Predicted temperatures in purlin cross-section S1

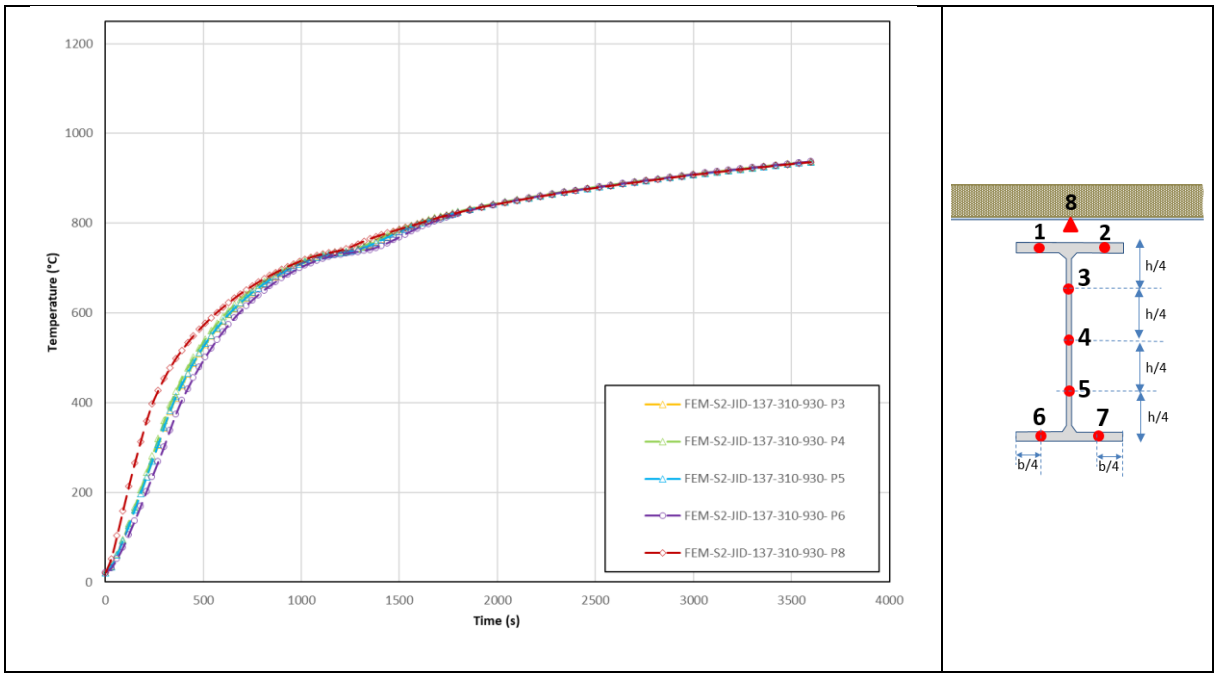

Figure A.20: Predicted temperatures in purlin cross-section S2

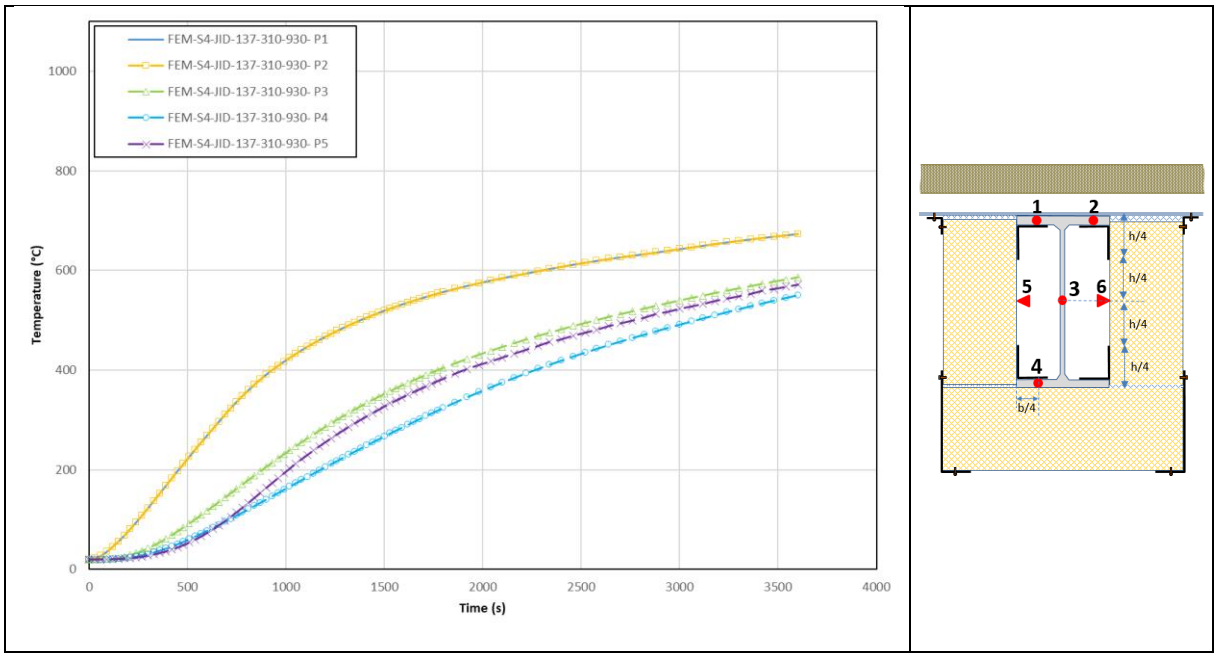

Figure A.21: Predicted temperatures in purlin cross-section S4

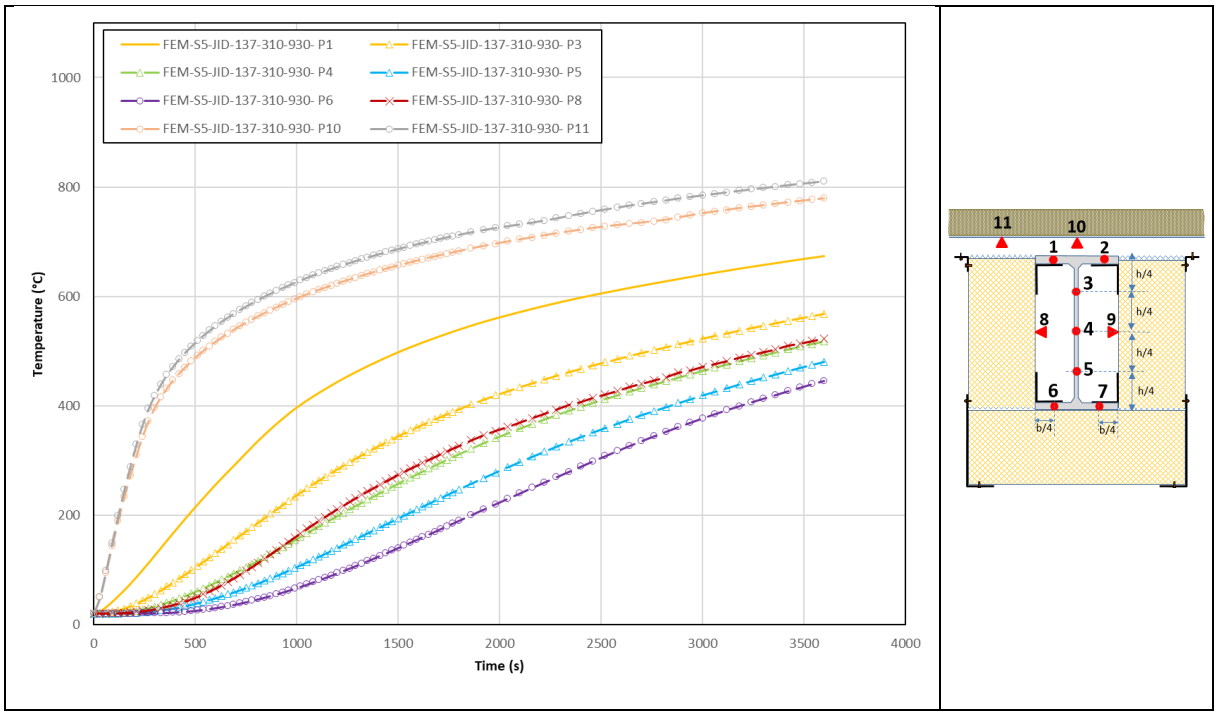

Figure A.22: Predicted temperatures in purlin cross-section S5

A.5. Thermal analysis with additional wave cavity filling

A.5.1. Purlin with steel sheet JI-42-252-1010

This section shows the predicted temperature rises in the purlin that supports the JI-42-252-1010 type steel sheets with filled waves troughs located at the level of the encasement.

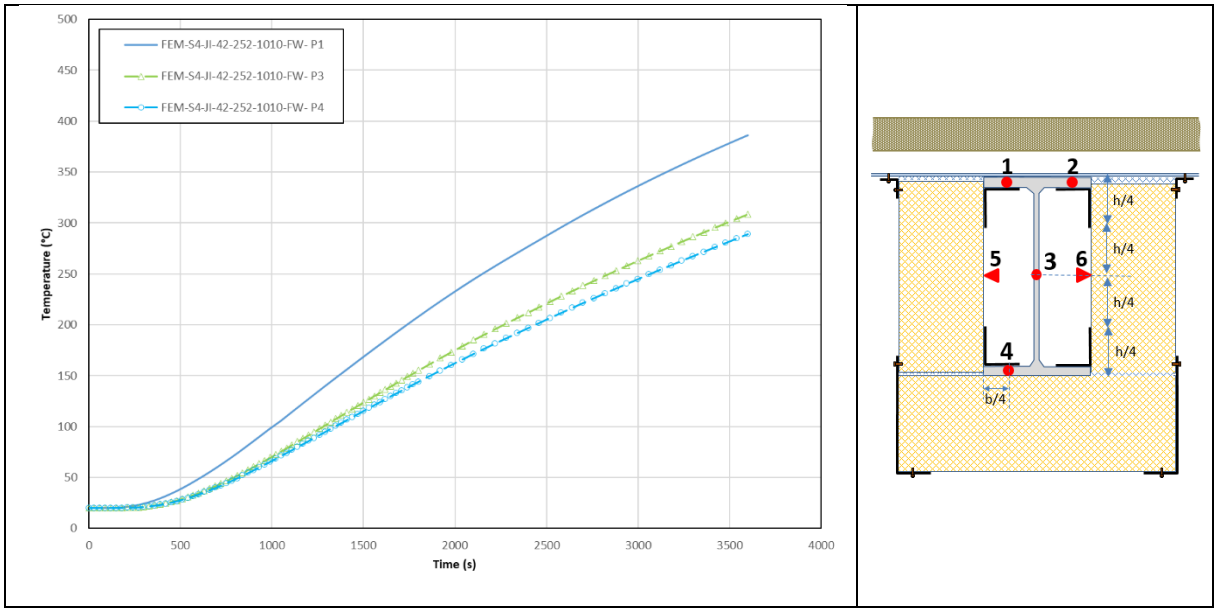

Figure A.23: Predicted temperatures in purlin cross-section S4

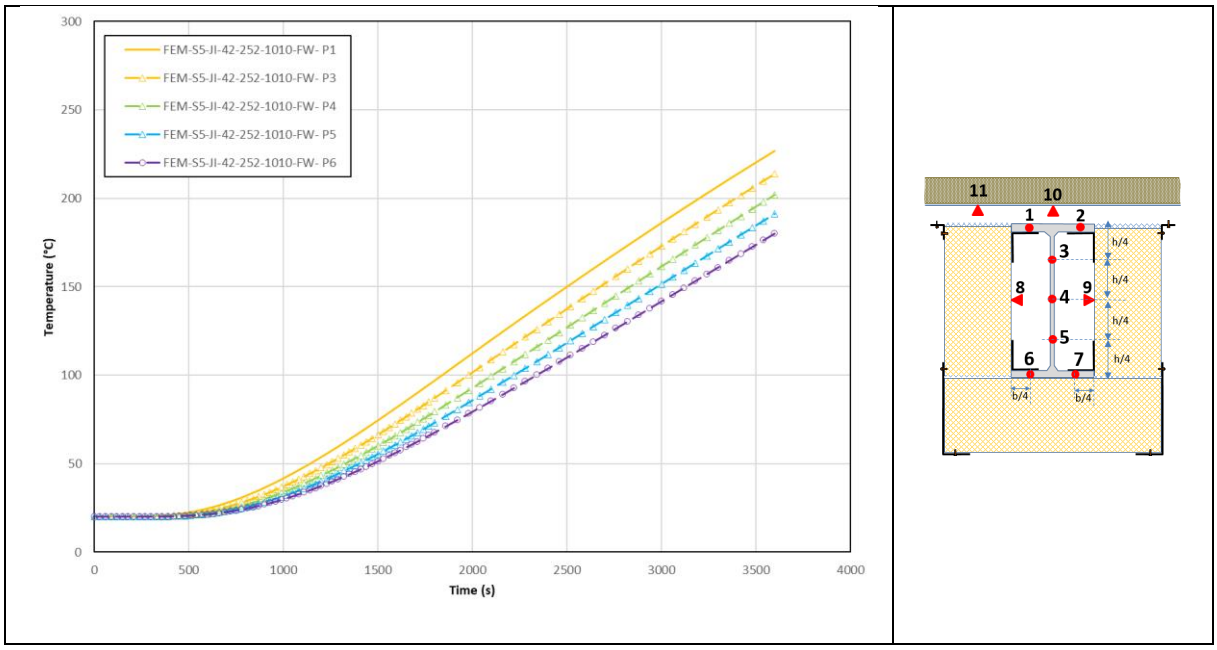

Figure A.24: Predicted temperatures in purlin cross-section S5

A.6. Purlin with steel sheet JID-137-310-930

This section shows the predicted temperature rises in the purlin that supports the JID-137-310-930 type steel sheets with filled waves troughs located at the level of the encasement.

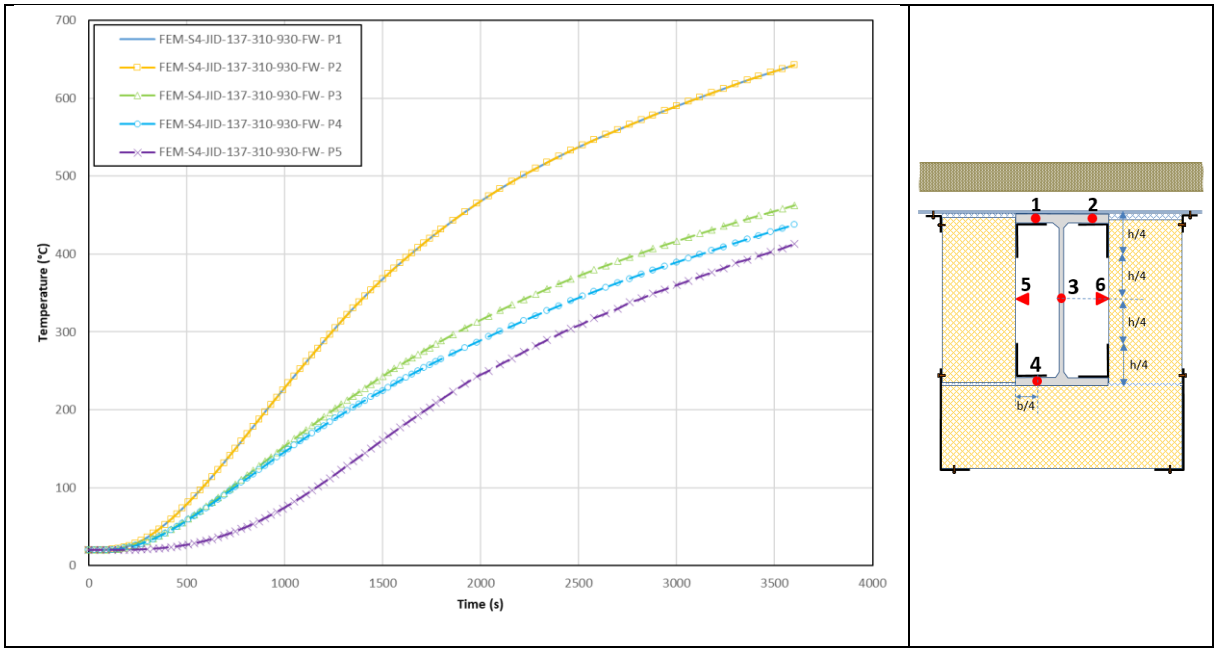

Figure A.25: Predicted temperatures in purlin cross-section S4

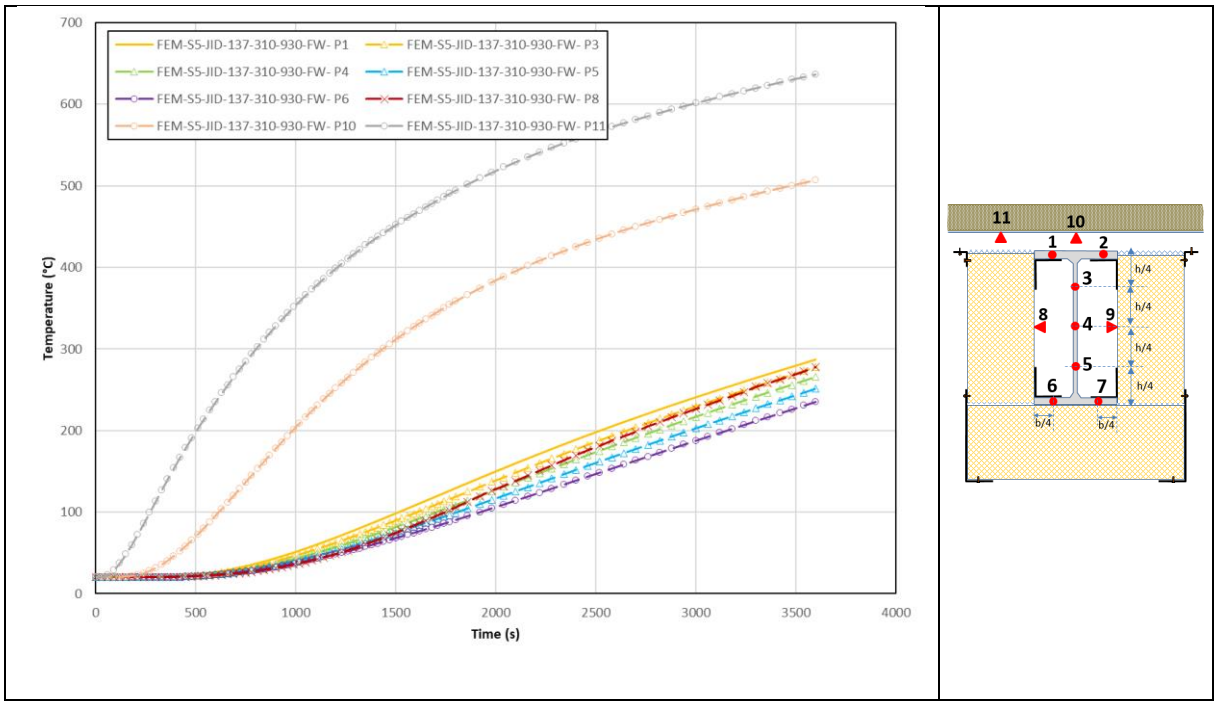

Figure A.26: Predicted temperatures in purlin cross-section S5

APPPENDIX B. HEATING OF FUSIBLE LINKS UNDER REAL FIRE SCENARIOS

This annex provides a comparison of the fusible link temperatures calculated using 3D finite element (FE) models with those predicted using the simplified method presented in deliverables D5.2 [23] and D5.3 [24]. These calculations were performed on two fusible links: one located at each end of the most heated steel portal frame for the three fire scenarios relating to the building reference number 2. the link heating has been calculated by considering the hot gas temperature predicted in the vicinity of the considered fusible link by the FDS fire simulations carried out in the project [22]. Moreover, the fusible link considered corresponds to the first developed solution. Its main geometric characteristics are reported in the following table.

Table B.1: Main geometric characteristics of the considered fusible link

U-shaped steel profile	Thickness : 6 ot 10mm
	Size ($b_{tf,u} \times h_u \times b_{bf,u}$) : 90×150×140mm
	Stiffener ($t_{s,u}$): 10 mm
Steel rods	Diameter: M16
	Length (wall thickness): 175mm
L-shaped steel plate	Size ($h_L \times b_L$) : 127 ×100 mm
	Thickness ($t_{b,L}$, $t_{w,L}$) : 10mm

It should be noted that the values of the section factor used in the simplified temperature calculations were set to Am/v = 130 m^{-1} and Am/v = 99 m^{-1} for the link with a 6 mm thick U-shaped steel profile and a 10 mm thick U-shaped profile, respectively.

B.1. Fire scenario W.2.3

The location of the considered fusible links in the fire compartment is indicated in Figure B.1

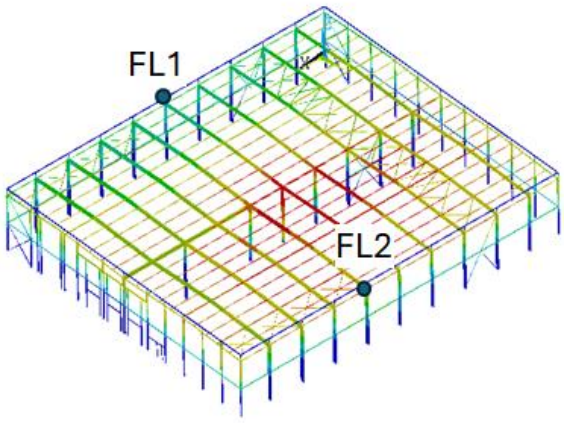

Figure B-1 Location of the studied fusible links

The Figure B-2 to Figure B-5 show a temperatures comparison for the considered fusible link solution, distinguishing the fusible link with a 6mm thick U-shaped steel profile and this is a 10 mm thick. The temperature comparison is provided for the flanges and the web of the U-profile, the steel rods (at points located in the upper quarter of the rods exposed to the fire) and the aluminum bolts only.

Applying the simplified rules proposed for calculating the heating of fusible links globally leads to satisfactory predictions of their heating under the considered fire scenario, since these rules underestimate temperatures.

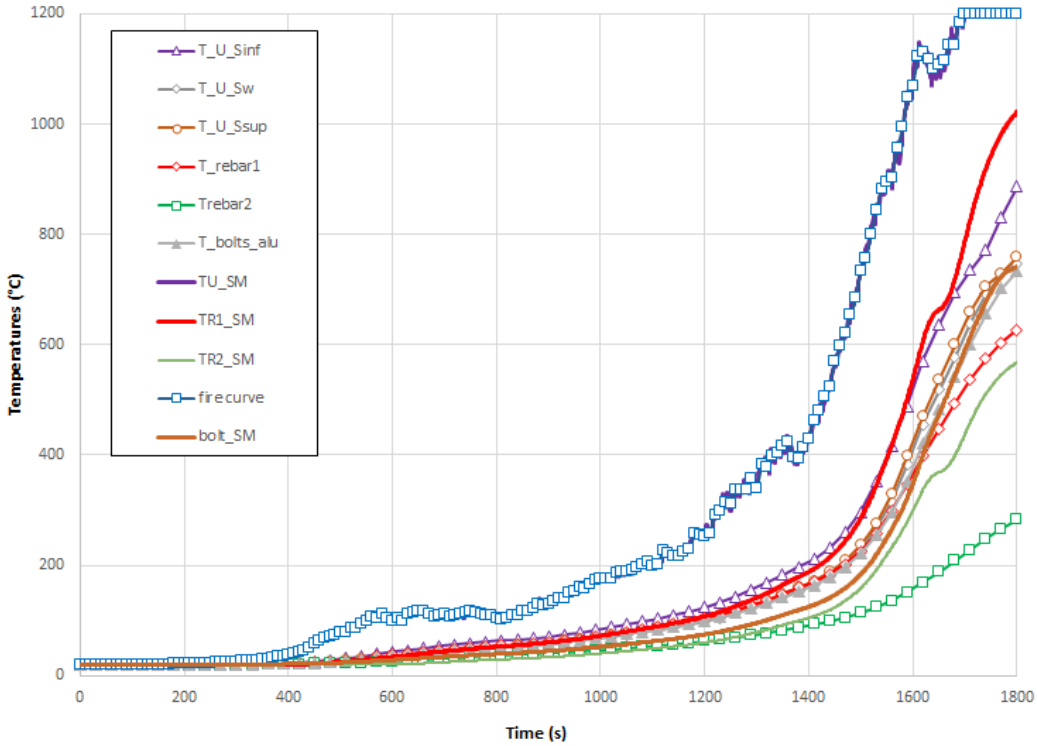

Figure B.2: Temperature rises calculated at some point of the fusible link "FL1" with 6mm thick U profile for the considered fire scenario – Comparison between the numerical results and the simplified method

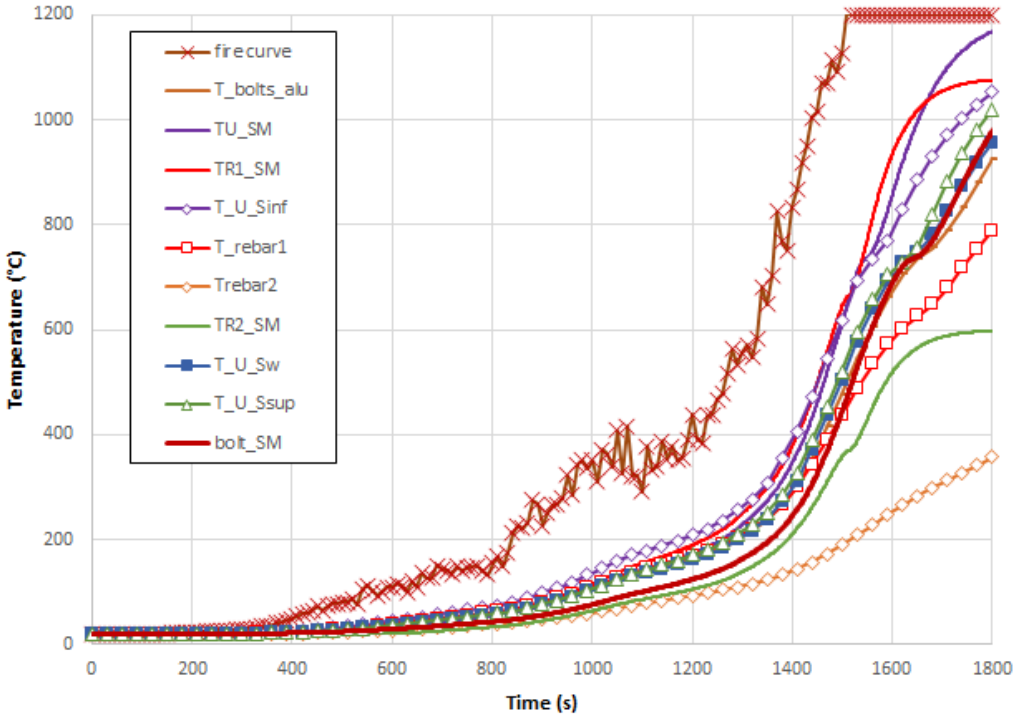

Figure B.3: Temperature rises calculated at some point of the fusible link "FL2" with 6mm thick U profile for the considered fire scenario – Comparison between the numerical results and the simplified method

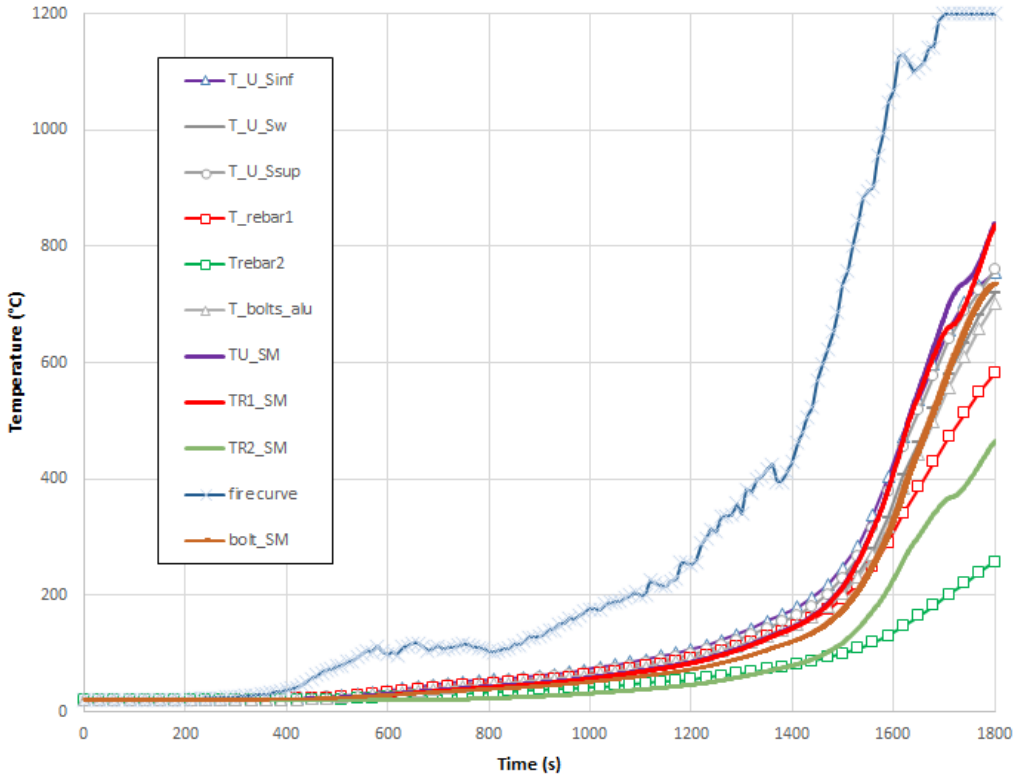

Figure B-4: Temperature rises calculated at some point of the fusible link "FL1" with 10mm thick U profile for the considered fire scenario – Comparison between the numerical results and the simplified method

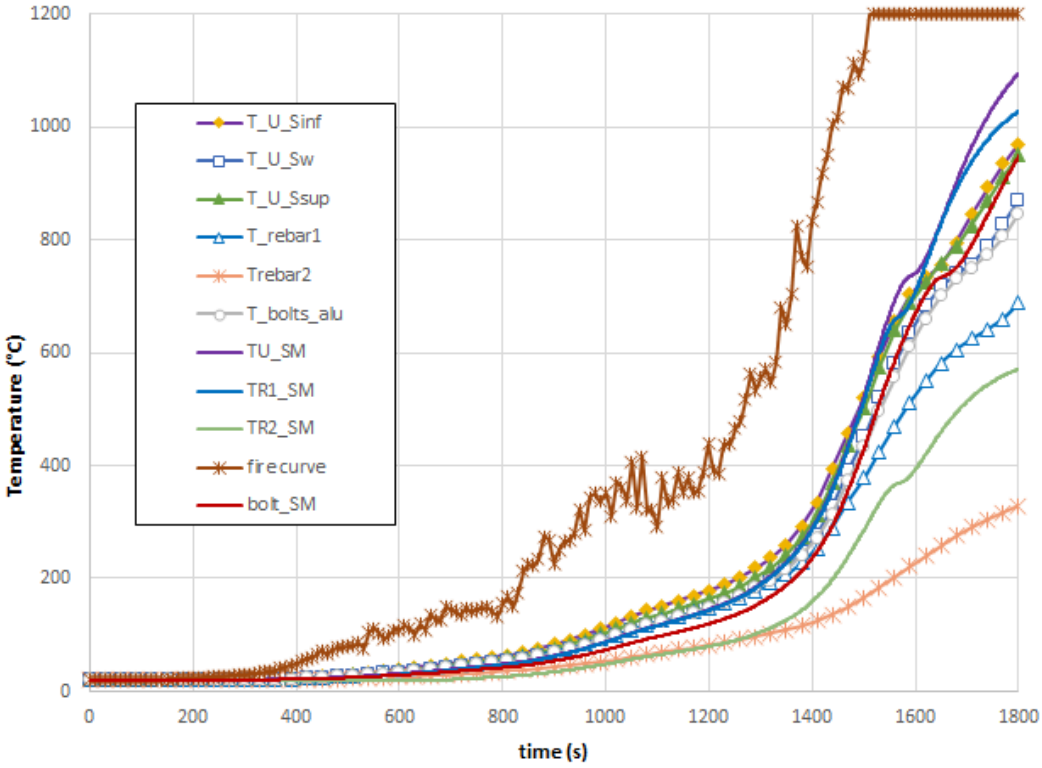

Figure B-5: Temperature rises calculated at some point of the fusible link "FL2" with 10mm thick U profile for the considered fire scenario – Comparison between the numerical results and the simplified method

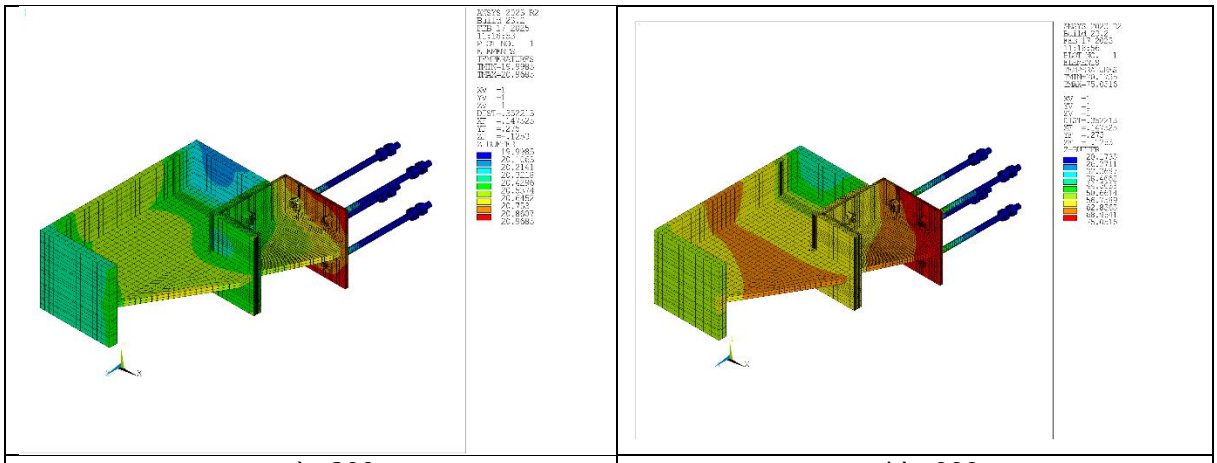

a) 300s | b) 900s

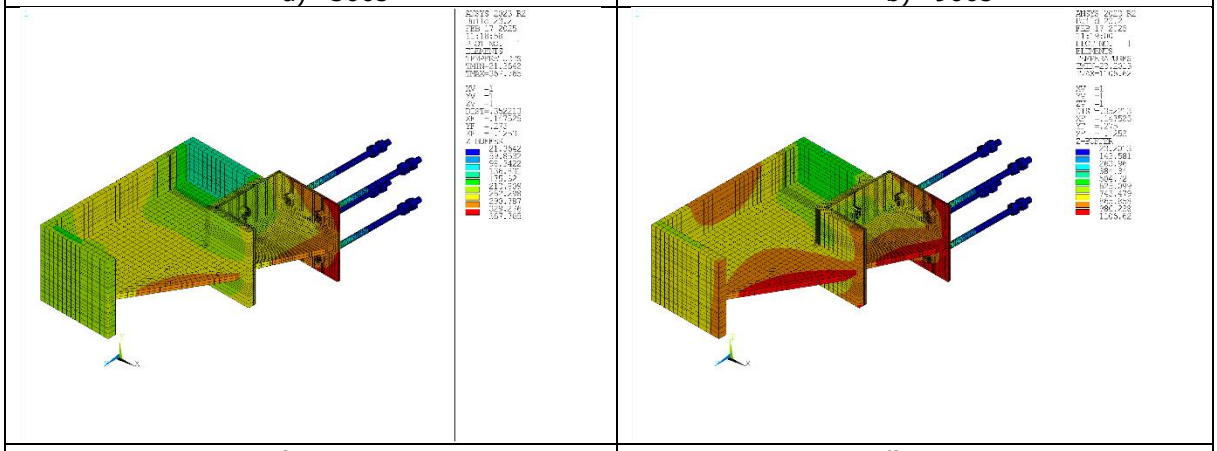

c) 1500 s | d) 1800s

Figure B-6: temperature field predicted in the fusible link "FL1"at different exposure time to fire for the considered fire scenario

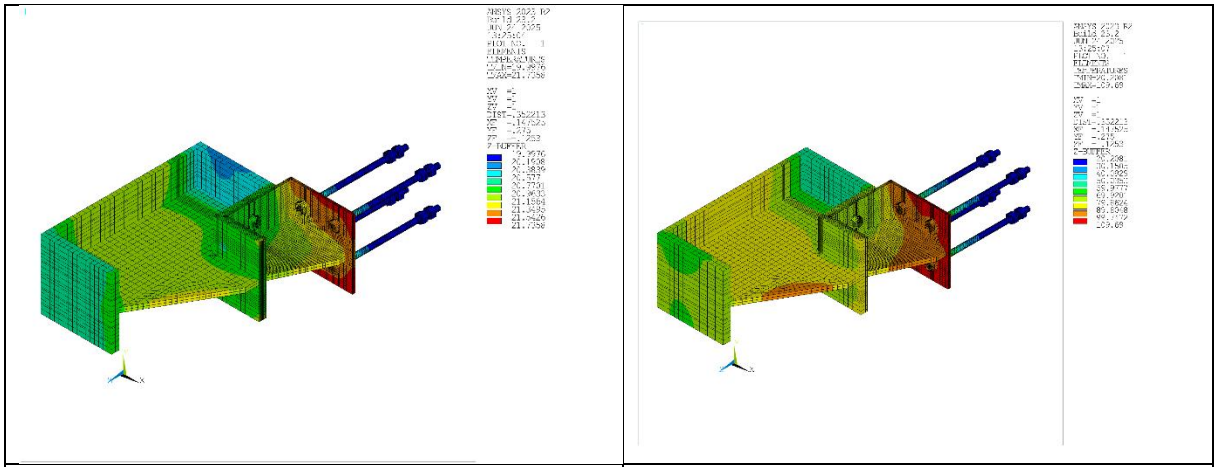

a) 300s | b) 900s

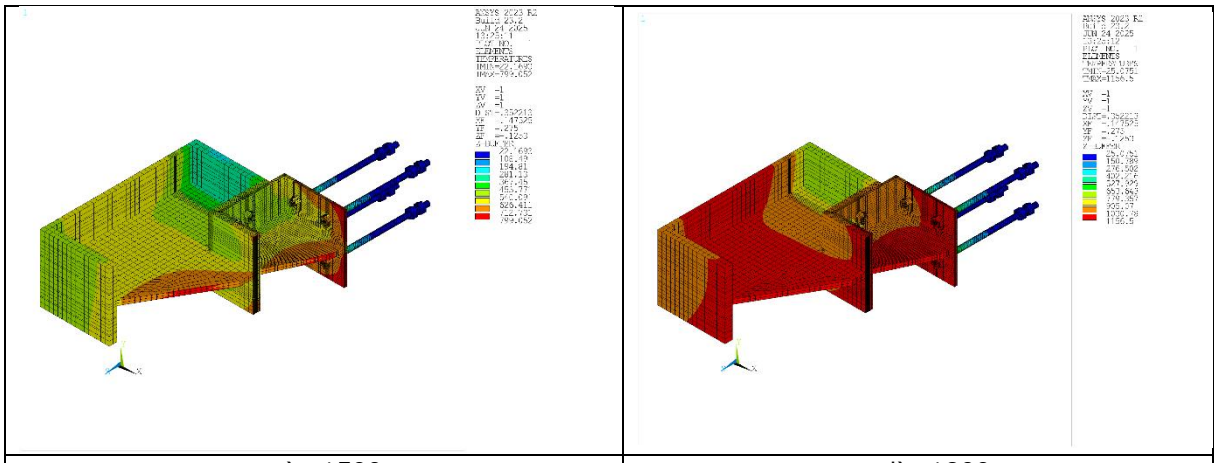

c) 1500 s	d) 1800s

Figure B-7: temperature field predicted in the fusible link "FL2"at different exposure time to fire for the considered fire scenario

B.2. Fire scenario S.2.3

The location of the considered fusible links in the fire compartment is indicated in Figure B-8.

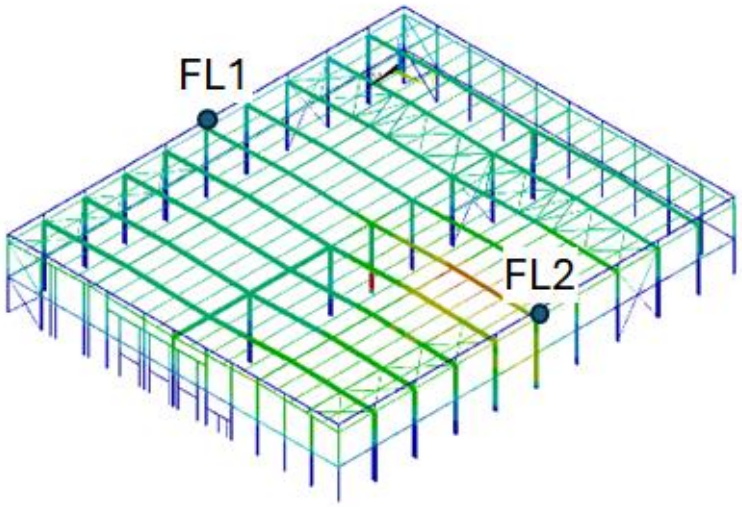

Figure B-8: Location of the studied fusible links

The **Erreur ! Source du renvoi introuvable.** to Figure B-12 show a temperatures comparison for the considered fusible link solution, distinguishing the fusible link with a 6mm thick U-shaped steel profile and this is a 10 mm thick. The temperature comparison is provided for the flanges and the web of the U-profile, the steel rods (at points located in the upper quarter of the rods exposed to the fire) and the aluminum bolts only.

Globally, applying the simplified rules proposed for calculating the heating of fusible links leads to satisfactory predictions of their heating under the considered fire scenario. The temperatures calculated for the steel profiles and the hottest parts of the steel rods are very similar. On the other hand, the temperature given for the part of the rods that are heated the least is underestimated. However, the impact of this underestimation on the rods' resistance should be limited as the maximum temperatures reached are below 200 °C and steel strength is only slightly affected by this temperature

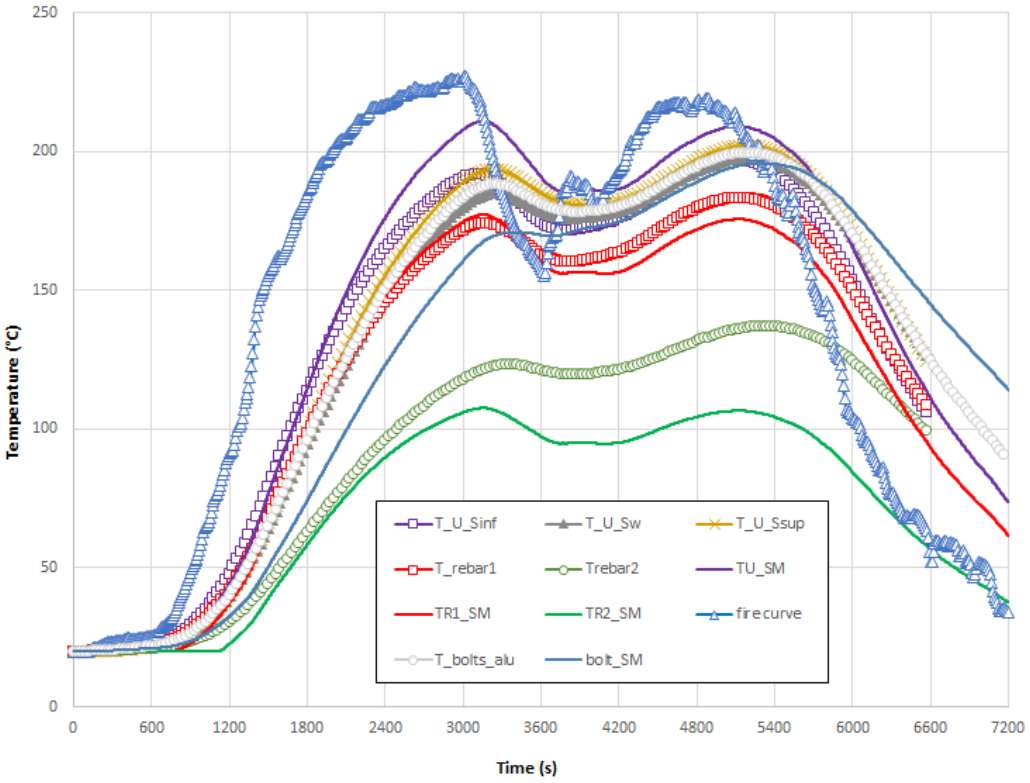

Figure B-9: Temperature rises calculated at some point of the fusible link "FL1" with 6mm thick U profile for the considered fire scenario – Comparison between the numerical results and the simplified method

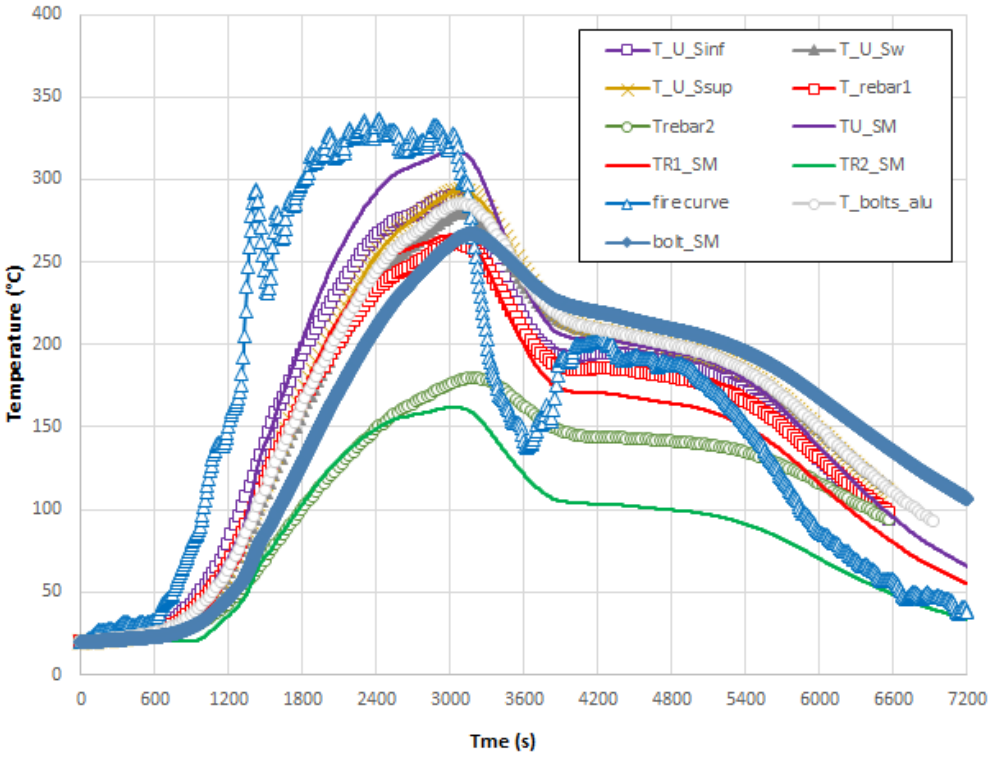

Figure B-10: Temperature rises calculated at some point of the fusible link "FL2" with 6mm thick U profile for the considered fire scenario – Comparison between the numerical results and the simplified method

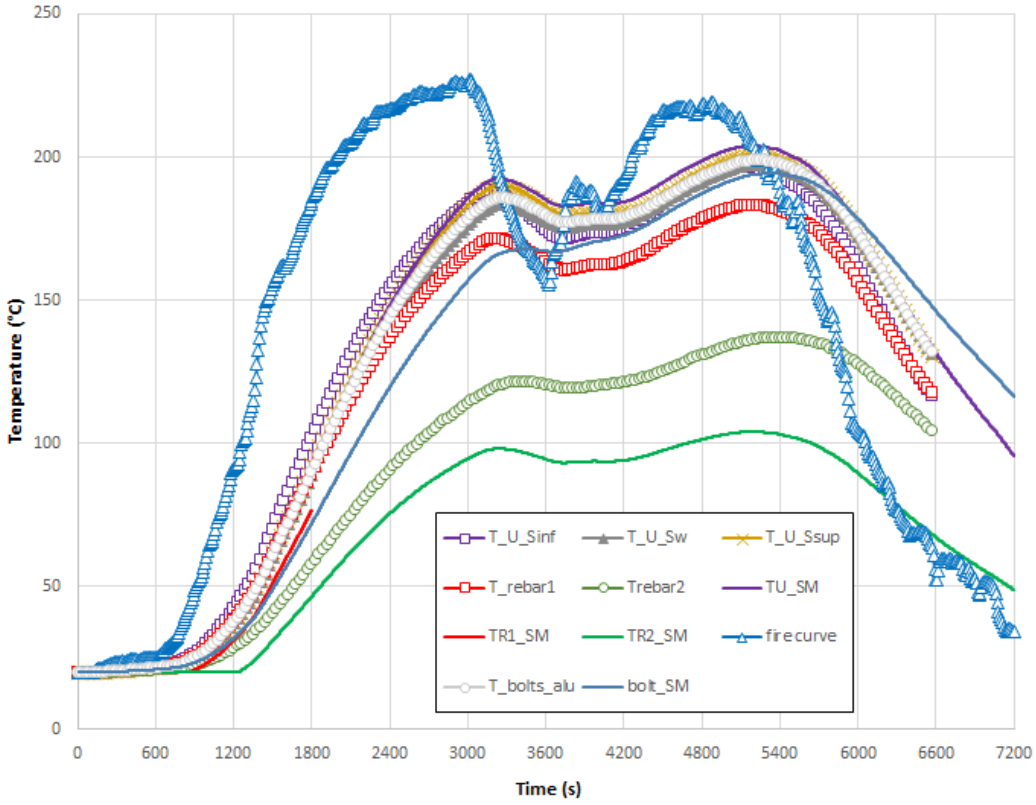

Figure B-11: Temperature rises calculated at some point of the fusible link "FL1" with 10mm thick U profile for the considered fire scenario – Comparison between the numerical results and the simplified method

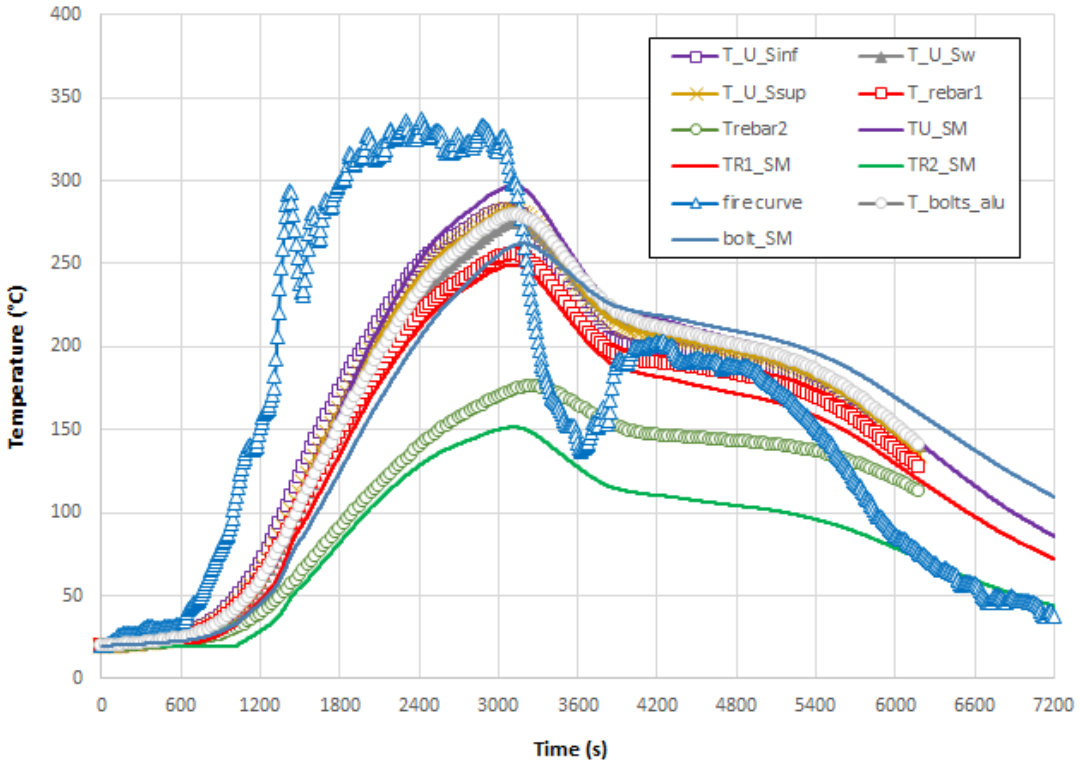

Figure B-12: Temperature rises calculated at some point of the fusible link "FL2" with 10mm thick U profile for the considered fire scenario – Comparison between the numerical results and the simplified method

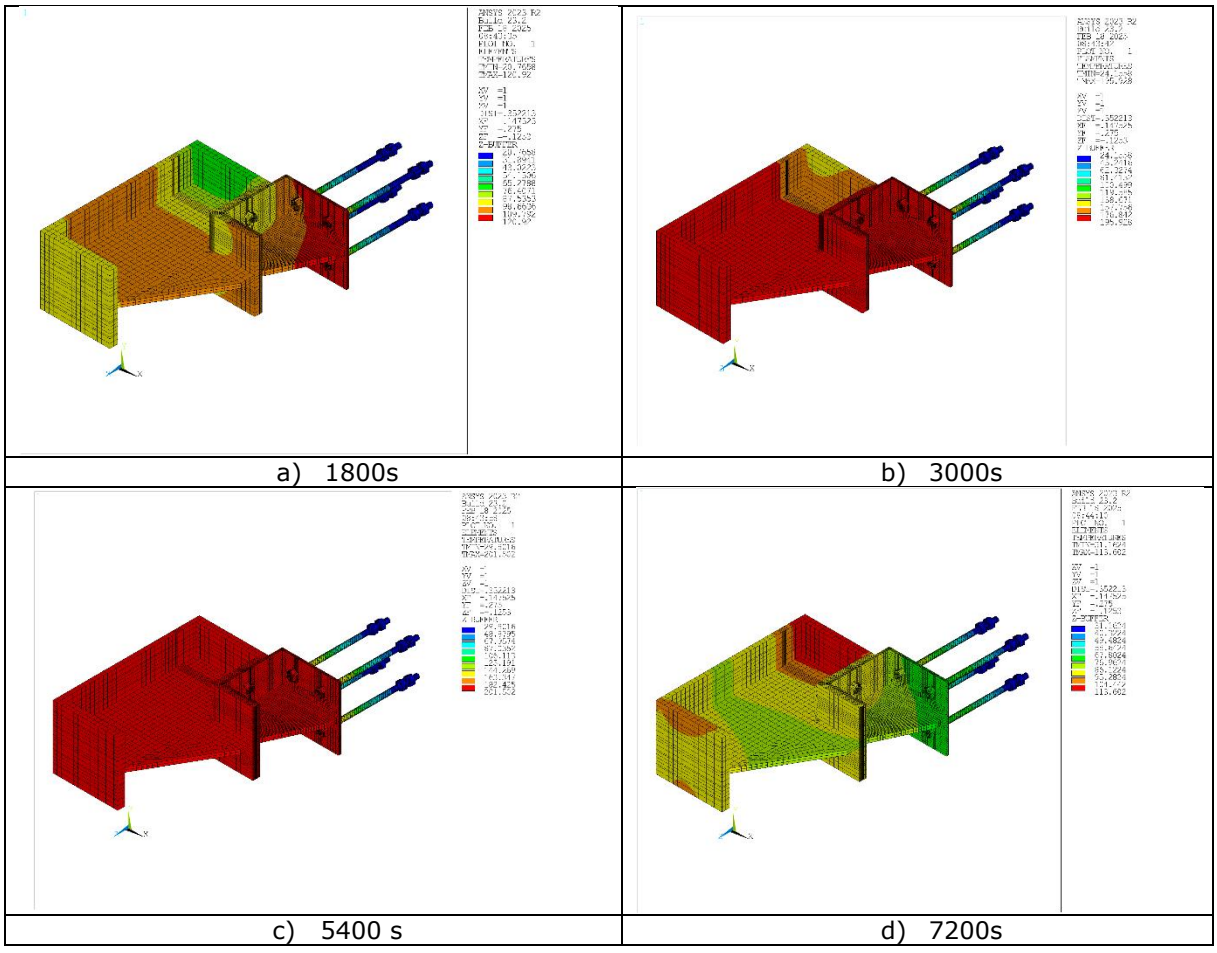

a) 1800s | b) 3000s

c) 5400 s | d) 7200s

Figure B-13: temperature field predicted in the fusible link "FL1" with 6mm thick U profile at different exposure time to fire for the considered fire scenario

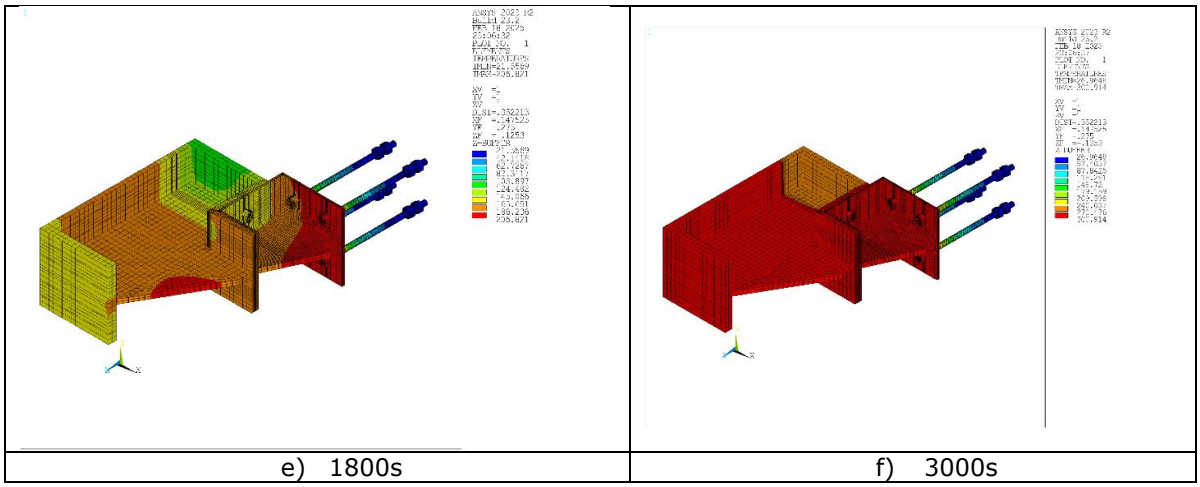

e) 1800s | f) 3000s

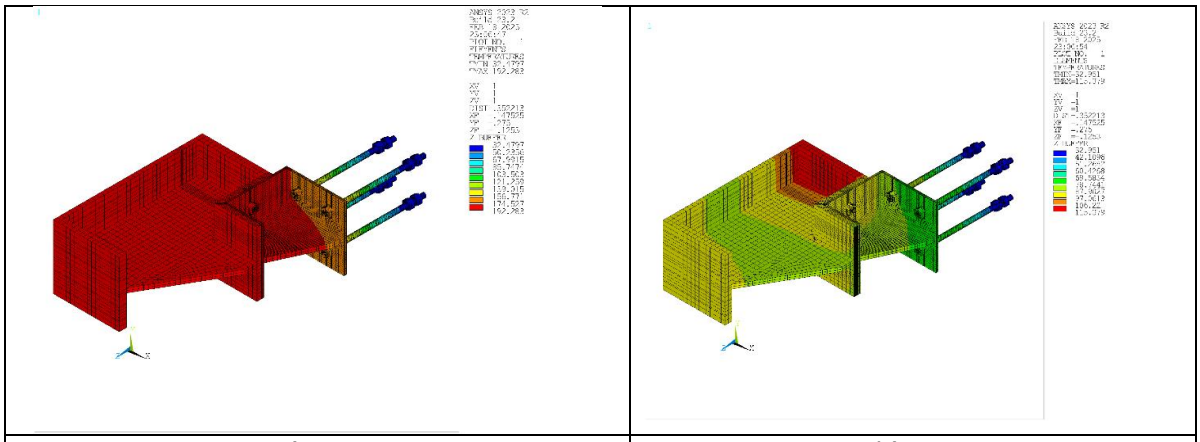

g) 5400 s	h) 7200s

Figure B-14: Temperature field predicted in the fusible link "FL2" with 10mm thick U profile at different exposure time to fire for the considered fire scenario

B.3. Fire scenario I.2.2

The location of the considered fusible links in the fire compartment is indicated in Figure B-15:

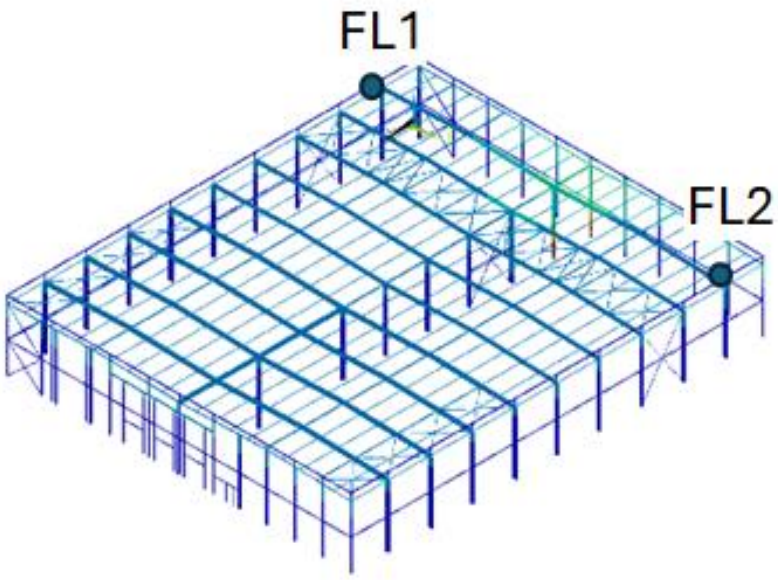

Figure B-15: Location of the studied fusible links

The Figure B-16 to Figure B-19 show a temperatures comparison for the considered fusible link solution, distinguishing the fusible link with a 6mm thick U-shaped steel profile and this is a 10 mm thick. The temperature comparison is provided for the flanges and the web of the U-profile, the steel rods (at points located in the upper quarter of the rods exposed to the fire) and the aluminum bolts only.

Globally, applying the simplified rules proposed for calculating the heating of fusible links leads to satisfactory predictions of their heating under the considered fire scenario. The temperatures calculated for the steel profiles and the hottest parts of the steel rods are very similar. On the other hand, the temperature given for the part of the rods that are heated the least is underestimated. However, the impact of this underestimation on the rods' resistance should be limited as the maximum temperatures reached are below 200 °C and steel strength is only slightly affected by this temperature

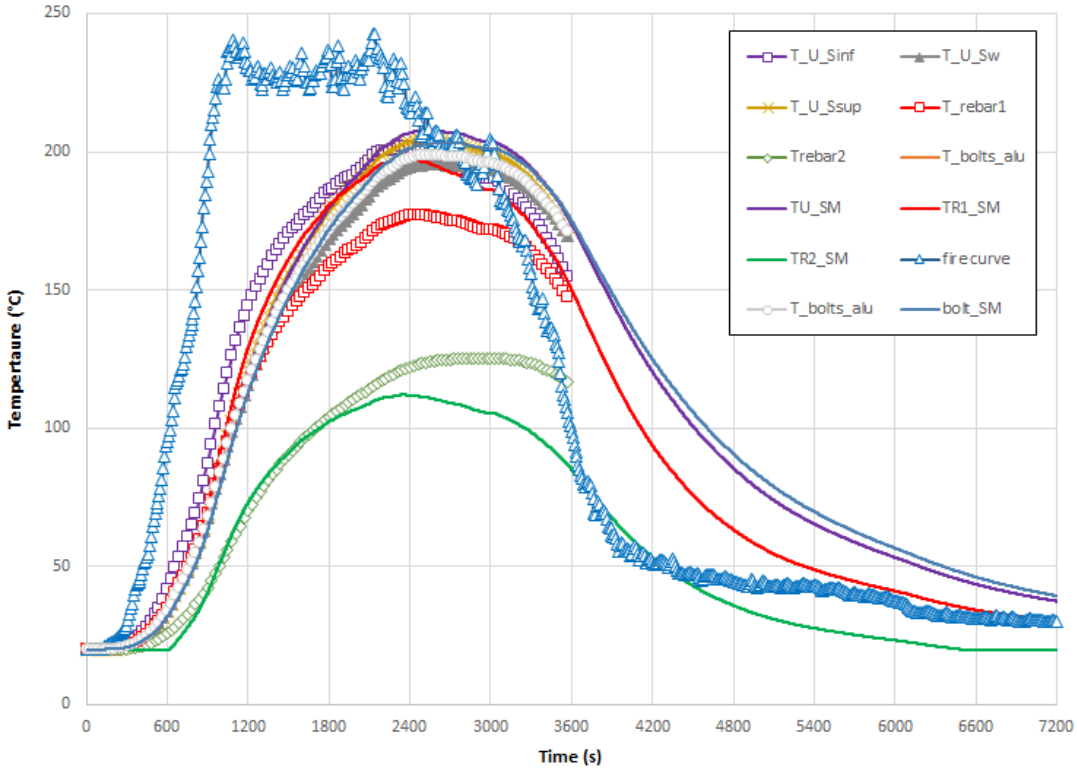

Figure B-16: Temperature rises calculated at some point of the fusible link "FL1" with 6mm thick U profile for the considered fire scenario – Comparison between the numerical results and the simplified method

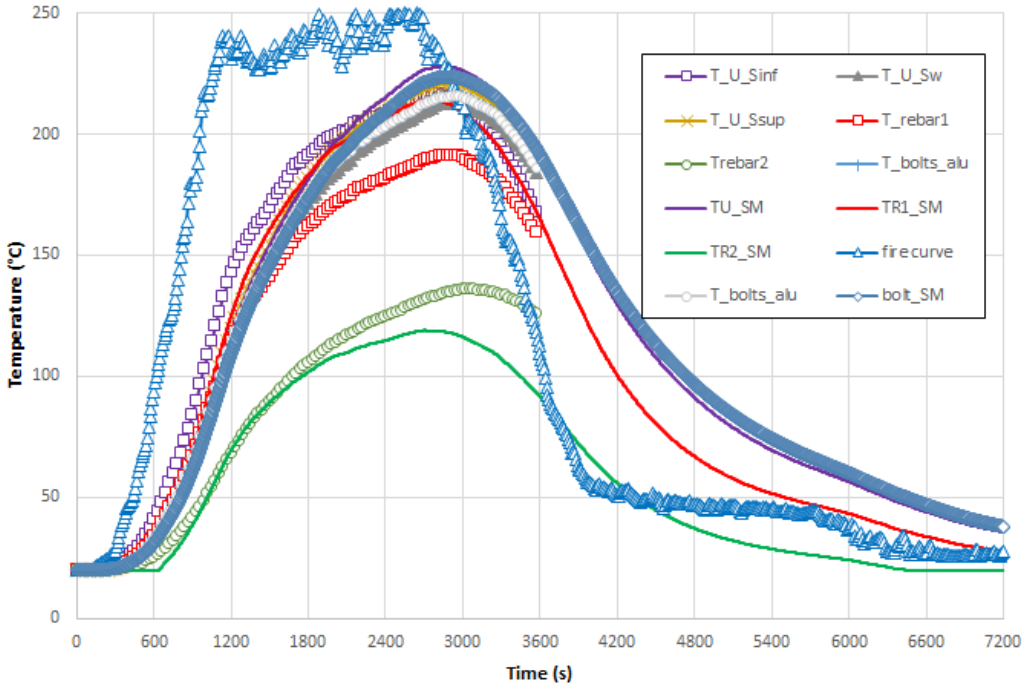

Figure B-17: Temperature rises calculated at some point of the fusible link "FL2" with 6mm thick U profile for the considered fire scenario – Comparison between the numerical results and the simplified method

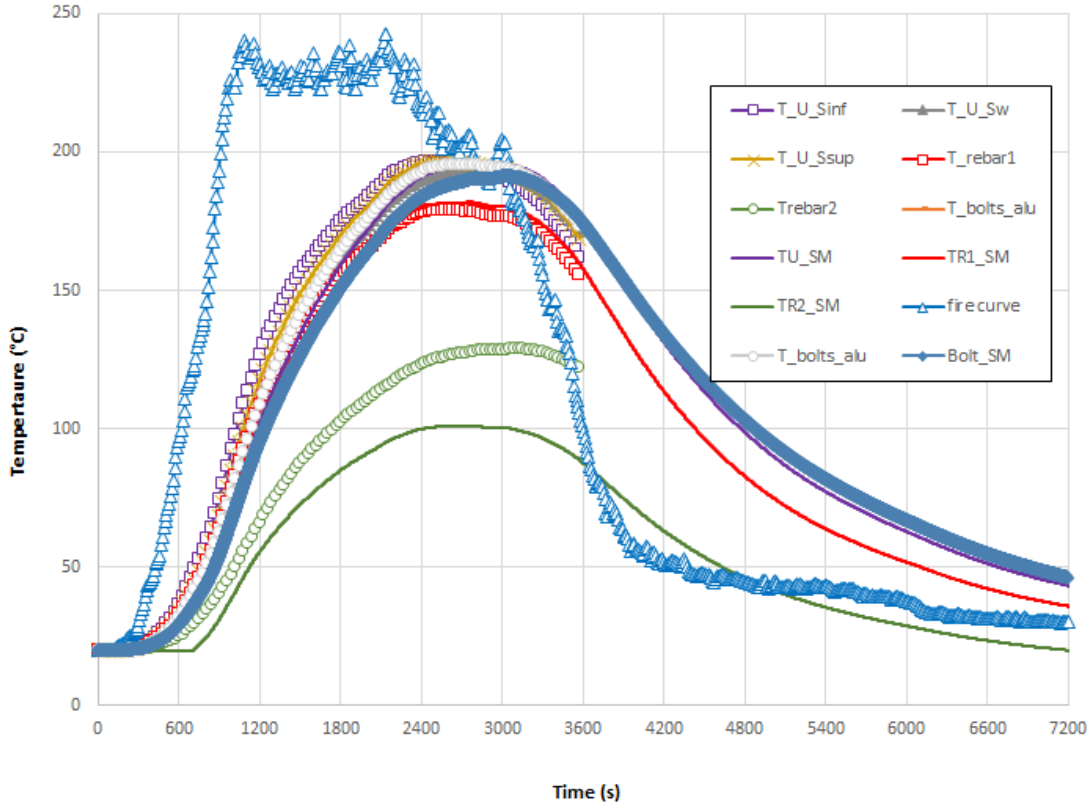

Figure B-18 Temperature rises calculated at some point of the fusible link "FL1" with 10mm thick U profile for the considered fire scenario – Comparison between the numerical results and the simplified method

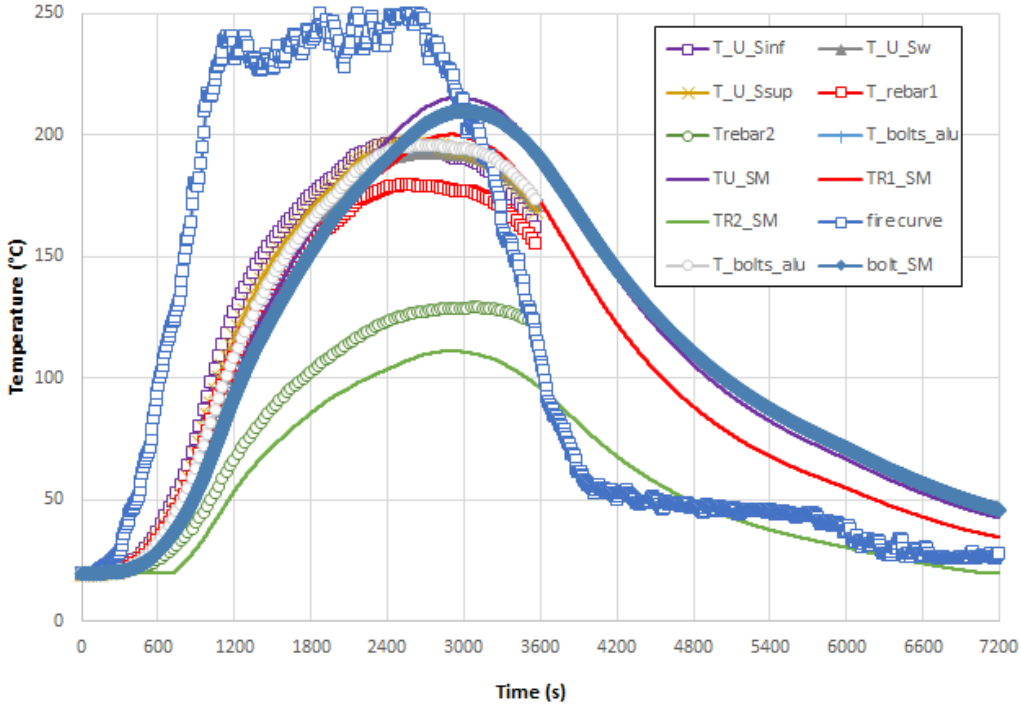

Figure B-19 Temperature rises calculated at some point of the fusible link "FL2" with 10mm thick U profile for the considered fire scenario – Comparison between the numerical results and the simplified method

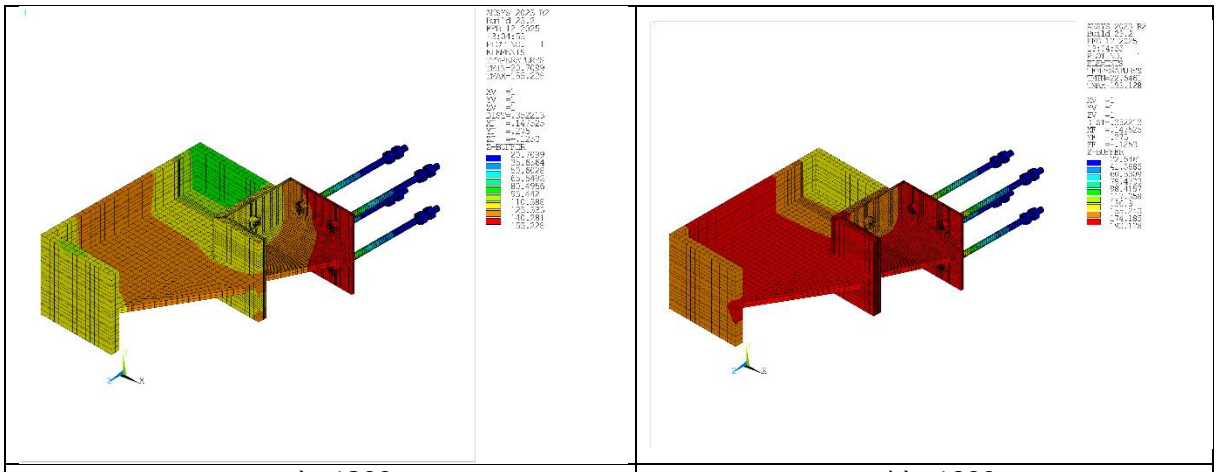

a) 1200s | b) 1800s

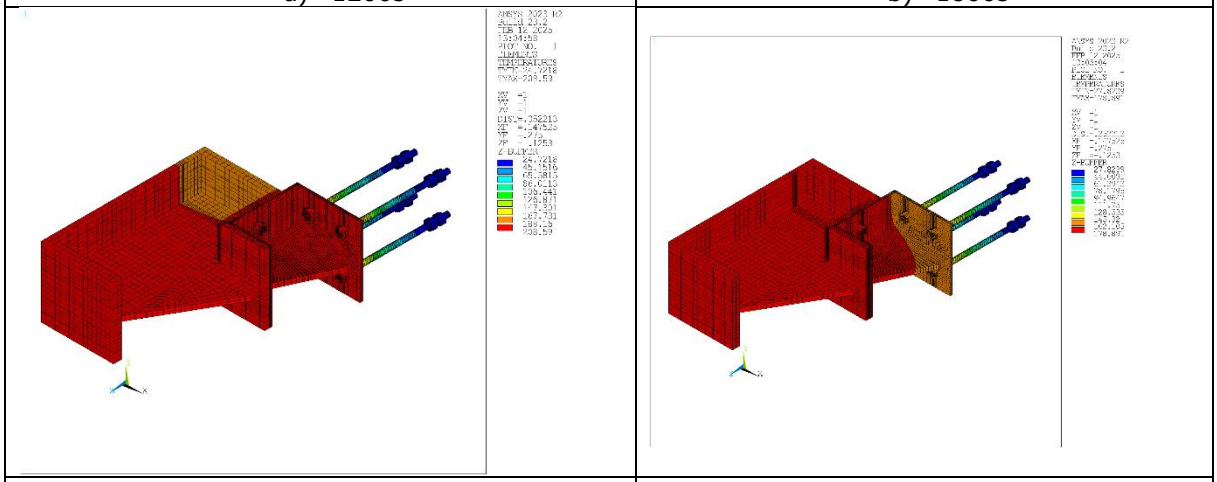

c) 2400 s | d) 3600s

Figure B-20: temperature field predicted in the fusible link "FL1" with 6mm thick U profile at different exposure time to fire for the considered fire scenario

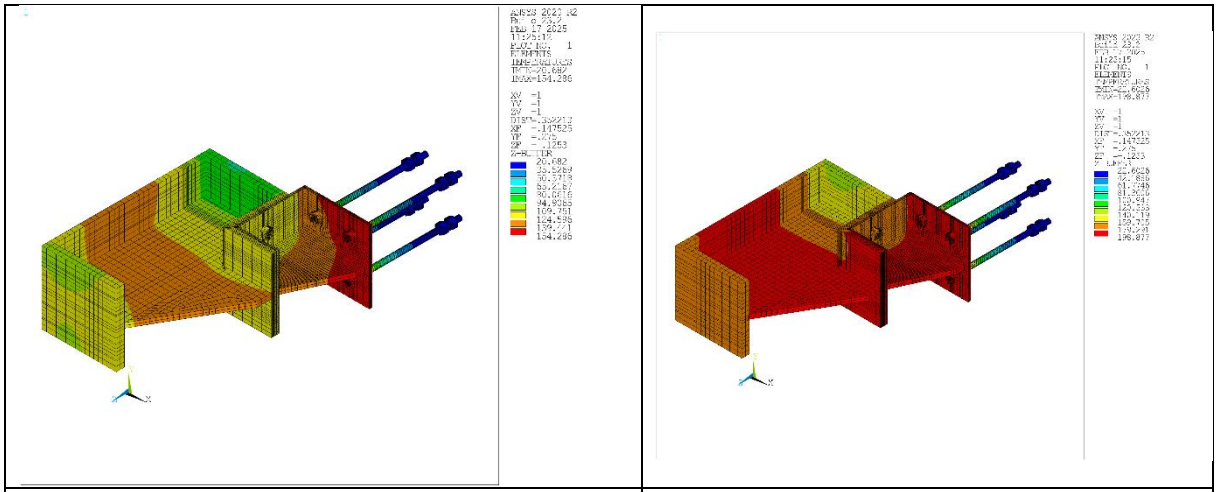

a) 1200s | b) 1800s

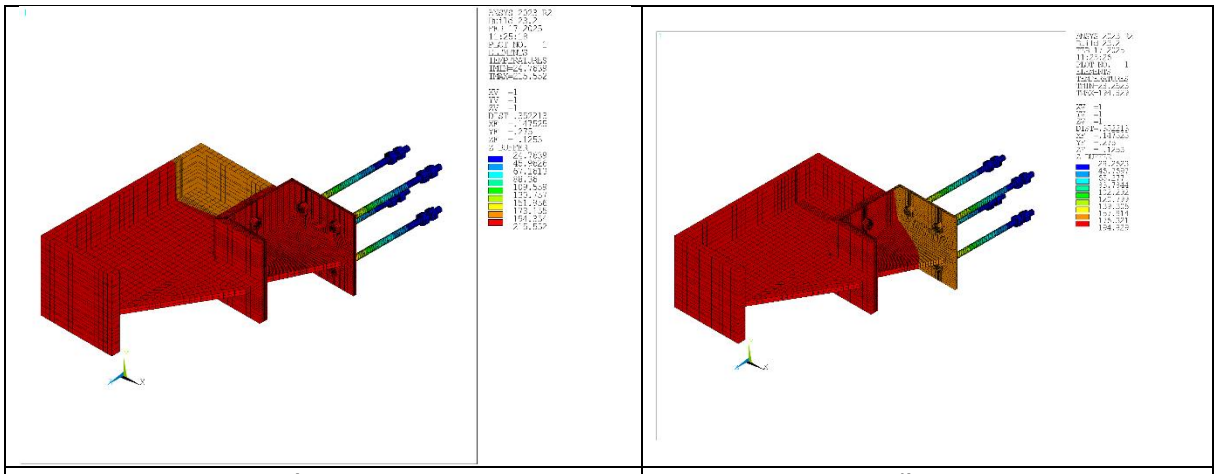

c) 2400 s	d) 3600s

Figure B-21 temperature field predicted in the fusible link "FL2" with 10mm thick U profile at different exposure time to fire for the considered fire scenario

APPPENDIX C. FIRE DESIGN LOADS FOR FUSIBLE LINKS

The design loads to be considered in the fire design of the fusible links are the forces that could be induced by the collapse of the heated part of the structure. They can be calculated from the simple rules given in this section, which are based on those developed in an earlier RFSC project [17].

There are two possible wall configurations to be considered: the fire wall is either perpendicular to the steel frame or parallel to the steel frame.

C.1. Fire wall perpendicular to steel portal frames

C.1.1. Pushing forces:

There are two possible situations to consider:

1. The fire occurs in a compartment in the middle of the building (see Figure C-1).
2. The fire occurs in a compartment at one end of the building (see Figure C-2).

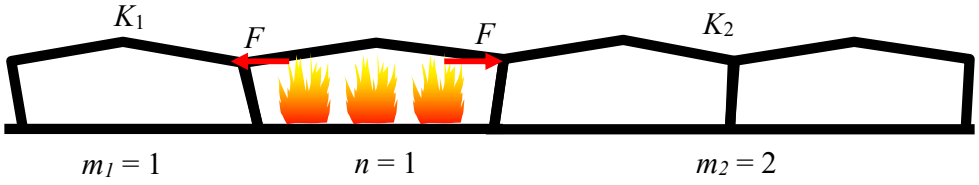

Figure C-1: Fire located in a compartment at the middle of the building

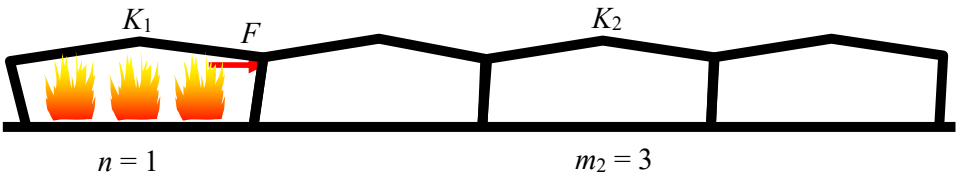

Figure C-2: Fire located in a compartment at one end of the building

When a fire occurs in a fire compartment of a building, the horizontal pushing force F generated at the ends of the compartment due to the thermal expansion of the roof structure (beams and purlins) exposed to the fire can be calculated:

$$F = c_{th} \frac{K_1 K_2}{K_1 + K_2} n\ell \qquad \text{(C.1)}$$

where :

K_i is the equivalent lateral stiffness of the considered steel structure i

ℓ is the span of heated bays [m]

n is the number of heated bays of the fire-exposed portal frames

c_{th} is an empirical coefficient (dependent on the slope of the roof) according to Table C.1. For intermediate values of the slope, linear interpolation may be used.

Table C.1: values of c_{th}

Slope of the roof	c_{th}
0%	0,01
5%	0,011
10%	0,015

If the fire compartment is in the middle of the building (as illustrated in Table C.1), K_1 and K_2 are the equivalent lateral stiffnesses of structures not exposed to fire, on either side of the fire compartment exposed to fire. They can be easily obtained using standard structural analysis software.

If the compartment exposed to fire is at a building end (as illustrated in Table C.2), K_2 should be calculated as for a fire in the middle of the building. K_1 is the lateral stiffness of the steel structure exposed to fire. It should be calculated as follows:

- When the number of heated bays n in the compartment exposed to fire is equal to 1: $K_1 = 0{,}065K$, where K is the equivalent lateral stiffness at ambient temperature of the steel structure exposed to fire.
- When the number of heated bays n in the compartment exposed to fire is greater than or equal to 2: $K_1 = 0{,}13K$.

C.1.2. Tensile forces

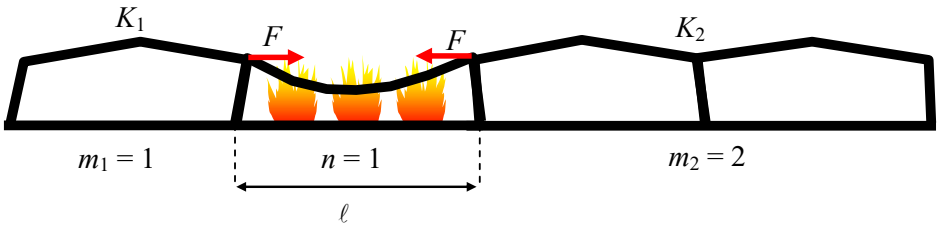

Figure C-3: Horizontal tensile force at the fire compartment ends

When a fire occurs in a compartment of the building, the horizontal tensile force F at the compartment ends resulting from the collapse of the roof structure can be obtained from:

$$F = c_p n_{eff} q_{fi,Ed} \ell \quad \text{(C.2}$$

where:

n_{eff} is the design number of heated bays in the fire compartment (see Table C.2). Note that the number of bays n_{eff} to be considered must not exceed 2, even if the number of bays in the compartment exposed to fire is greater than 2.

$q_{fi,Ed}$ is the design linear load applied on the beams [N/m], equal to the uniformly distributed load on the roof multiplied by the spacing between portal frames and calculated in fire situation ($q_{fi,Ed}$ = G + $\psi \times S_n$), where *G* is the permanent load (including the self-weight of the steel frame and service overloads Q), S_n is the snow load and ψ ($\Psi_{1,1}$ or $\Psi_{2,1}$) is the load factor according to load combination coefficients defined in EN 1990 and corresponding national annexes

c_p is an empirical coefficient depending on the slope of the roof (see Table C.3). For intermediate values of the slope, linear interpolation may be used

ℓ is the span of heated bays [m]

Table C.2: values of n_{eff}

Number of bays in fire	Setting of the compartment exposed to fire	
	Building end	Building center
n = 1	n_{eff}=0,5	n_{eff}=1,0
$n \geq 2$	n_{eff}=1,0	n_{eff}=2,0

Table C.3: values of c_p

Slope of the roof	c_p
0%	1,19
5%	1,16
10%	1,10

C.2. Fire wall perpendicular to steel portal frames

C.2.1. Pushing forces:

The pushing forces exerted at each purlin end can be safely calculated using equation (C.3).

C.2.2. Tensile forces:

Perpendicular to portal frames, horizontal tensile forces result from the catenary action of purlins exposed to fire. The tensile force at the purlin's ends can be obtained from:

$$F = 1{,}19 q_{fi,Ed} \times L \qquad \text{(C.3)}$$

Where L is the spacing between the steel portal frames and $q_{fi,Ed}$ is the design linear load applied on the purlin [N/m], equal to the uniformly distributed load on the roof multiplied by the spacing between purlins and calculated in fire situation ($q_{fi,Ed}$ = G + $\psi \times S_n$), where *G* is the permanent load (including the self-weight of the steel frame and service overloads Q), S_n is the snow load and ψ ($\Psi_{1,1}$ or $\Psi_{2,1}$) is the load factor according to load combination coefficients defined in EN 1990 and corresponding national annexes.

APPPENDIX D. A SIMPLIFIED PREDICTION OF THE FORCES IN THE FUSIBLE LINKS

2D structural analyses of isolated steel portal frames were also carried out using the Dlubal RFEM 5.34.01 software. This is the same portal frame as the one considered in §4.3.2.1 subjected to the fire scenario W.2.3. The results were verified against simulations provided by the LS-DYNA software.

D.1. Model

The numerical modeling of the steel portal frames was performed using Dlubal RFEM 5.34.01 software. A beam model was created, with the portal frame geometry illustrated in Figure D.1 and the portal frame configuration showed in Figure D.2. The connections were considered rigid. The column base was modelled as a simple support. The calculation was performed in the second order, taking into account the deformation on the internal forces in the structure.

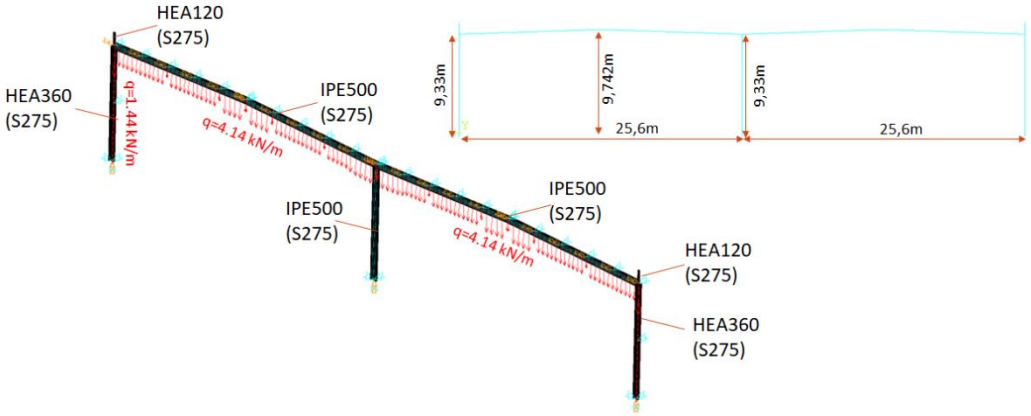

Figure D.1: Portal frame geometry

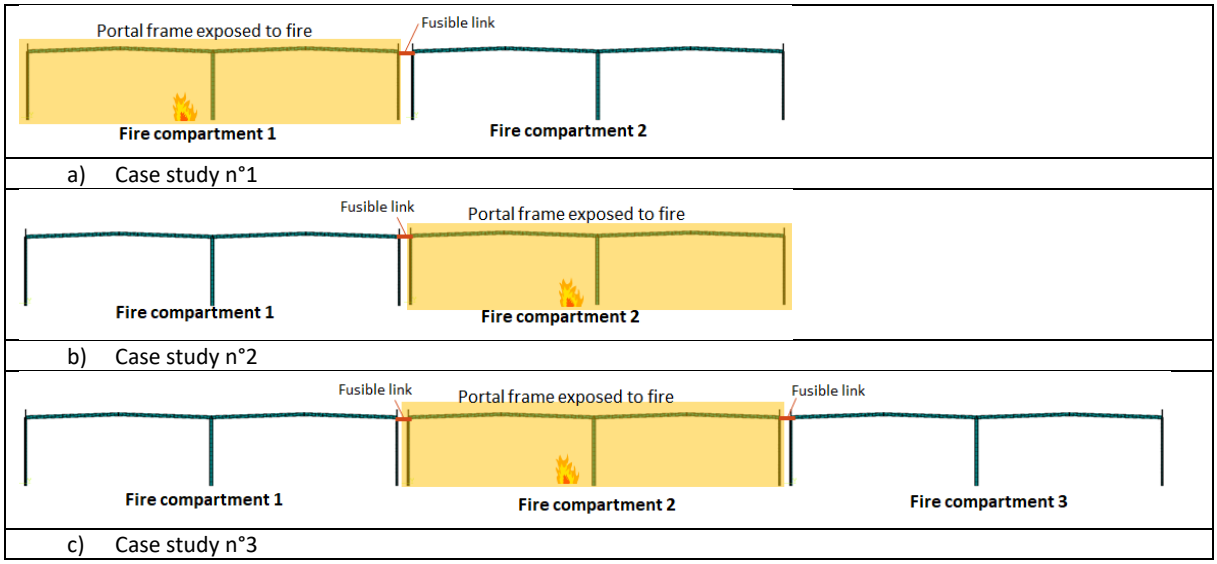

Figure D.2: Portal frame configurations

D.2. Loading

The beam elements were loaded with live and dead loads. The software took the structure's own weight into account. Due to the increased temperature during the selected fire scenario, the elongation of the structure and changes to its material characteristics were considered (see Figure D.3). The beam elements were divided into sub-segments, each of which was loaded at an appropriate temperature based on the natural fire simulation. The yield strength and modulus of elasticity of the material were then reduced for each given segment (see Figure D.4).

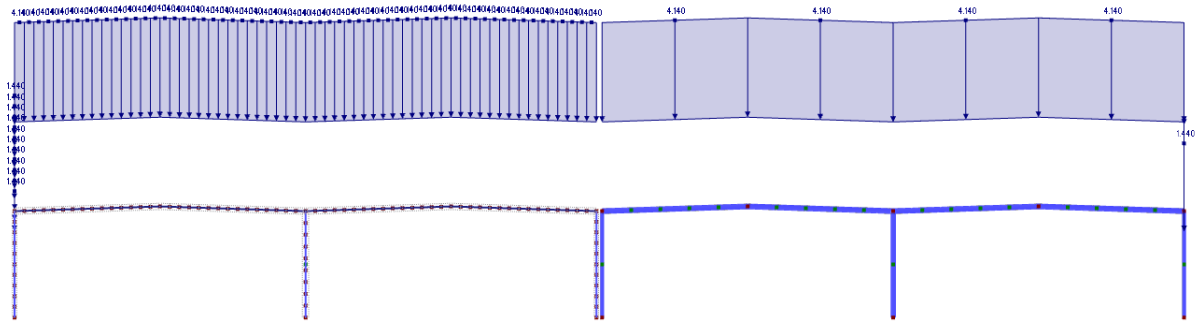

Figure D.3: Mechanical load on structure frame 1

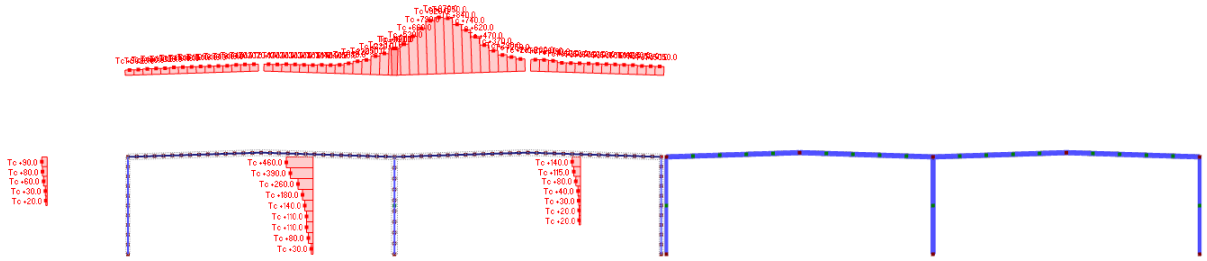

Figure D.4: Thermal load on frame 1 of the structure

D.3. Fusible link

The connections between the steel portal frame of each fire compartment were made using a fusible link as illustrated in Figure D.5. The fusible link itself was modelled as a rigid, inflexible rod, with stiffness and flexibility defined at the joints at either end. The characteristics of each joint depended on whether it was exposed to increased temperature, as shown in Figure D.6 and Figure D.7.

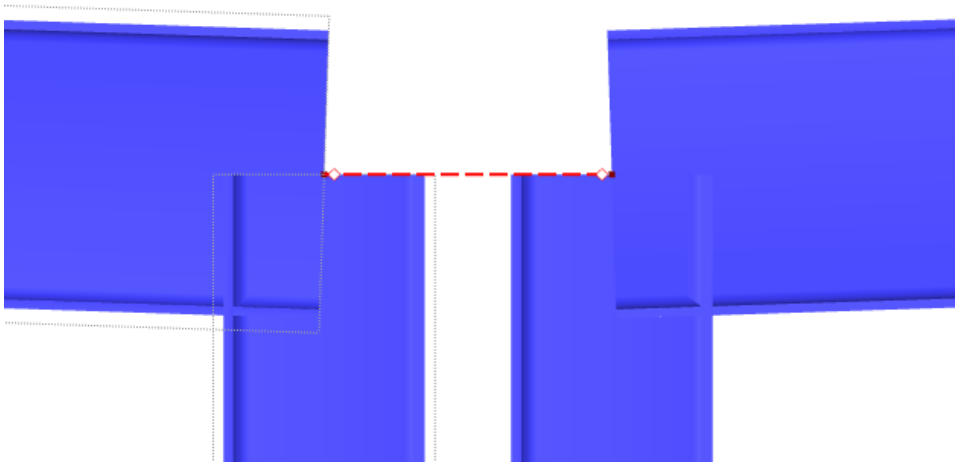

Figure D.5: Fusible link using a rigid rod

	+ux [m]	Px [MN]
1	0.000	0.000
2	0.00144547	0.215759
3	0.00328158	0.252045

	-ux [m]	Px [MN]
1	0.000	0.000
2	-1.167E-03	-0.202654
3	-3.898E-03	-0.30277

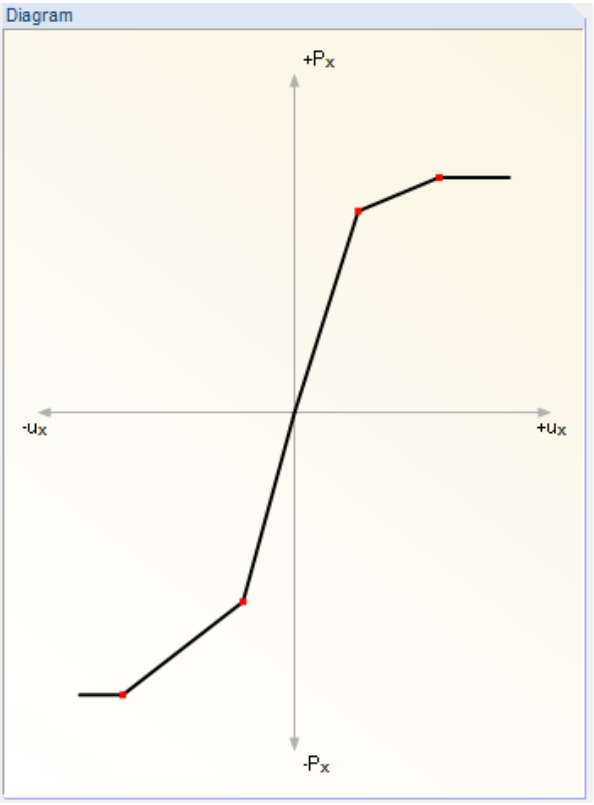

Figure D.6: Working diagram of a joint at the end of a rigid rod simulation of a fusible link not exposed to elevated temperatures

	+ux [m]	Px [MN]
1	0.000	0.000
2	8.8608E-04	0.13226
3	0.00328158	0.202045

	-ux [m]	Px [MN]
1	0.000	0.000
2	-6.776E-04	-0.0364778
3	-3.898E-03	-0.102302

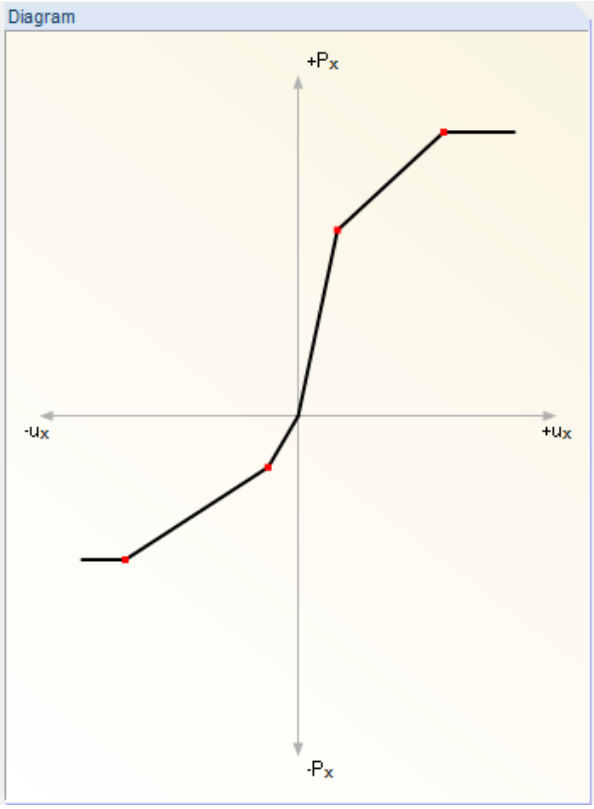

Figure D.7: Working diagram of a joint at the end of a rigid rod simulation r a fusible link exposed to elevated temperatures

D.4. Verification of force predictions in the fusible link

The value of the axial force generated in the fusible link during the structural collapse was selected for verification and design verification. In cases 1 and 3, this was 18 minutes, whereas in case 2 it was 17 minutes. To illustrate this, images of the structural deformations for each case are provided in Figure D.8 to Figure D.9. A comparison of the forces is provided in Table D.1 to Table D.3. There is a good agreement with both simulations. The deviation in the prediction of forces acting in the fusible link between the scientific software model with continuous fire load and the engineering software model with fire load considered in parts is up to 16 %.

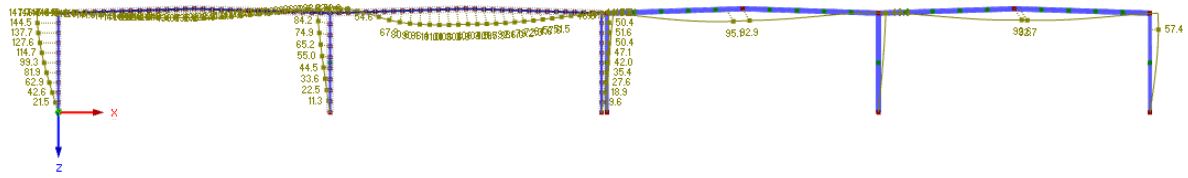

Figure D.8: Resulting deformations for the study case n°1

Table D.1: Comparison of axial forces in fusible link bewteen Ls-dyna and RFEM5 for case n°1

Case n°1	LS-DYNA	RFEM5	**LS DYNA / RFEM 5**
Time (min)	18,566	18	**1,03**
Force (KN)	-23,44	-22,311	**1,05**

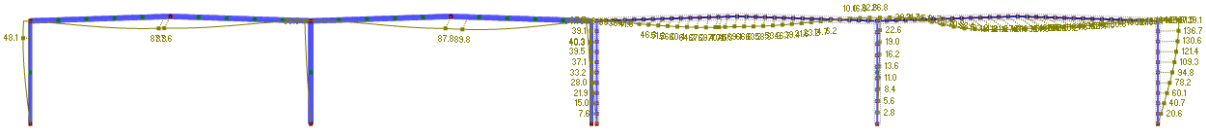

Figure D.9: Resulting deformations for the study case n°2

Table D.2: Comparison of axial forces in fusible link bewteen Ls-dyna and RFEM5 for case n°2

Case n°2	LS-DYNA	RFEM5	**LS DYNA / RFEM 5**
Time (min)	17,017	17	**1,00**
Force (KN)	14,86	17,649	**0,84**

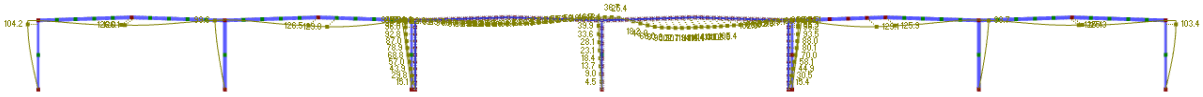

Figure D.10: Resulting deformations for the study case n°3

Table D.3: Comparison of axial forces in fusible link bewteen Ls-dyna and RFEM5 for case n°3

Case n°3	LS-DYNA	RFEM5	**LS DYNA / RFEM 5**
Time (min)	17,566	18	**0,98**
Force 1 (KN)	-36,9	-44,142	**0,84**
Force 2 (KN)	-42,52	-45,036	**0,94**